



**HAL**  
open science

# Modélisation multi-physique de l'électrode de graphite au sein d'une batterie lithium-ion : Etude des hétérogénéités et des mécanismes de vieillissement

Nicolas Dufour

► **To cite this version:**

Nicolas Dufour. Modélisation multi-physique de l'électrode de graphite au sein d'une batterie lithium-ion : Etude des hétérogénéités et des mécanismes de vieillissement. Mécanique des matériaux [physics.class-ph]. Université Grenoble Alpes, 2019. Français. NNT : 2019GREAI007 . tel-02148211

**HAL Id: tel-02148211**

**<https://theses.hal.science/tel-02148211>**

Submitted on 5 Jun 2019

**HAL** is a multi-disciplinary open access archive for the deposit and dissemination of scientific research documents, whether they are published or not. The documents may come from teaching and research institutions in France or abroad, or from public or private research centers.

L'archive ouverte pluridisciplinaire **HAL**, est destinée au dépôt et à la diffusion de documents scientifiques de niveau recherche, publiés ou non, émanant des établissements d'enseignement et de recherche français ou étrangers, des laboratoires publics ou privés.

## THÈSE

Pour obtenir le grade de

### **DOCTEUR DE LA COMMUNAUTE UNIVERSITE GRENOBLE ALPES**

Spécialité : 2MGE (Matériaux, Mécanique, Génie civil, Electrochimie)

Arrêté ministériel : 25 mai 2016

Présentée par

**Nicolas DUFOUR**

Thèse dirigée par **Yann BULTEL**, Professeur, Grenoble INP<sup>2</sup>  
préparée au sein du **Laboratoire LMP, CEA-Liten, Grenoble**  
dans l'**École Doctorale d'Ingénierie - Matériaux, Mécanique,**  
**Environnement, Energétique, Procédés, Production (I-MEP2)**

### **Physics-based modeling of graphite electrodes inside lithium-ion battery: Study of lithiation heterogeneities and aging mechanisms.**

Thèse soutenue publiquement le **8 Février 2019**

devant le jury composé de :

**M. Sylvain FRANGER**

Professeur des Universités, Université Paris Sud, Examineur, Président  
du Jury

**M. Charles DELACOURT**

Chargé de Recherche, CNRS, Rapporteur

**M. Stéphane RAËL**

Professeur des Universités, Université de Lorraine, Rapporteur

**M<sup>me</sup>. Nathalie LEGRAND**

Ingénieur-chercheur, Saft Batteries, Examineur

**M. Yann BULTEL**

Professeur des Universités, Grenoble INP, Directeur de thèse

Et des membres invités :

**M<sup>me</sup>. Marion CHANDESRIS**

Ingénieur-chercheur, CEA Grenoble, Invité

**M. Mikael CUGNET**

Ingénieur-chercheur, CEA Grenoble, Invité





*L'auteur compte moins que sa pensée.*

—Confucius Ranfourard

# Remerciements

Ces années de thèse représentent la somme de travaux que je n'aurais pu mener seul. Je tiens à remercier toutes celles et ceux qui ont pu contribuer de près ou de loin à ce travail de recherche.

Avant toute chose, je remercie Monsieur Charles Delacourt et Monsieur Stéphane Raël d'avoir accepté de rapporter mon manuscrit. Leurs relectures approfondies et leur remarques constructives ont été d'un grand intérêt et ont permis d'ouvrir des nouvelles pistes de recherches. Je remercie Monsieur Sylvain Franger d'avoir accepté de présider mon jury de thèse, et Madame Nathalie Legrand d'avoir accepté d'y participer.

Je suis très heureux d'avoir eu Yann Bultel comme directeur de thèse; ton humanité, ta patience et ta compréhension font de toi un directeur exemplaire. Je remercie très chaleureusement mes encadrants Marion Chandesris et Mikael Cugnet: Marion pour sa rigueur, précision et motivation infaillible qui permettent d'être fier de son travail et Mikael pour ses contre-éclairages et ses relectures millimétriques.

Je voudrais remercier Samuel Tardif et toute l'équipe de l'expérience Synchrotron pour avoir pu mener ce beau projet très complexe en un temps très limité. Andreas Johannes pour son temps et sa patience de pilote de ligne (ID13).

Au sein du laboratoire, merci à Sylvie Génies qui a toujours su prendre du temps pour expliquer les choses de l'électrochimie et m'introduire aux joies et mystères de l'expérimental. Merci à Pierre Bernard pour m'avoir appris et apporté pleins de conseils techniques (notamment la fameuse règle des 3 secondes au sol). Merci à Pascal pour les lumières, Ramon pour le texte et Guillaume pour le son.

Un grand merci au gang des naufragés de 324 avec qui j'ai passé des années intellectuellement et philosophiquement intenses: Bobo, Maxime, et Gauthier. Une pensée pour Yusef chez qui le refuge climatique aura duré 2 mois, décisifs. Merci à toutes celles et ceux qui m'ont apporté des environnements d'écriture hors normes, notamment Esther pour la clim, Dorian pour GoT, Paul pour la BM, et Jerem pour l'Atlas.

A ma mère, mon père, mon frère, aux amis de St Rémy et de Grenoble qui m'ont apporté la quadruple compétence Ingénieur-Docteur-Rénovateur-d'appartement-Voyageur et qui représentent toutes les grandes étincelles de ma vie.

# Contents

<b>1</b>	<b>Introduction</b>	<b>1</b>
<b>2</b>	<b>Development and validation of a porous graphite electrode model</b>	<b>6</b>
2.1	Electrochemical study of graphite and NMC electrodes . . . . .	7
2.2	Half-cell model presentation . . . . .	14
2.3	Physical parameters validation . . . . .	25
2.4	Half-cell model validation . . . . .	40
2.5	Conclusion . . . . .	46
<b>3</b>	<b>Performance limitations of graphite electrode : lithiation heterogeneities during operations</b>	<b>48</b>
3.1	Evaluation of the lithiation heterogeneities inside the electrode . . . . .	50
3.2	Study of the lithiation heterogeneity mechanism . . . . .	59
3.3	Particles shape and size distribution influence on lithiation heterogeneities . . . . .	65
3.4	Experimental <i>operando</i> observations of lithiation heterogeneities . . . . .	76
3.5	Conclusion . . . . .	82
<b>4</b>	<b>Aging phenomena in lithium-ion cell</b>	<b>83</b>
4.1	Aging sources inside lithium-ion batteries . . . . .	84
4.2	Experimental cell aging . . . . .	89
4.3	Full cell model development and validation . . . . .	98
4.4	Aging parameter study . . . . .	104
4.5	Conclusion . . . . .	108
<b>5</b>	<b>Aging models of the graphite electrode</b>	<b>109</b>
5.1	Primary aging source : the Solid Electrolyte Interface . . . . .	110
5.2	Secondary aging source : the lithium-plating reaction . . . . .	125
5.3	Conclusion . . . . .	133
<b>6</b>	<b>Perspectives and Conclusion</b>	<b>134</b>

# List of Figures

1.1	Principles of a lithium-ion cell during discharge . . . . .	2
2.1	SEM pictures of graphite particles (a) and cross-section of the $W_3$ graphite electrode (b) . . . . .	8
2.2	Cell voltage of a lithium-graphite coin-cell with a $W_2$ loading ( $7.9 \text{ mg} \cdot \text{cm}^{-2}$ ) at different lithiation C-rates . . . . .	10
2.3	Experimental normalized lithiated fraction of graphite with respect to current-density (a) and C-rate (b) for different mass-loadings . . . . .	11
2.4	SEM image of an NMC electrode . . . . .	12
2.5	Experimental cell voltage of $W_2$ lithium-NMC coin-cell during different delithiation rates (a) and relation between current-density and final delithiated fraction of NMC for different mass loadings (b) . . . . .	13
2.6	Scheme of the continuum media approach . . . . .	15
2.7	Diagram of the half-cell model . . . . .	19
2.8	Equilibrium potential curves of graphite (a) and NMC (b) extracted from experimental galvanostatic charge and discharge . . . . .	29
2.9	Extraction of lithium exchange current density from experimental Current-Voltage step curve . . . . .	30
2.10	Simulated lithiation curves of a $W_2$ graphite at C/2 with different charge transfer rate . . . . .	31
2.11	Simulated lithiation curves of a $W_2$ graphite at C/2 with different lithium diffusion coefficients inside graphite a) and different Bruggeman coefficients b) . . . . .	32
2.12	Simulated lithiation curves of a $W_2$ graphite at C/2 with different porosity (a), particles radius ( $\mu\text{m}$ ) (b) and ionic lithium diffusion coefficient ( $\text{m}^2 \cdot \text{s}^{-1}$ ) (c) . . . . .	34
2.13	Simulated cell voltage difference between spherical particle and cylindrical particle models during lithiation at C/10, C/4, C/2 and 1C. . . . .	35
2.14	Calibrated model and experimental result on different lithiation current (C/10, C/2, 1C, 2C) for mass-loading $W_1$ , $W_2$ and $W_3$ on lithium-graphite cell . . . . .	42
2.15	Calibrated model and experimental result on different delithiation current (C/10, C/2, 1C, 2C) for mass-loading $W_1$ , $W_2$ and $W_3$ on lithium-NMC cell . . . . .	43

2.16	Comparison between constant and variable coefficient diffusion (a) and effects on cell voltage during a simulated C/2 lithiation (b)	45
2.17	Experimental and simulation comparison on cell voltage relaxation on a $W_2$ lithium-graphite cell after a C/2 lithiation	46
3.1	Simulated lithium salt concentration profiles inside the electrode at the end of lithiation, at C/10 and 1C for different mass-loadings (5.7, 7.9, and 12.0 mg · cm <sup>-2</sup> )	51
3.2	Simulated overpotential profiles inside electrode at 20 % SOL, for different mass loadings (5.7, 7.9, and 12.0 mg · cm <sup>-2</sup> ) and C-rates (C/10 and C/2)	52
3.3	Simulated lithium stoichiometry at particle surface and center through electrode thickness at 20 % SOL for a C/10 and C/2 lithiation on a $W_3$ graphite electrode (12.0 mg · cm <sup>-2</sup> )	52
3.4	Simulated NAAD of particle surface stoichiometry at different mass-loadings (5.7, 7.9, and 12.0 mg · cm <sup>-2</sup> ) and C-rates (C/10, C/2, 3/4C).	54
3.5	NAAD of particle surface stoichiometry obtained for different constants of charge-transfer on a simulated $W_2$ graphite lithiation (C/2)	55
3.6	NAAD of particle surface stoichiometry obtained at different particle shape (a) and particle radius (b) on a simulated $W_2$ graphite lithiation (C/2)	56
3.7	NAAD of intercalated lithium concentration at different solid diffusion coefficient (a) and average lithium stoichiometry at particle surface (b) obtained for a simulated $W_2$ graphite lithiation (C/2)	56
3.8	NAAD of particle surface stoichiometry at different Bruggeman number (a) and lithium salt diffusion coefficient (b) obtained for a simulated $W_2$ graphite lithiation (C/2)	57
3.9	Interpolated experimental resistances for different mass-loadings (5.7, 7.9, and 12.0 mg · cm <sup>-2</sup> ) and graphite equilibrium potential	58
3.10	Decomposition of potentials along a possible pathway followed by a charge inside graphite electrode during lithiation.	60
3.11	Pathway resistance decomposition at 10 % electrodes depth (a, up) and 90 % electrodes depth (a, bottom) during lithiation and complete pathway resistance at 10, 50 and 90 % electrodes depth during lithiation (b).	63
3.12	Schematic interpretation of the three main steps leading to heterogeneous and homogeneous graphite intercalation along electrode during lithiation.	64
3.13	Comparison between equilibrium curves and NAAD of $W_2$ graphite, LFP and NMC electrodes during a simulated C/2 lithiation	65
3.14	Mean lithiation stoichiometry for two particle shapes at two different thickness position during a simulated lithiation (C/2) on a $W_2$ graphite	68

3.15	NAAD of $x_{\text{Li}}$ and maximum stoichiometry difference during a simulated lithiation (C/2) of a $W_2$ graphite with two different shapes . . . . .	69
3.16	Experimental graphite and NMC particle-size distributions . . . . .	70
3.17	Cell voltage and mean lithiation on two different particles at two different thickness position during a simulated lithiation (C/2) on a $W_2$ graphite with two particles sizes . . . . .	70
3.18	NAAD of $x_{\text{Li}}$ and maximum stoichiometry difference during a simulated lithiation (C/2) on a $W_2$ graphite . . . . .	71
3.19	Particle size distribution of graphite and polynomial approximation . . . . .	72
3.20	Cell voltage and stoichiometry differences during a simulated C/2 lithiation on a $W_2$ graphite . . . . .	73
3.21	Graphite lithium stoichiometry at particle surface (a) and normalized maximal stoichiometry difference between surface and center (b) at the end of a simulated C/2 lithiation on a $W_2$ graphite electrode . . . . .	74
3.22	Simulated cell voltage through different particle models during a C/10 (a) and C/2 (b) lithiation on a $W_2$ graphite . . . . .	75
3.23	Picture of the <i>operando</i> lithium-graphite cell (4 cm high) . . . . .	78
3.24	Diagram of the <i>operando</i> measurement of local graphite SOL . . . . .	79
3.25	Lithium-graphite phases recognition for a given diffraction spectra (a) and localized intensities of $\text{LiC}_{12}$ , $\text{LiC}_{24}$ and graphite phases inside electrode near end of delithiation (0.45 V) (b) . . . . .	80
3.26	Experimental potential of the $W_3$ graphite electrode ( $12.0 \text{ mg} \cdot \text{cm}^{-2}$ ) during delithiation at $0.5 \text{ mAh} \cdot \text{cm}^{-2}$ . . . . .	80
3.27	Experimental lithium phase distribution through the graphite electrode thickness at 0.11 V (a), 0.21 V (b), 0.32 V (c), and 0.53 V (d) during a delithiation at $0.5 \text{ mAh} \cdot \text{cm}^{-2}$ . . . . .	81
4.1	Degradation mechanisms in lithium-ion cells (reproduced from [1], summarized from [2, 3]) . . . . .	85
4.2	Prismatic cell and measured potential differences (a) and reference electrode details (b) . . . . .	89
4.3	Experimental normalized capacity of the cells discharged through cycling (a) and charged during the floating step (b) . . . . .	91
4.4	Experimental premature capacity loss (a) and average cell voltage during discharge through cycle (b) . . . . .	92
4.5	Experimental cell voltage (a), positive electrode (b, up), and negative electrode (b, down) potentials during check-up at C/5 before and after aging (cycling conditions) . . . . .	93
4.6	Experimental capacity through initial (up) and final (down) check-up cycles for a pouch in cycling conditions . . . . .	94

4.7	Experimental normalized reversible capacity of the cells in calendar aging . . . . .	95
4.8	Experimental potential variations at the negative side (a) and positive side (b) through calendar aging . . . . .	96
4.9	Capacity through initial (up) and final (down) check-up cycles for a cell aged in calendar conditions . . . . .	96
4.10	Experimental cell voltage (a), negative electrode and positive electrode potential (b) before and after aging during calendar conditions (100 % SOC) . . . . .	97
4.11	Diagram of the different aging phases through cycling . . . . .	98
4.12	Pouch cell model diagram . . . . .	100
4.13	Formation cycle and initial conditions in a graphite/NMC cell . . . . .	101
4.14	Experimental and simulated cell voltage during a check-up cycle on a fresh cell (a) and after 900 cycles (b) . . . . .	103
5.1	SEI growth principles . . . . .	111
5.2	Fits of SEI growth models : simulated and experimental normalized capacity (a) and simulated SEI thickness evolutions (b) on a selected cell . . . . .	117
5.3	Cell capacity decomposed as cyclable lithium loss and positive material loss . . . . .	118
5.4	Experimental and simulated normalized discharge capacity (a) and simulated average SEI thickness and negative potential during the first cycle at C/2 (b) . . . . .	120
5.5	. . . . .	121
5.6	Average SEI thickness and graphite potential during first cycle (a) and local SEI thickness at the end of the first lithiation (b) on a continuous size distribution model	122
5.7	Experimental and simulated reversible capacity (a) and average SEI thickness evolution and negative electrode potential (b) during the last check-up . . . . .	124
5.8	Negative electrode potential (a) and lithium layer (b) during simulated cell charge at C/10, 3C/4, 1C, and 2C. . . . .	127
5.9	Average thickness of the lithium layer during a simulated 2C charge for different initial states of lithiation of the graphite electrode ( $SOL_{gr}^{ini}$ ) . . . . .	128
5.10	Porosity versus SEI thickness evolution . . . . .	130
5.11	Pore-clogging model (a) and tortuosity model (Equation 5.32) versus SEI thickness evolution (b) . . . . .	131
5.12	Simulated discharge capacity and local tortuosity evolution (0, 5, 10, 50, and 90 % depth from the separator) throughout cycling (C/2) with a tortuosity model . . . . .	132
5.13	Normalized plating rate as a function of SEI thickness at a 2C cell charge . . . . .	133

# List of Tables

2.1	Experimental electrode characteristics of graphite (a) and NMC (b)	14
2.2	Governing equations in the P2D model	24
2.3	Reliable physical parameters of graphite a) and NMC b)	27
2.4	List of separators, electrolyte, and lithium electrode parameters on a simulated $W_2$ graphite lithiation at C/2	36
2.5	List of graphite electrode parameters on a $W_2$ graphite lithiation at C/2	38
2.6	List of NMC electrode parameters on a $W_2$ NMC delithiation at C/2	39
2.7	Adjusted parameters for the graphite a) and NMC b) electrode model	41
3.1	Current and lithiation changes during reference simulation (C/2 lithiation) between different particle size models	75
4.1	Parameters of the full cell model	103
4.2	Simulated capacity losses and impedance rise fitted by adjusting different model parameters	105
4.3	SEI properties (from [4])	106
5.1	Fitting results on SEI growing models	116
5.2	Parameters for the reversible SEI model	124
5.3	Lithium plating reaction parameters	127

# Chapter 1

## Introduction

Energy availability issues, limited resources of our world and the sudden biodiversity collapse [5, 6] raise awareness to the critical need of efficiency, durability and low ecological footprint in all human processes [7]. In complement to a mandatory sustainable and resilient society [8], a hypothetical energy storage system, using a limited quantity of material resources, robust and highly recyclable could be a key to a viable future in regard to the intermittent renewable energy sources. The current problematic relies on the right technology choice that can reversibly store and convert energy into electricity, which is currently used in almost all human tools.

Electrochemical batteries, one of the existing solution [9], store reversibly electrical energy thanks to electrochemical reactions. Different devices exist depending on the chemistry used, but principles remain the same: two separate redox processes exchange electrons through an external electrical circuit. This phenomenon is allowed by the ionic conductivity and electronic insulating medium (electrolyte) between two reactive materials (electrodes). Optimization and controls of electrochemical batteries require a deep understanding of main principal phenomena. In this context, predictive models start to be more and more used to optimize performance and durability of those systems.

### The lithium-ion technology

The lithium-ion batteries (LIB) are electrochemical accumulators based on the redox processes of lithium-based material. Commercialized by SONY in the 90s, lithium-ion batteries were gradually used, and sometimes replace lead-based accumulators or nickel-based batteries (NiCd and NiMh). With excellent power and energy densities, lithium-ion batteries are nowadays commonly found in almost all portable electronic devices and are promising candidates for electromobility and stationary energy storage. In recent years, development of new materials has increased the specific energy of the averaged commercial cell<sup>1</sup> from the original SONY at  $80 \text{ Wh} \cdot \text{kg}^{-1}$  [10], to more than  $200 \text{ Wh} \cdot \text{kg}^{-1}$  in 2018 [11]. These developments push forward the material capacity, the stability

---

<sup>1</sup>In comparison, the specific energy produced by the detonation of trinitrotoluene (TNT) is up to  $1250 \text{ Wh} \cdot \text{kg}^{-1}$

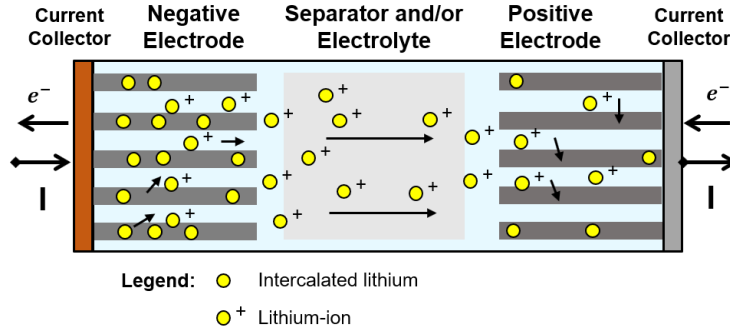


Figure 1.1: Principles of a lithium-ion cell during discharge

of high-potential electrodes, electronic and ionic conductivity, economic scale factor aspects and safety [12].

LIB are characterized by their capacity (mAh) and nominal output voltage (V), which define the amount of energy available (Wh). In order to compare similar charge or discharge between batteries, a normalized rate is defined, named *C-rate*. At a given constant current, the corresponding C-rate is the inverse of time (in hours) theoretically required for a full cell charge or discharge. To have the current/C-rate correspondence, it is therefore necessary to know the capacity of the cell.

A LIB is composed of different cells, associated in serie or parallel. The cell is the smallest functional element of LIB and they come in different formats: cylindrical, prismatic or as pouch bag. They are composed of two electrodes separated by an electrical insular media, which can be a solid electrolyte or a separator filled with electrolyte (Figure 1.1). On both sides of this pile-up, two current collectors are found, in copper at negative side and in aluminum at positive side. When the cell is connected to an external circuit, electrochemical reactions occur within the electrodes to counter the solicitation, allowing charged species transport in the electrolyte. A lithium-ion cell can be charged and discharged reversibly.

When the cell is discharged, reduction reactions occur at the positive electrode: electrons are captured by the terminals and recombined with the lithium-ions into the active material. These materials are called *intercalation material* because lithium are intercalated into the material crystallographic structure. These electrodes are based principally on cobalt, nickel, manganese, or iron-phosphate and are classed according to their lattice structure: olivine ( $\text{LiFePO}_4$  or LFP), layered transition-metal oxides ( $\text{LiCoO}_2$  or LCO) or spinel ( $\text{LiMn}_2\text{O}_4$  or LMO) [13]. Today, NMC-based materials ( $\text{LiNi}_x\text{Mn}_y\text{Co}_{1-x-y}\text{O}_2$ ) tends to equip most of electric vehicle due to recent large energy density improvements [10].

On the other side of the cell, the negative electrode is oxidized during discharge. That is to say, lithium ions are extracted from the electrode material, releasing electrons collected by the current collector. This electrode, named *anode* in this situation, may be a lithium metal sheet (Li), or a porous structure often composed with graphite ( $\text{LiC}_6$ , silicon can be added), sometimes lithium

titanate ( $\text{Li}_4\text{Ti}_5\text{O}_{12}$ ) [10][14].

Introduced in the 90', graphite has increased the durability and safety of first electrodes made of lithium. When cycled, lithium electrodes suffered from dendritic formations, which lead to dramatic short-circuits. However, recent developments return to lithium electrode but combined with a solid electrolyte separator (so-called solid-state battery [15]), which enhances durability, safety, and specific energy (more than  $480 \text{ Wh} \cdot \text{kg}^{-1}$  predicted [16])

Graphite, which is safer, is still used in most current LIB, even if it has less specific energy than lithium. This material displays nonetheless a reversible lithium intercalation mechanism with good structural and interfacial stability, good electronic conductivity, as well as good a specific capacity of  $372 \text{ mAh} \cdot \text{g}^{-1}$  and a low operating potential [17]. In addition to the non-toxicity and low cost, all these properties make graphite a reliable, cheap and sustainable active material for negative electrodes. Nevertheless, it undergoes a multitude of aging mechanisms, which modify its physical and electrochemical properties and mainly contribute to the overall LIB performance degradation [2]. These aging mechanisms lead to the consumption of lithium-ions, destruction of the active material and loss of active surface. Overall, aging mechanisms result in a loss of capacity and power performance [18].

Recent efforts are devoted to reduce these aging impacts as well as increase the security, in particular under extreme operating conditions (fast charges [19], unusual temperatures [20, 21]) which may lead to thermal runaway [22]. The knowledge, understanding and quantification of degradation issues are the key in this new phase of optimisation of lithium-ion technology. Unfortunately these multiple degradation phenomena are interdependent and are difficult to characterize individually [2]. To decouple and understand them, mathematical models are useful tools to achieve this challenge.

## Lithium-ion cells modeling

Many mathematical models can describe LIB behaviors and aging phenomenon. They may operate on a wide range of scales, from the atomic one, describing the intercalation mechanisms, to the battery packs scale, whose thermal responses are sometimes approximated using equivalent electrical circuits. Models fall into three main categories: first-principle based, empirical ones or electrochemical based.

First-principle models are based on molecular dynamics or density functional theory (so called DFT). Fundamental physics-based approaches and quantum mechanics are used to model atomic interactions and predict molecular behavior. They bring guidelines for new electrode materials syntheses or interfacial chemistry characterizations [23, 24]. The complex interactions of lithium displacement and degradation in crystallographic structure can thus be modeled and predicted [25].

Empirical or statistical models are more focus into the macroscopic and observable quantities of the system [26]. These models can be built on equivalent thermal or electrical circuits, adjusted

(or trained) by experimental data. They simplify electrochemical behavior and they are mainly used in the cell management electronics, so called Battery Management System (BMS), where computational resources are limited. They predict state of charge (SOC), state-of-health (SOH), internal resistance or any information that can be used to manage the system. If these models are relatively simple to use and implement, they can be long to adjust, cannot be extrapolate to other cells or LIB technology, and partially or totally disconnected from physical reality.

On the opposite, electrochemical models are physics-based, translating electrochemical phenomena into mathematical equations. Focus is made on the microscopic scale, on which mechanisms are averaged. To this aim, these models couple different physics, which are mechanistically described: electrochemical reactions, transport equations and thermal effects. Local conditions inside the cell (such as local potential or concentrations) and global physical variables of the electrochemical cell are thus accessible. The best-known electrochemistry based models is the porous electrode model developed by J. Newman and co-workers. Until today, a lot of study are performed on its basis [27, 28]. As instance, this physical model, based on conservation equations, can be up-graded by adding other physical phenomena such as thermal coupling [29], side reactions [30] or operations with large electrode surfaces [31]. If electrochemical models sound useful for material, electrode and cell designs, they need a lot of computational resources, especially for n-dimensionnal studies, if exact geometrical and physical electrode structures are involved [32].

## **Topic of the current thesis**

Although characterized and used since the 90', the graphite electrode is still studied today. All LIB rely on this active material, which is a important bottle-neck for performance and durability improvements. The demand of high energy densities and quick charges put pressure on this material. The graphite properties are thus optimized, including all its aspects: surface kinetics, particle size and morphology. Models, especially physics-based models, are not frequently used, but are useful to quickly question the viability of new improvements, as instance, on internal operation or aging tendencies. This kind of model approach the physics reality, giving an average representation of the local conditions inside the cells.

In the context of this thesis, we will focus on electrode scale models in order to draw conclusions on the graphite electrode performance, driving forces of inhomogeneous operations and aging mechanisms. To this goal, experimental results on graphite electrodes are thus needed to build and validate the basis of a physics-based model. Principal mechanisms are selected and represented, given the model simplification framework. Next step is to used the physics based models in a real cell configuration (graphite/NMC), describe graphite performance limits due to internal physics and reproduce by modelling, the principal aging mechanisms.

In a first part of this thesis, electrochemical responses of different mass-loaded graphite electrodes are investigated for a wide range of lithiation current and a porous electrode model is used

to predict these behaviors. A sensitivity analysis coupled with a minimal exploitation on lithiation experiments is used to deduce which set of parameters has a strong influence on the porous electrode model of graphite. Electrochemical results are then used to validate this model.

In a second part, electrode parameters and the local conditions inside the validated model are explored, to draw the limits to its homogeneous lithiation and quantify spatial lithiation heterogeneities inside the electrode thickness. Simulation results are compared experimentally to an *operando* measurement of the distribution of lithium through the graphite electrode.

In a third part, experimental results on graphite-NMC cells are analyzed to draw the aging tendencies (in calendar and cycling). The porous graphite electrode model is adapted and validated in a full cell configuration (against NMC) and the most influential model parameters on aging are derived from its study.

Finally, different models of degradations are developed in regard to the experimental findings, focusing on mechanisms impacting the negative electrode (SEI growth and Li plating). Evolution of discharge capacity loss, sudden capacity loss, and capacity recovery are modeled and implemented via physics-based mechanisms on the performance model. The different impacts of these mechanisms are apprehended globally and locally.

# Chapter 2

## Development and validation of a porous graphite electrode model

### Contents

---

<b>2.1</b>	<b>Electrochemical study of graphite and NMC electrodes . . . . .</b>	<b>7</b>
2.1.1	Graphite electrode study . . . . .	7
2.1.2	NMC electrode study . . . . .	11
2.1.3	Electrodes characteristic summary . . . . .	13
<b>2.2</b>	<b>Half-cell model presentation . . . . .</b>	<b>14</b>
2.2.1	Macroscopic description and governing equations . . . . .	14
2.2.2	Model hypotheses . . . . .	18
2.2.3	Resolution . . . . .	23
<b>2.3</b>	<b>Physical parameters validation . . . . .</b>	<b>25</b>
2.3.1	Parameter review . . . . .	26
2.3.2	Sensitivity analysis protocol . . . . .	30
2.3.3	Results and summary of the sensitivity analysis . . . . .	35
<b>2.4</b>	<b>Half-cell model validation . . . . .</b>	<b>40</b>
2.4.1	Validation procedure . . . . .	40
2.4.2	Simulation results . . . . .	40
2.4.3	Model limitations . . . . .	43
<b>2.5</b>	<b>Conclusion . . . . .</b>	<b>46</b>

---

In this chapter, the development and validation of a porous electrode model are explained for lithium-graphite and lithium-NMC configurations. Both electrodes are cycled in a coin-cell format against a lithium metal counter-electrode, which is called a *half-cell configuration*.

Different half-cells (lithium-graphite and lithium-NMC) are produced at different mass-loadings of electrode material. Half-cells are investigated, lithiated and delithiated at various applied currents in order to analyze their electrochemical performance. These experimental investigations provide the basis to set-up and validate physics-based models.

Then, a model of a porous electrode in a half-cell configuration is developed according to the modeling framework of NEWMAN *et al.* [33]. This type of model requires to adjust a large amount of physical parameters. Thus, a model sensitivity analysis is performed to classify and quantify each parameter according to its electrochemical influence. The aim of the sensitivity analysis is to limit the number of parameters to adjust. As a result, model validation requires the calibration of only three parameters corresponding to the kinetic and diffusive phenomena inside the porous electrode.

Finally, experimental and simulated cell voltages are presented for graphite electrode lithiation and NMC electrode delithiation. Model limitations are briefly introduced to improve the calibration process of the modeling electrode.

## 2.1 Electrochemical study of graphite and NMC electrodes

An electrochemical study has been performed on graphite and NMC porous electrodes cycled against a lithium metal counter-electrode in coin cells. Both graphite and NMC electrodes have been manufactured at the laboratory at controlled composition and for different mass-loadings. Active material powders are analyzed by Scanning Electron Microscopy (SEM). Electrodes from each mass-loading are cycled in a coin-cell format at different current densities. The purpose is to study graphite electrochemistry and collect data to validate our porous electrode model in various configurations and operating conditions. In order to validate our graphite electrode model in full-cell configuration, NMC electrodes are analyzed too.

### 2.1.1 Graphite electrode study

#### 2.1.1.1 Electrode composition and half-cell configuration

Three graphite electrodes have been manufactured considering three different mass-loading of 5.7, 7.9, and 12.0  $\text{mg} \cdot \text{cm}^{-2}$ , respectively named  $W_1$ ,  $W_2$ , and  $W_3$  in the following. The graphite electrodes contain 96 wt% of SLP30 graphite powder from Timcal. The graphite powder is the electrochemically active material in the porous electrode. The remaining part of the electrode is composed of carboxymethyl cellulose (CMC) at 2 wt% and Styrene-Butadiene Rubber (SBR) also at 2 wt%. CMC and SBR are mechanical binders, used to enhance the mechanical behavior of the

whole electrode. With a graphite theoretical capacity of  $372 \text{ mAh} \cdot \text{g}^{-1}$  and a 96 % weight fraction, electrode areal capacities are expected to be 2.0, 2.8, and  $4.3 \text{ mAh} \cdot \text{cm}^{-2}$ . The porosity is set during the manufacturing process to ensure the same value for all the electrodes. During calendaring, the electrode thickness is calculated, considering the electrode mass-loading and a porosity goal of an average 35 % volume fraction. Therefore, only thicknesses differ among electrodes and are directly correlated to their respective mass-loading

The studied coin-cells consist of a metal lithium sheet on an aluminum collector, two Celgard 2400 separators, and a graphite coated copper collector. Inside the coin-cell, graphite electrodes are round chips of 14 mm diameter. Coin-cells are filled with an electrolyte composed of 1 M lithium hexafluorophosphate ( $\text{LiPF}_6$ ) in 1:1:1 weight proportion of ethylene carbonate (EC), ethyl methyl carbonate (EMC), and dimethyl carbonate (DMC). We note that the electrolyte does not contain any additives such as vinylene carbonate (VC) or fluoroethylene carbonate (FEC) to stabilize aging process and irreversible lithium loss during the first lithiation [34, 35]. This choice has been made because the amount of available lithium is not a limiting factor in a half-cell configuration thanks to the lithium metal counter-electrode and moreover, in this chapter, we are only interested in material performance.

To model the electrode, we need to know the graphite particle geometry. SEM observations show the typical shape of the SLP30 graphite powder that is similar to literature references available for the same graphite type [36] (Figure 2.1a). Graphite particles are 2 to 10  $\mu\text{m}$  thick flakes or flat cylinders of 16  $\mu\text{m}$  average diameter, horizontally stacked along the electrode thickness, their base being parallel to the current collector (Figure 2.1b)

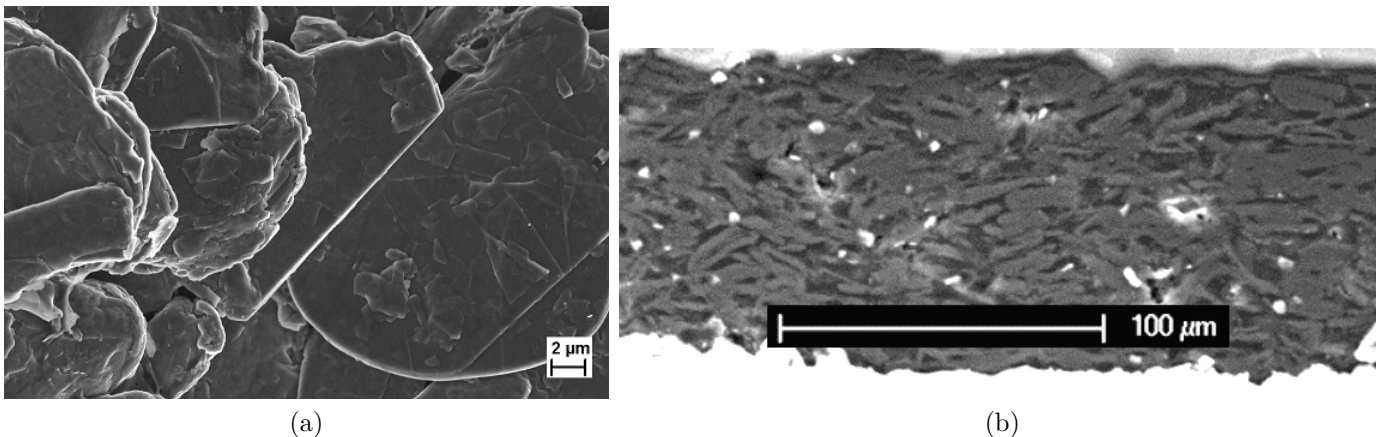


Figure 2.1: SEM pictures of graphite particles (a) and cross-section of the  $W_3$  graphite electrode (b)

### 2.1.1.2 Graphite electrochemical study

#### Formation

After assembly, coin-cells are subjected to a formation protocol. Two cycles of full lithiation/delithiation are performed between 0 and 1.6 V at C/10 to get good Solid Electrolyte Interface (SEI) properties [37]. The applied current corresponding to a C/10 rate is calculated considering the coin-cell theoretical capacity. A slow first lithiation of graphite enhances SEI mechanical and electrical properties. During the two first cycles, we measure a capacity loss between the first lithiation and the first delithiation at an average 4 % for the three mass-loadings. This loss corresponds in a large part to the SEI formation and parasitic reactions, which can involve lithium ions. All the electrochemical measurements on coin-cells are performed using a modular potentiostat/galvanostat/EIS VMP3 from Bio-Logic, Claix, France. Ambient temperature is controlled and kept at 20 °C, but the cell temperature is not monitored.

#### C-rate signature

After the formation protocol, experimental capacities of the three different coin-cells are given for the first C/10 lithiation and delithiation curves with a constant voltage floating at the end of the delithiation process. Reversible capacities reach 2.93, 4.14, 6.43 mAh for loading  $W_1$ ,  $W_2$ , and  $W_3$  respectively. They correspond to practical areal capacities of respectively 1.9, 2.7, and 4.2 mAh · cm<sup>-2</sup>, 7 %, 5 %, and 3 % lower than the expected theoretical values. We note that the areal capacity increases with increased mass-loading, but due to the non-uniformity of collector coating during electrode synthesis, this tendency is not relevant. Indeed, mass-loading deviation on the electrode fabrication process reaches 3.5 %, 4 %, and 5 % for mass-loading  $W_1$ ,  $W_2$ , and  $W_3$  respectively, corresponding to an areal capacity deviation of 0.07, 0.1, and 0.2 mg · cm<sup>-2</sup>. Nevertheless, the obtained electrode specific capacity reaches 340 mAh · g<sup>-1</sup> on average, which is in accordance with the literature (320-360 mAh · g<sup>-1</sup> [38]). Graphite electrode characteristics are summarized in Table 2.2a.

Coin cells are then lithiated until 0 V at various currents from 0.1 to 5C, always starting from a delithiation state, in order to study their electrochemical performance with the same initial conditions. Figure 2.2 shows the cell voltages during lithiation for different C-rates on the  $W_2$  graphite electrode. As can be seen, during the C/10 lithiation, characteristic voltage plateaus of graphite are well defined, but this graphite voltage signature fades away as the C-rate increases. When the C-rate increases, if we look at a fixed charged quantity, the cell voltage decreases. It depicts a cell resistive behavior and a loss in power performance. Moreover, when current increases, the cell voltage reaches the cut-off voltage sooner and lithiation stops, a fewer amount of graphite being lithiated. Consequently, the higher the applied current, the lower is the capacity and power cell performance.

Rate capability limitations of the electrode are emphasized in Figure 2.3a. Lithiated fractions

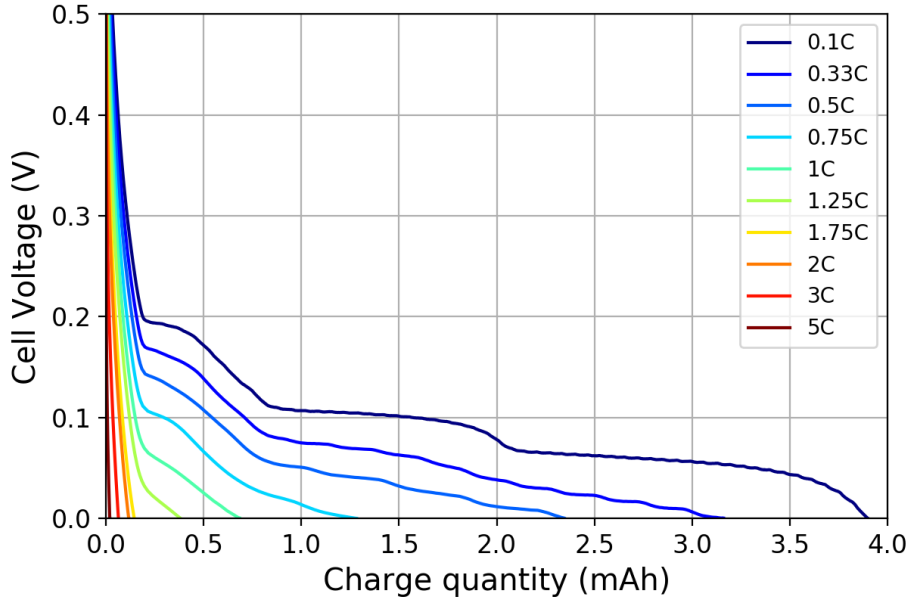


Figure 2.2: Cell voltage of a lithium-graphite coin-cell with a  $W_2$  loading ( $7.9 \text{ mg} \cdot \text{cm}^{-2}$ ) at different lithiation C-rates

of graphite are normalized with the theoretical capacity of respective coin-cells. The mass-loading seems not to have a strong influence on the normalized lithiated fraction, whatever the current density. As the current density rises, the normalized lithiated fraction decreases abruptly for all electrodes. Between 1 and  $3 \text{ mA} \cdot \text{cm}^{-2}$ , the normalized lithiated fraction for each loading goes from 70 % to less than 10 %. Above  $3 \text{ mA} \cdot \text{cm}^{-2}$ , the normalized lithiated fraction falls down to less than 5 % for each mass loading. GALLAGHER *et al.* [39] found out that for any graphite cell, a current density above  $4 \text{ mA} \cdot \text{cm}^{-2}$  should be avoided, because it leads to irreversible processes (lithium plating essentially). Below  $3 \text{ mA} \cdot \text{cm}^{-2}$ , the reduction of the mass-loading slightly improves the lithiation. A maximum of 10 % normalized lithium fraction improvement is observed going from  $W_3$  to  $W_1$  at  $1 \text{ mA} \cdot \text{cm}^{-2}$ . The graphite electrode performance appears to be not correlated to the mass-loading or the cell thickness.

The normalized lithiated fraction of graphite can also be plotted with respect to C-rate instead of current density (Figure 2.3b). The C-rate is defined from the rated capacity usually obtained at a low discharge current (10 hour discharge or more). A C-rate applied on different mass-loadings correspond to different current densities, allowing us to compare equivalent lithiation rate independently from the cell capacity. For all C-rates, the  $W_3$  electrode shows the worst performance compared to all other electrodes. At  $C/5$ , less than 10 % of  $W_3$  is lithiated, whereas almost 30 % of  $W_2$  and more than 50 % of  $W_1$  are lithiated. Between  $C/3$  and  $1.5C$ , the  $W_1$  electrode is always slightly better than  $W_2$ , which is itself better than  $W_3$ . Therefore, the mass-loading (or electrode thickness) has a strong influence on the electrode performance: the higher the mass-loading, the lower is the rate capability.

At first sight, the overall lithiation behavior of graphite appears to be determined only by

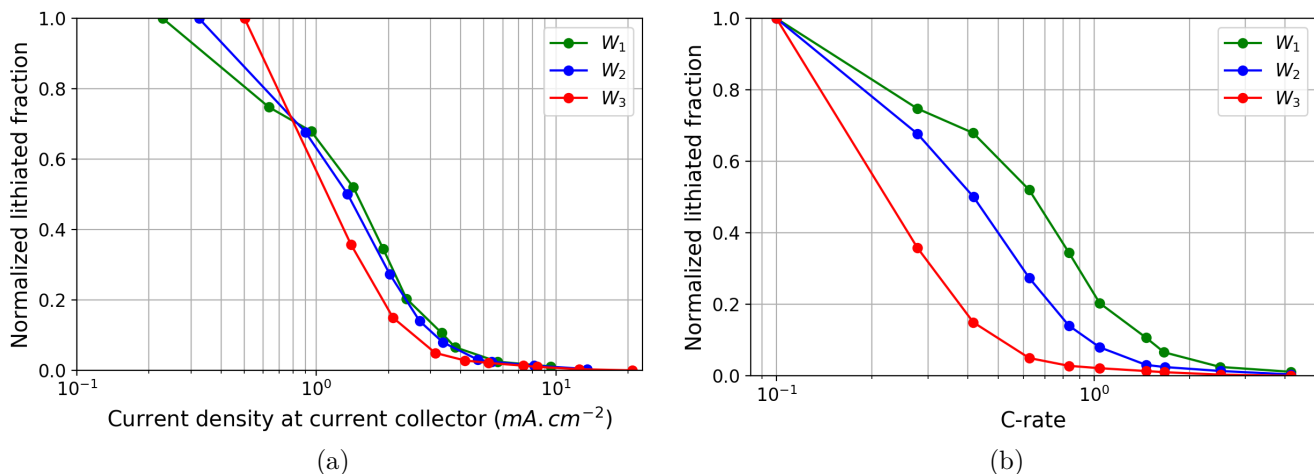


Figure 2.3: Experimental normalized lithiated fraction of graphite with respect to current-density (a) and C-rate (b) for different mass-loadings

its own material properties and to be limited to a specific current density value ( $4 \text{ mA} \cdot \text{cm}^{-2}$ ). However, mass-loading/electrode thickness plays a major role in the graphite rate capability.

## 2.1.2 NMC electrode study

Lithium-NMC half-cells are also built to validate our graphite electrode model in full-cell configuration (cf. Chapter 4).

### 2.1.2.1 Electrode composition and half-cell configuration

NMC electrodes have been produced at the laboratory for different mass-loadings. NMC electrodes are composed of 92 wt% of NMC (111), 2 wt% of Super P C65 (electronic conductor), 2 wt% of VGCF (electronic conductor and mechanical binder) and 4 wt% of PVDF (mechanical binder). The electrode thicknesses have also been controlled in order to have a 35 % porosity for each loading, considering the electrode density. Three electrodes have been manufactured with different mass-loadings:  $11.4$ ,  $16.7$ , and  $24.8 \text{ mg} \cdot \text{cm}^{-2}$ , also named  $W_1$ ,  $W_2$ , and  $W_3$  respectively. The theoretical specific capacity of NMC(111) is  $278 \text{ mAh} \cdot \text{g}^{-1}$ , calculated from the lithium fraction hosted inside the NMC structure. However, this material can only be cycled over a limited lithium stoichiometry (ranging from 0.4 to 1), without any structure collapse which could potentially reduce the intercalation reversibility [40, 41]. It corresponds to a specific capacity of  $177 \text{ mAh} \cdot \text{g}^{-1}$ . So, theoretic areal capacities are expected to be  $1.8$ ,  $2.6$ , and  $3.8 \text{ mAh} \cdot \text{cm}^{-2}$ , for  $W_1$ ,  $W_2$ , and  $W_3$  respectively.

Lithium-NMC coin-cells have the same configuration as the lithium-graphite ones. They are composed of a lithium metal sheet on an aluminum collector, two Celgard 2400 separators, and an NMC-coated aluminum collector. Lithium-NMC coin-cells are filled with the same electrolyte

and NMC electrodes have the same diameter of 14 mm. As a reminder, only the positive electrode composition differs between the lithium-NMC and lithium-graphite coin-cells.

SEM images show that NMC agglomerates differ from graphite ones not only in shape but also in size (Figure 2.4). The NMC active material appears as spherical agglomerates of spherical micro-particles. NMC agglomerates of 6  $\mu\text{m}$  diameter are smaller than graphite particles.

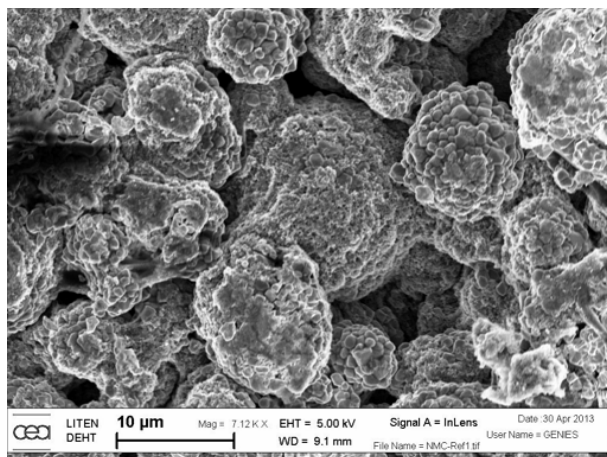


Figure 2.4: SEM image of an NMC electrode

### 2.1.2.2 NMC electrochemical study

#### Formation

A formation protocol has been applied on NMC half-cells, even if NMC electrodes do not need it to form their SEI. Before formation, NMC electrodes are manufactured in a fully lithiated state. Two cycles of delithiation/lithiation are carried out between 2.6 and 4.3 V at C/10. We note an irreversible loss of about 15 % on the first cycle, because a not fully complete re-lithiation happens due to a material structural change at the first delithiation [41]. After these cycles, reversible capacities reach 2.6, 3.9, and 5.7 mAh for loading  $W_1$ ,  $W_2$ , and  $W_3$  respectively. It corresponds to areal capacities of 1.7, 2.5, and 3.7  $\text{mAh} \cdot \text{cm}^{-2}$ . The areal capacity is reduced by 2 % on average compared to the theoretical value. Nevertheless, the specific capacity of electrodes reaches 150  $\text{mAh} \cdot \text{g}^{-1}$ , accordingly to the literature [42]. These information are summarized in Table 2.2b.

#### C-rate signature

After formation, coin-cells are delithiated at various currents from 0.1 to 5C, after a previous complete lithiation at C/10. The electrode delithiation corresponds in this coin-cell configuration to a charging step. The cell voltage rises from 2.6 to 4.3 V. Cell voltages obtained during delithiation are shown in Figure 2.5a for the  $W_2$  electrode. On this figure cell voltages start from 3.7 V at the beginning of delithiation, whereas former lithiation stops at 2.6 V. It is explained by the fact

that in a high lithiation state, the polarization resistance of NMC is large, leading the cell voltage to fall down to 2.6 V at the end of lithiation. During the rest period following the lithiation process, the electrode voltage gradually increases up to 3.6 V, slowly returning to its equilibrium state. As the applied current increases, so does the cell voltage and less electrical charges are extracted from the electrode. Unlike the graphite electrode, the NMC cell voltage appears to be quite monotonic along delithiation. No fade or sudden rises in cell voltage can be seen even at the end of the delithiation. Figure 2.5b presents the normalized delithiated fraction of NMC

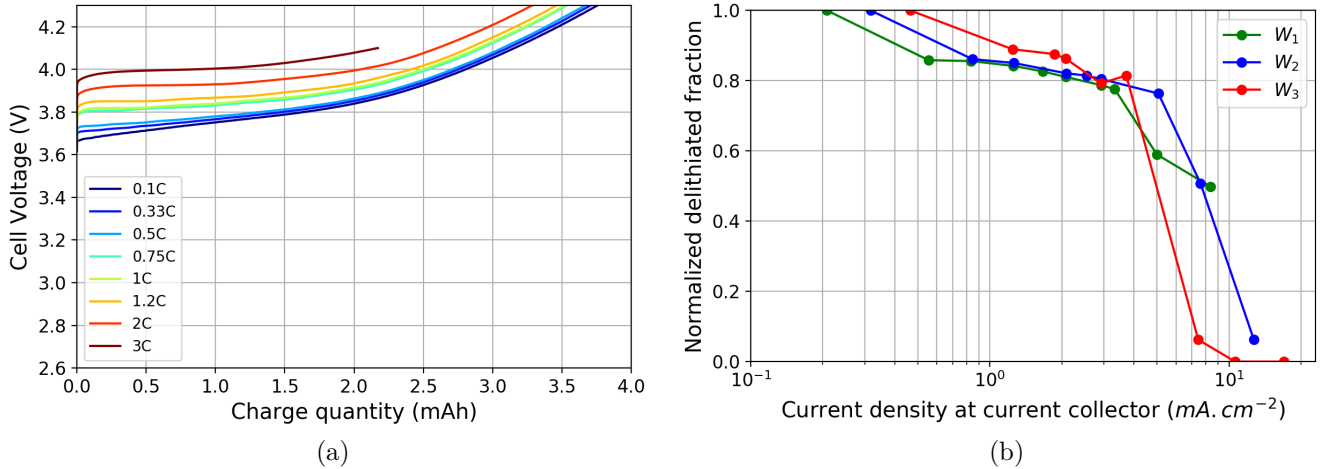


Figure 2.5: Experimental cell voltage of  $W_2$  lithium-NMC coin-cell during different delithiation rates (a) and relation between current-density and final delithiated fraction of NMC for different mass loadings (b)

for different mass-loadings as a function of applied current densities. The lithium-NMC coin-cells have a good performance compared to graphite ones (Figure 2.3a). At  $2 \text{ mA} \cdot \text{cm}^{-2}$ , the NMC electrode can be delithiated at 70 % for all mass-loadings studied, whereas for the same current the different graphite electrodes can be lithiated at a maximum of 30 %. Rate capability falls down after  $8 \text{ mA} \cdot \text{cm}^{-2}$ , but it is up to 4 times better than the graphite performance.

### 2.1.3 Electrodes characteristic summary

Electrode characteristics are summarized in Table 2.2a for graphite electrodes and in Table 2.2b for NMC electrodes. During the first cycle, NMC electrodes show more irreversibilities than the graphite ones. In one hand, the practical specific capacity of graphite is more than twice the practical specific capacity of NMC. On the other hand, NMC can be delithiated at almost 70 % up to  $8 \text{ mA} \cdot \text{cm}^{-2}$ , which is four times the limit current density of graphite. Graphite electrodes display good formation and capacity performances while NMC electrodes display good power performance.

Table 2.1: Experimental electrode characteristics of graphite (a) and NMC (b)

Graphite	$W_1$	$W_2$	$W_3$	NMC	$W_1$	$W_2$	$W_3$
Mass-loading ( $\text{mg} \cdot \text{cm}^{-2}$ )	5.7	7.9	12.0	Mass-loading ( $\text{mg} \cdot \text{cm}^{-2}$ )	11.4	16.7	24.8
Theoretical areal capacity ( $\text{mAh} \cdot \text{cm}^{-2}$ )	2.0	2.8	4.3	Theoretical areal capacity ( $\text{mAh} \cdot \text{cm}^{-2}$ )	1.8	2.6	3.8
Irreversibility at first cycle (%)	2	4	6	Irreversibility at first cycle (%)	18	13	14
Practical areal capacity ( $\text{mAh} \cdot \text{cm}^{-2}$ )	1.9	2.7	4.2	Practical areal capacity ( $\text{mAh} \cdot \text{cm}^{-2}$ )	1.7	2.5	3.7
Practical specific capacity ( $\text{mAh} \cdot \text{g}^{-1}$ )	333	340	347	Practical specific capacity ( $\text{mAh} \cdot \text{g}^{-1}$ )	146	152	150
Reversible coin-cell capacity (mAh)	2.9	4.1	6.4	Reversible coin-cell capacity (mAh)	2.6	3.9	5.7

(a)

(b)

## 2.2 Half-cell model presentation

A physics-based modeling approach has been chosen in this work to study the local behavior of the graphite electrode. Our model is derived from the porous electrode theory introduced by NEWMAN and TIEDEMANN [33] and concentrated solution approximations [43]. This approach provides the global physical quantities characterizing the electrode during operation (voltage, current, temperature...). It also explores the physics governing the electrode behavior along its thickness and down to the radii of active material particles. The different physical mechanisms operating inside the cell are represented by a system of partial differential equations. The continuous approach of the Newman-based model compared to a full morphological modeling can be seen as a limitation for the identification of local heterogeneity [32]. However, the Newman’s modeling approach has been selected to ensure acceptable computational performance and to provide a versatile model suitable for various electrode materials.

### 2.2.1 Macroscopic description and governing equations

Our physico-chemical model is based on the previous work done for lithium-ion batteries by DOYLE *et al.* [44]. The different physical mechanisms operating inside the cell are then modeled at this continuous macroscopic level by a system of equations based on charge and species conservation laws, including their specific transfer/transport mechanisms and their corresponding boundary conditions. Some hypotheses are made to reduce the modeling complexity of the functional elec-

trode.

### Continuum media approach

In the porous electrode theory, the idea is to account for the essential features of the electrode without going into the description of the exact 3D micro-structure of its inner geometry. To that end, the different phases of the electrode (solid matrix and pore-filling electrolyte) are represented using a continuous porous description which is obtained by averaging each physical quantity over a representative elementary volume of the electrode. In this macroscopic description, the micro-structure of the electrode are not spatially discretized. At any geometrical point, the different phases of the electrode coexist, quantitatively present according to their respective volume fraction  $x_v$ . Moreover, to each point is associated a representative particle of active material. The active material is a component of the solid matrix phase and fills a volume fraction of it. In the elementary volume of the electrode, the surface area of active material in contact with liquid phase is noted as  $a$ , the specific interfacial area in  $\text{m}^2 \cdot \text{m}^{-3}$ .

In our study, we consider all the solid phases as electronic conductive media. When it is necessary to distinguish between the different phases, variables relative to the liquid phase are noted with a “2” subscript, while variables relative to the solid phase with a “1” subscript. Variables specific to each active material have a “*gr*” or a “*nmc*” subscript depending on their nature (graphite or NMC). A diagram of this approach is drawn in Figure 2.6.

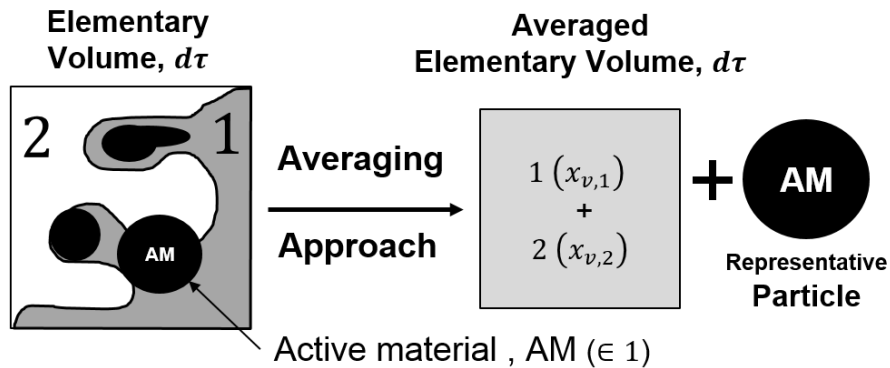


Figure 2.6: Scheme of the continuum media approach

This averaging approach applies to the electrode but also to the separator because of its porous structure filled with electrolyte. Differences with the electrode are that in the separator the solid phase is electrically insulated, no active phase is present and no charge transfer occurs.

### Electroneutrality and conservation of charge

The electrode is considered to remain electrically neutral during operation, because a separation of charge noticeable in a distance characteristic of the pore size requires a large electrical force. The

electric double layer effect at the interface between active material and the electrolyte is neglected in the model [43]. Charge currents are provided from displacement of electrons in solid phase and displacement of ions in liquid phase. Thus, the divergence of the total current density can be written in any point of the electrode as the sum of two terms: the divergence of the current density in the conductive solid phase ( $i_1$ ) and the divergence of the current density in the liquid phase ( $i_2$ ) :

$$\nabla \cdot i_2 + \nabla \cdot i_1 = 0 \quad (2.1)$$

### Faradaic processes inside the porous electrode

Inside the porous electrode, an intercalation reaction occurs at the interface between active material and electrolyte. In our study, two insertion mechanisms can happen depending on the active host material. Insertion reactions for graphite and NMC are given respectively:



At any point of the electrode, the current which corresponds to the charge transfer between the active material phase and the liquid phase is equal to the divergence of the ionic current density and minus the divergence of the electronic current:

$$\nabla \cdot i_2 = -\nabla \cdot i_1 = ai_n \quad (2.4)$$

The product  $ai_n$  represents the charge flux per electrode volume in  $\text{A} \cdot \text{m}^{-3}$  and  $i_n$  the intercalation current density in  $\text{A} \cdot \text{m}^{-2}$ . On the active material surface, this intercalation current is modeled by a Butler-Volmer Equation. This equation binds the intercalation current density  $i_n$ , to the electrode overpotential,  $\eta$ , via the exchange current density  $i_o$  :

$$i_n = i_o \left( \exp\left(\frac{\alpha_i F \eta}{RT}\right) - \exp\left(-\frac{(1 - \alpha_i) F \eta}{RT}\right) \right) \quad (2.5)$$

In [Equation 2.5](#),  $\alpha_i$  is the symmetry factor associated with the intercalation reaction in the material  $i$ . The over voltage  $\eta$  is defined as the difference between the electrode potential ( $\phi_1 - \phi_2$ ) and its equilibrium potential,  $E_i^0$ .

$$\eta = \phi_1 - \phi_2 - E_i^0(x_{\text{Li}}) \quad (2.6)$$

At the surface of the active material, the equilibrium voltage depends on the local lithium stoichiometry  $x_{\text{Li}}$ . The lithium stoichiometry  $x_{\text{Li}}$  at the surface of the host material  $i$  is written as in [Equation 2.7](#), with  $\rho_i$  the active material density,  $q_i$  the theoretical specific capacity calculated for a full stoichiometry utilization and  $c_1^s$  the lithium concentration at the surface of the host structure

*i.*

$$x_{\text{Li}} = \frac{F c_1^s}{q_i \rho_i} \quad (2.7)$$

The exchange current density of the Butler-Volmer relation (Equation 2.8) depends on the concentration of species involved in the charge transfer process at the interface: the fraction of intercalated lithium  $x_{\text{Li}}$ , the fraction of vacancy sites in the host material  $(1 - x_{\text{Li}})$  and the concentration of lithium cations at interface  $c_2$  over a reference concentration  $c_2^0$ . The parameter  $k_i$  represents the charge transfer rate in  $\text{mol} \cdot \text{m}^{-2} \cdot \text{s}^{-1}$ .

$$i_0^i = F k_i (1 - x_{\text{Li}})^{(1-\alpha_i)} (x_{\text{Li}})^{\alpha_i} \left(\frac{c_2}{c_2^0}\right)^{(1-\alpha_i)} \quad (2.8)$$

### Charge and mass balances in the porous liquid phase

In the liquid phase different species, charged or neutral, coexist. For lithium, the mass balance in a elementary volume in the pore-filling electrolyte is written in Equation 2.9, where  $c_2$  is the concentration of lithium in electrolyte, and  $N_{\text{Li}}$  its flux:

$$\frac{\epsilon \partial c_2}{\partial t} = -\nabla \cdot N_{\text{Li}} + \frac{a i_n}{F} \quad (2.9)$$

In the liquid phase, the ionic current results from the movement of ions. This movement can be driven by migration, diffusion, and convection. As we do not have any mechanical driven flow in our closed system, only the gradient of concentration (diffusion) and gradient of ionic potential (migration) drives the movement of the different charged species. A classical simplification in the Newman approach is to consider the electrolyte as a strictly binary electrolyte. In our case, it means only three species : the solvent, the anions and cations of the salt. In addition, we take into consideration the interactions between charged species, since the electrolyte salt concentration is high. The concentrated solution theory and the binary electrolyte assumption can be associated [43] to lead to an expression for the ionic current (see Equation 2.11) and a mass balance for lithium the liquid phase (see Equation 2.10):

$$\epsilon \frac{\partial c_2}{\partial t} - \nabla \cdot (D_2^{\text{eff}} \nabla c_2) = \frac{a i_n}{F} (1 - t_+^0) \quad (2.10)$$

$$i_2 = -\kappa^{\text{eff}} \left( \nabla \phi_2 - \frac{2RT}{F} (1 - t_+^0) \left( 1 + \frac{d \ln f_{\pm}}{d \ln c} \right) \frac{\nabla c_2}{c_2} \right) \quad (2.11)$$

In Equation 2.10 and Equation 2.11, the spatial variables are respectively  $c_2$ , the concentration of lithium ions in the electrolyte and  $\phi_2$ , the ionic potential of the liquid phase. The other terms are the volume fraction of the liquid phase, or namely the porosity of the electrode  $\epsilon$ , the effective conductivity and diffusivity of the salt, respectively  $\kappa^{\text{eff}}$  and  $D_2^{\text{eff}}$ , and transport parameters relative to the concentration solution theory which described the lithium salt :  $t_+^0$ , the cationic transference

number and  $f_{\pm}$ , the activity coefficient.

### Electronic transport in solide phase

We consider that the displacement of electrons in the solid conductive phase (graphite or NMC) is driven by the gradient of electric potential  $\phi_1$ . The Ohm's law in conductive material phase is considered :

$$i_1 = -\sigma_1^{\text{eff}} \nabla \phi_1 \quad (2.12)$$

where,  $\sigma_1^{\text{eff}}$  is the effective electronic conductivity of the solid phase.

### Mass balance in active material

In an elementary volume of active material, the mass balance of intercalated lithium is written as :

$$\frac{\partial c_1}{\partial t} = -\nabla \cdot (-D_1 \nabla c_1) \quad (2.13)$$

$D_1$  being the diffusion coefficient of lithium inside active material and  $c_1$  the concentration of intercalated lithium in the host-structure. The flux density of lithium inside active material is thus assumed to follow a Fick's law, which means that the gradient of lithium concentration is the driving force of the lithium movement inside the active material. This hypothesis can be questioned in some cases, the lithium diffusion and distribution inside active material being more complex, especially for multiphasic materials as graphite [45, 46]. However, if the precise concentration profile inside active particles is not needed, Fick's law with an effective diffusion can be sufficient to simulate the lithium concentration at particle's surface  $c_1^s$  [47, 48]. At the interface between active material and electrolyte, the value of the boundary flux is given by the ratio  $i_n/F$ , considering the Faraday's law and null flux density in the center of the particle.

## 2.2.2 Model hypotheses

Some specific geometrical and physical hypotheses are made, given our lithium-porous electrode coin-cell system. These assumptions concern the electrode geometry, the lithium electrode, the transport parameters in porous media, and the active particle geometry.

### Thermal effects

According to coin-cell size, as well as the thermal regulation in the climatic chamber, temperature variations can be assumed negligible in a first approach. The model is therefore isothermal and assumes a temperature equal to 20 °C.

## Dimension reduction of the considered system

Even if the physical phenomena occur along the three spatial dimensions of the cell, the first assumption considers only the spatial dimension normal to the electrode plane is significant. Indeed, the major changes of physical quantities are especially observed throughout the electrode and separator thicknesses. Moreover material properties are rather homogeneous and isotropic and at all conditions the electric potentials both on lithium surface and on positive current collector are uniform due to the combination of good metal conductivity and small dimension of the coin-cell. Then, in addition to the electroneutrality assumption, the ionic current density on the lithium electrode surface and the electric current on the positive current collector is uniform and identical on each points. Consequently, inside the cell, potential and concentration gradients along the coin-cell thickness are far superior than gradients in direction parallel to the current collector. So, only physical phenomena along the thickness direction of electrode are considered in our modeling approach. This dimension along the electrode thickness can be seen on the schematic diagram of the model (Figure 2.7). Mass balance equation (Equation 2.10) and transport equations (Equation 2.12 and Equation 2.11) are written in Cartesian coordinates, along a 1D axis which represents the thickness of the cell. Equations along this dimension can be found in numerous references [49, 50, 51] and are summarized in Table 2.2.

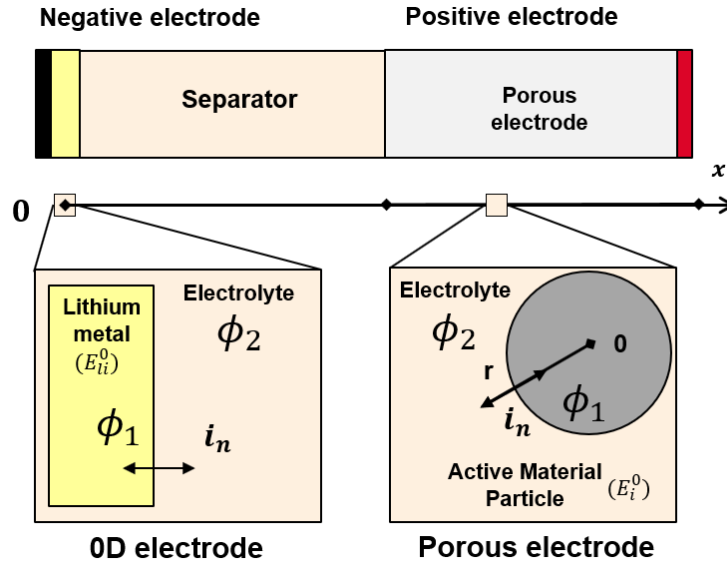


Figure 2.7: Diagram of the half-cell model

As our coin-cell electrodes are rather small and aluminum and copper are extremely good electronic conductor, the dimension reduction makes sense. However for large pouch cells, which contain large current collectors and small electrode terminals, this assumption may not be valid and a possible potential distribution on current collectors should be considered [52].

## Lithium electrode model

At the lithium counter-electrode, a charge transfer reaction occurs: a metallic lithium atom can be oxidized into a lithium anion atom, via the following red-ox reaction at 0 V versus  $\text{Li}^+/\text{Li}$  (noted  $E_{\text{Li}}^0$ ).



The lithium electrode of the cell dissolves partially during lithiation of the porous electrode (graphite or NMC), but during the whole process the thickness variation does not affect the electrochemical reaction because the lithium electrode is constantly pressed to the separator. This thickness variation can thus be assumed negligible. As a reminder, a 5 mAh delithiation on a coin-cell sized lithium electrode represents a thickness variation of 15  $\mu\text{m}$  that can be compared to the 100  $\mu\text{m}$  thickness of the original lithium sheet. As electrochemical reaction only happens on surface due to its bulk structure, this electrode is modeled by an interface where the electrochemical process occurs, and described by a Butler-Volmer Equation.

$$i_n = i_0^{\text{Li}} \left( \exp\left(\frac{\alpha_{\text{Li}} F \eta}{RT}\right) - \exp\left(-\frac{(1 - \alpha_{\text{Li}}) F \eta}{RT}\right) \right) \quad (2.15)$$

$$\eta = \phi_1 - \phi_2 - E_{\text{Li}}^0 \quad (2.16)$$

The electric potential of the lithium metal electrode ( $\phi_1$ ) is set at 0 V. The lithium electrode model is represented in Figure 2.7, Equation 2.15 is applied at the origin of the x-axis.

## Transport parameters approximations

Transport parameters are known for bulk materials as electrolyte or active material, but in the macroscopic electrode description, we need to estimate their effective values in porous media. The porous model requires effective transport parameters for lithium-ion migration in liquid phase and lithium diffusion in both liquid and solid phases. A common way to describe an effective transport properties in a porous medium is given in the Equation 2.17, where  $P$  is a transport parameter in a bulk phase,  $P^{\text{eff}}$  the effective transport parameter in the bulk phase of the porous medium described by the volume fraction of the considered phase  $\epsilon$  and its tortuosity  $\tau$  [53]:

$$P^{\text{eff}} = P \frac{\epsilon}{\tau} \quad (2.17)$$

A tortuosity equals to one indicates the absence of any physical barrier through the porous medium, whereas a tortuosity superior to ones means a longer transport path between two points of the porous medium. As the tortuosity is a parameter difficult to estimate precisely [54, 55], Bruggeman-type relations are often used to estimate the transport parameters in battery models [49, 51, 56]. They relate the volume fraction of the phase to its tortuosity, through the Bruggeman coefficient,

$br$ :

$$\tau = \epsilon^{1-br} \quad (2.18)$$

This relation indicates that a decrease of porosity is related to an increase of tortuosity for Bruggeman number superior to one. It is commonly found in lithium-ion battery model that the Bruggeman coefficient is equal to 1.5 [51]. This value is true for analytic structures such as transport through a compact pile up of spherical particles, but should be used with caution with others porous structures [57].

In our particular case, we face two different porous structures: separator and electrode. Inside the separator, migration and diffusion occur. For migration of charged species, the effective ionic conductivity  $\kappa^{\text{eff}}$  can be derived from the conductivity of the bulk electrolyte and the MacMullin number,  $N_m$ . This number is characteristic of the separator micro-structure, independent of the salt concentration and defined as the ratio of the electrolyte and separator conductivities [58]. Effective conductivity in the separator is thus written as :

$$\kappa^{\text{eff}} = \frac{\kappa}{N_m} \quad (2.19)$$

In commercial cells, typical MacMullin values are lower than eight. Concerning ionic lithium diffusion inside the separator, the effective diffusion coefficient is also given by a Bruggeman relation, (see Equation 2.22). Inside porous electrodes, Bruggeman-type relations are used to estimate the transport parameters in solid or liquid phase, namely: the effective ionic conductivity  $\kappa^{\text{eff}}$ , the effective electronic conductivity  $\sigma^{\text{eff}}$  and the electrolyte diffusivity  $D_2^{\text{eff}}$  :

$$\sigma^{\text{eff}} = \sigma(1 - \epsilon)^{br} \quad (2.20)$$

$$\kappa^{\text{eff}} = \kappa\epsilon^{br} \quad (2.21)$$

$$D_2^{\text{eff}} = D_2\epsilon^{br} \quad (2.22)$$

In Tables Equation 2.20, Equation 2.21, and Equation 2.22,  $\epsilon$  refers to the material porosity.

Transport parameter in the solid phase is discussed in the next section.

### Active particle shape

The active particles are assumed to be identically and ideally shaped. In literature, the common representation of particles in a Newman-type approach is a sphere [32, 51, 59]. In our study, active material agglomerates appear as flakes for graphite (see Figure 2.1a) and spheres for NMC (see Figure 2.4). As can be seen in Figures 2.1a and 2.4, active particles are porous and appear as agglomerates. Choice was made to represent a modeled particle as a homogeneous material at the agglomerate scale and doing so, not to consider the inner porosity of real particles. Moreover, the inner porosity of particles remains quite low compare to the electrode porosity, thus effective

diffusion should be close to the bulk diffusion. Additional studies on inner porosity of NMC particles (10 %) have been conducted by CABELGUEN [60]. Value of effective lithium diffusion coefficient inside active particles is taken as the value of the lithium diffusion coefficient  $D_1$ .

In case of graphite, the study of SEI formation shows that reactions occur rather on prismatic planes than basal planes [38] and confirms that only side wall of particle flakes are electrochemically active for lithium intercalation. The particle model is then assumed cylindrical, instead of the classical spherical representation and we suppose that lithium is intercalated only on side walls, considered as prismatic planes. In case of NMC, as shown in SEM picture of Figure 2.4, a classical spherical representation provides a better match with the averaged particles agglomerate shape.

According to active particle shape, only phenomena along the radial dimension,  $r$ , are considered. Mass balance of lithium inside the particle is then written in cylindrical (or spherical) coordinates. In the half-cell model two dimensions are now considered, the thickness dimension through the cell and the radial dimension through the particles. This fact illustrates the common name found in literature for this modeling approach, the pseudo-2D model (P2D) [32].

Considering the cylindrical or spherical shape, the specific interfacial area  $a$  (in  $\text{m}^2 \cdot \text{m}^{-3}$ ) and the mass balance are written for an electrode  $i$  as :

$$a = \frac{n}{R_i} (1 - \epsilon_i) \frac{\rho_1}{\rho_i} w_i \quad (2.23)$$

$$\frac{\partial c_1}{\partial t} = -\frac{1}{r^{n-1}} \frac{\partial}{\partial r} \left( r^{n-1} D_1 \frac{\partial c_1}{\partial r} \right) \quad (2.24)$$

In Equation 2.23 and Equation 2.24,  $n$  is a geometrical parameter (dimension number) equals to two for the cylindrical case and three for the spherical case. Non-canonical shape can be obtained for other  $n$  values. As an example, a particle with a  $n$  value between 2 and 3 correspond to a non-euclidean object with a developed surface between a cylindrical and a spherical shape. These forms can be studied via the investigations of fractal objects and anomalous diffusion [61, 62].

The other parameters of Equation 2.23 are  $\epsilon_i$ , the porosity of electrode  $i$ ,  $R_i$  the mean radial dimension of the particle model,  $\rho_1$  the density of the solid phase,  $\rho_i$  the density of the active material, and  $w_i$  the weight fraction of the active material. In the literature, a parameter named  $x_a$  can also be found, which corresponds to the active material volume fraction in the solid phase of the electrode [51] ( $\frac{\rho_1}{\rho_i} w_i$  in our case).

For both spherical and cylindrical cases, boundary conditions must be applied on Equation 2.24. At the particle center, the value of the lithium flux is set to zero by symmetry. At the particle surface, it is equal to  $i_n/F$ .

In summary, the choice of particles shape changes the expression of the solid-state diffusion along the radial direction and influences the global kinetics of reaction through the parameter  $a$  (see Equation 2.5). Effects of this geometrical assumption will be discussed in section 2.3.2.2, where a sensitivity analysis on model parameters is performed.

### 2.2.3 Resolution

The equations of the model are implemented in the commercial software COMSOL Multiphysics 5.3 and solved with the Finite Elements Methods. All the equations are written in Cartesian coordinates through two axis: the first one represents the cell thickness (spatial variable  $x$ ) and the second one the particle's radius (spatial variable  $r$ ). These equations can be found in numerous literature sources [33, 49, 59, 63, 64] and are summarized in Table 2.2. It is necessary to specify the boundary conditions according to the operating conditions imposed on the cell model. During a galvanostatic charge or discharge, information about state of charge of the cell, and relations between C-rate and applied current are critical. These information derive from the value of the cell capacity.

#### Cell voltage and operating conditions

The cell voltage  $U$  corresponds to the electric potential difference between the two current collectors separated in this model by the separator and positive electrode, whose lengths are respectively  $L_s$  and  $L_p$  (see Figure 2.7). The cell voltage is written as :

$$U = \phi_1(L_p + L_s) - \phi_1(0) \quad (2.25)$$

As the electric potential is assumed equal to 0 V on the lithium electrode, the coin-cell voltage is identical to the potential of the working electrode. The boundary conditions of the governing equations are treated similarly to the literature [32, 49, 59, 51, 56].

Depending on the operating conditions, galvanostatic or potentiostatic mode, current or cell voltage is imposed to the cell. This is translated into a boundary condition at the current collector position related to Equation 2.4 and depending on operation type. This point is at the position noted  $L_s + L_p$  in Figure 2.7. During a galvanostatic charge or discharge, a Neumann condition sets the flux density at the collector/electrode boundary and the cell potential is readable as the electric potential value on this point. During a potentiostatic mode, a Dirichlet condition imposes the electric potential at this boundary and the observed cell-current is readable on this point as the boundary flux. Dynamic modes either on applied current or potential are feasible to simulate cyclic voltammetry, or floating current.

#### Cell capacity

In the present model, the negative electrode is a lithium foil which is considered as a non-limiting reservoir of lithium in comparison to the porous electrode capacity. The capacity of the modeled coin-cell is then equal to the working electrode capacity. This cell capacity  $Q_{\text{cell}}$ , expressed in mAh

Table 2.2: Governing equations in the P2D model

Physical phenomenon	Governing equations	Limit conditions
Ionic current density in liquid phase	$i_2 = -\kappa\epsilon_i^{br} \left( \frac{\partial\phi_2}{\partial x} - \frac{2RT}{F}(1-t_+^0) \left( 1 + \frac{d\ln f_{\pm}}{d\ln c_2} \right) \frac{\nabla c_2}{c_2} \right)$	at $x = L_i + L_{sep}$ : $-\kappa\epsilon_i^{br} \frac{\partial\phi_2}{\partial x} = 0$ at $x = 0$ : $-\kappa\epsilon_i^{br} \frac{\partial\phi_2}{\partial x} = 0$
Mass balance in liquid phase	$\epsilon \frac{\partial c_2}{\partial t} - \frac{\partial}{\partial x} (D_2 \epsilon^{br} \frac{\partial c_2}{\partial x}) = \frac{a i_n}{F} (1 - t_+^0)$	at $x = L_i + L_{sep}$ : $-D_2 \epsilon^{br} \frac{\partial c_2}{\partial x} = 0$ at $x = 0$ : $-D_2 \epsilon^{br} \frac{\partial c_2}{\partial x} = \frac{I}{S_i F} (1 - t_+^0)$
Kinetics at electrolyte/ $i$ interface	$i_n = a F i_0^i \left( \exp\left(\frac{\alpha_i F \eta}{RT}\right) - \exp\left(-\frac{(1-\alpha_i) F \eta}{RT}\right) \right)$ $\eta = \phi_1 - \phi_2 - E_{gr}^0$	
Electrode exchange current density	$i_0^i = k_i (1 - x_{Li})^{(1-\alpha_i)} x_{Li}^{\alpha_i} \left( \frac{c_2}{c_2^0} \right)^{(1-\alpha_i)}$	
Kinetics at electrolyte/lithium interface	$i_n = i_0^{Li} \left( \exp\left(\frac{\alpha_{Li} F \eta}{RT}\right) - \exp\left(-\frac{(1-\alpha_{Li}) F \eta}{RT}\right) \right)$ $\eta = \phi_1 - \phi_2 - E_{Li}^0$	
Mass balance in active material	$\frac{\partial c_1}{\partial t} = -\frac{1}{r^{n-1}} \frac{\partial}{\partial r} (r^{n-1} D_1 \frac{\partial c_1}{\partial r})$	at $r = R$ : $-D_1 \nabla c_1 = \frac{i_n}{F}$ at $r = 0$ : $-D_1 \nabla c_1 = 0$
Electronic current density in solid phase	$i_1 = -\sigma_1 (1 - \epsilon)^{br} \frac{\partial\phi_1}{\partial x}$	at $x = 0$ : $\phi_1 = 0$ at $x = L_{sep}$ : $i_1 = 0$ at $x = L_{sep} + L_i$ : $i_1 = \frac{I}{S_i}$
Electroneutrality	$\nabla \cdot i_2 = -\nabla \cdot i_1$	

is calculated as a function of  $W_j$  loading composed of an active material  $i$ :

$$Q_{\text{cell}} = q_i \Delta x_{\text{Li}} W_j w_i S \quad (2.26)$$

where  $q_i$  represents the theoretical capacity of active material ( $\text{mAh} \cdot \text{g}^{-1}$ ),  $\Delta x_{\text{Li}}$  the stoichiometry interval used for cycling,  $w_i$ , the mass fraction of active material in solid phase of the electrode, and  $S$  the geometrical surface of the electrode. In this context, the cell capacity determines the State Of Charge (SOC), the State of Lithiation of the graphite electrode (SOL) and the current related to an imposed C-rate.

The C-rate is calculated as the ratio of the applied current and the actual capacity of the cell. In graphite, the SOL is the ratio of the amount of intercalated lithium and the maximum available capacity of the cell,  $Q_{\text{cell}}$ . In the special case of NMC, the SOL is the ratio of the amount of intercalated lithium superior to a 0.4 stoichiometry and  $Q_{\text{cell}}$ . The SOC, more commonly used, is on opposite to the SOL in a lithium-graphite configuration: the cell is charged (SOC = 1) when the graphite electrode is fully delithiated (SOL = 0).

In the following, the global SOL should be distinguished from the local SOL. In case of graphite electrodes versus lithium, the local SOL at particle surface is equal to the lithium stoichiometry at the surface of the representative particle, noted  $x_{\text{Li}}$  (Equation 2.7). Inside the particle, the lithium stoichiometry can be heterogeneous and the average lithium stoichiometry of the particle can differ from  $x_{\text{Li}}$ . In graphite, we differentiate the local stoichiometry on the particle surface (named  $x_{\text{Li}}$ ), the amount of lithium intercalated inside a local particle over the capacity of the particle (named the local SOL), the SOL of the whole electrode (SOL) and the SOC of the cell (SOC).

The P2D model can be solved according to different modes. The set of equations simulates the different physical events happening inside the electrode, namely transport through porous media, insertion and diffusion of lithium in the active material. The model allows to see locally different variables through the thickness of the cell, such as the electric and ionic potentials at the interfaces, or the lithium salt concentration. Nevertheless, to obtain results with physical consistency, it is necessary to compare and adjust this model to experimental results.

## 2.3 Physical parameters validation

The values of the physical parameters, which appear in the governing equations, are needed to solve the model. The determination of these parameters is crucial since they may have a high impact on the global cell electrochemical behaviors (cell voltage, current, temperature...), as well as on the internal state of the battery that we want to analyze and for which experimental validation is rarely available. The predictability and consistency of model simulations depend on the physical accuracy of these parameters. In our study, we classify these parameters between accurate and less accurate (or less accessible) parameters. A reference value and an interval domain are estimated

for each unknown parameter. A sensitivity analysis protocol is performed on these parameters. The final goal of this sensitivity analysis is double: to reduce the number of parameters that have to be adjusted in our model and to understand qualitatively and quantitatively how the different parameters affect the rate capability and the cell output voltage during operations.

### 2.3.1 Parameter review

Values for the physical parameters are found in literature sources, handbooks, or material manufacturer data-sheets. These parameters are relative to the separator, electrolyte, the lithium electrode, and the porous electrode. Among all parameters, we distinguish physical theoretical parameters, accurate, from less accessible parameters, either directly obtained from inaccurate measurements, or indirectly derived from usual electrochemical techniques [65]. The considered accurate parameters are described as *reliable parameters* and less accurate parameters are noted as *uncertain parameters*. If possible and relevant, some parameters will be re-adjusted thanks to experiments. In case of uncertain parameters, a reference value and interval domain are estimated from the data deviation observed in the literature, in order to give an interval on which a sensitivity analysis will be performed.

#### 2.3.1.1 Reliable physical parameters

The physical parameters related to well-known intrinsic properties of active material and those associated to the measurable geometry are considered as physically accurate in the following. The sensitivity analysis protocol is not performed on these parameters, listed in Table 2.3 for graphite and NMC. The density  $\rho_i$ , ( $\text{kg} \cdot \text{m}^{-3}$ ), specific capacity  $q_i$  of active material ( $\text{mAh} \cdot \text{g}^{-1}$ ), electrode geometrical surface, and equilibrium potential of active material are concerned.

#### 2.3.1.2 Uncertain physical parameters

Transport, kinetics, and geometrical parameters of porous electrode and separator have to be estimated. Unfortunately, porous structure parameters remain in most case difficult to estimate correctly, because of its complex geometry. On the one hand, the common averaging porous electrode hypothesis, that is often made to analyze and extract parameter values from diverse electrochemical experiments, conceals the physical reality. On the other hand, physical calculations on reconstructed electrode structures are rather dependent on the selected sample and should be extrapolated to the bulk of material with cautions [32]. For example, as the real developed surface of the active material and the poly-disperse distribution of particles are not known precisely [66], a charge transfer rate parameter can not accurately be deduced from electrochemical experiments.

To know averaged electrode structure parameters, MALIFARGE *et al.* recently proposed a technique based on impedance spectra analysis on symmetric electrochemical cell in order to es-

Table 2.3: Reliable physical parameters of graphite a) and NMC b)

NMC	Symbol	Value	Graphite	Symbol	Value
Equilibrium potential of NMC (V)	$E_{NMC}^0$	section 2.3.1.3	Equilibrium potential of graphite (V)	$E_{gr}^0$	section 2.3.1.3
NMC electrode surface (cm <sup>2</sup> )	$S_{NMC}$	1.54	Graphite electrode surface (cm <sup>2</sup> )	$S_{gr}$	1.54
Density of the solid phase of NMC electrode (kg · m <sup>-3</sup> )	$\rho_{1,NMC}$	4214	Density of the solid phase of graphite electrode (kg · m <sup>-3</sup> )	$\rho_{1,gr}$	2236
Density of NMC active material (kg · m <sup>-3</sup> )	$\rho_{NMC}$	4750	Density of graphite active material (kg · m <sup>-3</sup> )	$\rho_{gr}$	2230
Specific capacity of NMC (mAh · g <sup>-1</sup> )	$q_{NMC}$	278	Specific capacity of graphite (mAh · g <sup>-1</sup> )	$q_{gr}$	372

(a)
(b)

timate tortuosity [67]. A derivated method is explained by SULTHAR *et al.* to evaluate in-plane tortuosity [68].

The measurement of lithium diffusion coefficient in the active material, often extracted from galvanostatic intermittent titration techniques (GITT) [69, 70] is both difficult to reproduce and dependent of the material structure. In the literature, a difference of four orders of magnitude can be observed between references for graphite electrodes [71] and NMC particles [60].

Transport properties in electrolyte cannot be estimated in an accurate way and the values available in the literature are limited to common electrolytes [72, 73]. In order to characterize transport in electrolyte, four independent parameters are needed: the ionic conductivity, lithium salt diffusivity, cationic transference number, and the activity coefficient. A recent technique developed by FARKHONDEH *et al.* [74], which couples a 4-electrode electrochemical cell and a modeling approach, allows to measure transport properties of electrolytes.

For each of these *uncertain parameters*, a reference value and an interval domain is also proposed in 2.4, 2.5 and 2.6. It concerns parameters relative to the electrode structure ( $\epsilon$ ,  $r$ ,  $br$ ,  $L$ ), the electrode kinetics ( $k$ ,  $\alpha$ ), and the transport parameters ( $D_1$ ,  $D_2$ ,  $t_+^0$ ,  $\frac{dlnf_{\pm}}{dln c}$ ,  $\kappa$ ).

### 2.3.1.3 Experimental validation of some *uncertain* and *reliable parameters*

The effective separator ionic conductivity, the equilibrium potential of graphite and NMC, and the exchange current density of lithium are experimentally measures from the electrochemical cells manufactured in this work.

**Separator ionic conductivity** Separator and electrolyte ionic conductivity measurements have been made on coin cells composed of electrolyte, with or without a Celgard 2400 separator, between two aluminum current collectors. A hollow plastic cap is used as a separator for cell coins without Celgard. The electrolyte concentration is  $1 \text{ mol} \cdot \text{L}^{-1}$ . These two conductivities are extracted from electrochemical impedance spectroscopy measurements carried out on the respective coin-cells [75]. The ratio of separator conductivity and the electrolyte conductivity corresponds to the MacMullin number,  $Nm$ , equal to 6.5 in our case. This number is independent from the electrolyte concentration [58]. The relation between salt concentration and electrolyte conductivity is found in ECKER *et al.* [49] and written as follows:

$$\kappa = 1.726 + 17.919c_2 - 12.983c_2^2 + 2.667c_2^3 \quad (2.27)$$

Knowing  $\kappa$  at different salt concentrations  $c_2$  and  $Nm$ , the effective conductivity  $\kappa^{\text{eff}}$  inside the porous structure of the separator can be calculated for a wide range of salt concentrations (Equation 2.19). This expression is more accurate and experimentally correlated than a classical Bruggeman relation type (Equation 2.18).

**Equilibrium voltage of graphite and NMC** The equilibrium potential, noted  $E^0$  is an important model parameter. From a global point of view, it is the cell voltage skeleton on which the different resistive contributions will be added. From a local point of view, the equilibrium potential influences intercalation kinetics, according to the concentrations of species at the interface. Local equilibrium potential can be heterogeneous inside the electrode, depending on local lithiation conditions. Experimentally, the equilibrium potential curve of graphite and NMC are measured by averaging the cell voltage of the lithiation and delithiation of a  $W_1$  coin cell at C/10. Doing so, we assume that resistance contributions are equivalent and sufficiently small at these currents not to affect the global shape of this curve with regard to intercalated lithium concentration.

In Figure 2.8, half-cell potentials during lithiation (blue) and delithiation (red) are drawn for each electrode. The strategy used to obtain the interpolated equilibrium potential shown in black consists of two steps. The first step is to calculate the mean difference between the lithiation and delithiation potentials. Since we want the equilibrium potential to be located between the lithiation and delithiation ones, we will keep only half of the mean difference previously calculated, that is to say 17 mV for NMC and 28 mV for graphite. The second step is specific to each electrode. In the case of graphite, the equilibrium potential is the sum of the lithiation potential and half the mean difference, in order to keep the shape of the plateaus. In the case of NMC, the equilibrium potential is given by the delithiation potential minus half the mean difference, to avoid the excessive polarization observed at high lithium content during lithiation. We notice a higher overall polarization of the graphite electrode than NMC for the same current.

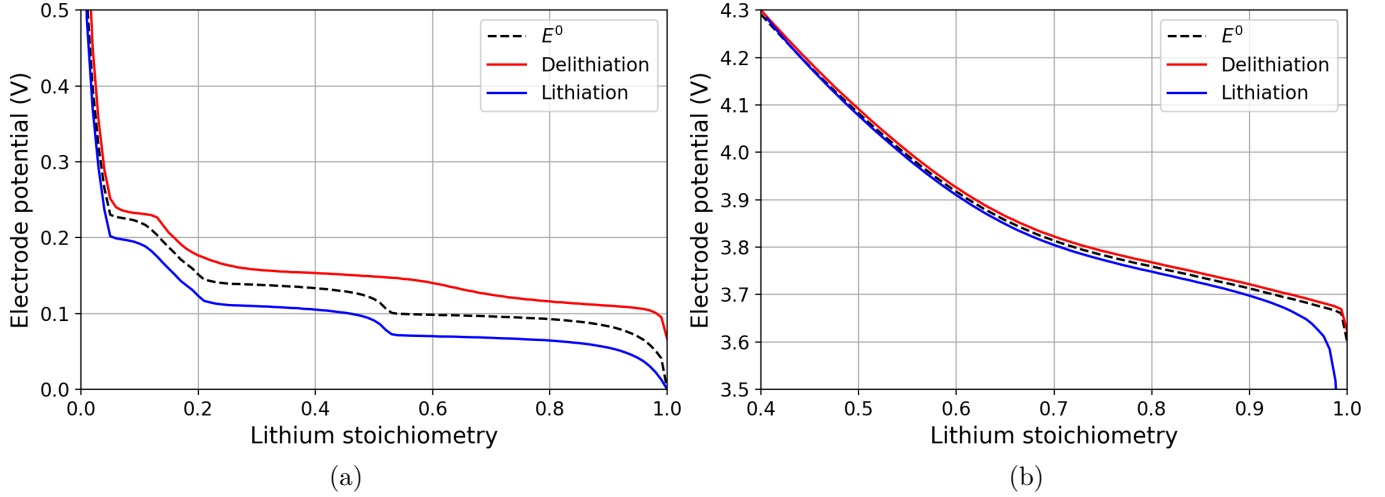


Figure 2.8: Equilibrium potential curves of graphite (a) and NMC (b) extracted from experimental galvanostatic charge and discharge

**Exchange current density of the lithium electrode** To characterize the lithium foil, a double lithium-lithium coin-cell with two Celgard 2400 separators, filled with the same electrolyte as our coin-cell, has been assembled. Several steps of current have been applied in charge and discharge to measure the cell polarization, leading to the current-potential curve presented in Figure Figure 2.9. The exchange current density of the lithium electrode is extracted from this curve using a linear approximation of the Butler-Volmer Equation for small overpotential (see Equation 2.28), considering the separator resistance as negligible.

$$\frac{I}{S} = \frac{i_0 F}{RT} \frac{U_{\text{Li/Li}}}{2} \quad (2.28)$$

In Equation 2.28,  $I$  is the applied current in Ampere (A),  $S$  is the electrode geometrical surface ( $\text{m}^2$ ) and  $U_{\text{Li/Li}}$  the cell voltage (V). Experimental Current-Potential points and linear regression are shown in Figure 2.9. The relation between current and potential is linear for a polarization lower or equal to 0.2 V. With the obtained regression coefficient and the overpotential linear approximation in the small potential range, the exchange current density ( $i_0$ ) is  $10 \text{ A} \cdot \text{m}^{-2}$ . This value agrees with the  $5.5 \text{ A} \cdot \text{m}^{-2}$  found in [64]. The difference can be explained by the fact that a solid electrolyte is used in the cell in reference [64]. To explain the smaller value, we suppose that the solid electrolyte tends to keep the lithium surface flat. With non-solid electrolyte, the effective lithium surface extends due to mossy lithium formation. An *operando* X-ray tomography coupled with a spatially-resolved diffraction on a lithium-sulfur system shows that the lithium interface tends to be non-uniformly oxidized along cycles and forms a porous lithium interface [76]. This surface modification could explain the exchange current density differences, since  $S$  is considered constant in Equation 2.28.

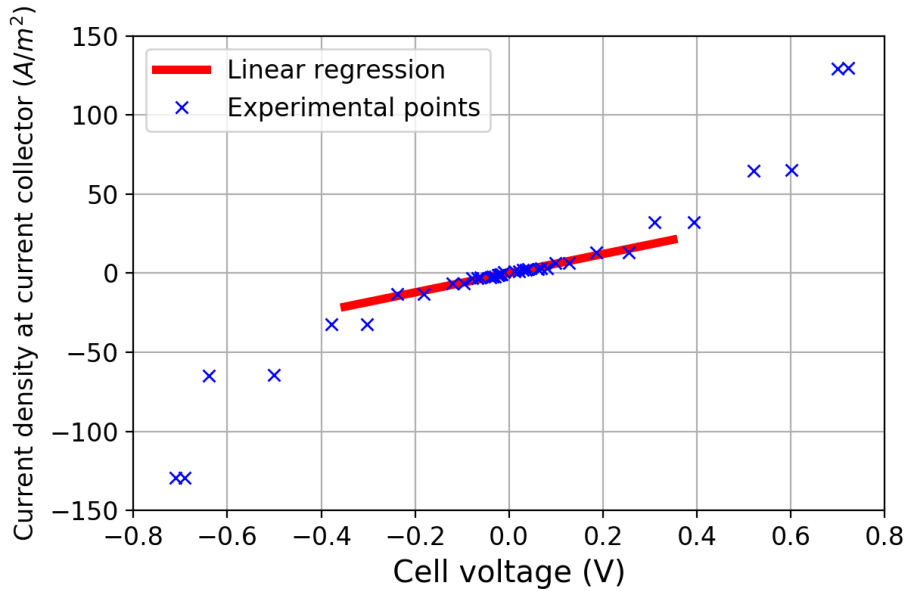


Figure 2.9: Extraction of lithium exchange current density from experimental Current-Voltage step curve

### 2.3.2 Sensitivity analysis protocol

A sensitivity analysis of *uncertain parameters* is undertaken. In literature, an example of sensitivity analysis has been performed by EDOUARD *et al.* on a simplified electrochemical model close to our own [77]. In this work, we want to quantify the impact of parameter variations on the cell voltage during a standard lithiation. The standard lithiation (or delithiation for the NMC electrode) used for the sensitivity analysis has been performed at a C/2 rate in a half-cell configuration, with a  $W_2$  mass-loading starting from 100 % SOC (or 0 % for the NMC electrode) to 0 V (or 2,6 V). We also want to understand how model parameters globally modify the voltage curve shape and rate capacity in order to reduce the set of parameters to adjust.

For each parameter, simulations are run for different values inside its interval domain, all other model parameters being set to their reference values. The results of our sensitivity analysis allow to classify parameters according to their influences on the cell voltage and capacity. Not only the size but also the shape of active material particles are considered in the sensitivity analysis.

#### 2.3.2.1 Classification

Physical parameters can be categorized depending on their effects on half-cells. We distinguish two different classes (resistance and capacity), and for each class, three magnitudes (low, medium, and high). Parameters are classified depending on their impact on either the cell voltage or rate capability. The magnitude value is calculated from a reference state with respect to the belonging class.

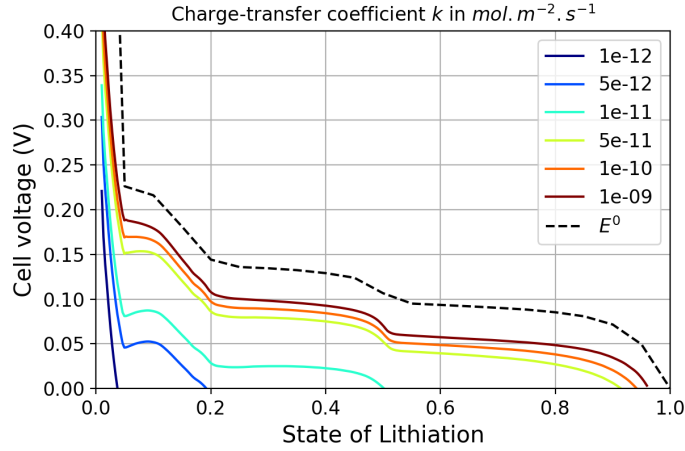


Figure 2.10: Simulated lithiation curves of a  $W_2$  graphite at  $C/2$  with different charge transfer rate

### Resistance class parameters

Among the parameters having their highest influence on cell voltage appears the graphite charge-transfer rate,  $k$ , plotted in Figure 2.10. On this figure is drawn cell voltages during graphite lithiation with various charge-transfer values, ranging from  $10^{-12}$  to  $10^{-9}$   $\text{mol} \cdot \text{m}^{-2} \cdot \text{s}^{-1}$ . When  $k$  decreases, the electrode polarization increases, and so does the resistance. To quantify this visual resistance change, we calculate a sensitivity coefficient as follows:

$$\Theta_R = \frac{\Delta U (\log_{10}(k_{max})) - \Delta U (\log_{10}(k_{min}))}{\log_{10}(k_{max}) - \log_{10}(k_{min})} \quad (2.29)$$

where  $k_{min}$  and  $k_{max}$  are the minimum and maximum values  $k$  can take on its interval domain. According to Equation 2.29, the sensitivity coefficient for  $k$  is equal to  $287 \text{ mV} \cdot \log(k)^{-1}$ . This sensitivity coefficient is generalized to all the uncertain parameters we want to classify.

### Capacity class parameters

The capacity class parameters influence the cell capacity or rate capability. Figure 2.11a shows that the variation of the lithium diffusion coefficient in graphite  $D_1$  influences the rate capability of the cell, rather than the cell voltage.  $D_1$  varies from  $10^{-14}$  to  $10^{-9}$   $\text{m}^2 \cdot \text{s}^{-1}$ . When  $D_1$  varies, the cell voltage does not follow a resistive behavior. As the diffusion coefficient decreases, the final SOL decreases. The sensitivity coefficient for the rate capability is calculated as the same way as Equation 2.29 :

$$\Theta_Q = \frac{\Delta Q (\log_{10}(D_{max})) - \Delta Q (\log_{10}(D_{min}))}{\log_{10}(D_{max}) - \log_{10}(D_{min})} \quad (2.30)$$

In this case, the sensitivity coefficient equals  $1 \text{ mAh} \cdot \log(D_1)^{-1}$ .

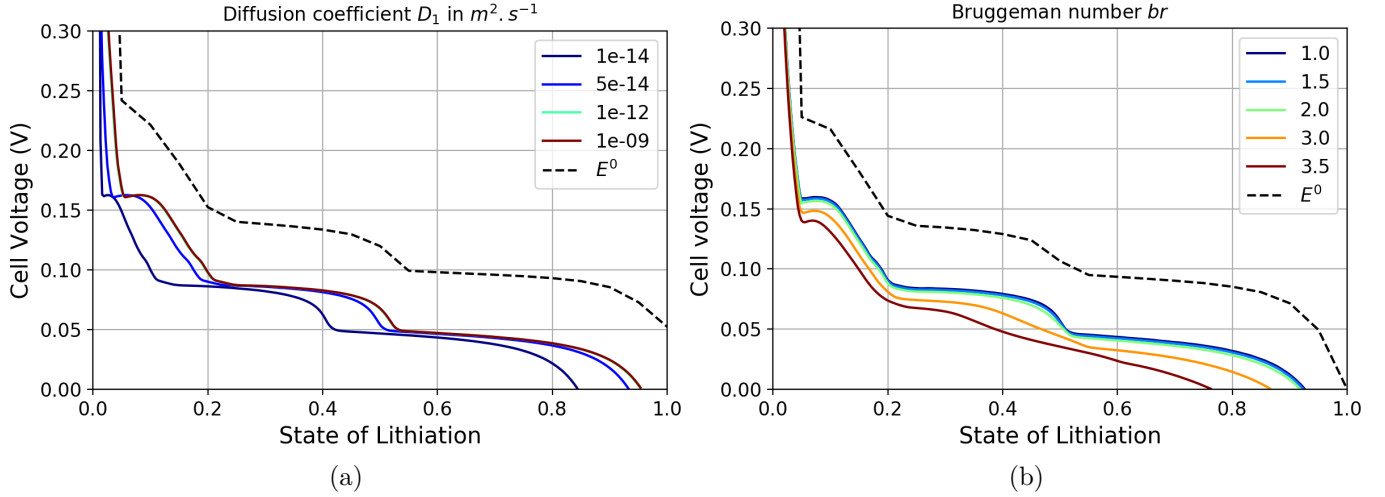


Figure 2.11: Simulated lithiation curves of a  $W_2$  graphite at  $C/2$  with different lithium diffusion coefficients inside graphite a) and different Bruggeman coefficients b)

### Mixed class parameters

Nevertheless some parameters have an impact on both capacity and resistance, such as the Bruggeman parameter,  $br$  (Figure 2.11b). The Bruggeman number is a parameter which drives the effective transport parameter  $\kappa^{\text{eff}}$  and  $D^{\text{eff}}$ . From Equation 2.21 and Equation 2.22, we can see that when we increase the Bruggeman number, the effective transport parameters decrease. That is why in Figure 2.11b, the cell voltage decreases as the Bruggeman number increases. The voltage shape is smoothed with increasing the Bruggeman parameter. At the maximum value of Bruggeman number, the cell voltage becomes virtually linear between 20 and 100 % SOL. The effect and origin of the plateaus smoothing, linked to the electrode heterogeneity during operation, are extensively studied in the Chapter 3.

#### 2.3.2.2 Impact quantification

To go further on the sensitivity analysis, it is important to note that the sensitivity coefficient shows only the impact of one order of magnitude parameter change on either the cell voltage or capacity. However, the interval domain allocated to each parameter can be very different. It means that between two parameters having the same sensitivity coefficient but not the same interval domain, the one that will have the most influence on either the cell voltage or capacity will be the one the largest interval domain. In other words, to truly quantify the impact of each parameter, we need to define a factor taking into account this interval domain. For resistance class parameter, we propose the impact factor  $P_R$  defined as:

$$P_R = \frac{\int U_{\text{max}}(\text{SOL})d\text{SOL} - \int U_{\text{min}}(\text{SOL})d\text{SOL}}{\int U_{\text{ocv}}(\text{SOL})d\text{SOL}} \quad (2.31)$$

$U_{\max}$  and  $U_{\min}$  represents respectively the upper and lower cell voltage curves obtained for the parameter interval studied. Each of those cell voltage curves is integrated over the SOL range and the difference is compared to the equilibrium cell voltage  $U^{ocv}$  also integrated over the full SOL range. For the NMC electrode case,  $P_R$  is modified. Only cell voltages minus 3.6 V are integrated, in order to focus on the voltage range of interest.

For the capacity class parameter, the impact factor  $P_Q$  is calculated as the difference between the maximal and the minimal lithiation capacity over the theoretical capacity of the cell:

$$P_Q = \frac{Q_{\max} - Q_{\min}}{Q_{\text{cell}}} \quad (2.32)$$

### Parameters with low and medium impacts

A parameter is considered to have a low impact if it shows a resistance or capacity impact factor lower or equal to 1 %. A resistance or a capacity impact higher than 1 % but lower than 15 % is considered to have a medium impact. For illustration, the cell voltages obtained for the sensitivity analysis of the particle size and porosity are drawn on respectively Figures 2.12a and 2.12b. Inside their interval domain, particle size and porosity have respectively a medium and a low impact.

### Parameters with a high impact

An impact higher or equal to 15 % is considered to have a high impact. Parameters belonging to this category are the charge transfer coefficient,  $k$ , the ionic lithium diffusion coefficient,  $D_2$ , the solid diffusion coefficient,  $D_1$ , and the fraction of active material,  $w_i$ . Figure 2.12c presents cell voltages from the sensitivity analysis of the ionic lithium diffusion coefficient,  $D_2$ . The ionic lithium diffusion coefficient varies from  $10^{-9}$  to  $10^{-13} \text{ m}^2 \cdot \text{s}^{-1}$  and its impact on rate capability represents over 90 % of the cell capacity. We noticed that this parameter exhibits a threshold beyond which its impact vanishes, like the charge-transfer coefficient (Figure 2.10). Indeed, the ionic lithium diffusion coefficient does not have a significant effect on the capacity anymore for values higher than  $10^{-10} \text{ m}^2 \cdot \text{s}^{-1}$ .

### The special case of the particle shape

The impact of the particle shape cannot be analyzed with the protocol described in the previous section. The particle shape influences both the lithium transport in particle and the specific interface  $a$  as presented in Equation 2.24.

The impact of particle shape is estimated by comparison between a spherical and a cylindrical particle model. Figure 2.13 shows the cell voltage difference between the spherical and cylindrical model during a C/10, C/2, 1C, and 2C lithiation rates for a  $W_2$  graphite electrode. The cell voltage difference between the models is kept below 25 mV. As can be seen from comparison with Figure 2.12a, it represents a low resistance impact on the cell voltage. The capacity difference

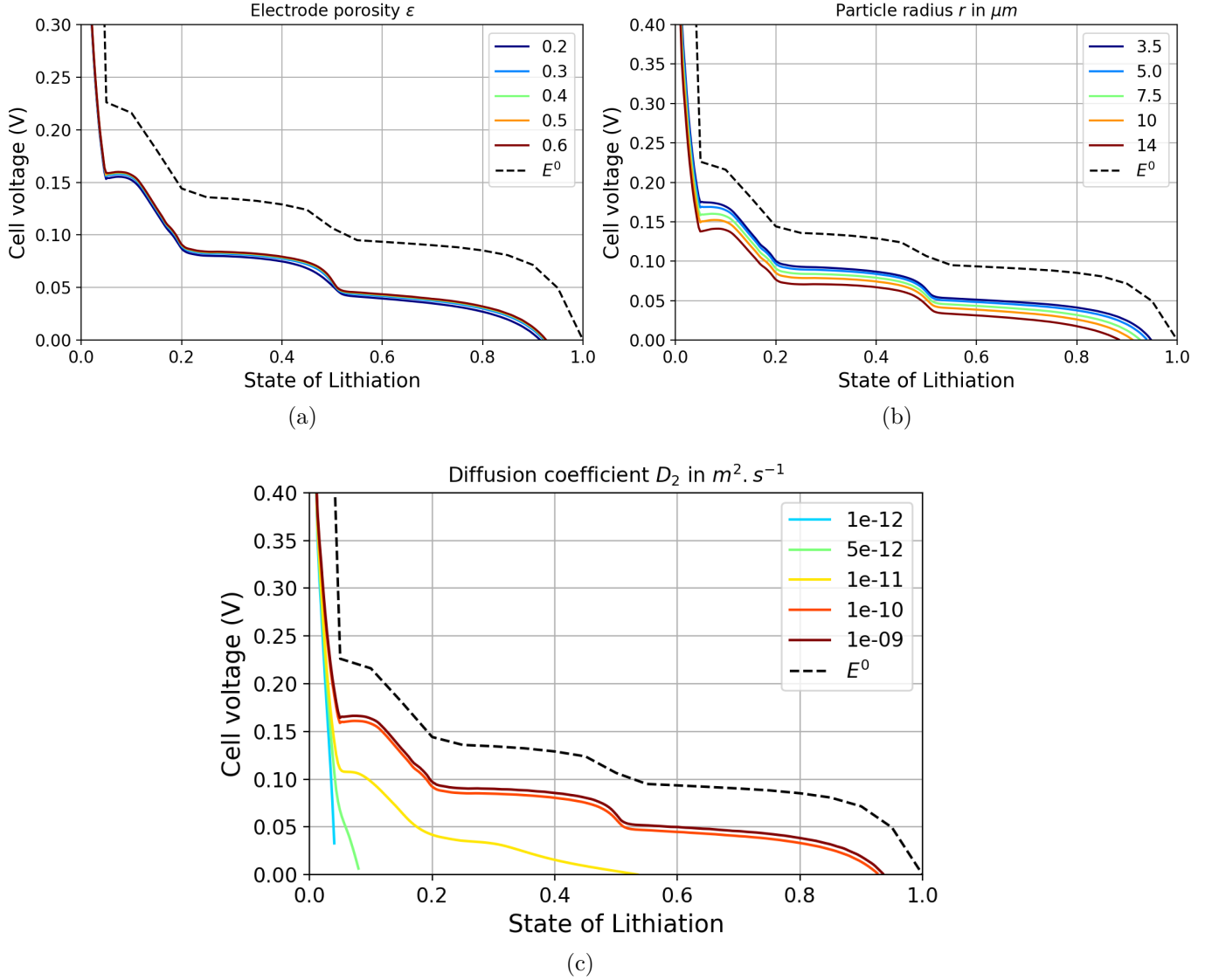


Figure 2.12: Simulated lithiation curves of a  $W_2$  graphite at C/2 with different porosity (a), particles radius ( $\mu\text{m}$ ) (b) and ionic lithium diffusion coefficient ( $\text{m}^2 \cdot \text{s}^{-1}$ ) (c)

is below 5 % SOL for all C-rates, which is also a low impact on rate capability. We notice that the cylindrical model induces more resistive loss than the spherical model. It is due to the smaller value of the specific interface  $a$  in a cylindrical model, which is 1.5 times lower than in the spherical model (see Equation 2.23). For the same active material volume, less amount of surface is available for intercalation, so it affects the value of the charge flux per electrode volume during lithiation. Nevertheless, since the reaction at interface is quite efficient, only a relatively low difference of local overpotential is needed in order to have the same charge flux per electrode volume between the two models. So at the global scale, the cell voltage difference is quite low. The choice of model does not have a high impact on the cell voltage during lithiation and delithiation. But given the geometry of our particles and experimental data, we have decided to keep a cylindrical model for

the graphite electrode and a spherical model for the NMC electrode.

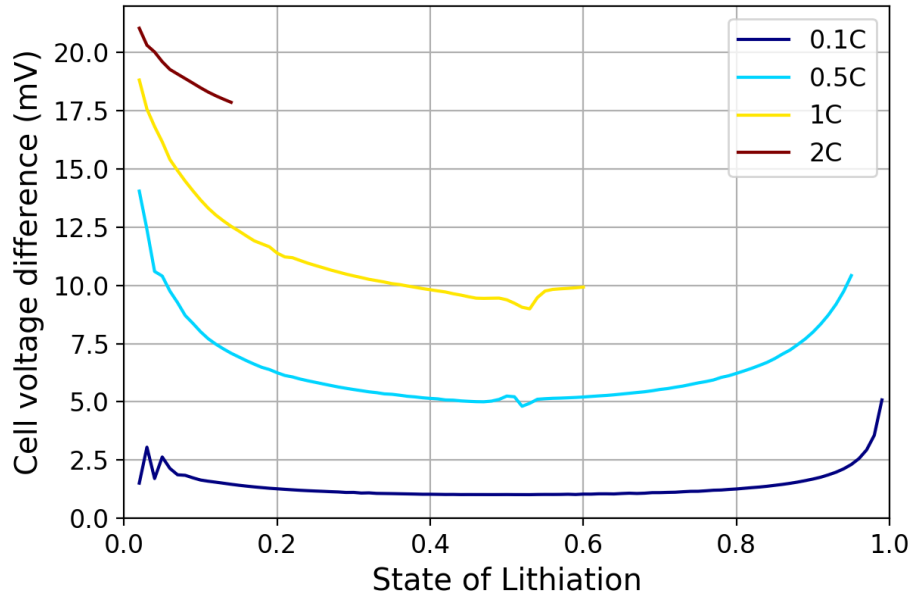


Figure 2.13: Simulated cell voltage difference between spherical particle and cylindrical particle models during lithiation at C/10, C/4, C/2 and 1C.

### 2.3.3 Results and summary of the sensitivity analysis

The sensitivity analysis is performed on a reference configuration: a  $W_2$  mass-loaded electrode, graphite or NMC, in a half-cell configuration and during a C/2 lithiation rate for graphite electrode (or a C/2 delithiation rate for NMC electrode) from an empty state of charge (a full state of charge for NMC electrode). For all *uncertain parameters*, their effects on the cell voltage and rate capability are classified and quantified. The obtained results of sensitivity analysis are presented in Tables 2.4, 2.5 and 2.6 for respectively separators, electrolyte, and lithium electrode as well, graphite electrode, and NMC electrode. In these tables, *uncertain parameters* are listed with their reference value, interval domain, relative class, and magnitude impact.

Resistance class parameters either affect the mobility of ionic species in the electrolyte or charges in the electrode, or influence the kinetics of lithium intercalation, like the charge-transfer coefficient,  $k$ , and the exchange coefficient  $\alpha$ . It results directly into a cell voltage loss that can be assimilated to a resistive behavior.

The capacity class parameters favor or reduce the transport of species in liquid or solid phase, the electrode capacity, and the rate capability. This is the case for mass fraction of active material in electrode solid phase, lithium diffusion coefficient in active material, and the Bruggeman parameter for example.

## Separator, electrolyte, and lithium electrode parameters

Table 2.4 presents parameters relative to the separator, electrolyte, and the lithium electrode. The separator-related parameters have only a low to medium impact on cell voltage. The electrolyte-related parameters, however, have a higher impact, especially the lithium diffusion coefficient in the liquid phase. Only this parameter has both a large interval domain and a strong sensitivity coefficient that justified its adjustment. In contrast, all other parameters have low to medium influence on cell voltage or capacity.

Table 2.4: List of separators, electrolyte, and lithium electrode parameters on a simulated  $W_2$  graphite lithiation at  $C/2$

Parameter	Symbol	Ref	Interval	Class	Impact	Sensitivity coefficient	Resource
Separator porosity	$\epsilon$	0.41	$\pm 0.2$	R	Medium (5 %)	$25 \frac{mV}{\log(\epsilon)}$	Data-sheet
Separator MacMullin number	$N_m$	6.5	$\pm 0.2$	R	Low (< 0.1 %)	$-0.7 \frac{mV}{\log(N_m)}$	Measured
Separator thickness ( $\mu\text{m}$ )	$L_s$	50	$\pm 0.5$	R	Low (< 0.1 %)	$-18 \frac{mV}{\log(L_s)}$	Data-sheet
Lithium salt concentration ( $\text{mol} \cdot \text{L}^{-1}$ )	$c_2^0$	1	$\pm 10\%$	R	Low (3 %)	$65 \frac{mV}{\log(c_2^0)}$	Data-sheet
Transference number	$t_+^0$	0.3	0.1 – 1	R	Medium (10 %)	$17 \frac{mV}{\log(t_+^0)}$	[78, 49, 4, 79, 80, 59, 72]
Activity coefficient	$\frac{d \ln f_{\pm}}{d \ln c}$	0	0 – 5	R	Medium (15 %)	$-6 mV / \log(\frac{d \ln f_{\pm}}{d \ln c})$	[78, 49, 4, 79, 80, 59, 72]
Diffusion coefficient in lithium salt ( $\text{m}^2 \cdot \text{s}^{-1}$ )	$D_2$	$7 \cdot 10^{-11}$	$10^{-13} - 10^{-9}$	C, R (10 %)	High (90 %)	$0.8 \frac{mAh}{\log(D_2)}$	[50, 81, 51, 82, 59, 32, 4, 83]
Electrolyte conductivity ( $\text{mS} \cdot \text{cm}^{-1}$ )	$\kappa$	[78]	$\pm 25$	R	Low (< 0.1 %)	$0.9 \frac{mV}{\log(\kappa)}$	[49, 78]
Symmetry factor of lithium	$\alpha_{Li}$	0.5	$\pm 0.1$	R	Low (2 %)	$24 \frac{mV}{\log(\alpha_{Li})}$	[50, 81, 51, 82, 59, 32, 4, 83]
Exchange current density of lithium ( $\text{A} \cdot \text{m}^{-2}$ )	$i_{Li}^0$	10	4 – 14	R	Medium (13 %)	$64 \frac{mV}{\log(i_{Li}^0)}$	Measured

## Graphite and NMC parameters

Sensitivity analysis results related to porous electrode parameters are presented in Table 2.5 for graphite and in Table 2.6 for NMC. These parameters have globally a higher resistance and capacity impact (medium to high) than lithium, separator and electrolyte parameters. It is noticed that the electronic conductivity has only a very low impact on cell potential with both electrodes. Parameters with a high impact are relative to intercalation kinetics, diffusive phenomena, and electrode composition : the charge-transfer coefficient  $k$ , the lithium diffusion coefficient in active material  $D_1$ , and the mass fraction of active material in solid phase of electrode,  $w_i$ . The effective working mass fraction of NMC or graphite in the final electrode can differ from the initial synthesis parameter, depending on the coating procedure and structural change during lithiation and delithiation cycles.

Table 2.5: List of graphite electrode parameters on a  $W_2$  graphite lithiation at C/2

Parameter	Symbol	Ref	Interval	Class	Impact	Sensitivity coefficient	Resource
Graphite electrode porosity	$\epsilon_{gr}$	0.32	$\pm 0.2$	R	Low (2 %)	$10 \frac{mV}{\log(\epsilon)}$	Synthesis
Bruggeman number of graphite electrode	$br_{gr}$	1.5	[1 – 3.5]	C , R (14%)	Medium (16 %)	$-0.76 \frac{mAh}{\log(br)}$	[84, 32, 67, 71, 83]
Diffusion coefficient in graphite ( $m^2 \cdot s^{-1}$ )	$D_1$	$10^{-15}$	$[10^{-17} - 10^{-9}]$	C	High (64 %)	$1 \frac{mAh}{\log(D_1)}$	[71]
Mean particle radius ( $\mu m$ )	$R_{gr}$	8	[3.5 – 14]	R	Medium (14 %)	$-40 \frac{mV}{\log(r)}$	Data-sheet
Electronic conductivity ( $S \cdot m^{-1}$ )	$\sigma_{gr}$	10	[10 – 100]	R	Low (< 1 %)	$10^{-2} \frac{mV}{\log(\sigma)}$	[50, 81, 51, 82, 59, 32, 4, 83]
Charge-transfer rate ( $mol \cdot m^{-2} \cdot s^{-1}$ )	$k_{gr}$	$10^{-10}$	$[10^{-12} - 10^{-9}]$	R	High (48 %)	$287 \frac{mV}{\log(k)}$	[50, 81, 51, 82, 59, 32, 4, 83]
Symmetry factor of graphite	$\alpha_{gr}$	0.5	$\pm 0.1$	R	Medium (20 %)	$-51 \frac{mV}{\log(\sigma)}$	[50, 81, 51, 82, 59, 32, 4, 83]
Mass fraction of active material in solid phase of electrode	$w_{gr}$	0.96	[0.86-1]	C, R (2 %)	High (16 %)	$5.5 \frac{mAh}{\log(w)}$	Synthesis
Initial lithium concentration in graphite	$x_{Li}(0)$	0.01	[0 – 0.05]	C	Medium (4 %)	$-0.2 \frac{mAh}{\log(x_{Li})}$	Measured

Table 2.6: List of NMC electrode parameters on a  $W_2$  NMC delithiation at C/2

Parameter	Symbol	Ref	Interval	Class	Impact	Sensitivity coefficient	Resource
NMC electrode porosity	$\epsilon_{NMC}$	0.35	$\pm 0.2$	R	Low ( $< 1\%$ )	$10^{-3} \frac{mV}{\log(\epsilon)}$	Synthesis
Bruggeman number of NMC electrode	$br_{NMC}$	1.5	[1 – 3.5]	C	Medium (14 %)	$-34 \frac{mV}{\log(br)}$	[60, 85, 86, 32, 87, 88]
Diffusion coefficient in NMC ( $m^2 \cdot s^{-1}$ )	$D_1$	$10^{-12}$	$[10^{-16} - 10^{-11}]$	C	High (84 %)	$0.5 \frac{mAh}{\log(D_1)}$	[60, 85, 86, 32, 87, 88]
Mean particle radius ( $\mu m$ )	$R_{NMC}$	4	[2 – 5]	R	Low ( $< 0.1\%$ )	$-10^{-3} \frac{mV}{\log(r)}$	Data-sheet
Electronic conductivity ( $S \cdot m^{-1}$ )	$\sigma_{NMC}$	50	[1 – 100]	R	Low ( $< 0.1\%$ )	$10^{-6} \frac{mV}{\log(\sigma)}$	[60, 85, 86, 32, 87, 88]
Charge-transfer rate ( $mol \cdot m^{-2} \cdot s^{-1}$ )	$k_{NMC}$	$10^{-9}$	$[10^{-13} - 10^{-5}]$	R	High (20 %)	$97 \frac{mV}{\log(k)}$	[60, 85, 86, 32, 87, 88]
Symmetry coefficient of NMC	$\alpha_{NMC}$	0.5	$\pm 0.1$	R	Low ( $< 1\%$ )	$-10^{-1} \frac{mV}{\log(\alpha)}$	[60, 85, 86, 32, 87, 88]
Mass fraction of active material in solid phase of electrode	$w_{NMC}$	0.92	[0.82-1]	C, R (2 %)	High (20 %)	$5 \frac{mAh}{\log(w)}$	Synthesis
Initial lithium concentration in NMC	$x_{Li}(0)$	0.95	[0.95 – 0.99]	C	Medium (8 %)	$0.5 \frac{mAh}{\log(x_{Li})}$	Measured

**Sensitivity analysis summary** Many parameters are necessary to run a half-cell model simulation. A sensitivity analysis is performed on *uncertain parameters* to get an overview of their respective impacts on the global cell behavior during galvanostatic operations. It is possible to categorize them according to their effect on cell voltage and rate capability.

Results indicate that few parameters have a high sensitivity coefficient combined with a sufficiently large interval domain. The charge-transfer rate,  $k$ , the lithium diffusion coefficient in solid phase,  $D_1$ , the lithium diffusion coefficient in liquid phase,  $D_2$ , and the mass-fraction of active material  $w_i$  have a complementary behavior (capacity and resistance) . These four parameters correspond to critical phenomena and cell characteristics: intercalation kinetics, species transport, and cell capacity.

Simulated cell voltage and rate capability can then be adjusted to experimental results by tuning these four parameters.

## 2.4 Half-cell model validation

In this part, the validation procedure and the fitted results obtained for half-cell models (graphite or NMC) operated at various mass-loadings and C-rates are presented.

### 2.4.1 Validation procedure

To adjust  $w_i$ ,  $k$ ,  $D_1$ , and  $D_2$ , the first step consists in determining the cell capacity, so called the cell balancing step [49]. In the expression of cell capacity (Equation 2.26),  $q_i$ ,  $\rho_i$  and  $S$  are assumed to be accurately known, while  $W_i$  and  $r_i$  are known from active material synthesis. Thus, only  $w_i$  is considered as the adjustable parameter in Equation 2.26. This analytic expression compared to the experimental measured capacities gives an adjusted value of  $w_i$ , different from the synthesis value of 96 %wt for graphite electrode and 92 %wt for NMC electrode. Adjusted mass fractions are presented in Table 2.7 and deviations from the synthesis value are below 6 % for all electrodes.

A fitting procedure is then developed under COMSOL Multiphysics linked with MATLAB to identify the three parameter set ( $k$ ,  $D_1$ ,  $D_2$ ) that minimize both errors on cell voltage and capacity between simulated and experimental galvanostatic operations. The fitting procedure is composed of two steps. The first step uses intrinsic nonlinear least-squares algorithms of Matlab (lsqcurvefit). Final results of this step reduce parameter value intervals, which are then adjusted manually. The sensitivity coefficients calculated during the sensitivity analysis help to reduce the number of iterations that is needed to get the right set of parameters.

### 2.4.2 Simulation results

The obtained calibrated parameters are presented in Table 2.7 and the corresponding cell voltage results are shown in Figure 2.14 for graphite electrodes lithiation, and in Figure 2.15 for NMC electrodes delithiation at various rates (C/10, C/3, C/2, 1C, 2C, and 3C). Cell voltages are shown as a function of lithiated capacity per electrode mass ( $\text{mAh} \cdot \text{g}^{-1}$ ) in order to compare the performance according to the mass-loading. For C-rates greater than C/10, a specific capacity loss can be experimentally observed for a mass-loading rise and simulations fit this tendency. Simulation errors do not exceed 15 % on cell voltage and 14 % on lithiated capacity. Cell voltage errors may be reduced by considering temperature variation and its impact on the charge transfer rate  $k$  (see section 2.4.3). Errors on capacity may be lowered with a lithium concentration dependent diffusion coefficient  $D_1$  (see section 2.4.3).

The experimental cell voltages of graphite electrode are smoother than simulated ones for lithiation rates greater than C/5 (Figure 2.14). As seen during the sensitivity analysis, a higher Bruggeman number could fit this tendency by lowering the effective transport inside the porous electrode. The average errors on NMC cell voltage and capacity are lower than graphite ones (less than 10 %). Nevertheless polarization resistances which occurs at the beginning of delithiation

Table 2.7: Adjusted parameters for the graphite a) and NMC b) electrode model

Graphite	$W_1$	$W_2$	$W_3$	NMC	$W_1$	$W_2$	$W_3$
Mass fraction $w_{gr}$	0.90	0.92	0.93	Mass fraction $w_{NMC}$	0.87	0.91	0.90
Charge transfer rate $k_{gr}$ ( $\text{mol} \cdot \text{m}^{-2} \cdot \text{s}^{-1}$ )	$6 \cdot 10^{-11}$	$6 \cdot 10^{-11}$	$2 \cdot 10^{-11}$	Charge transfer rate $k_{NMC}$ ( $\text{mol} \cdot \text{m}^{-2} \cdot \text{s}^{-1}$ )	$5 \cdot 10^{-6}$	$5 \cdot 10^{-6}$	$5 \cdot 10^{-6}$
Diffusion coefficient $D_1$ ( $\text{m}^2 \cdot \text{s}^{-1}$ )	$1 \cdot 10^{-12}$	$5 \cdot 10^{-13}$	$5 \cdot 10^{-13}$	Diffusion coefficient $D_1$ ( $\text{m}^2 \cdot \text{s}^{-1}$ )	$5 \cdot 10^{-11}$	$5 \cdot 10^{-11}$	$1 \cdot 10^{-11}$
Diffusion coefficient $D_2$ ( $\text{m}^2 \cdot \text{s}^{-1}$ )	$5 \cdot 10^{-11}$			Diffusion coefficient $D_2$ ( $\text{m}^2 \cdot \text{s}^{-1}$ )	$7.5 \cdot 10^{-11}$		
	(a)				(b)		

are not taken into account in our model and errors on simulated cell voltage are noticeable (Figure 2.15). This should be adjusted with a variable lithium diffusion coefficient in NMC. For the  $W_3$  NMC electrode, the capacity extracted falls down abruptly at 2C. This tendency is fitted with the adjusted model.

As can be observed in Table 2.7, some variations are observed for adjusted parameter when considering the three loading. The lithium diffusion coefficient in solid phase of graphite electrode varies from  $5 \cdot 10^{-13}$  to  $10^{-12} \text{ m}^2 \cdot \text{s}^{-1}$  when mass-loading increases from  $W_1$  to  $W_3$ . Nevertheless, parameters stay relatively in the same order of magnitude whatever the mass-loading, and this proves the consistency of the adjusted sets of parameters.

The values of charge-transfer rate and lithium diffusion coefficient inside active materials are lower in the graphite electrodes (respectively  $10^{-11} \text{ mol} \cdot \text{m}^{-2} \cdot \text{s}^{-1}$  and  $10^{-13} \text{ m}^2 \cdot \text{s}^{-1}$ ) compared to the NMC ones (respectively  $10^{-6} \text{ mol} \cdot \text{m}^{-2} \cdot \text{s}^{-1}$  and  $10^{-11} \text{ m}^2 \cdot \text{s}^{-1}$ ). So intercalation kinetics and solid state diffusion are more efficient inside NMC than graphite and it justifies experimental results previously presented (subsection 2.1.3).

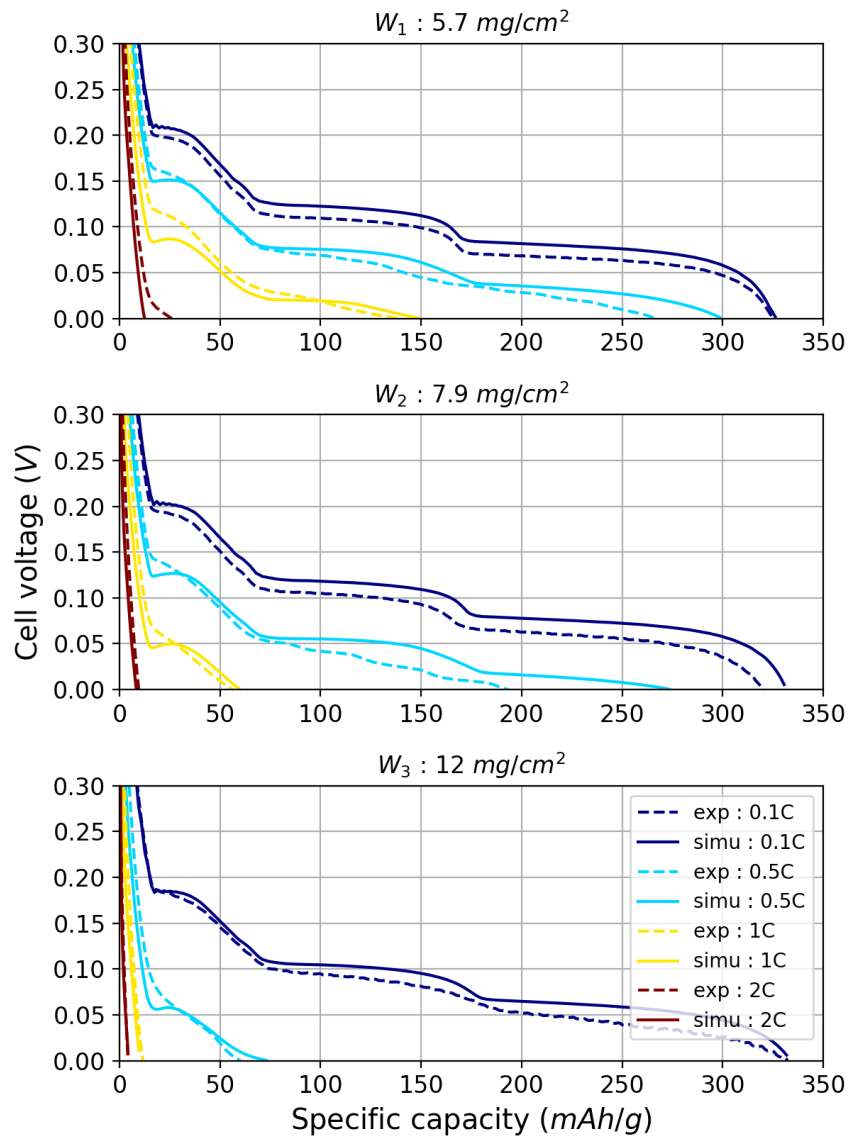


Figure 2.14: Calibrated model and experimental result on different lithiation current ( $C/10$ ,  $C/2$ ,  $1C$ ,  $2C$ ) for mass-loading  $W_1$ ,  $W_2$  and  $W_3$  on lithium-graphite cell

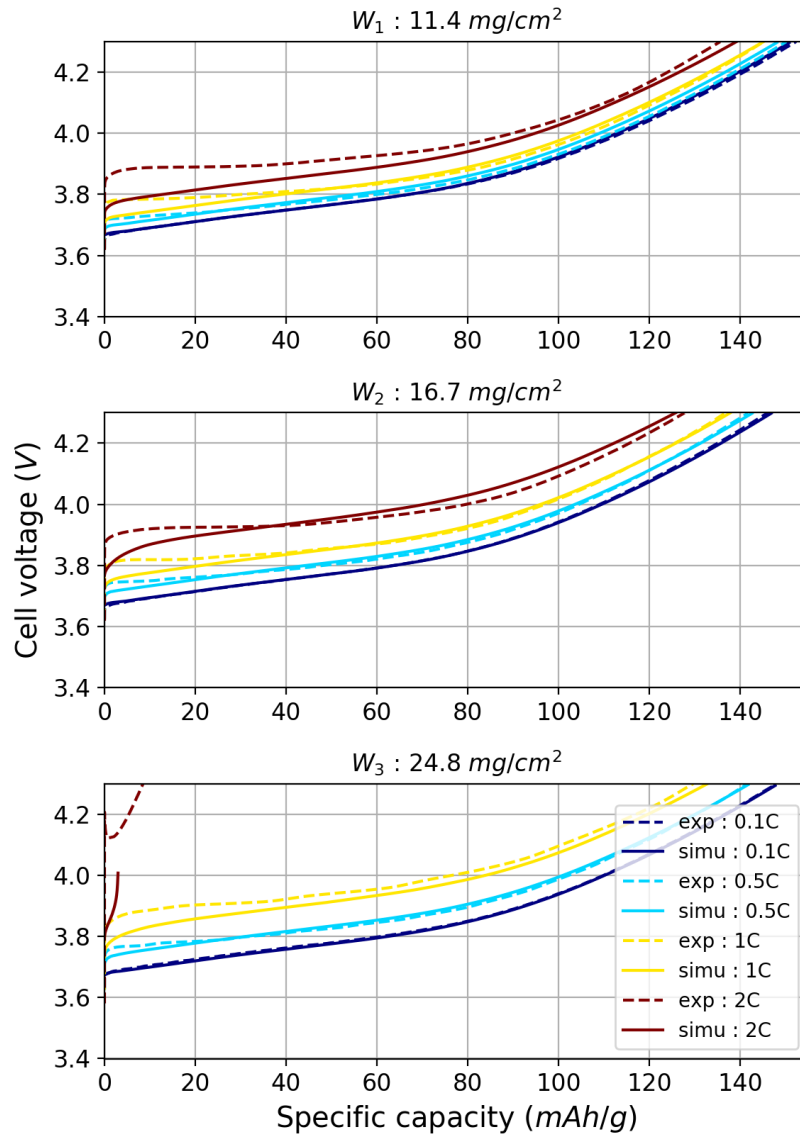


Figure 2.15: Calibrated model and experimental result on different delithiation current (C/10, C/2, 1C, 2C) for mass-loading  $W_1$ ,  $W_2$  and  $W_3$  on lithium-NMC cell

### 2.4.3 Model limitations

The model hypotheses may explain some discrepancies between experimental data and simulation results. In this subsection, we will address several topics that could help increasing the model fidelity to experimental data: cell temperature, lithium content dependency of the diffusion coefficient in the active material, electric double layer, and relaxation phenomenon.

## Impact of temperature

In literature, a common way to introduce thermal influence is to consider a general energy balance of the electrochemical system [89, 90, 91] and temperature dependent parameters [92, 77]. It is well-known that temperature enhances electrochemical reactions, and transport phenomena. An Arrhenius law is often used to predict the temperature impact on these parameters [93].

In a real system, when the C-rate increases, the coin-cell temperature rises due to the Joule effect and consequently intercalation kinetics improves. A constant charge-transfer rate is used in our model, whatever the applied C-rate. At C/2, the experimental cell polarization is larger than the simulated one (Figure 2.14), while at 1C, the opposite is true. The temperature difference between a high and a low C-rate may explain these respective under- and over-estimation of cell polarization in the adjusted model.

## Impact of lithium content on the diffusion coefficient in the active material

The lithium diffusion coefficient inside active material,  $D_1$  is an *uncertain parameter* and difficult to estimate. ECKER *et al.* derives  $D_1$  inside graphite from GITT measurements and shows that this parameter decreases by four orders of magnitude from low to high lithiation state [78]. In Figure 2.16a is drawn experimental lithium diffusion coefficients of reference [78] with respect to lithium stoichiometry in graphite. A logarithmic average value of  $D_1$  is displayed for comparison. At high intercalation state, lithium transport inside active material is more difficult, time relaxation increases and subsequently, diffusion coefficient decreases.

Simulations are run for the  $W_2$  graphite electrode model during a C/2 lithiation with two configurations: constant and variable diffusion coefficient  $D_1$  from Figure 2.16a. As observed on cell voltage results (Figure 2.16b), cell polarization do not differ in both cases, but capacity is limited with a variable  $D_1$ . Cell voltage falls down after 50 % SOL, when the transport inside particle becomes a limiting step.

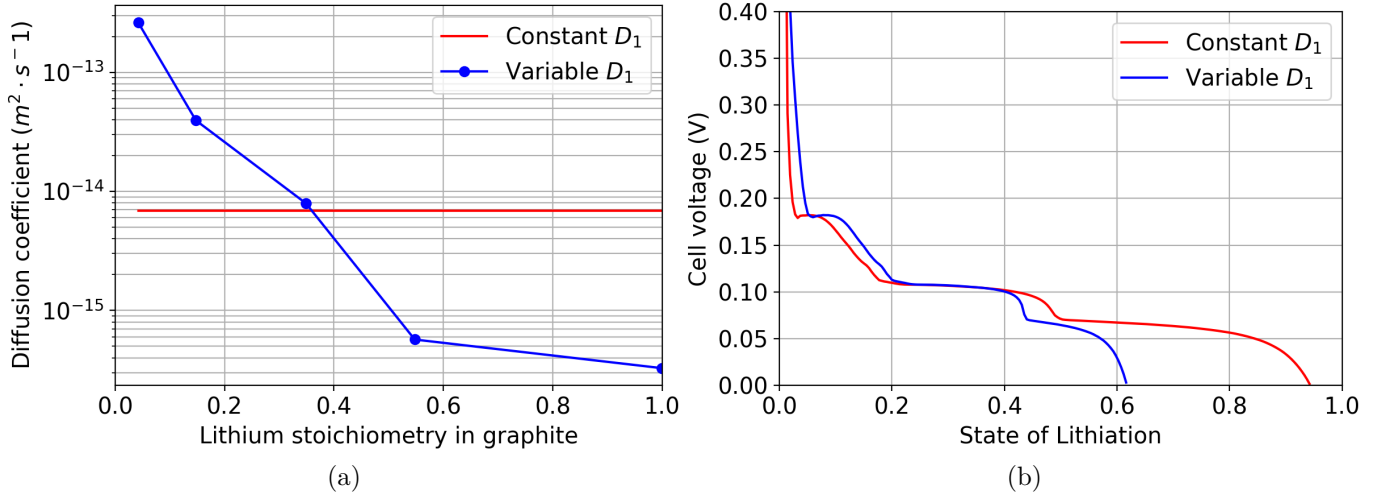


Figure 2.16: Comparison between constant and variable coefficient diffusion (a) and effects on cell voltage during a simulated C/2 lithiation (b)

SUBRAMANIAN *et al.* explores the difference in a nickel composite graphite electrode between the constant and variable diffusion coefficient hypotheses [94]. Beyond 6C or at high intercalation state, simulations with the constant coefficient hypothesis diverge from those with variable coefficient hypothesis. In the framework of this thesis, an experimental lithiation lower than expected in simulation can be explained with diffusion limitation at high intercalation state.

### Impact of electrical double layer

Fast transient phenomena are not taken into account in the current model, as for example charging and discharging of the double layer capacitance located at electrode/electrolyte interfaces. The predictability of the model is limited at transient regimes ranging from milliseconds to tenths of a second. ONG *et al.* developed a modified P2D model, adding a non-faradaic Helmholtz double-layer capacitive contribution to the total interfacial current density [95]. The impedance response of a porous electrode can then be accurately simulated, as demonstrated by MEYERS *et al.* [96].

### Impact of relaxation

In the current model, two relaxation mechanisms occur when galvanostatic operations stop: the lithium concentration equilibrium in liquid phase through electrode thickness and in solid phase through particles radii. Respective time constants,  $\tau$ , are calculated with Equation 2.33, where  $l$  is a dimension corresponding to the studied object and  $D$  the corresponding diffusion coefficient:

$$\tau = l^2/D \quad (2.33)$$

Graphite particle radii are 8  $\mu\text{m}$  and the electrode thickness lies between 40  $\mu\text{m}$  and 85  $\mu\text{m}$ . The respective lithium diffusion coefficients  $D_1$  is about  $10^{-13} \text{ m}^2 \cdot \text{s}^{-1}$  and the effective ionic lithium diffusion coefficient  $D_2$  is about  $5 \cdot 10^{-12} \text{ m}^2 \cdot \text{s}^{-1}$ . Therefore, lithium concentration relaxations last two minutes inside the particles and up to 20 minutes inside the electrode thickness (ten times more).

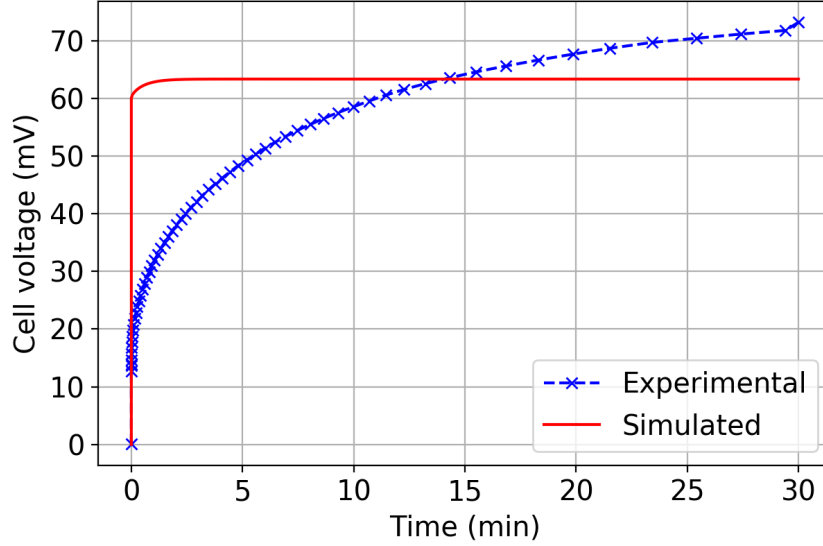


Figure 2.17: Experimental and simulation comparison on cell voltage relaxation on a  $W_2$  lithium-graphite cell after a  $C/2$  lithiation

The experimental and simulated cell voltages that follows a  $C/2$  lithiation on the adjusted  $W_2$  graphite electrode are compared in Figure 2.17. The experimental relaxation is ten times slower than the simulated one. The time constant associated with the salt relaxation is not taken into account on simulation results. FULLER *et al.* have studied intensively this relaxation process inside the P2D model [97]. DARLING *et al.* have gone further and analyzed the non-ideality aspect [30]: a two particle model relaxes slower than a one particle model. Indeed, as the current model is quite homogeneous and ideal, the simulated relaxation process is faster than the experimental one. The lack of similarity between experimental and simulated results denotes that the porous electrode structure and lithium-ion concentration equilibration processes are more complex in reality [98].

## 2.5 Conclusion

In this chapter, the development and validation of a porous graphite electrode model in a lithium-graphite and a graphite-NMC configuration is presented. Different half-cells were studied electrochemically at different mass-loadings of electrode material (graphite and NMC). It appears that graphite electrodes show higher impedance and lower rate capability than NMC electrodes. Both graphite material properties and electrode structure are involved in these limitations.

A model of a porous electrode in a half-cell configuration is then developed. This modeling effort requires a large amount of physical parameters to adjust. Parameters are sorted as either *reliable* or *uncertain*. For *uncertain parameters*, a sensitivity analysis is performed to classify and quantify their impact on cell voltage or capacity according to their influence and interval domain. Results indicate that the four predominant and complementary *uncertain parameters* that are needed to be adjusted are related to the main physical limitations of the cell : intercalation kinetics ( $k$ ) , species transport ( $D_1$  and  $D_2$ ), and cell capacity ( $w_i$ ).

The model is fitted to experimental galvanostatic operations of graphite and NMC electrodes. The adjusted parameters confirm that graphite tends to be a less electrochemically active electrode than NMC.

The final model predicts with good accuracy the voltage response of half-cells under various constant currents. It also gives access to *operando* internal conditions such as local potentials, lithium concentration in electrolyte or inside active material. One goal of **Chapter 3** is therefore to use this validated model to get insights on the impact of mass-loading and C-rate on the local heterogeneity and the contribution of the different physical phenomena to the overall cell's resistance.

# Chapter 3

## Performance limitations of graphite electrode : lithiation heterogeneities during operations

### Contents

---

<b>3.1</b>	<b>Evaluation of the lithiation heterogeneities inside the electrode . . .</b>	<b>50</b>
3.1.1	Simulation of the graphite electrode lithiation . . . . .	50
3.1.2	Description of the NAAD parameter . . . . .	53
3.1.3	Influences of C-rate and mass-loading on heterogeneities . . . . .	53
3.1.4	Influences of kinetics and diffusion parameters on lithiation heterogeneities	54
3.1.5	Experimental correlations . . . . .	57
<b>3.2</b>	<b>Study of the lithiation heterogeneity mechanism . . . . .</b>	<b>59</b>
3.2.1	Electrode resistances . . . . .	59
3.2.2	Equilibrium potential influences on lithiation heterogeneity . . . . .	63
3.2.3	Generalization to other active materials . . . . .	64
<b>3.3</b>	<b>Particles shape and size distribution influence on lithiation hetero- geneities . . . . .</b>	<b>65</b>
3.3.1	Particle shape distribution . . . . .	66
3.3.2	Particle size distribution . . . . .	68
3.3.3	Comparison of particle distribution models . . . . .	74
<b>3.4</b>	<b>Experimental <i>operando</i> observations of lithiation heterogeneities . . .</b>	<b>76</b>
3.4.1	Experimental studies . . . . .	77
3.4.2	Experiment principle and requirements . . . . .	77

3.4.3	Experimental set-up . . . . .	78
3.4.4	Preliminary results and perspectives . . . . .	79
<b>3.5</b>	<b>Conclusion . . . . .</b>	<b>82</b>

---

The graphite electrode is limited in power and rate capability, and these limitations are related to the electrode mass-loading, the porous structure, and intrinsic physical properties of the active material. The half-cell model validated in the previous chapter allows to explore internal conditions inside this specific electrode and quantify these limitations.

At the porous electrode scale, the main performance limitations of graphite are found in the intercalation kinetics, and the lithium transport inside the porous media and active material. The local surface stoichiometry of graphite,  $x_{\text{Li}}$ , is a variable that depends on both the kinetics and transport limitations during lithiation. Thus, its value along electrode thickness is a versatile indicator for intercalation heterogeneity. These lithiation heterogeneities are studied according to the different influences of C-rate, mass-loading, and predominant physical parameters.

During operation, the real lithium distribution is complex to model, because of structural heterogeneities, active material distribution in shape and size, local defects, and aging mechanisms. To approach the actual lithium distribution, the validated lithium-graphite model is extended to study quantitatively the influence of the diversity of particle shapes and sizes.

In a last part, an experimental validation of the theoretical heterogeneity mechanism is presented. An *operando* measurement of local lithiation state inside a graphite electrode is performed during lithiation, using a synchrotron source.

## 3.1 Evaluation of the lithiation heterogeneities inside the electrode

### 3.1.1 Simulation of the graphite electrode lithiation

The intercalation kinetics in graphite electrode is influenced by local conditions, such as ionic and electronic potentials, lithium salt, and intercalated lithium concentrations. The local intercalation current per electrode volume is given by a B-V equation function of surface stoichiometry ( $x_{\text{Li}}$ ), lithium salt concentration ( $c_2$ ) and overpotential ( $\eta$ ) :

$$ai_n = \frac{n}{r}(1 - \epsilon)\frac{\rho_1}{\rho}w_iFk(1 - x_{\text{Li}})^{1-\alpha}(x_{\text{Li}})^\alpha\left(\frac{c_2}{c_2^0}\right)^{1-\alpha}\left(\exp\left(\frac{\alpha F\eta}{RT}\right) - \exp\left(-\frac{(1 - \alpha)F\eta}{RT}\right)\right) \quad (3.1)$$

In [Equation 3.1](#),  $n$  and  $r$  corresponds respectively to the shape and the size of the particle model, 2 and 16  $\mu\text{m}$  in the graphite case.

First, we investigate how mass-loadings and C-rates locally affect the lithium salt concentration. The salt concentration profile through electrode thickness can be obtained at the end of lithiation for various mass-loading ( $W_1$ ,  $W_2$ , and  $W_3$ ) and C-rate, thanks to our adjusted model ([Figure 3.1](#)). In this [Figure](#), salt concentration profiles are plotted against the cell thickness, the x-axis origin

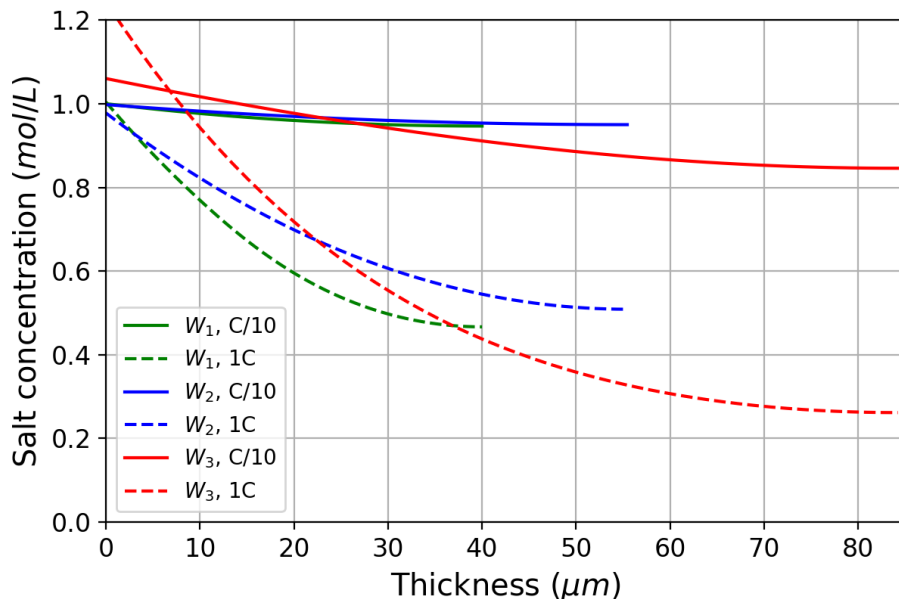


Figure 3.1: Simulated lithium salt concentration profiles inside the electrode at the end of lithiation, at C/10 and 1C for different mass-loadings (5.7, 7.9, and 12.0  $\text{mg} \cdot \text{cm}^{-2}$ )

corresponds to the separator/electrode boundary. At C/10, lithium salt diffuses easily through thickness whatever the mass-loading, transport limitations are negligible. The salt concentration is quite homogeneous: close to  $1 \text{ mol} \cdot \text{L}^{-1}$  at the end of lithiation, and the maximal variation is less than 20 % along thickness. However at 1C, the lithium salt depletion is much stronger. Inside a  $W_3$  electrode, the salt concentration at the current collector boundary falls down to  $0.3 \text{ mol} \cdot \text{L}^{-1}$ . Salt depletion is more limited in the  $W_2$  and  $W_1$  electrodes due to their smaller thickness.

Salt transport limitations appear preferentially at high C-rates or large mass-loadings. They impact the homogeneity of intercalation kinetics through electrode via the salt concentration (Equation 3.1). Gallagher *et al.* proposes an analytical formula to predict the lithium salt depletion and the concentration profile along the cell thickness [39]. They underline a limited length for salt penetration, function of the applied current and electrolyte transport properties inside the porous electrode structure.

The electrode overpotential ( $\eta$ ) is also visible along the electrode thickness, through C-rate and mass-loading. As can be seen in Figure 3.2, at 20 % SOL (State Of Lithiation), the overpotential is very homogeneous at low C-rate (C/10) but a little bit heterogeneous for a higher lithiation rate. The mass-loading emphasizes also this heterogeneity, especially for the higher loading.

The local lithium stoichiometry can be monitored both along the electrode thickness and particle radii. Figure 3.3 plots the local lithium stoichiometry profile at particles surface (named  $x_{\text{Li}}$ ) and center through thickness at 20 % SOL during a C/10 and C/2 lithiation of a  $W_3$  electrode. The lithium stoichiometry at surface of particles varies from about 10 % at C/10 between separator and current collector, and rises up to 50 % at C/2. Inside particle, the stoichiometry difference between surface and center is negligible at low C-rates, but as the lithiation rate rises,

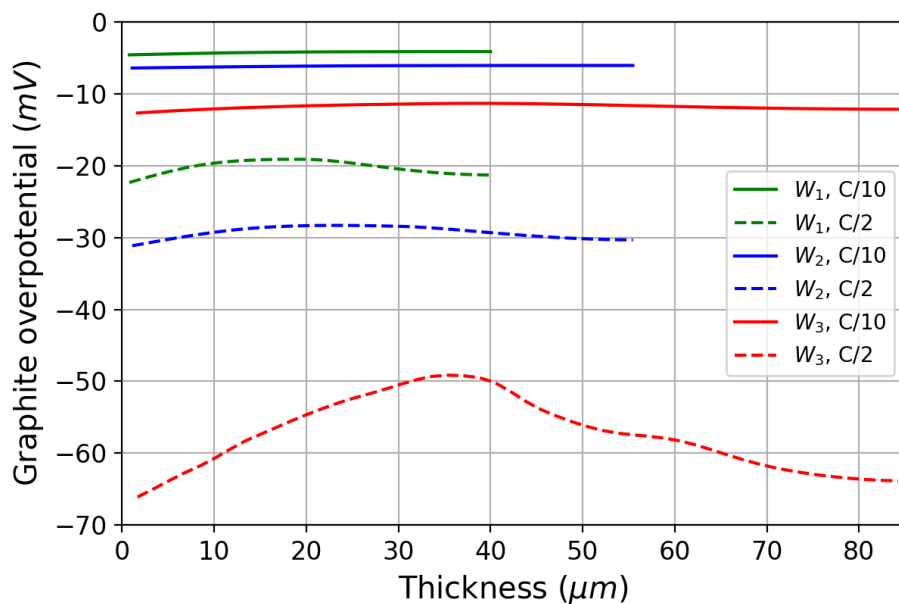


Figure 3.2: Simulated overpotential profiles inside electrode at 20 % SOL, for different mass loadings ( $5.7, 7.9, \text{ and } 12.0 \text{ mg} \cdot \text{cm}^{-2}$ ) and C-rates (C/10 and C/2)

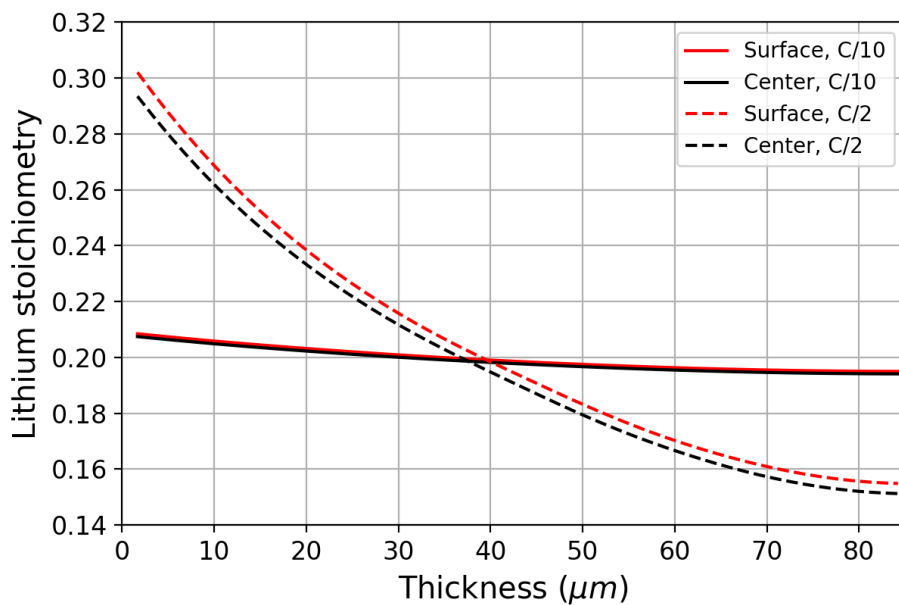


Figure 3.3: Simulated lithium stoichiometry at particle surface and center through electrode thickness at 20 % SOL for a C/10 and C/2 lithiation on a  $W_3$  graphite electrode ( $12.0 \text{ mg} \cdot \text{cm}^{-2}$ )

this difference increases due to transport limitations of lithium inside active material.

As seen on simulation results, the graphite electrode does not work in a homogeneous way and this reduces performance and accelerates aging [99, 100, 101, 102, 103, 104]. The particle surface stoichiometry distribution has directly an influence on local intercalation currents (Equation 3.1) and is thus an *operando* indicator of the local kinetics and transport performances. The non-uniformity of this variable along the thickness decreases optimal electrode lithiations and delithiations. In the following, the thickness inhomogeneity of  $x_{Li}$  is investigated for different parameters in order to predict lithiation heterogeneity. The values of C-rate, mass-loading and parameters related to the intercalation kinetics or the lithium transport (in liquid or in solid phase) modify amplitude and appearance of these lithiation heterogeneities.

### 3.1.2 Description of the NAAD parameter

In order to quantify and analyze  $x_{Li}$  heterogeneities, a marker called NAAD, or Normalized Absolute Averaged Deviation is introduced. The NAAD represents the normalized deviation of a variable from its spatial averaged value and is expressed in %. It was used by GU to study spatial heterogeneities of current distribution in a Zn/NiOOH cell [105]. This number is given, for any physical quantity  $Y$  and its spatial averaged value  $\bar{Y}$  over graphite electrode's length  $L_{gr}$ , by :

$$NAAD(Y) = \frac{1}{L_{gr}} \int_0^{L_{gr}} \frac{|Y(x) - \bar{Y}|}{\bar{Y}} dx \quad (3.2)$$

A high NAAD value corresponds to a high spatial heterogeneity whereas a low value is linked to a small spatial dispersion.

### 3.1.3 Influences of C-rate and mass-loading on heterogeneities

The NAAD of  $x_{Li}$  are shown in Figure 3.4 obtained for the different electrodes and lithiation currents. The NAAD is monitored during a C/10 lithiation rate for  $W_1$ ,  $W_2$ , and  $W_3$ , but also during a C/2 and a 3/4C lithiation rate for the medium mass-loading  $W_2$ . Heterogeneities depend strongly on the SOL: the NAAD curve has a particular wave shape with three maximums, located at 10 %, 35 % and 70 % SOL, and three minimums, located at 5 %, 20 % and 50 % SOL. These maximum and minimum values are correlated with the shape variations of the global equilibrium potential of graphite. As explain by OHZUKU *et al.* [17] and seen in Figure 3.4, graphite material shows a typical shape of equilibrium voltage composed of plateaus region and transition. As a reminder, the origin of this shape is due to the structure of graphite. Different specific intercalation compounds (or stages) are formed when lithium is intercalated into graphite. Five compounds are defined and they correspond to different ordering of lithium into the crystallographic structure of graphite [106]. Two compounds could coexist in the active material at the same moment. On

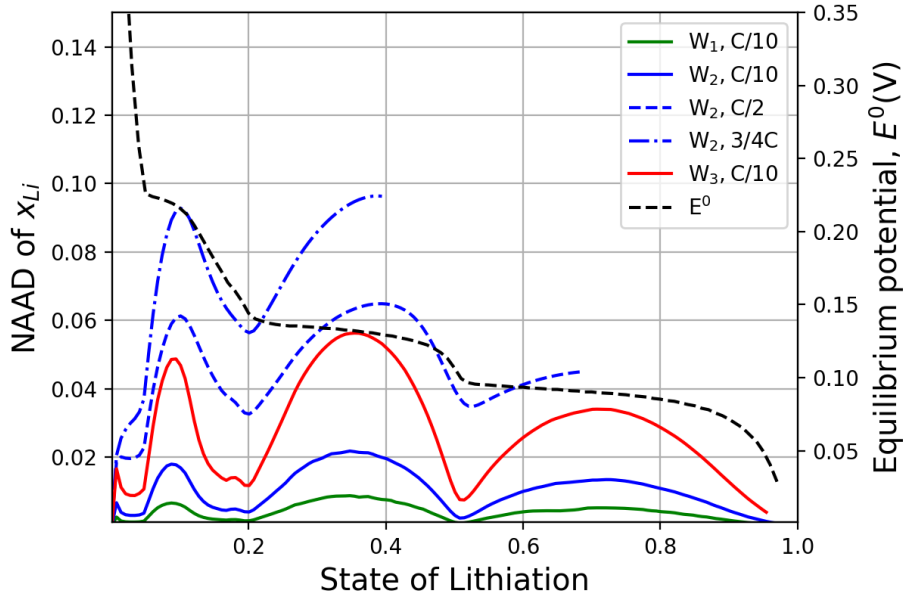


Figure 3.4: Simulated NAAD of particle surface stoichiometry at different mass-loadings (5.7, 7.9, and  $12.0 \text{ mg} \cdot \text{cm}^{-2}$ ) and C-rates (C/10, C/2, 3/4C).

equilibrium potential curve, the transition between two compounds, so the coexistence of two stages in a diphasic behavior, corresponds to a plateau of potential. A monophasic behavior, correspond to the presence of only one stage and is related to a variation of equilibrium potential, so a transition between two plateaus. Model results show that SOL of plateau regions correspond to heterogeneous  $x_{\text{Li}}$  zones, while SOL of transition zones, between plateaus, correspond to homogeneous zones. Moreover, it can be noticed in Figure 3.4 that increasing lithiation current as well as mass-loading increases stoichiometry heterogeneities. In details, a high lithiation current prevents a return to a homogeneous electrode after a plateau in contrary to the effect of a high mass loading for which the return to a homogeneous electrode is more effective. So a high lithiation current and a heavy loading promote heterogeneities, but only current keeps lithiation disparities.

### 3.1.4 Influences of kinetics and diffusion parameters on lithiation heterogeneities

The sensitivity analysis data from the previous chapter is used to study the influences on the  $x_{\text{Li}}$  NAAD of parameters relative to the kinetics, diffusion in solid phase, and diffusion in liquid phase. As a reminder, the reference simulation is a C/2 lithiation until 0 V, from an empty state of charge on a lithium-graphite model at a medium  $W_2$  mass-loading ( $2.7 \text{ mg} \cdot \text{cm}^{-2}$ ). Model parameters are selected in Table 2.5 and in Table 2.7 for the adjusted ones.

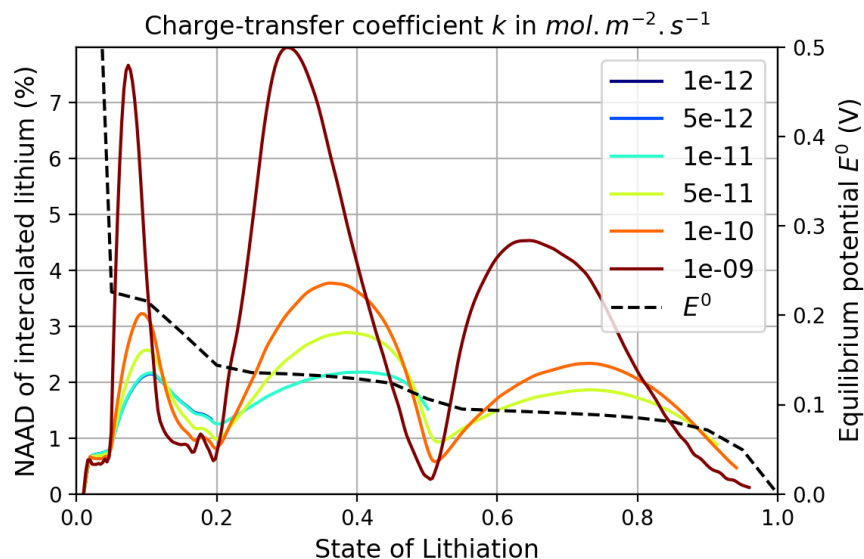


Figure 3.5: NAAD of particle surface stoichiometry obtained for different constants of charge-transfer on a simulated  $W_2$  graphite lithiation ( $C/2$ )

### Intercalation kinetics

The intercalation kinetics is mainly influenced by the charge-transfer rate, and also, among other, by the particle geometry: shape and size (see Equation 3.1). A low constant of charge-transfer increases directly the cell polarization, whereas a smaller particle size or a spherical particle instead of a cylindrical one, reduces the cell polarization, because it increases the developed electrochemically active surface per electrode volume at fixed mass-loading. In Figure 3.5, is drawn the NAAD of particle surface stoichiometry as a function of SOL during reference simulations with different constants of charge-transfer. For all parameters taken, the typical lithiation heterogeneity shape is conserved, with maximum and minimum peaks as previously seen in Figure 3.4. With a high charge-transfer rate of  $10^{-9} \text{ mol} \cdot \text{m}^{-2} \cdot \text{s}^{-1}$ , the heterogeneity peaks reach a maximum value (at 8 %). Along the interval domain of charge-transfer values, the heterogeneities peaks can increased by 700 %. Particle radius and shape disparities have less effects on heterogeneity with a maximal 50 % variation along radii and shape (Figure 3.6a and 3.6b). Shrinking the reference particle size by half adds only 30 % to the peaks of NAAD value.

As seen in Figures 3.5, 3.6a, and 3.6b, parameters related to the kinetics modify the maximal value of heterogeneity, but do not excessively change its minimal value along graphite lithiation. To conclude, an improvement of the local intercalation kinetics via modifications on exchange current highlights other heterogeneities sources through electrode thickness as lithium salt transport limitations. Then this kinetics improvement enhances the temporary heterogeneities during SOL corresponding to cell voltage plateau region.

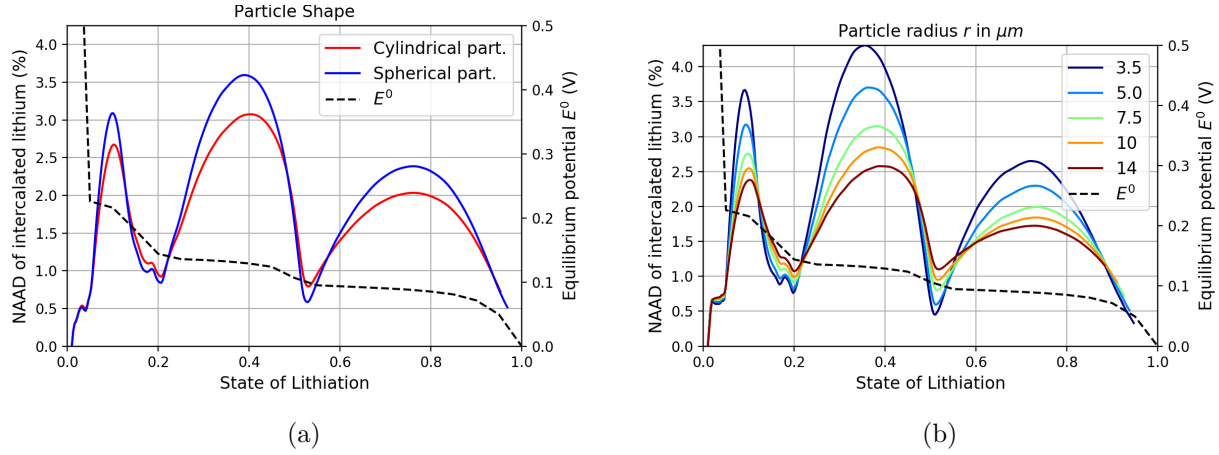


Figure 3.6: NAAD of particle surface stoichiometry obtained at different particle shape (a) and particle radius (b) on a simulated  $W_2$  graphite lithiation ( $C/2$ )

### Diffusion inside active material

Lithium transport inside active material is determined by the lithium diffusion coefficient  $D_1$  and the particle shape, which modify the lithium transport equation (Equation 2.24). Figure 3.7a

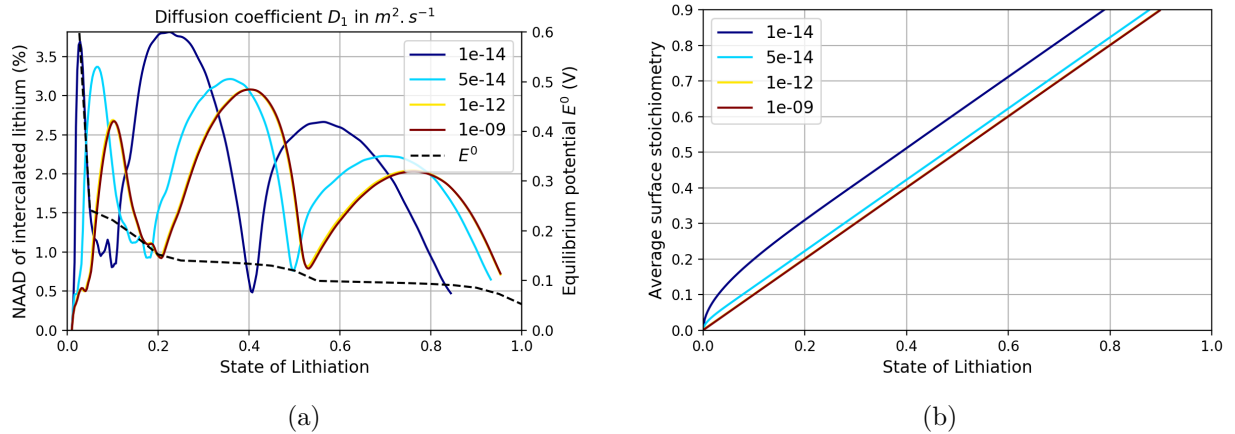


Figure 3.7: NAAD of intercalated lithium concentration at different solid diffusion coefficient (a) and average lithium stoichiometry at particle surface (b) obtained for a simulated  $W_2$  graphite lithiation ( $C/2$ )

shows the impact of  $D_1$  variations on  $x_{Li}$  NAAD during the reference simulation. Only a maximum 0.5 % magnitude difference is obtained through the interval domain of  $D_1$ . Nevertheless, the characteristic heterogeneities peaks are shifted to lower SOL as the diffusion coefficient decreases. When the diffusion coefficient  $D_1$  decreases, the graphite surfaces are prone to be saturated. So, the lithium surface stoichiometry averaged along thickness becomes higher than SOL (Figure 3.7b). Thus NAAD peaks are shifted to lower SOL values, because they are correlated with the equilibrium potential plateau corresponding to lithium surface stoichiometry  $x_{Li}$ .

For a diffusion coefficient superior to  $10^{-12} \text{ m}^2 \cdot \text{s}^{-1}$ ,  $D_1$  has no influence on NAAD anymore, the residual heterogeneity is due to other limitations (transport or kinetics) along the thickness.

Diffusion inside active material has no influence on heterogeneity magnitudes but shifts the heterogeneity appearance from the SOL of the electrode.

### Transports in electrolyte

As the electrolyte transport properties and electrode structure influence the transport of lithium salt through the porous electrode and modify the lithium salt profile, they may impact the NAAD of intercalated lithium concentration. In Figures 3.8a and 3.8b, NAAD values of  $x_{\text{Li}}$  are displayed

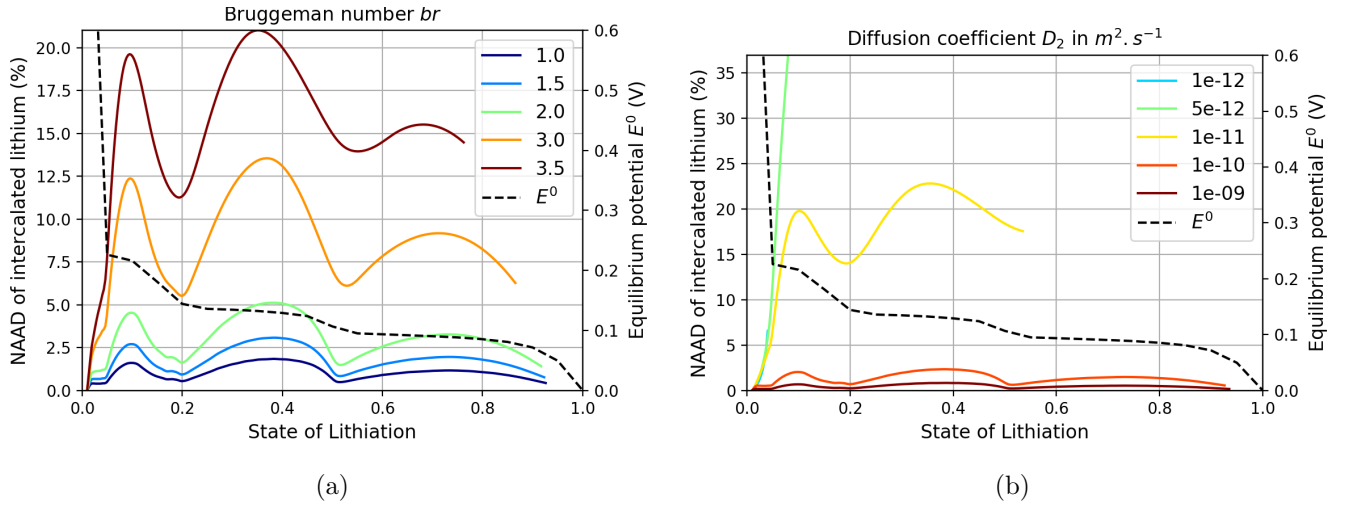


Figure 3.8: NAAD of particle surface stoichiometry at different Bruggeman number (a) and lithium salt diffusion coefficient (b) obtained for a simulated  $W_2$  graphite lithiation ( $C/2$ )

during lithiation respectively for different Bruggeman number ( $br$ ) and diffusion coefficients ( $D_2$ ). When the Bruggeman number increases or the diffusion coefficient decreases, the average heterogeneity rises. Maximum peak value reaches a 20 % heterogeneity for a Bruggeman number of 3.5, and more than 35 % when  $D_2$  equals  $5 \cdot 10^{-12} \text{ m}^2 \cdot \text{s}^{-1}$ . The related lithium salt transport parameters influence the lithium salt concentration variation across thickness ( $c_2$ ), which modifies the intercalation kinetics, the local lithium stoichiometry, and then the average value of heterogeneity. Nevertheless, for any value of a related lithium salt transport parameter, heterogeneity peaks are always correlated to the SOL.

### 3.1.5 Experimental correlations

Experimentally, no *operando* information about local state of lithiation exists so as to comfort correlations between lithiation heterogeneity, C-rate, mass-loading, and other parameter variations. Nevertheless cell voltages of the experimental graphite electrode ( 2.2) are studied to find the theoretical correlation between mass-loadings and lithiation heterogeneity evolution.

It is assumed that the cell polarization exhibits at a given SOC a linear dependency to the lithiation current [105]. Doing so, a cell resistance (namely  $R^{int}$ ) can be extracted by a linear regression at this given SOC[107]. This linear regression is then carried out for each configuration (SOC and mass-loading) between applied currents  $I$  and corresponding cell polarizations ( $U - E_{gr}^0$ ).

$$U - E_{gr}^0(SOC) = R^{int}(SOC, W_i)I \quad (3.3)$$

In Equation 3.3,  $U$  is the cell voltage and  $R^{int}$  is the interpolated cell resistance, which depends on both the state of charge (SOC) and the mass-loading ( $W_i$ ). The obtained interpolated resistances are presented in Figure 3.9 as a function of State of Lithiation (SOL), which is here the opposite of the SOC.  $R^{int}$  appears to be highly correlated to the plateaus and transition zones of the

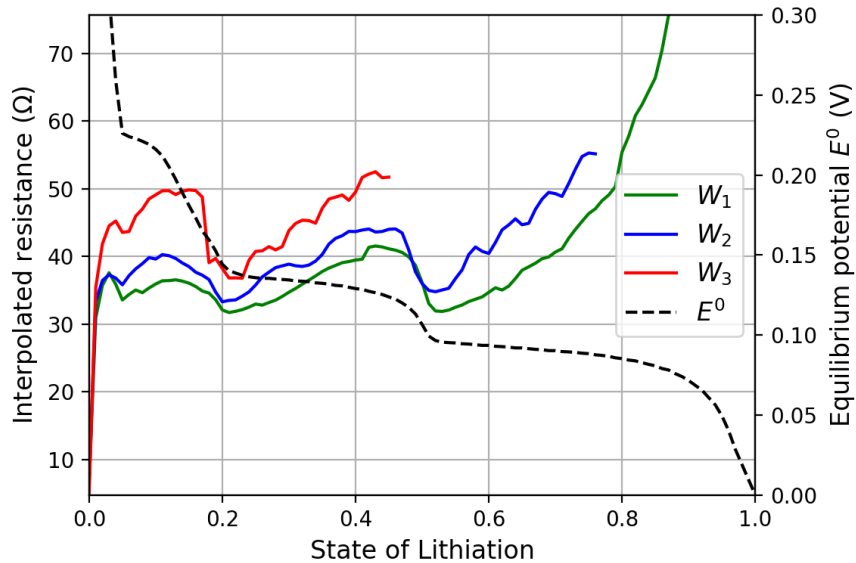


Figure 3.9: Interpolated experimental resistances for different mass-loadings (5.7, 7.9, and  $12.0 \text{ mg} \cdot \text{cm}^{-2}$ ) and graphite equilibrium potential

equilibrium potential of graphite. On plateaus,  $R^{int}$  increases, while on potential transition zones,  $R^{int}$  decreases. When the Crate increases, cell voltage plateaus are less flat (see Figure 2.2), and therefore the interpolated resistances increase in these zones. In reference [108], Wang *et al.* measure the reaction resistance on graphite anode, doing a current pulse study. A similar resistance profile is obtained and electrode resistances are in the same order of magnitude.

A strong correlation and a similar dependence to mass-loading is seen when comparing the simulated intercalated lithium heterogeneities (Figure 3.4) and the experimental interpolated resistances (Figure 3.9). Complementary experiments with access to *operando* local lithium stoichiometry of graphite are needed to definitely conclude on this correlation.

At this point, the interpolated resistance rise at a specific SOL could be related to any local or global variation of intercalation kinetics or transport properties.

## Summary:

Model parameters influence the lithiation heterogeneity according to their impact:

- Parameters related to solid phase transport properties shift homogeneous/heterogeneous periods through SOL (or SOC), via their impact on the local surface stoichiometry  $x_{\text{Li}}$ .
- Parameters related to kinetics properties modify the amplitude of heterogeneous periods. Good kinetics at particle scale highlights transport limitations through thickness, which temporary increases the lithiation heterogeneity.
- Parameters related to liquid phase transport properties modify the average lithiation heterogeneity via their consequences to the lithium salt profile, which influences the local intercalation through thickness.

However, the influence does not explain the heterogeneity mechanism inside the graphite electrode.

## 3.2 Study of the lithiation heterogeneity mechanism

The contribution of the different physical phenomena to the overall electrode resistance is analyzed to understand mechanisms at the origin of appearance and disappearance of heterogeneities. The goal of this section is to study the electrode potential according to different lithium intercalation pathways. Along an intercalation pathway, the electrode potential is decomposed into resistances associated to the different potential drops encountered.

### 3.2.1 Electrode resistances

#### Potential decomposition

Focus is made on an intercalation pathway at 10, 50, and 90 % of electrode's depth from the separator boundary. The electrode potential which is the potential difference between the electrode/separator boundary and the current collector can be written as:

$$\Delta\phi = \phi_1(L_{gr} + L_s) - \phi_2(L_s) \quad (3.4)$$

To dissociate the different physical contributions of the electrode overall resistance, the electrode potential drop following a given pathway on which a lithium atom intercalates at any  $x$  position can be decomposed as:

$$\Delta\phi = \phi_1(L_{gr} + L_s) - \phi_1(x) + \phi_1(x) - \phi_2(x) + \phi_2(x) - \phi_2(L_s) \quad (3.5)$$

This potential decomposition is shown in Figure 3.10 and can be seen also in [109].

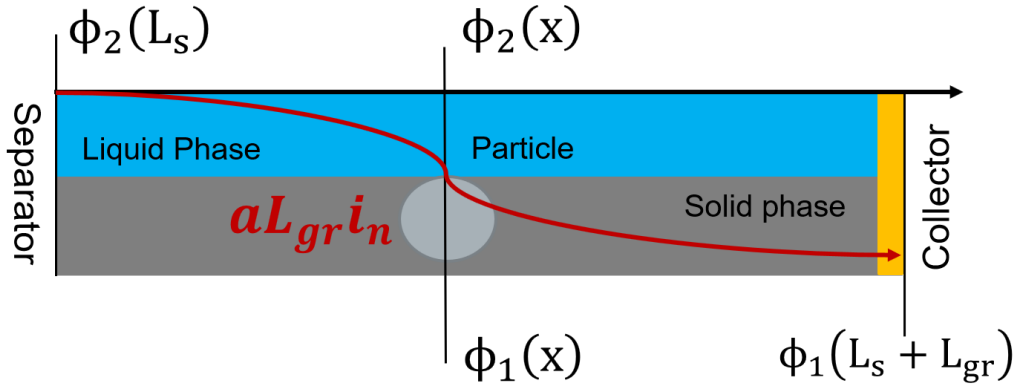


Figure 3.10: Decomposition of potentials along a possible pathway followed by a charge inside graphite electrode during lithiation.

The goal is to translate this potential decomposition into a resistance decomposition, function of the different physical phenomena, to apprehend the evolution of preferential intercalation pathway and compare the impact of the different contributions.

A first hypothesis to calculate the pathway resistance is to assume that a constant density current line can be identified along the potential drop and corresponds to the intercalation current density  $i_n$  on the surface of active material. Along this line, the current is electronic in the solid phase and ionic in the electrolyte. This assumption is represented with the red line in Figure 3.10. This current density is expressed in amps per square meter of active material surface. The roughness value of the electrode active material is given by the product  $aL_{gr}$  which represents the material surface area developed per geometric surface area. The current density per square meters of electrode along the studied current line is therefore  $aL_{gr}i_n$ . The potential drop that only corresponds to the potential losses due to the specific pathway through the solid and liquid phases is related to the transport of charge Equation 3.6 and can be approximated by a linear resistance along the current line, using the current density  $aL_{gr}i_n$  :

$$\phi_1(L_{gr} + L_s) - \phi_1(x) + \phi_2(x) - \phi_2(L_s) = R_{ohm}(x) \cdot aL_{gr}i_n(x) \quad (3.6)$$

where  $R_{ohm}$  is a resistance per square meters of electrode corresponding to the potential loss due to ionic and electronic transports.

The potential drop at the electrolyte - active material interface can be expressed as the sum of local overpotential  $\eta$  and local equilibrium potential,  $E_{gr}^0$ , written as:

$$\phi_1(x) - \phi_2(x) = \eta(x) + E_{gr}^0(x) \quad (3.7)$$

The local kinetic resistance  $R_{in}$  along the current density line which is calculated using the Butler

Volmer approximation can be introduced to represent this local overpotential:

$$\eta(x) = R_{in}(x) \cdot aL_{gr}i_n(x) \quad (3.8)$$

At a given SOL, the local equilibrium potential  $E_{gr}^0(x)$  (Equation 3.7) may deviate from the overall electrode open circuit voltage  $U^{ocv}$ , defined as the equilibrium potential of graphite of electrode SOL, by a quantity  $\Delta E_{gr}^0(x)$ , because of the heterogeneous lithiation of particles.

$$E_{gr}^0(x) = U^{ocv} + \Delta E_{gr}^0(x) \quad (3.9)$$

This local potential variation,  $\Delta E_{gr}^0$ , can be translated into an additional thermodynamic resistance  $R_{th}$ , which represents the local driving force to lithium intercalation as a deviation from the overall open circuit voltage

$$\Delta E_{gr}^0(x) = R_{th}(x) \cdot aL_{gr}i_n(x) \quad (3.10)$$

It should be noted that this resistance can be either negative or positive. Knowing that  $i_n$  is always negative during lithiation (cathodic reaction),  $R_{th}$  is negative too when  $E_{gr}^0$  is superior to  $U^{ocv}$ . It implies, because  $E_{gr}^0$  is a decreasing function of lithium content, that the local surface stoichiometry,  $x_{Li}$ , is inferior to the SOL. On the opposite,  $R_{th}$  is positive if  $E_{gr}^0$  is inferior to  $U^{ocv}$ , when  $x_{Li}$  is superior to the SOL.

Using Equation 3.6, Equation 3.8, Equation 3.9, and Equation 3.10, the potential drop through the electrode thickness can be therefore decomposed as a sum of three resistances along a current density line and an overall open circuit voltage:

$$\Delta\phi = U^{ocv} - (R_{ohm} + R_{in} + R_{th}) \cdot (-aL_{gr}i_n) \quad (3.11)$$

$\Delta\phi$  is pathway independent but its terms are themselves pathway dependent. On a given  $x$  position, the value of the current line is imposed by the Butler-Volmer relation. When a high local current density on a given pathway appears, the corresponding local resistances must be small in order to keep the product constant. This preferential intercalation pathway is therefore visible as the less resistive pathways. We compute these resistance values from the simulation results of the  $W_3$  graphite electrode, lithiated at a C/4 rate.

## Simulation results

Figure 3.11a gives the obtained resistance decomposition during the lithiation at respectively 10 % depth for the top figure and 90 % depth for the bottom figure.

The comparison of kinetic resistance  $R_{in}$  between 10 % and 90 % depth shows that the kinetic is roughly not impacted by the position inside electrode. Nevertheless,  $R_{in}$  is slightly higher ( $2 \Omega \cdot \text{cm}^2$ ) at 90 % compared to 10 % electrode's depth. This can be explained by the low lithium

salt concentration near the current collector, which influences the exchange current density as well as the poor ionic conductivity.

The solid phase potential drop contribution in transport resistance  $R_{ohm}$  is negligible because graphite is a good conductor. Its contribution is below  $10^{-5} \Omega \cdot \text{cm}^2$ . The most part of the transport resistance is due to potential drop in liquid phase, caused by the low ionic conductivity in electrolyte. The difference on transport resistance  $R_{ohm}$  between 90 % and 10 % depth is up to  $10 \Omega \cdot \text{cm}^2$ , because the pathway in electrolyte is physically longer for 90 % depth than for 10 %. To compare with, the separator and lithium electrode resistances, at the same C-rate and mass loading configuration, are respectively  $24 \Omega \cdot \text{cm}^2$  and  $12 \Omega \cdot \text{cm}^2$  and are constant with SOL.

The determining part of overall resistance is the thermodynamic resistance  $R_{th}$ . At 10 % depth, this resistance increases strongly between 40 and 45 % SOL. This corresponds to a strong local equilibrium voltage variation from  $U^{ocv}$ . The resistance behavior is on opposite at 90 % depth: from 45 % SOL,  $R_{th}$  becomes negative and the sum of resistance indicates that position is favorable for intercalation. At 90 % depth, thermodynamic resistance overrides the transport resistance, because the local equilibrium potential  $E_{gr}^0$  is higher than  $U^{ocv}$  and so it improves thermodynamically and locally the intercalation process. At 10 % depth, the local equilibrium potential  $E_{gr}^0$  is lower than  $U^{ocv}$  and so the intercalation process comes weak compare to 90 % depth, even with a better salt concentration and a higher ionic potential  $\phi_2$ .

In Figure 3.11b, we compare the *total pathway resistance*, noted  $R_t$ , for 10, 50 and 90 % of electrodes depths. At a given SOL, the preferential intercalation pathway corresponds to the lowest resistance. At the beginning of lithiation, and for most part of it, total resistances are proportional to the intercalation position inside electrode. The less resistive pathway is the resistance for a 10 % electrode depth and the more resistive for the 90 % electrode depth. This configuration promotes the lithiation process close to separator and induces heterogeneities of lithiation along thickness. Zones of transition are visible at 12-20 % and 40-50 % SOL. These zones correspond to the gradual local transition of the equilibrium potential from one plateau to another one, leading to strong spatial heterogeneities in intercalation current. During the 40-50 % SOL zone, the preferential pathway resistance gradually passes from 50 to 90 % of electrodes depth. After this transition step, the electrode becomes homogeneous on  $x_{Li}$ , (Figure 3.4), and intercalation is now favored again on area near the separator.

The typical shape of the graphite equilibrium potential has a strong influence on the thermodynamic resistance  $R_{th}$  and so on the favorable intercalation pathway as illustrated in Figure 3.11a. When the global thermodynamic potential  $U^{ocv}$  is on a plateau and the local one  $E_{gr}^0$  is almost constant through electrode thickness, the favorable intercalation pathway is found near the separator because it minimizes the kinetics and transport resistance. It leads to a heterogeneous lithiation of the electrode. When the local equilibrium potential  $E_{gr}^0$  near separator goes down on another plateau, the local thermodynamic resistance increases strongly, leading to a smaller intercalation current compared to deeper area.

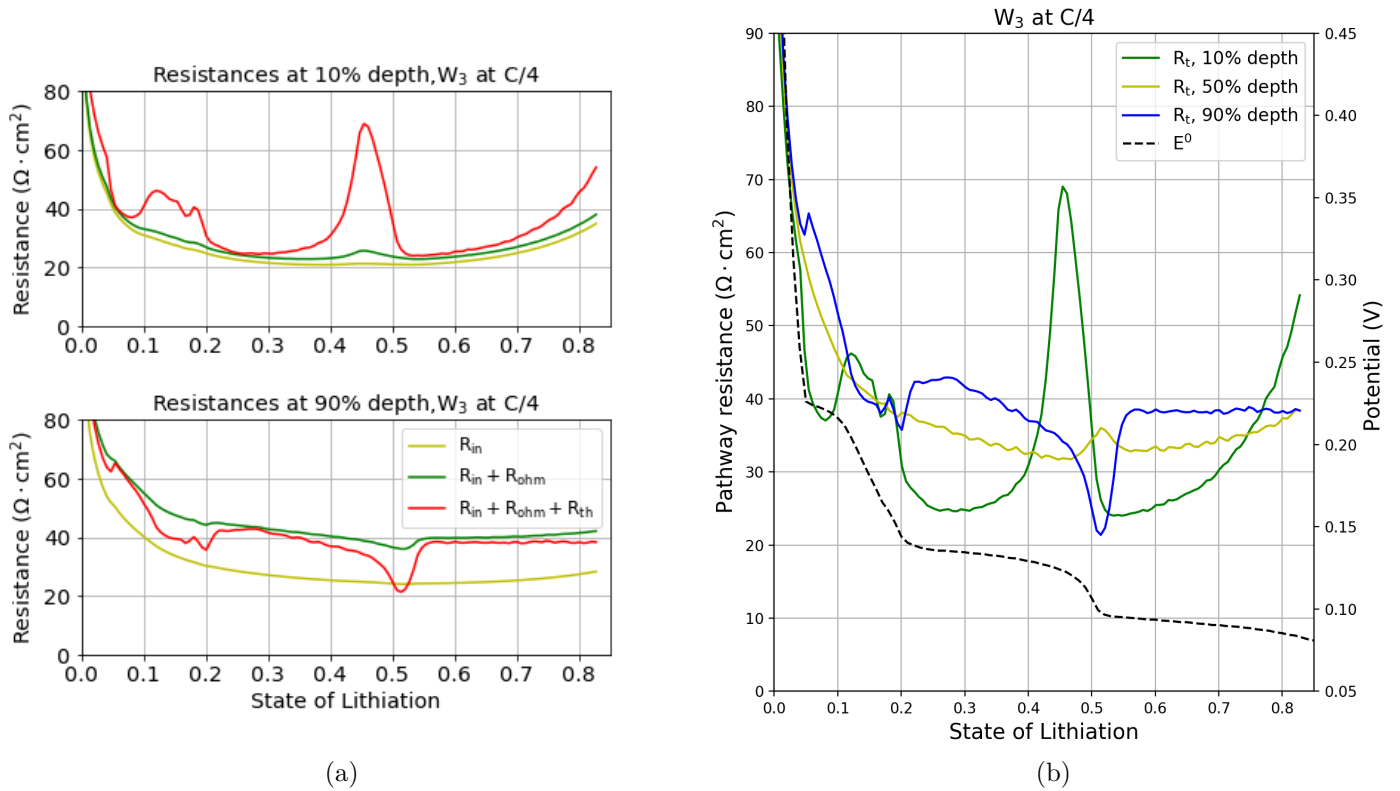


Figure 3.11: Pathway resistance decomposition at 10 % electrodes depth (a, up) and 90 % electrodes depth (a, bottom) during lithiation and complete pathway resistance at 10, 50 and 90 % electrodes depth during lithiation (b).

### 3.2.2 Equilibrium potential influences on lithiation heterogeneity

For a given SOL, the preferential intercalation location is given as the minimum value of the *total pathway resistance*. At the beginning of lithiation, the total pathway resistance indicates that lithiation occurs preferentially near the separator. Then, this preferential path moves gradually on deeper area until the transition between two equilibrium potential plateaus.

The physical interpretation of the heterogeneity mechanism is presented in Figure 3.12. The overpotential can be deduced in this Figure from the difference between  $\phi_1 - \phi_2$  and  $E^0$ . During step 1, uniform lithiation leads to a constant graphite equilibrium potential. When a current is applied, particles near the separator are the first lithiated. Further particles are less lithiated, intercalation being kinetically less favorable compare to area near separator because of poor ionic conductivity and diffusivity (a higher *total resistance pathway*). Indeed, the gradients of ionic potential  $\phi_2$  and salt concentration  $c_2$  are strong through thickness and induce a low ionic potential and a low salt concentration close to the current collector.

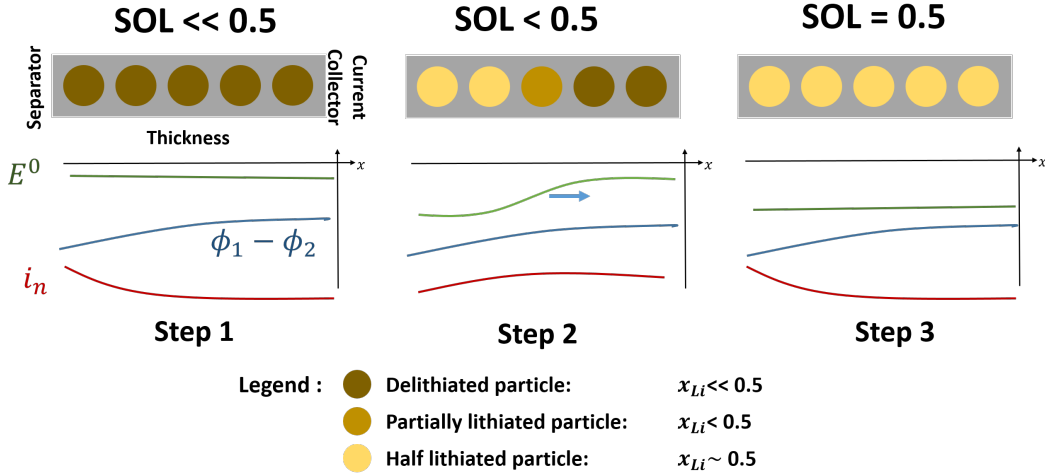


Figure 3.12: Schematic interpretation of the three main steps leading to heterogeneous and homogeneous graphite intercalation along electrode during lithiation.

As consequence, the graphite equilibrium potential being almost constant through the electrode, a weaker overpotential is obtained close to the current collector. It favors  $x_{Li}$  heterogeneities. During step 2, heterogeneity is at its peak, particles near separator have a lithium stoichiometry  $x_{Li}$  corresponding to a change towards a lower plateau value, while particles close to the current collector remains in the former plateau. Due to the difference in equilibrium potential, the intercalation kinetics becomes less favorable for particles near separator, than in electrode's depth. This leads to a homogenization of  $x_{Li}$  through the electrode (leading to step 3). Local intercalation current densities vary along this three-step mechanism. They are strong near separator in step 1 and 3, but become weak during step 2 to favor a return to lithiation state homogeneity.

The typical shape of graphite equilibrium potential influences graphite electrode heterogeneities during lithiation. The local competition between transport and intercalation depends on local equilibrium potential and its shape drives the lithiation heterogeneity of the electrode.

### 3.2.3 Generalization to other active materials

The actual heterogeneity mechanism can be applied to electrode models with other active materials. Thus lithiation heterogeneities can be predicted based on the shape of their equilibrium potential. For example an electrode composed of lithium iron phosphate (or LFP) has a constant equilibrium potential through lithium stoichiometry. Doing so, a LFP electrode model should present a strong lithiation heterogeneity. As opposite, NMC has a quasi-monotonic equilibrium potential between 4.3 V and 3.6 V. So the corresponding model would depict a quite homogeneous lithiation.

The  $W_2$  graphite-lithium model is used as a reference to study the lithiation heterogeneities for different active materials. Three electrode models are built (graphite, LFP and NMC) and for each of them, only the equilibrium potential is modified. The graphite and NMC equilibrium potentials come from experiments (2.8) and the LFP one from the literature [83]. As anticipated,

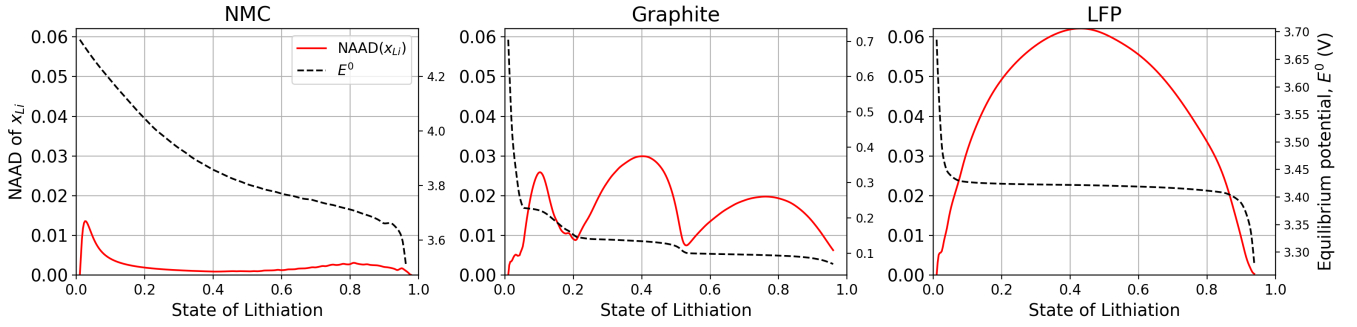


Figure 3.13: Comparison between equilibrium curves and NAAD of  $W_2$  graphite, LFP and NMC electrodes during a simulated C/2 lithiation

NMC is fully homogeneous along lithiation, graphite moderately homogeneous, and LFP very heterogeneous, as shown in Figure 3.13. NAAD of  $x_{Li}$  reaches 6, 3, and less than 0.05 % for respectively LFP, graphite, and NMC.

The intercalation kinetics and lithium transport through active material are different between the three electrodes. Differences between NMC and LFP for intercalation kinetics mechanism can be appreciated experimentally by LIU *et al.* [110]. Inside LFP, lithium transport is driven by a phase transformation mechanism (so called the “domino-cascade model” [111]), whereas lithium transport is driven by solid state diffusion inside NMC. Inside graphite, it is a mix of these two phenomena [48].

LFP is a particular material. As its electronic conductivity is very low compared to the other material, lithiation starts in this electrode from region close to the current collector [110] depending on the ionic/electronic resistance ratio (opposite case in [112]). Our model framework justifies this finding because, when the electronic resistance is much higher than the ionic one, an intercalation in area near collector minimizes the *total pathway resistance*. To simulate the particular lithium transport inside LFP, FERGUSSON *et al.* propose a phase field model to study lithiation at a particle scale [113]. SAFARI *et al.* model and validate the LFP lithiation and delithiation mechanism with a derived Newman’s model combined with a multi-particles approach [59], which is numerically simplified by MAJDABADI *et al.* [83].

Nevertheless, simulations are qualitatively in agreement with the experimental remarks found in literature [110]. The NMC electrode operates in a very homogeneous way and LFP is very heterogeneous during operation.

### 3.3 Particles shape and size distribution influence on lithiation heterogeneities

Some other sources of lithiation heterogeneity are not predicted with the graphite electrode model, due to the Newman’s averaging approach [32]. The porous model considers all active material par-

ticles as the same particle, averaging the variety of shape and size. Inside a real electrode, however, particles are all different in shape and size. Some particles are far away from the representative shape and even some agglomerate.

Common multi-particle models based on the Newman’s one are found in literature. The first one is from DARLING *et al.*, which presents a two-particle model of a  $\text{LiMn}_2\text{O}_4$  electrode [30]. Different particle distributions are investigated with respect to a constant specific surface and volume fraction. As a result, DARLING *et al.* show that simultaneous relaxations in particles of different radii delay lithium redistribution, because relaxation is slowed by a small amount of large particles. It highlights the fact that a diffusion coefficient fitted with an average particle model to cell voltage relaxation drastically overestimates the mass-transfer limitations. MAO *et al.* assign different particle sizes to describe the performance of a blended electrode [86]. LEE *et al.* propose also a discrete multi-particle model of a NMC electrode with three particle sizes [114] and study different distribution cases. In conclusion, the more heterogeneous the distribution is, the less energy is available at high C-rate. This conclusion set up to a tolerance level of particle distribution, based on vehicle usage profile. ENDER *et al.* went further and present a 11-particle model on a graphite electrode [71]. The different particle sizes and approximated tortuosities are obtained from tomography images of graphite electrode. Rate capability losses caused by particle distribution are also noticed, as well as the cell voltage smoothing effect, due to the lithiation inhomogeneity. RÖDER *et al.* built a continuous size distribution model and explore particles dispersity variations through agglomeration or cracking via a Weibull approximation [115].

We propose here to quantify additional impacts on lithiation heterogeneities due to particle dispersity, with a two-particle model and a continuous particle size distribution, derived from experimental measures.

### 3.3.1 Particle shape distribution

The shape does not have a noticeable effect on the cell voltage predicted with a porous electrode model with an ideal particle representation (named the *one-particle model* in the following, refer to [section 2.3.2.2](#)). However a shape distribution consideration would scatter intercalation currents through particles and thus induce lithiation heterogeneity. In order to quantify this phenomenon, the ideal-particle model is extended into a two-particle model of different shapes: cylindrical and spherical.

In the two particles case, the total intercalation current density ([Equation 2.4](#)) is subdivided into two parts in any point of the cell thickness, corresponding to the local intercalation current density on a spherical particle and on a cylindrical particle:

$$\nabla \cdot i_2 = a_s x_s i_{n,s} + a_c x_c i_{n,c} \quad (3.12)$$

Variables relative to the spherical particle are noted with a *s* subscript, and variables related to

cylindrical particle, with a  $c$  subscript. Differences between the two terms of the total intercalation current density are found in the specific interfacial surface  $a_j$  (Equation 3.14), overpotential  $\eta_j$ , (Equation 3.15), exchange current,  $i_{0,j}$ , and volume fraction  $x_j$  of the particle  $j$  in the active material phase.

$$i_{n,j} = i_{0,j} \left( \exp \left( \frac{\alpha F \eta_j}{RT} \right) - \exp \left( - \frac{(1 - \alpha) F \eta_j}{RT} \right) \right) \quad (3.13)$$

$$a_j = \frac{n_j}{r} (1 - \epsilon) \frac{\rho_1}{\rho_{gr}} w_{gr} \quad (3.14)$$

$$\eta_j = \phi_1 - \phi_2 - E^0(x_{Li,j}) \quad (3.15)$$

Each particle type has its own surface stoichiometry ( $x_{Li,j}$ ) and average lithium stoichiometry given by its own transport equation (Equation 2.24). In order to simplify calculations, the lithium concentration profile is approximated by a parabolic curve along the radial axis of the particle, as explained in [116]. Details about this approximation are presented in subsection 4.3.1. As no information on particle shape distribution has been derived from SEM images, we suppose that the two different particles have at the same radius (7.5  $\mu\text{m}$ ) and occupy the same volume fraction inside active material (50 %).

Given the two-particle distribution, the surface lithium stoichiometry averaged along thickness ( $\overline{x_{Li}}$ ) and the NAAD of  $x_{Li}$  are redefined as :

$$\overline{x_{Li}} = \sum_j x_j \cdot \frac{1}{L_{gr}} \int_0^{L_{gr}} x_{Li,j}(x) dx \quad (3.16)$$

$$NAAD(x_{Li}) = \sum_j x_j \cdot \frac{1}{L_{gr}} \int_0^{L_{gr}} \frac{|x_{Li,j}(x) - \overline{x_{Li}}|}{\overline{x_{Li}}} dx \quad (3.17)$$

To complete the analysis, the maximum surface lithium stoichiometry difference between particles of electrode is defined as:

$$\Theta_{\max} = \max_{x,j} (\Delta x_{Li,j}(x)) \quad (3.18)$$

This variable describes the lithium stoichiometry heterogeneity with no volume fraction ponderation. As illustration, a high  $\Theta_{\max}$  value combined with a low NAAD value indicate that at least two particles have a large stoichiometry difference but one of them is present at a small volume fraction. The reference simulation (C/2 lithiation) is applied on the given two-shape model, and the resulting averaged lithiation stoichiometry of the two particles are shown in Figure 3.14. In this Figure, the lithium stoichiometry of cylindrical particles at 10 % and 90 % depth from the electrode/separator boundary are drawn in red, and in blue for the spherical ones. The spherical

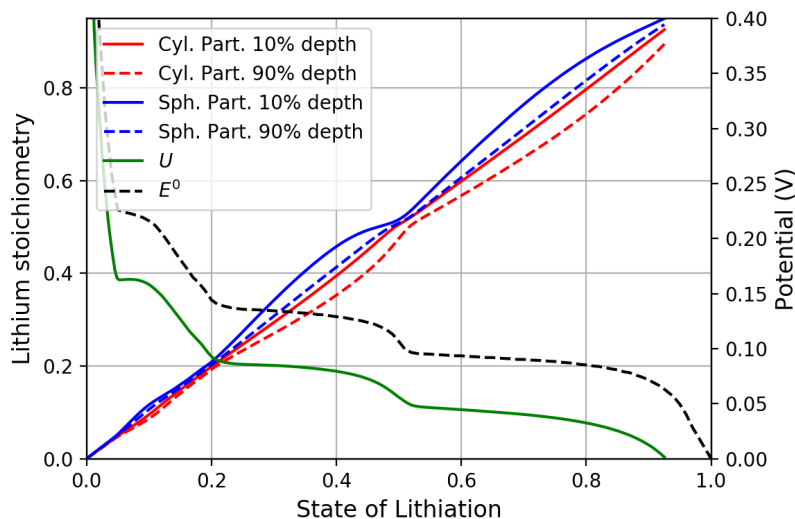


Figure 3.14: Mean lithiation stoichiometry for two particle shapes at two different thickness position during a simulated lithiation (C/2) on a  $W_2$  graphite

particles are more lithiated than the cylindrical ones at any time and at any location, due to their extra developed surface that give them a kinetics advantage. The maximum lithium stoichiometry differences between particles are up to 13 % and appear during SOL zones corresponding to an equilibrium potential plateau (30-50 % and 50-90 %, see Figure 3.15). An homogenization occurs between all particles during equilibrium potential transitions, as previously observed for the NAAD value in the one-particle model. The NAAD shape is identical to what has been previously observed (Figure 3.4), but the maximal heterogeneity value increases from 6 to 10.5 %. Nevertheless, the maximum value of NAAD decreases as the lithiation occurs, whereas the maximum value of  $\Theta_{\max}$  increases. It means that the parts of electrode which deviate from average stoichiometry become smaller, but the stoichiometry deviation of these parts increases.

### 3.3.2 Particle size distribution

Particles are also found in various sizes inside the electrode. Information about the actual particle size distribution paired with an appropriate electrode model will help to quantify actual lithiation heterogeneities.

#### 3.3.2.1 Porosimetry study on graphite and NMC powders

The particle-size distribution of the graphite powder used is obtained with a laser diffraction spectrometry. Measurements are performed also on NMC powders for comparison. Results of these diffractions are shown in Figure 3.16. The NMC particle size distribution is narrower than the graphite one. So, this particle-size distribution combined with the typical monotonic equilibrium potential causes a more homogeneous lithiation inside NMC electrode compared to the graphite

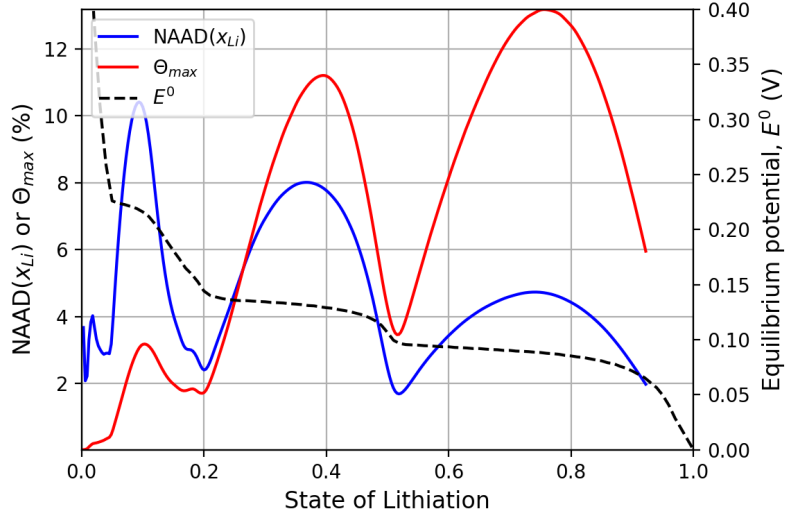


Figure 3.15: NAAD of  $x_{Li}$  and maximum stoichiometry difference during a simulated lithiation ( $C/2$ ) of a  $W_2$  graphite with two different shapes

one.

### 3.3.2.2 A two-particle size case

A two-particle size model is developed under the same equation framework as the two-particle shape model. Particles are considered cylindrical, divided in two sizes. Two particles radii of 4 and 15  $\mu\text{m}$  are firstly considered in order to take into account the non-ideality of the particle size.

The Figure 3.17 displays the simulation results at  $C/2$ : cell voltage and the average particle stoichiometry at 10 % and 90 % of electrode depth along lithiation. Small particles lithiate quicker than large particles. The maximum stoichiometry difference between particles can reach 20 % at the end of lithiation (Figure 3.18). The NAAD value and  $\Theta_{\max}$  values have the same trend along lithiation as the two-particle shape model, but with higher maximum values.

Even with a constant applied current, each particle lithiation is not a linear function of time. Local intercalation current increases or decreases according to particle size and position. The local lithiation rate of small and big particles slows down when their respective lithium stoichiometry reach 25 % and 50 %, corresponding to a transition between the plateaus of equilibrium potential. These decelerations happen at 40 % SOL for small particles and at 55 % SOL for the big ones (Figure 3.17). There is a stoichiometry delay between same particle size at a 10 and a 90 % electrode's depth. This delay rises from a 0 % stoichiometry at start to 5 % near end. A particle located in electrode depth lithiates slightly slower than an identical one near the separator.

This distribution of lithiation state affects the cell voltage in a visible manner. In Figure 3.17, the cell voltage transition between plateaus occurs at 40 % SOL, corresponding to the equilibrium potential transition of small particles. A perturbation in the cell voltage is also noticed at 55 % SOL, it corresponds then to the equilibrium potential transition of large particles. The cell voltage

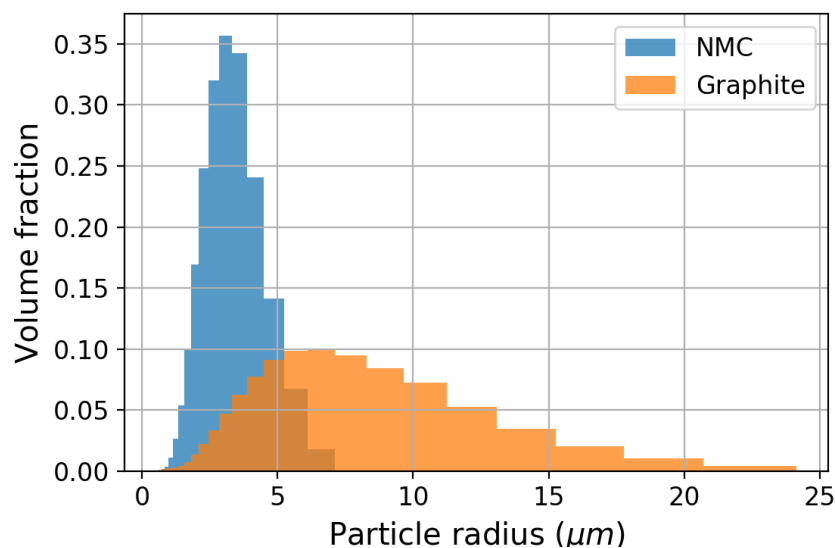


Figure 3.16: Experimental graphite and NMC particle-size distributions

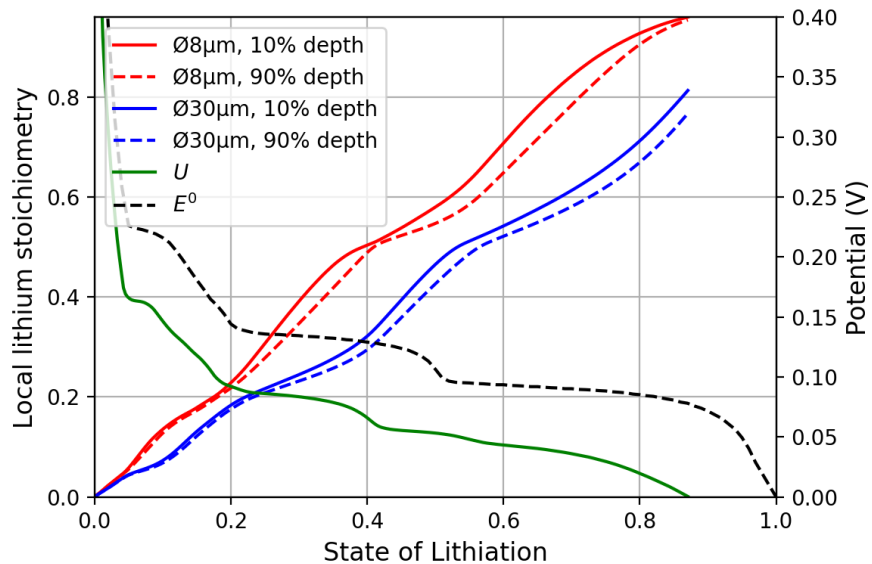


Figure 3.17: Cell voltage and mean lithiation on two different particles at two different thickness position during a simulated lithiation ( $C/2$ ) on a  $W_2$  graphite with two particles sizes

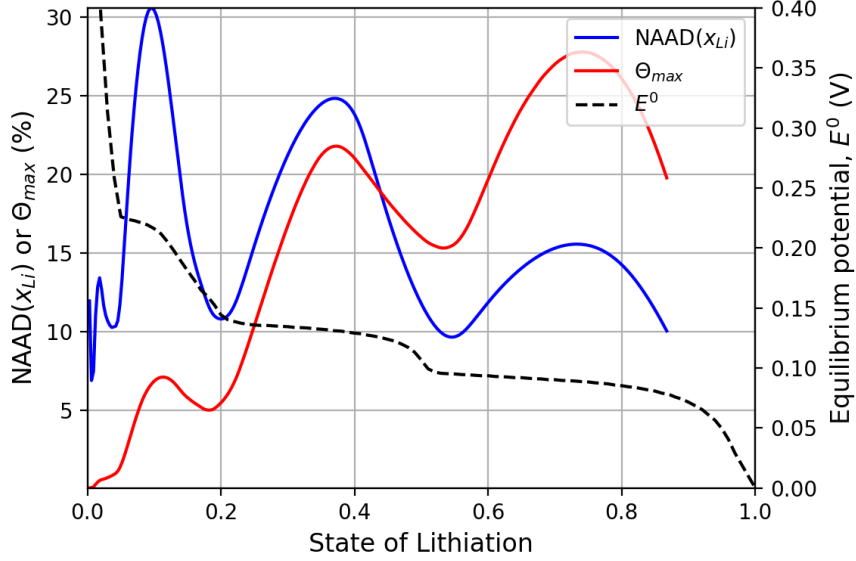


Figure 3.18: NAAD of  $x_{Li}$  and maximum stoichiometry difference during a simulated lithiation (C/2) on a  $W_2$  graphite

decreases monotonously between 40 and 80 % SOL, and that is not as flat as the one-particle model (see Figure 2.14).

### 3.3.2.3 A continuous particle size distribution case

A common way to approach particle size distribution is to discretize the actual one into a finite number of particle sizes, linked with corresponding volume fractions [71, 86, 114, 115]. To go further, a finer representation of particle distribution is considered, based on the size distribution (Figure 3.16). Graphite particle sizes ( $r$ ) were measured between 0.5  $\mu\text{m}$  and 24  $\mu\text{m}$ , respectively named  $R_{min}$  and  $R_{max}$ . Between these radii, the size distribution is approximated by using a polynomial function of the volume fraction:

$$x_r(r) = 6 \left( \left( \frac{r - R_{min}}{R_{max}} \right) - \left( \frac{r - R_{min}}{R_{max}} \right)^2 \right) \quad (3.19)$$

The constraint is to have the integrated volume fraction over the existence domain of the particle sizes ( $R_{min}, R_{max}$ ) equals to unity, in order to respect mass balance. Figure 3.19 shows the actual and approximate particle size distributions. For particle sizes below 4  $\mu\text{m}$  and above 13  $\mu\text{m}$ , the particle-size distribution approximation (Equation 3.19) over-estimates the real volume fraction. The opposite is true inside this radius interval. Nevertheless, the particle-size distribution approximation remains in the same order of magnitude of the experimental one.

This continuous approximation of the actual particle size distribution is here implemented into the porous electrode model. The divergence of the ionic current is written at each point as the integral of all the intercalated current densities associated to particular particle sizes between  $R_{min}$

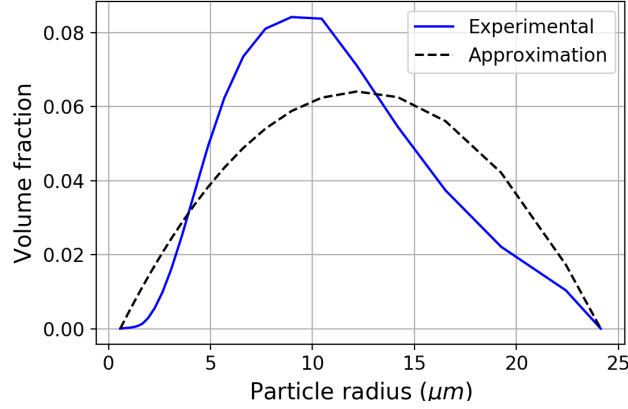


Figure 3.19: Particle size distribution of graphite and polynomial approximation

and  $R_{max}$ , weighted with their respective volume fraction inside the active material phase:

$$\nabla \cdot i_2 = \int_{r_{min}}^{r_{max}} x_r(r) \cdot a(r) \cdot i_{0,r} \left( \left( \exp \left( \frac{\alpha F}{RT} \eta(r) \right) \right) - \exp \left( -\frac{(1-\alpha)F}{RT} \eta(r) \right) \right) dr \quad (3.20)$$

The overpotential ( $\eta$ ), specific surface area ( $a$ ), and volume fraction ( $x_r$ ) are function of the particle radius ( $r$ ). Each particle is considered cylindrical. The lithium diffusion through the particle radius is carried out according to the parabolic approach [116]. The average surface lithium stoichiometry  $\overline{x_{Li}}$ , and the NAAD of  $x_{Li}$  are redefined in this multi-particle study, to account for the volume fraction of each particle radius:

$$\overline{x_{Li}} = \int_{R_{min}}^{R_{max}} x_r(r) \cdot \frac{1}{L_{gr}} \int_0^{L_{gr}} x_{Li}(r, x) dx dr \quad (3.21)$$

$$NAAD(x_{Li}) = \int_{R_{min}}^{R_{max}} x_r(r) \cdot \frac{1}{L_{gr}} \int_0^{L_{gr}} \frac{|x_{Li}(r, x) - \overline{x_{Li}}|}{\overline{x_{Li}}} dx dr \quad (3.22)$$

The maximum lithium stoichiometry difference encountered through all particles of electrode is defined as:

$$\Theta_{max} = \max_{x,r}(\Delta x_{Li}(r, x)) \quad (3.23)$$

The Figure 3.20 shows the cell voltage, the NAAD, and the maximum lithium stoichiometry difference during the reference simulation. The obtained cell voltage is smoothed and decreases quite linearly from 20 % SOL until the end. Consequently, the expected potential step at 50 % SOL disappears. Simulated cell voltage is similar to the experimental ones (Figure 2.14 in Chapter 2). Thus, the experimental smoothed cell voltage may be due to the lithiation heterogeneities due to the particle size distribution.

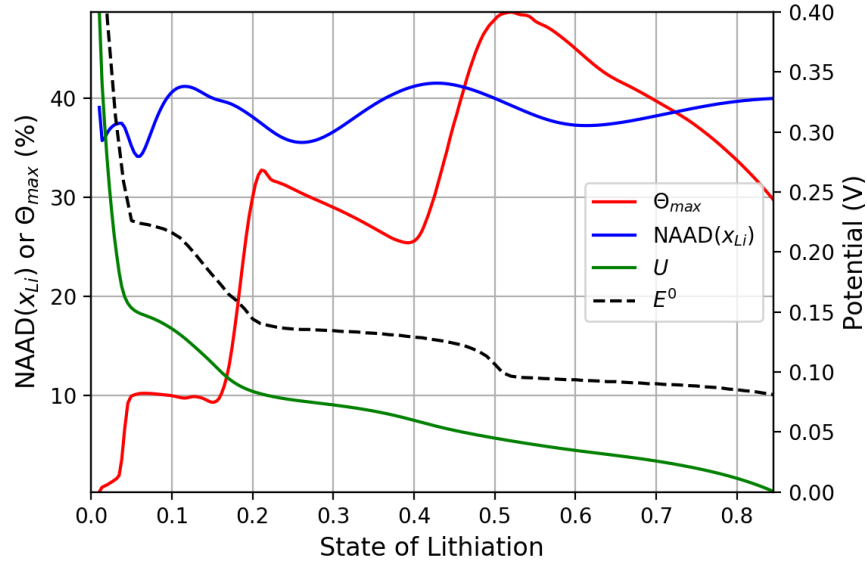


Figure 3.20: Cell voltage and stoichiometry differences during a simulated C/2 lithiation on a  $W_2$  graphite

The  $x_{Li}$  NAAD value stays near 40 % during the whole lithiation, indicating that the electrode lithiates heterogeneously. The heterogeneity mechanism caused by equilibrium potential deviation exists but remains negligible compared to the one caused by the particle size dispersity.

Finally, the maximum stoichiometry difference,  $\Theta_{max}$ , increases drastically during each global equilibrium potential transition and decreases during global constant equilibrium potential. Very small particles lithiate first when their lithium stoichiometry corresponds to an equilibrium potential plateau and doing so, they increase the  $\Theta_{max}$  value. Thus  $\Theta_{max}$  seems to have no correlation with the NAAD value, because as the NAAD takes into account the volume fraction, the particle present at small volume fraction do not impact the final NAAD value.

The Figure [Equation 3.22](#) displays the map of the lithium stoichiometry at particle surface ( $x_{Li}$ ) that is reached at the end of lithiation. In this Figure, particle radii are written through the y-axis and location from the separator are written through the x-axis. Maximum stoichiometry difference between particles near the separator reaches 15 % and rises to 25 % near current collector. Particles are not lithiated at the same rate and as consequence the final lithium stoichiometry between two particles at same position can be extremely large. Even at C/2, the particle size distribution model predicts much greater heterogeneities compared to the one-particle model. At higher rates, simulations suggest that the lithiation heterogeneity should be even larger (Figure [3.4](#)).

The local stoichiometry difference between particle surface and center at the end of lithiation is displayed in Figure [3.21b](#). This difference is expressed in percent of the particle surface stoichiometry. Thus, whatever the location through electrode, this difference changes only according to the particle size. Lithium is homogeneously distributed inside small particles (less than 0.1 % difference), but is more heterogeneously distributed inside large ones (up to 3 % difference), due

to graphite transport limitations.

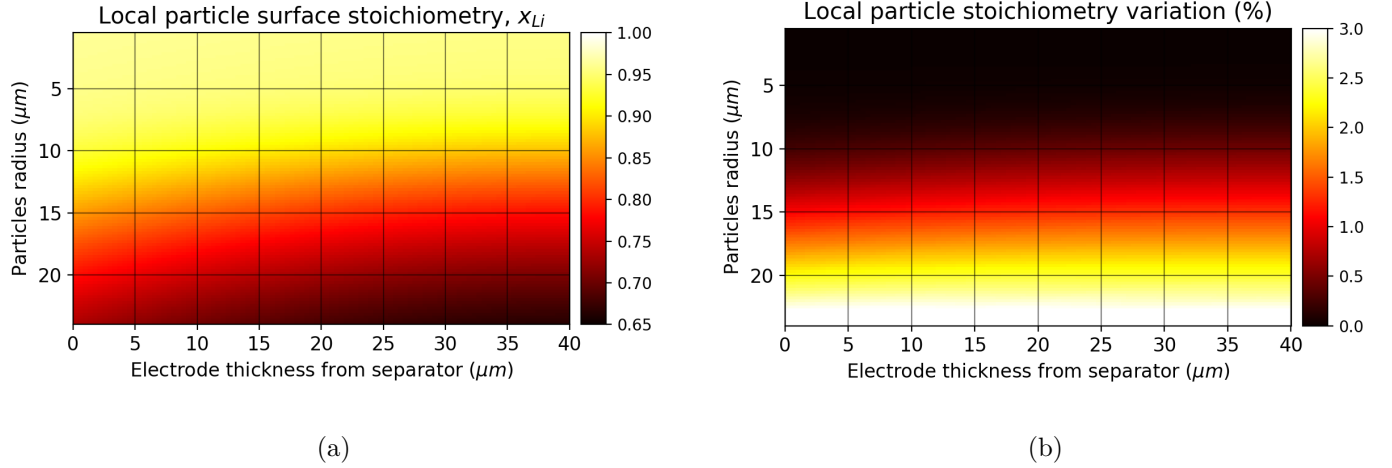


Figure 3.21: Graphite lithium stoichiometry at particle surface (a) and normalized maximal stoichiometry difference between surface and center (b) at the end of a simulated C/2 lithiation on a  $W_2$  graphite electrode

In summary, the cumulative information given by the cell voltage, the NAAD value of  $x_{\text{Li}}$ , the  $\Theta_{\text{max}}$  value, and final lithium distribution indicate that the modeled graphite electrode keeps a relative lithiation heterogeneity during the whole operation.

### 3.3.3 Comparison of particle distribution models

Considering the particle distribution model chosen and operating conditions applied, the predicted cell voltage, lithium, and intercalation current distributions can be quite different.

The Figures 3.22b and 3.22a display the cell voltage according to the different particle distribution models respectively at a C/2 and C/10 lithiation rate. At C/10, cell voltages are similar, the particle size distribution representation does not affect the cell behavior. At C/2, the cell voltage and rate capability of the one-particle model and two-particle shapes model are very close. The two-particle size model shifts the cell voltage step from 50 to 40 % SOL. The cell voltage is smoothed and the polarization is higher with the continuous particle distribution. Higher is the C-rate, larger is the impact of the choice of the particle distribution representation on the cell voltage.

Inner conditions can be compared through the different particle distribution models, such as the intercalation current distribution, the NAAD of  $x_{\text{Li}}$  and the lithium stoichiometry through the whole electrode. The Table 3.1 presents the maximum value of the following quantities through model variation: the NAAD of  $x_{\text{Li}}$ , the average particle stoichiometry difference and intercalation current density difference inside the electrode.

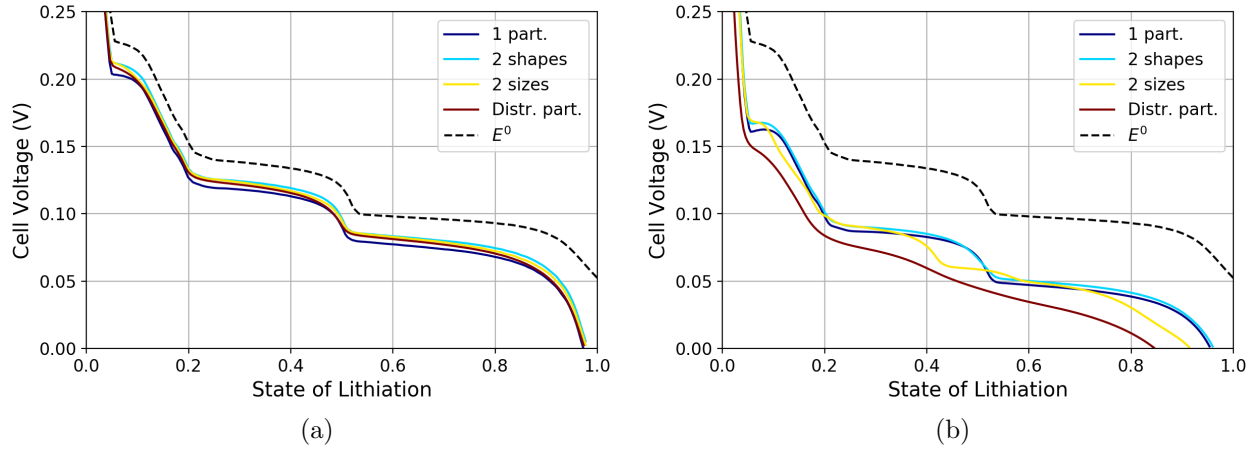


Figure 3.22: Simulated cell voltage through different particle models during a C/10 (a) and C/2 (b) lithiation on a  $W_2$  graphite

Table 3.1: Current and lithiation changes during reference simulation (C/2 lithiation) between different particle size models

Particles distribution representation	Maximal intercalation current density difference ( $SOL$ ) ( $A \cdot m^{-2}$ )	Maximal NAAD of lithium surface stoichiometry ( $SOL$ )	Maximal particle stoichiometry difference ( $SOL$ )	Maximal particle stoichiometry difference at end ( $SOL$ )
one-particle size	1.3 (50 %)	3.1 (40 %)	0.03 (95 %)	0.03 (95 %)
two-particle shape	2.2 (51 %)	10.5 (79 %)	0.13 (79 %)	0.055 (96 %)
two-particle size	5.2 (91 %)	31 (34 %)	0.27 (77 %)	0.18 (91 %)
Continuous size distribution	6.1 (84 %)	42 (43 %)	0.49 (52 %)	0.3 (84 %)

The maximal intercalation current density difference increases from  $1.3$  to  $6 \text{ A} \cdot \text{m}^{-2}$  as the span of particle sizes increases. The NAAD value of  $x_{\text{Li}}$  increases from  $3 \%$  with a one-particle model to  $42 \%$  with the continuous size distribution model. When increasing the particle distribution complexity, the lithiation heterogeneity systematically increases.

The maximum stoichiometry difference between particle at the end of lithiation can be large depending on particle distribution representation. This difference reaches only  $0.03$  with a one-particle model, but almost  $0.3$  with the continuous size distribution model. Moreover, the smaller particles always lithiate or delithiate completely, more than large ones. So, considering a cycle composed of a discharge followed by a complete charge, the bigger particles will be  $30 \%$  less delithiated than small ones at each cycle (Figure 3.21a). If aging is related to the total lithium quantity extracted [117], and if this cell scale assumption can be assumed at a particle scale, then an aging difference should be observed between particle sizes. This phenomenon could be cumulative with the lithiation heterogeneity due to the electrode thickness. Particles near separator operate in a wider stoichiometry range than ones located in deeper area (Figure 3.21a). Thus, the graphite particles that will have the longest life considering performance only, should be the largest one, located near current collector.

The current densities distribution affect also electrode aging [99, 102]. The volume expansion of particles is induced heterogeneously due to inhomogeneous currents, adding local mechanical stress between particles. As consequence particles are degraded and cracked [118]. Models indicate that small particles are under the largest intercalation current density variation, and this variation increases as the span of the electrode particle rises. Then small particles should have more consequences from mechanical stresses than big ones.

As a conclusion, the particle shape and size distributions inside the graphite electrode cause large lithiation heterogeneities, hiding the classical homogeneity/heterogeneity mechanism due to the equilibrium potential shape. These lithiation heterogeneities can be quantified with an appropriate multi-particle model. The global impact of these model is on the smoothing of the cell voltage for C-rates higher than  $C/10$ .

### 3.4 Experimental *operando* observations of lithiation heterogeneities

Lithium distribution has been modeled in previous section but direct experimental observation on a real operating electrode (*operando*) would be of great interest to validate the above-mentioned models and give support to the previous discussion. As previously observed, the local lithium stoichiometry in graphite is an important indicator of cell performance and aging, and efforts are devoted to develop direct measurement techniques. A lot of studies focus on *operando* or *in-situ* measurements to monitor the local intercalated lithium concentration using techniques such as

as colorimetry, X-ray diffraction, or neutron diffraction. Nevertheless, it is still difficult to have local *operando* measurements, because the suitable electrode specifically designed to allow such measurements can deviate largely from a real cell. Moreover, special care must be taken to ensure that the measurement strategy does not impact the current distribution inside the cell.

### 3.4.1 Experimental studies

With a cell containing multiple working electrodes and/or multiple layers of separators, it is possible to estimate local SOL, via current estimation. ZHANG *et al.* and NG. *et al.* measure *in-situ* local currents in different locations of their specially designed cells, respectively along a 1.8 m long electrode [119] and across electrode thickness [120]. NG *et al.* observed a heterogeneous current distribution through thickness even at C/37 rate. Along their electrode, ZHANG *et al.* measured local current deviations, which approach 100 % of the averaged value. Moreover at low C-rate, they observed a wavy current distribution through the electrode width. They also correlated these findings to the shape of equilibrium potential of graphite. In both cases, specific electrodes are manufactured with reference electrodes, which can influence the electrochemical system.

Graphite changes its color upon lithiation. Using this optical property, MAIRE *et al.* and recently HARRIS *et al.* developed *operando* methods to optically observe the lithium distribution inside very thick electrodes of specially designed cells [121, 122].

LIU *et al.* used X-ray micro-diffraction in order to map *ex-situ* the lithium distribution, in the through-plane and in-plane dimensions of LFP electrodes [112]. Measurements are done after a relaxation time, not *operando*, but the lithium map indicates a heterogeneous distribution, even after relaxation time.

Neutron diffraction is also a tool for direct and non-destructive observation of lithium intercalation into graphite electrode [103, 104, 123]. Diffraction data on the Bragg peaks of the  $\text{Li}_x\text{C}$  phases can be short enough (time intervals of two to five minutes), to have a measurement of lithium distribution. Nevertheless, measurements cannot be localized and therefore it is not possible to follow lithiation heterogeneities through the thickness of the electrode.

In the scope of this thesis, we have developed an experiment to observe the actual (*local*) lithium distribution in the graphite electrode during operation (*operando*) using X-ray micro-diffraction at ESRF (Grenoble).

### 3.4.2 Experiment principle and requirements

The principle of the experiment is to cycle a graphite electrode vs. Li foil and to follow the local lithiation state of graphite by monitoring the intensity of the (002) Bragg peaks of the  $\text{Li}_x\text{C}$  phases, measured on a 2D detector in transmission.

A Synchrotron beamline with microfocus is used to measure the local (micron-size) diffraction of the lithiated graphite electrode and thus to follow the distribution of intercalated lithium during



Figure 3.23: Picture of the *operando* lithium-graphite cell (4 cm high)

charges and discharges. High incoming photon flux and *operando* fast detection are necessary to get access to the local conditions, and capture the heterogeneities along the electrode thickness. High energy (13 keV) is also required to compensate the attenuation from the environment (cell body, electrolyte).

### 3.4.3 Experimental set-up

An electrochemical cell has been developed (Figure 3.23), and specifically designed to perform local micro-diffraction measurements along the electrode thickness. A PEEK polymer is used for the cell body, because its impact on X-ray diffraction is negligible. Current collectors (at up and bottom sides of the cell) are made of stainless steel. Inside the PEEK body, half-cell components are stacked: graphite electrode, two Celgard separators, and a lithium foil (Figure 3.24). The cell is filled with the same electrolyte than the half-cell previously studied (subsection 2.1.1.1). A  $W_3$  mass-loaded graphite is used ( $12 \text{ mg} \cdot \text{cm}^{-2}$ ).

The X-ray beam comes from the left to the right of the picture 3.24, passing through the cell body (transmission mode) to a 2D detector. The graphite electrode is at maximum 2 mm long through the beam direction, which allows X-ray diffraction, without too much attenuation. The electrode is 2 cm long in the dimension perpendicular to the beam. The graphite thickness is  $80 \text{ }\mu\text{m}$ ,  $50 \text{ }\mu\text{m}$  for the separator, and more than  $250 \text{ }\mu\text{m}$  for the lithium foil. Lithium is transparent to X-ray and the foil is thick to avoid the diffracted beam to be shaded by the upper stainless steel cap, when parts of graphite electrode close to the separator are measured.

A VSP potentiostat from Bio-Logic supplies the current to the electrochemical cell and records the cell voltage. The graphite is lithiated and delithiated at various constant currents between 0 and 1.5 V.

During galvanostatic operations, the microfocus X-ray Beam could map representative points

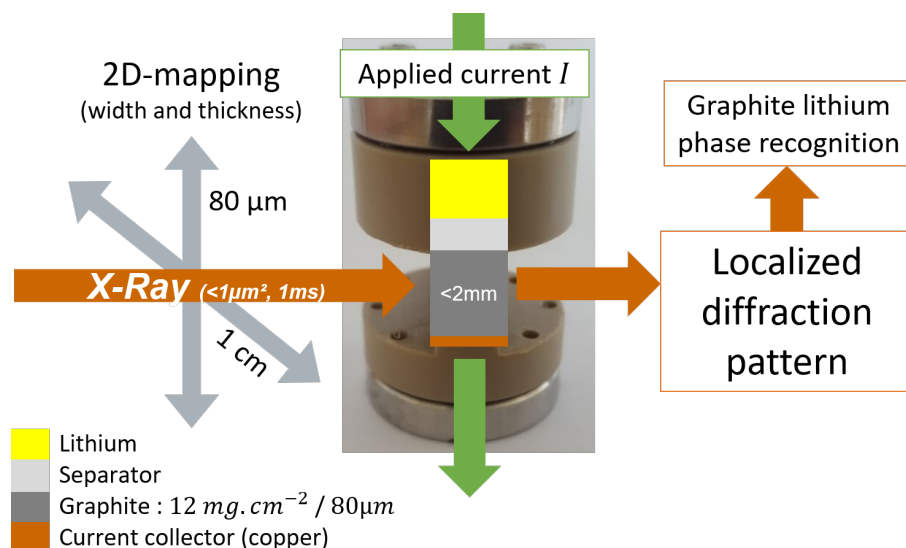


Figure 3.24: Diagram of the *operando* measurement of local graphite SOL

of the the whole electrode. The beam is diffracted in a way corresponding to the state of lithiation of graphite inside the electrode. This information is transmitted to the 2D detector located behind the cell, in order to see the specific diffraction pattern associated with the different lithiated phases of graphite. The microfocus beam area represents  $1 \mu\text{m}^2$  and an exposition time of less than 1 ms is sufficient to get enough information. Beam size and exposition time are small enough to map a representative area of the graphite electrode thickness in a relative short time (less than a minute) compared to galvanostatic operations (theoretically 2h at C/2).

### 3.4.4 Preliminary results and perspectives

During the experiment, 2D diffraction patterns are obtained on specific points. Each 2D diffraction pattern is integrated to have a mean value for each angle leading to diffraction spectra as the one presented in Figure 3.25a. On a diffraction spectra, the different graphite phases are identified through the location of the peaks as function of the angle  $q$ . We assume the peak-phase correspondence as presented in Figure 3.25a. For each peak associated to a phase, the signal intensity is integrated to have access to the quantitative amount the phase.

During cell operations, we measure 34 points through the whole electrode thickness, repeated in different locations along the width of the electrode. In less than one minute, an intensity map of the different phases in the electrode can be obtained (Figure 3.25b). The intensities can be integrated over the electrode width, to give the phase distribution as a function of the electrode thickness (Figure 3.27a)

Focus is made on a  $W_3$  graphite delithiation at  $80 \mu\text{A}$ , which corresponds roughly to a current density of  $0.5 \text{ mAh} \cdot \text{cm}^{-2}$  or C/8, given the electrode dimensions (1 cm and 1.5 mm) and theoretical capacity (0.650 mAh). The electrode was preliminary lithiated at  $35 \mu\text{A}$  (C/20) until 0 V, followed

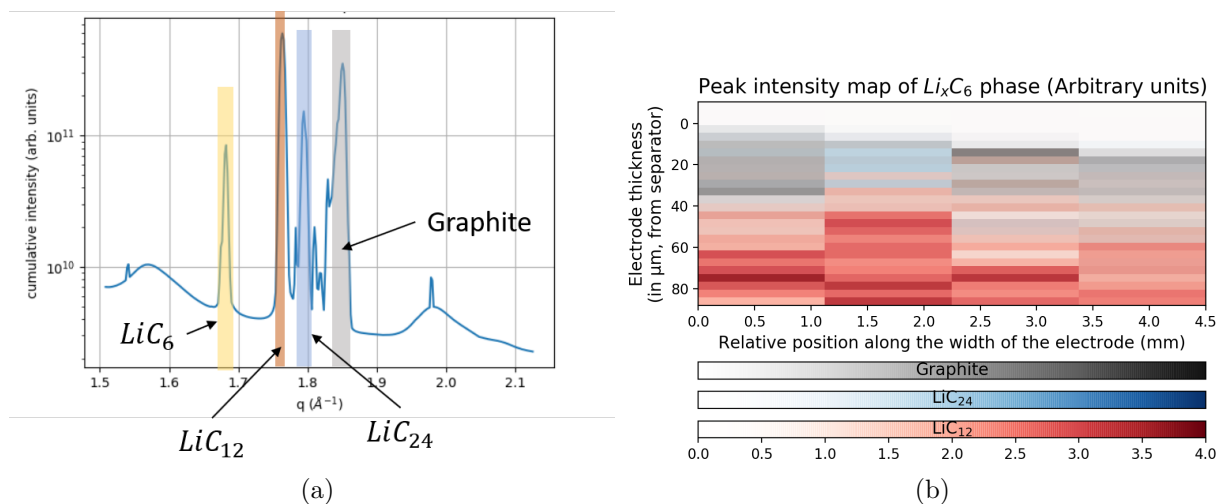


Figure 3.25: Lithium-graphite phases recognition for a given diffraction spectra (a) and localized intensities of  $\text{LiC}_{12}$ ,  $\text{LiC}_{24}$  and graphite phases inside electrode near end of delithiation (0.45 V) (b)

by a 15-minute break. Lithiation and delithiation were faster than expected (19 hours in total) and graphite plateaus are partially seen on cell voltage during delithiation. This indicates that maybe the cell capacity has been overestimated due to the difficulty to estimate the electrode surface in this specific cell design. (Figure 3.26).

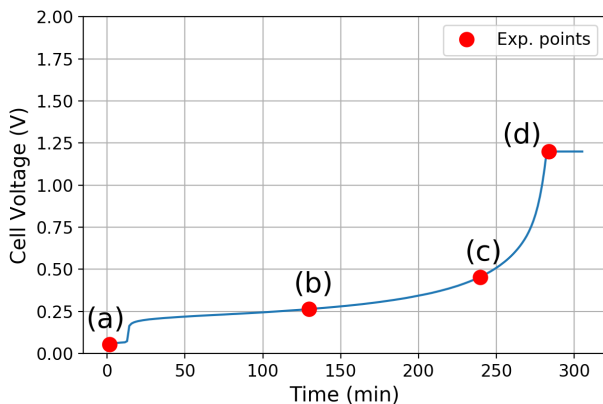


Figure 3.26: Experimental potential of the  $W_3$  graphite electrode ( $12.0 \text{ mg} \cdot \text{cm}^{-2}$ ) during delithiation at  $0.5 \text{ mAh} \cdot \text{cm}^{-2}$

Just at the end of lithiation before the 15-minute break,  $\text{LiC}_{12}$  and  $\text{LiC}_6$  phases are recognized through the cell thickness (Figure 3.27a). The lithiation was not fully completed and the  $\text{LiC}_6$  phase is a little higher close to the separator. When starting the delithiation, transition between the  $\text{LiC}_6$  phase and the  $\text{LiC}_{12}$  one occurs quite homogeneously along the cell thickness (Figure 3.27b). On the opposite, transitions to the  $\text{LiC}_{24}$  and the graphite phases are clearly heterogeneous (Figure 3.27c). Areas near separator are delithiated first, according to the model predictions. Above 0.5 V, a majority of dilute phases ( $x > 12$  in  $\text{LiC}_x$ ) are detected. At 1.2 V, the

graphite phase is mainly present along the cell thickness (Figure 3.27d). We notice some residual  $\text{LiC}_{12}$  phases in deep area inside the electrode (less than 20  $\mu\text{m}$  away from the current collector).

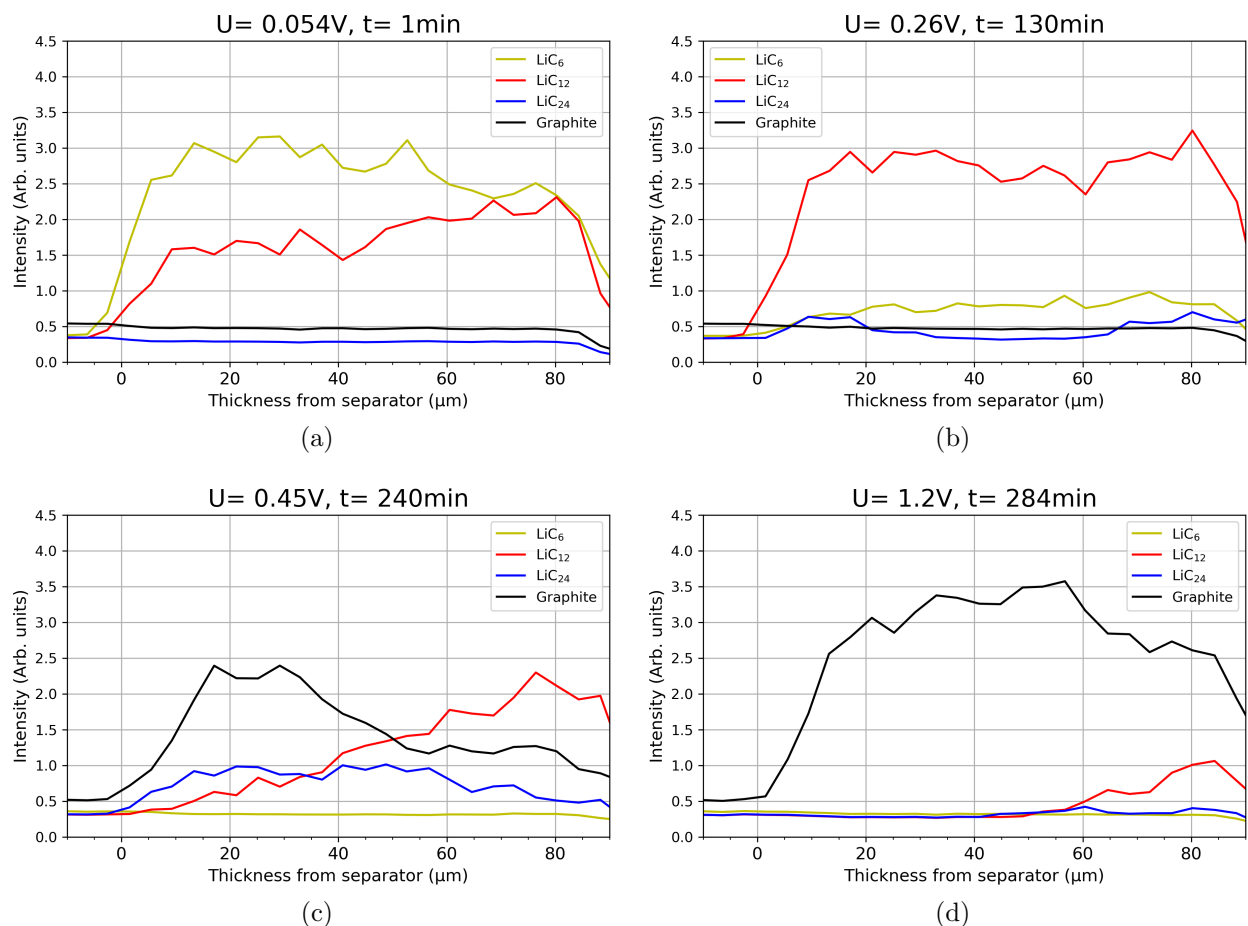


Figure 3.27: Experimental lithium phase distribution through the graphite electrode thickness at 0.11 V (a), 0.21 V (b), 0.32 V (c), and 0.53 V (d) during a delithiation at  $0.5 \text{ mAh} \cdot \text{cm}^{-2}$

Lithium distribution heterogeneities and homogeneities both observed *operando*, notably during the last phase transition. Moreover, even the C-rate was quite low (on the order of C/8) which numerically favors homogeneous lithium distribution, the observed heterogeneities are significant, especially around 0.45 V.

From the parameter NAAD study (subsection 3.1.4), a increasing charge-transfer rate constant is associated with stronger appearance of lithiation heterogeneities. To give a first interpretation of these results, maybe an intercalation kinetics strongly dependent on the considered lithium phase should be used. More precisely, we should consider that the dilute phase ( $x > 12$  in  $\text{Li}_x\text{C}_6$ ) have higher charge-transfer rates than lithiated phase. This hypothesis is coherent with the modeling approach by GALLAGHER *et al.* [124]. In their study, the graphite lithiation and delithiation are modeled with a Newman's model, including a multiple phase transition approach: each phase has its own kinetics.

The complete results of this experiment are still under post-treatment and these first findings should be confirmed and compared to lithiation, as well as reversibility. Incoming studies will quantify lithium distribution heterogeneities at higher C-rates.

Further experiments may be done with a narrower particle distribution (as MCMB graphite) in order to reduce heterogeneity sources and maybe observe the homogeneous/heterogeneous mechanism due to the equilibrium potential shape.

## 3.5 Conclusion

This part concludes the study of the heterogeneity sources through Newman's based models.

The optimal operation of a graphite electrode is limited by kinetics and diffusive constraints. According to the model studied at a fixed C-rate ( $C/2$ ), the intercalation kinetics varies across the electrode, influenced by the diffusive phenomena. Thus, despite an interesting specific capacity, the inhomogeneous lithium distribution (along lithiation / delithiation) of graphite limit its rate capability and power.

In the model framework, the equilibrium potential of the active material is the main driving force for lithiation heterogeneities. The graphite electrode has a rather characteristic heterogeneous lithiation signature, which is composed of heterogeneous zones during SOL corresponding to equilibrium potential plateau and homogeneous periods during potential transitions. Competitions between transport phenomena and intercalation kinetics lead to heterogeneities.

Other factors favor lithiation heterogeneity such as large distribution of particle shapes and sizes. Taking into account these distribution shows that the lithiation heterogeneity is not simply due to the equilibrium potential shape. Models shows that big particles are never fully lithiated during a cycle and small ones suffer large intercalation current variations. We believe that they age at different rates: small particles near separator should degrade earlier than big ones located near current collector.

An *operando* measurement of the actual and local lithium distribution in a graphite electrode has been performed using a X-ray micro-diffraction technique. Preliminary results indicate that the electrode effectively operates heterogeneously, also at low C-rates, but only during selected phase transitions. The experiment specially build in the scope of this thesis should be continued, interesting results are expected .

The goal of the next chapter is to study the different aging mechanisms that occur on a regular cell.

# Chapter 4

## Aging phenomena in lithium-ion cell

### Contents

---

<b>4.1</b>	<b>Aging sources inside lithium-ion batteries . . . . .</b>	<b>84</b>
4.1.1	The Solid Electrolyte Interface . . . . .	85
4.1.2	Lithium plating . . . . .	87
4.1.3	Active material degradations . . . . .	87
4.1.4	Positive electrode influences . . . . .	88
4.1.5	Aging mechanisms summary . . . . .	88
<b>4.2</b>	<b>Experimental cell aging . . . . .</b>	<b>89</b>
4.2.1	Experimental pouch cell . . . . .	89
4.2.2	Aging during cycling conditions . . . . .	90
4.2.3	Aging during calendar conditions . . . . .	94
4.2.4	Aging Summary . . . . .	97
<b>4.3</b>	<b>Full cell model development and validation . . . . .</b>	<b>98</b>
4.3.1	Model development . . . . .	98
4.3.2	Initial conditions and adjusting parameters . . . . .	100
4.3.3	Simulation results on fresh and aged cells . . . . .	102
<b>4.4</b>	<b>Aging parameter study . . . . .</b>	<b>104</b>
<b>4.5</b>	<b>Conclusion . . . . .</b>	<b>108</b>

---

Lithium-ion batteries age during their lifetime. At cell scale, the impedance rises and the intrinsic capacity is reduced. Multiple phenomena are involved in aging mechanisms, and literature reviews indicate that the graphite electrode has a large contribution to degradation processes.

In order to illustrate these mechanisms, the results of an aging campaign of prismatic cells previously manufactured at the laboratory are analyzed. The electrode potentials were separately measured thanks to a reference electrode. Impedance, capacity, and electrode potentials are quantified in function of the different aging modes: calendar or cycling operations.

The electrode potentials of a fresh and an aged cell are used to calibrate a cell model, based on the graphite and NMC electrode models, presented in [Chapter 2](#). The model allows to link aging consequences at cell scale with a parameter variation. Possible origins of aging can thus be deduced and quantified.

## 4.1 Aging sources inside lithium-ion batteries

A lithium-ion cell degrades continuously due to operations and external conditions. Two degradations are noticeable : a power loss and a capacity fade.

The power loss indicates that for a given applied current, the cell voltage obtained is lower than expected. The loss of power reflects an increase of the internal resistance, or cell polarization, during operations. Electronic and ionic transports inside electrode are less efficient and the charge-transfer reaction is less effective.

The capacity fade indicates that the cell contains less energy, a smaller amount of lithium can be intercalated into the electrode host structure. In a full cell, only a limited lithium quantity is present and used through operations. This lithium quantity is called *cyclable lithium* and is initially intercalated in the active material of the positive electrode. As no lithium atom can be introduced in a closed cell, cyclable lithium consumption in side reactions corresponds directly to a capacity loss. The electrode intercalation capabilities limit also the overall cell capacity: any damage to the active materials lowers the amount of cyclable lithium that can be intercalated. Capacity fade thus comes from two damage modes: either a loss of cyclable lithium or a loss of active material. These two degradation modes are often respectively named Loss of Lithium Ion (LLI) and Loss of Active Material (LAM) in the literature [[125](#), [126](#), [127](#)].

The cell ages through two different processes, cycling or calendar conditions, depending if the cell is in use or not. Both induce different aging mechanisms and therefore different losses. These losses are expressed essentially in function of cycles and time, respectively in cycling or calendar conditions. Because of the variety of cell possible operations, there is no consensus on the way to compare aging studies during cycling in the literature.

In both aging processes, losses in power and capacity come from the degradation of the different cell components: porous electrodes, separator, electrolyte and current collectors [[128](#)]. A lot of interdependent physical and chemical phenomena are at the origin of these degradations. Thus the

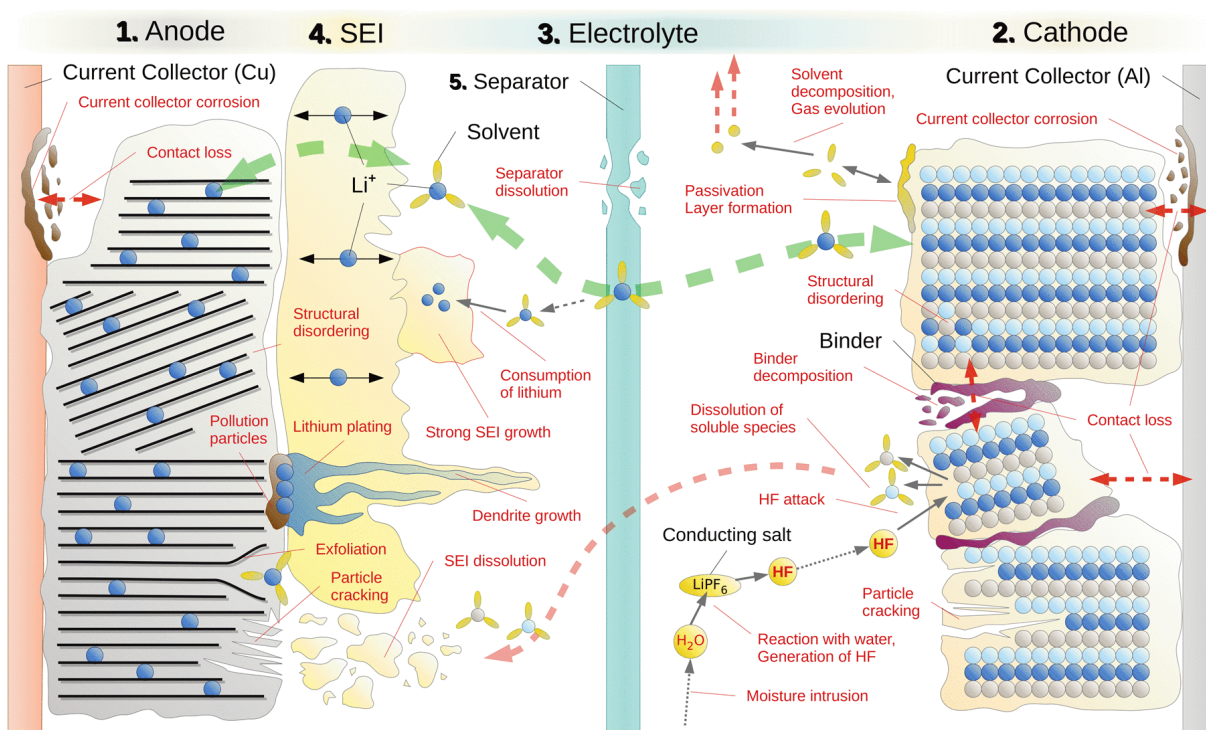


Figure 4.1: Degradation mechanisms in lithium-ion cells (reproduced from [1], summarized from [2, 3])

current collectors corrode, the separator decomposes, the electrode is mechanically delaminated via binder destruction, the crystallographic structure of the positive electrode changes or side-reaction products are formed. The Figure 4.1 presents a list of the main degradations that could occur. These degradations were summarized by ARORA *et al.* [128], by VETTER *et al.* [2] or recently by HENDRICKS *et al.* [129]. These mechanisms are difficult to isolate, both in time and space, which complicate their experimental study. The understanding is sometimes limited, even some existences subject to debate, due to the lack of direct observations (such as the exact influence of manganese dissolution on capacity fade [130, 131]). Thus, it remains hard to quantify, model, and predict the aging of a lithium-ion cell [128]. We propose here to briefly introduce the main aging sources in lithium-ion batteries.

#### 4.1.1 The Solid Electrolyte Interface

The species inside common liquid electrolytes have a narrow electrochemical potential stability window [132]. When lithiated, the graphite electrode has a potential close to 0 V vs  $\text{Li}^+/\text{Li}$ , which implies that electrolyte components may come out of their stability windows (typically from 1 to 4.5V vs  $\text{Li}^+/\text{Li}$  for carbonates [133]). At the first graphite lithiation, many species are decomposed below 1 V on the graphite surface and form a passivation layer that protects graphite from exfoliation and future electrolyte reductions [134]. This passivation layer is called the Solid Electrolyte Interface (SEI). A similar SEI exists at the positive/electrolyte interface, but thinner

and more chemically stable than the graphite one [135]. Current understanding of SEI are reviewed by GAUTHIER *et al.* [136].

SEI solid products are either organic or inorganic, derived from lithium compounds, have a low electronic and ionic conductivities and are mostly chemically unstable. Moreover, the SEI formation can produce also gases, that need to be evacuated [137]. All these products are suspected to form a porous mosaic, or a multilayered structure, as early established by PELED *et al.* [138]. As the SEI structure highly depends on additives and formation conditions, its representation does not reach a consensus yet [139]. Experimentally, it is confirmed that inorganic products, which come in majority from lithium salt decomposition, are more stable and are firstly formed on graphite surface (below 0.5 V) [140]. Organic compounds are secondly formed (below 0.3 V) and rather found on the upper side of SEI. They are more conductive but also less stable over time than inorganic ones. Studies show that there is a composition difference between SEI on basal plane and edge plane of graphite [141].

Through time and operating conditions, SEI evolves. Electrolyte components diffuse through SEI structure, parasitic reactions continue at graphite surface, and SEI becomes thicker. The suspected reactions are summarized in a review from VERMA *et al.* [142]. A possible formation mechanism is presented in the next chapter (Chapter 5). The SEI growth is one of the preponderant aging phenomenon. Its growth generally consumes cyclable lithium, contributing not only to capacity fade, but also to the cell impedance rise. SEI has indeed low electric and ionic conduction properties, that decreases intercalation kinetics, proportionally to the layer thickness. The thickness varies from five nanometers on fresh cell [139] to almost half a micrometer on cells at their end of life [143]. Over time, anode aging studies suggest that the organic compounds react into inorganic ones, turning the SEI into an even less ionic conductive layer [144, 145].

SEI evolution depends on many factors. In case of calendar aging, it is clear that its evolution depends particularly on electrolyte nature, electrode state of charge, and temperature [146, 147, 148]. In case of cycling, the graphite particles undergo volume expansion and contraction, respectively upon lithiation and delithiation. The graphite expansion is about 10 %, and induces SEI fracturations. So, some part of graphite particles are newly in contact with electrolyte and SEI is re-formed, accelerating the lithium consumption. To enhance mechanical SEI properties, various additives are added to the electrolyte such as vinylene carbonate (VC) [34] or fluoroethylene carbonate (FEC) [35]. In both aging modes, the transformation of SEI, its stabilization and growth occur throughout the cell life.

SEI has also an influence on the cell thermal behavior. Its morphology and composition change at high temperatures (over 80°C) [149, 150]. When the temperature rises, it is the first component of the cell that can be decomposed exothermically, and it leads to a cascade of uncontrolled chemical reactions called thermal runaway. SEI properties should thus be controlled in order to operate securely lithium-ion battery [151].

### 4.1.2 Lithium plating

The equilibrium potential of lithiated graphite is close to the equilibrium potential of lithium metal. The lithiated graphite surface is then a place of choice for lithium-ions reduction. In some cases, the intercalation reaction in graphite can be thermodynamically disadvantaged in benefits to the reduction of lithium-ions which forms finally metallic lithium deposits. This phenomenon is called lithium deposition or lithium-plating [152].

Lithium plating is expected for fast charges and low temperatures [153]. The temperature lowers the electrolyte conductivity and decreases the overall intercalation kinetics which promotes lithium plating. Fast charges, which correspond to the graphite lithiation in a full cell, favor the accumulation of intercalated lithium near particle surface due to the low transport properties within particles. Doing so, the intercalation kinetics is lowered, overpotential rises and lithium plating is promoted. This phenomenon can happen over a long period of time (overcharge), or a short period of time due to large local current [154].

If both electrodes have the same surface, the current density at the edge of the negative electrode will be large enough to boost lithium plating. To avoid this, negative electrode surface are regularly oversized [155]. For same reason, the areal capacity ratio of negative to positive electrodes is classically above unity (1.1-1.2), because it fades lithium plating effect and increase cycling performance [156]. Local structural electrode inhomogeneities can lead to large local intercalation currents and lithium plating too [32, 157].

Metallic lithiums deposited on the electrode surface can passivate, consume electrolyte, and impair the electrode conductivity [152]. It is suspected that this metallic lithium deposits can precipitate in electrolyte, and therefore be disconnected from the electrode conductive phase [158].

Lithium-plating is indirectly measured by the variation of the cell thickness [159, 160]. Thickness variation through operation indicates that lithium deposits can be reversible. Irreversible lithium deposits affect the electrode structure, its porosity, and tortuosity, which leads to local pore clogging and a premature end of life [157, 161, 162]. Moreover, this local lithium deposit has a significant effect on the safety behavior, because it lowers the onset temperature of thermal runaway [163], it can lead to separator perforations [58], and at the end to a deadly short-circuit of the cell [164].

### 4.1.3 Active material degradations

During aging, the crystallographic structure of active material of both electrodes (Graphite and NMC) becomes less organized. Nevertheless, the overall crystallographic changes are small [2] and can be considered as a minor effect on global capacity fade. Structural changes are located essentially near the active material surface for both electrodes. The graphite surface could exfoliate and fractures due to the solvent co-intercalation, mainly Propylene Carbonate (PC) [165]. During the first cycles, the lattice parameter of the NMC particle surface changes, as confirmed by X-ray

and *in-situ* neutron diffraction [41, 166].

A high intercalation state induces mechanical stress inside the electrode structure that may cause particle degradations [118]. Particles are fractured, pulverized, and electrically isolated. The higher the volume expansion and the strain applied on the cell, the greater are the resulting damages on the electrode structure [167]. The electrode structure changes (porosity and tortuosity) are qualitatively observed by post-mortem X-ray tomography and SEM studies [168, 169, 170, 171].

The active material loss, combined with parasitic reactions induces a shift in the lithiation stoichiometry range of both electrodes that can lead to an underutilization of the cyclable lithium inside the whole cell. For instance, when the positive electrode is completely lithiated, the negative one can be partially delithiated instead of being fully empty [125].

#### 4.1.4 Positive electrode influences

Lithium-ion cells are typically made with negative electrode larger in surface and capacity than the positive one. The negative/positive surface and capacity ratios have an impact on electrochemical performance. Capacity ratio (N/P ratio) has been studied experimentally by SON *et al.* [172], a N/P ratio under unity decreases cycle life. Surface ratio is numerically quantified by TANG *et al.* [155]. The protective effect of a negative edge extension over the positive one is observed above 0.4 mm and sufficient to prevent lithium deposition.

The graphite electrode being over-sized in surface and capacity, the capacity of the positive is thus the cell capacity. Any active material loss at the positive electrode causes directly a cell capacity decay. Moreover losses from positive material are often observed during cycling, whatever the material of the electrode [143, 173, 174, 175].

These active material losses can be an active surface decreasing or a dissolution of positive active materials into the electrolyte [176, 177, 174]. Extra metallic compounds (such as manganese, cobalt or nickel) are dissolved into the electrolyte, diffuse, and come into contact with the negative electrode particles. These compounds degrade the electronic insulating properties of the SEI, and act as a catalyst for its formation [131, 178].

#### 4.1.5 Aging mechanisms summary

In summary, the aging phenomena inside lithium-ion batteries are mainly linked to the graphite electrode, notably through the formation of a passivation layer (SEI). Positive active material degradations are also often noticed [179, 177, 180, 181]. These degradations continuously lower capacity and power performances over time. Lithium-plating occurs during specific conditions (high currents, low temperatures, or over-charges) or over long periods of time. It happens to localized area of electrode, and induces a sudden capacity decay.

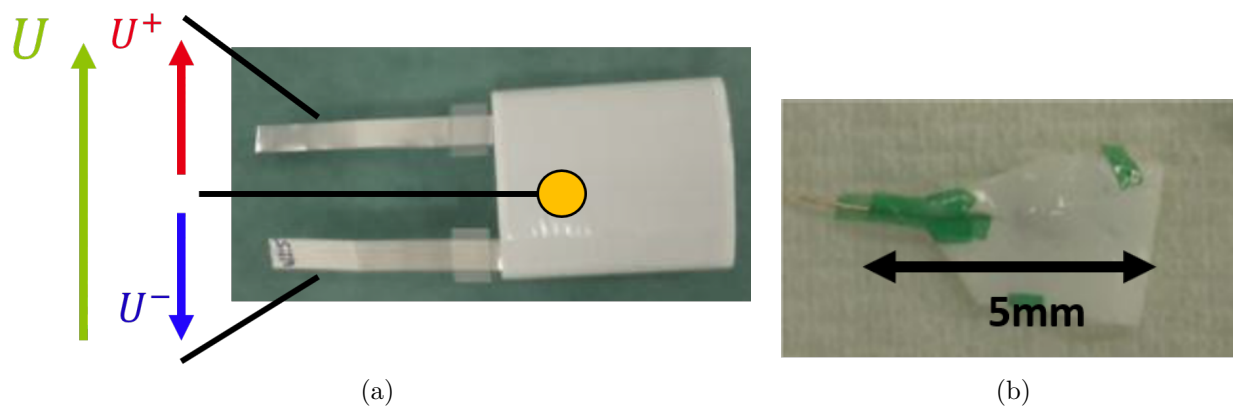


Figure 4.2: Prismatic cell and measured potential differences (a) and reference electrode details (b)

## 4.2 Experimental cell aging

In laboratory, prismatic cells with a reference electrode were aged, one part under calendar conditions and another part under cycling conditions. Some results of this experimental campaign are studied in the scope of this thesis, especially the discharge capacity through aging and the capacity recovery during check-up. Data are used to develop and validate aging models based on the performance model, which was developed in [Chapter 2](#) and [Chapter 3](#).

### 4.2.1 Experimental pouch cell

Standard prismatic cells are manufactured and composed of graphite and NMC electrodes.

#### 4.2.1.1 Cell set-up

Studied cells are 5 mm thick, 34 mm wide, and 37 mm high. [Figure 4.2a](#) displays a representative cell. Cells are manufactured in a prismatic format (5-34-37) inside a flexible packaging. The electrodes are wounded in the cell. Mass-loadings of electrodes are  $14.1 \text{ mg} \cdot \text{cm}^{-2}$  and  $7.3 \text{ mg} \cdot \text{cm}^{-2}$ , respectively for the NMC and graphite electrodes. The separator is a Celgard 2325, which is  $25 \text{ }\mu\text{m}$  thick. The electrolyte used is composed of 1 M lithium hexafluorophosphate ( $\text{LiPF}_6$ ) in 1:1:3 weight proportion of ethylene carbonate (EC), propylene carbonate (PC), and dimethyl carbonate (DMC), namely LP10. Vinylene carbonate (VC) is added at a 2 % volume fraction. Approximately 50 cells were manufactured.

Electrode composition and porous structures are similar to electrodes from [Chapter 2](#). However inside the cell, their relative geometric surface differ: the surface difference is as high as 1.25, mainly because an extra length is added at the end of the negative electrode band. With the electrode irreversible losses during formation, cells reach a theoretical 550 mAh capacity for a cell voltage range of 2.5-4.3 V.

#### 4.2.1.2 Reference electrode

A lithium-based reference electrode (RE) is located inside the cells to follow the potential of each electrode during operation. As this electrode is made of lithium metal and no transformation occurs, its potential is considered stable at 0 V versus  $\text{Li}^+/\text{Li}$ . The RE is manufactured from sheets of lithium pressed on a nickel wire of 250  $\mu\text{m}$  long, packed in a Celgard C2325 separator and introduced inside the cell (Figure 4.2b). The RE is integrated at the center of the wounded electrodes, close to the negative electrode side.

According to LA MANTIA *et al.* [182], a versatile reference electrode must be reproducible, reliable, and non-polarizable. Its potential must therefore be constant through time and under many external conditions. As shown by COSTARD *et al.* [183], the lithium electrode surface passivates, potential will shift over time due to its own aging, and shows signs of non-reproducibility at high currents. Moreover, measurement artifacts are partially due to the RE geometry. The correlation between geometry and artifacts is demonstrated numerically by ENDER *et al.* [184]. Lithium salt concentration affects also the measured potential [185]. So, the reference potential shifts through time and the RE perturbs the cell operations. As a consequence, measured electrode potentials are expected to be close to reality on fresh cells, but should be taken with caution on aged cells.

#### 4.2.1.3 Formation

The prismatic cells are initially formed, with the same protocol explained in Chapter 2. Gases emitted during the formation of the electrode/electrolyte interfaces are evacuated. Among functional cells, capacities range from 520 to 560 mAh, with an average value of 547 mAh and a standard deviation of 5 mAh.

### 4.2.2 Aging during cycling conditions

Some cells are cycled at 25 °C using a modular potentiostat/galvanostat VMP3 from Bio-Logic, Claix, France. The potentials of positive and negative electrodes (respectively,  $U^+$  and  $U^-$ ) are recorded simultaneously versus the lithium counter-electrode.

#### Cycling operating conditions

The cells are cycled according to the following protocol: cells are firstly charge at a C/2 rate, up to 4.2 V. Then, the cell potential is kept at 4.2 V until the current drops below C/50, which is referred as the floating step in the following. Then, after a 30-minute break, cells are discharged at a C/2 rate, up to 2.5 V. A 30 minute break is repeated before a new cycle begins. This cycle operation is performed as many times as possible. Some cells are taken out every 300 cycles for post-mortem analyses. Details and results of these analyses will not fall in the scope of this thesis.

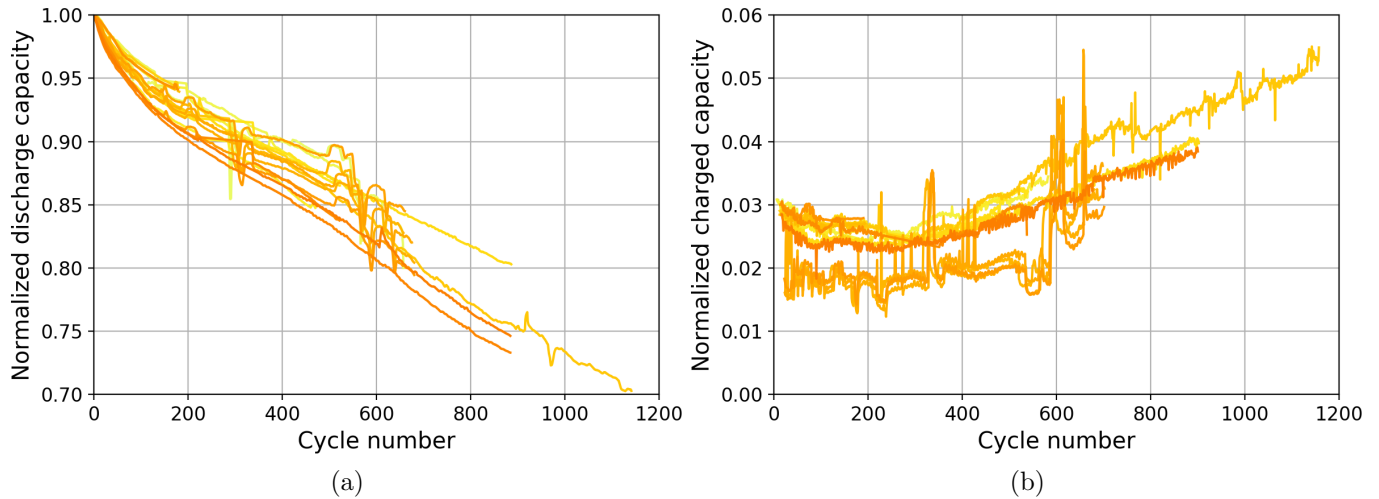


Figure 4.3: Experimental normalized capacity of the cells discharged through cycling (a) and charged during the floating step (b)

Check-up cycles are done on fresh cells and at their end of life. These checkups consist of a slower cycling at  $C/5$  between 2.5 V and 4.2 V. At the end of the first charge phase, an additional charge phase is done at  $C/20$  up to 4.2 V to fully charge the cell. A 30-minute break is set at the end of each step. This cycle is repeated three times.

### Ageing results

The charge and discharge characteristics vary during the cycling operation. This denotes an evolution of the different properties of the cells. On all the cells, discharge capacity decreases with the number of cycles. Cell discharge capacities normalized to their respective initial capacity are displayed in Figure 4.3a. Two ageing periods appear. The first one, up to 200 cycles, shows a quadratic capacity loss. The second one, over 200 cycles, shows a linear loss. Anyway, some cells are out of tendencies and display a sudden discharge capacity loss. Figure 4.4a shows one of these sudden drops on a particular cell. These drops can occur randomly through cycling and precipitate the cell to its end of life.

A dispersity is observed in discharge capacity values carried out on the different cells. At 800 cycles, there may be more than a 10 % difference between two cells. This dispersion at the end of life was also presented by BAUMHÖFER *et al.* [186] for commercial cells. This variance between discharge performances can be related to heterogeneities of the electrodes which are coated on a production line. Heterogeneities concern both the properties of the active materials and the quality of the coating. It is difficult to control all these parameters for the manufacture of several prototypes.

The amount of lithium intercalated during the floating charge step changes through time. Initially less than 3 % of the initial capacity is re-intercalated during this additional step which

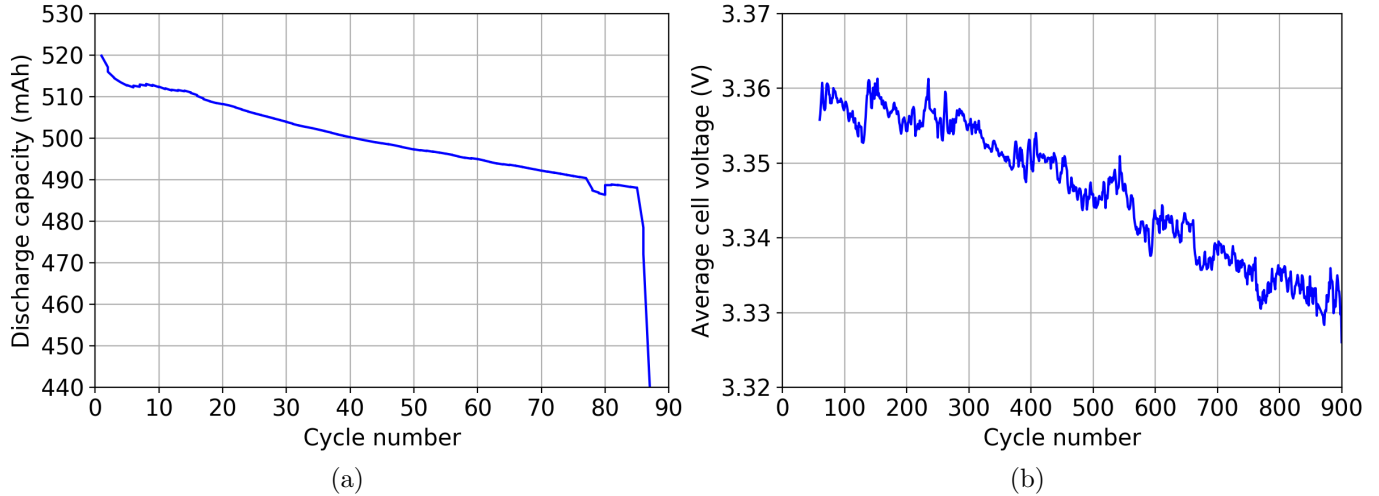


Figure 4.4: Experimental premature capacity loss (a) and average cell voltage during discharge through cycle (b)

is no more than 10 minutes long (Figure 4.3b). This value is quite stable, even a slight decrease can be seen, during early stages, up to 200 cycles. This decrease shows that a smaller amount of lithium remains to be intercalated at the end of the first charge step, which could result from an improvement in transport properties or an early cyclable lithium loss. On aged cells (up to 900 cycles), the amount of lithium that remains before the floating step exceeds 5 % of the initial capacity. At this point, the step is more than 20 minutes long. The cell performance is degraded, which can come from lower transport properties, both due to a change in porous structure, electrolyte, or active materials. A linear dependence to the number of cycles (or time) is noticeable. This means that the degradation phenomena relating to the intercalation and lithium transport in the liquid and solid phase may be linear functions of time [187].

The cell impedance evolves too. In Figure 4.4b is observed the average cell voltage of each discharge phase through cycling for a selected element. After a relative constant phase up to 200 cycles, the average cell voltage decreases linearly up to 30 mV at 900 cycles. As no impedance rise is noticeable on the first period, the cyclable lithium loss is the primary loss until 200 cycles. For the second period, as the current applied through the discharge phase has not changed, the cell voltage loss indicates the rise of the cell impedance through time.

In conclusion, a 2-step aging phenomenon is observed on the capacity extracted during discharge step (Figure 4.3a), capacity charged during floating step (Figure 4.3b) and cell impedance (Figure 4.4b). The first step indicates a quadratic loss of cyclable lithium without any cell impedance rise. The second step is a linear loss of discharge capacity.

## Check-up cycles

The check-up cycles are performed on fresh cells and at the end of life to compare the intrinsic cell capacities. Electrode potentials are recorded and used to validate the full cell model. For illustration, the electrode potentials are shown on Figure 4.5 during the first check-up cycle on a fresh cell and after 900 cycles. The particular potential signature of the graphite electrode is seen at the beginning of life. At the end of life, this potential is more flat. The reference electrode has drift over cycles or actually the stoichiometry range of the graphite electrode has changed.

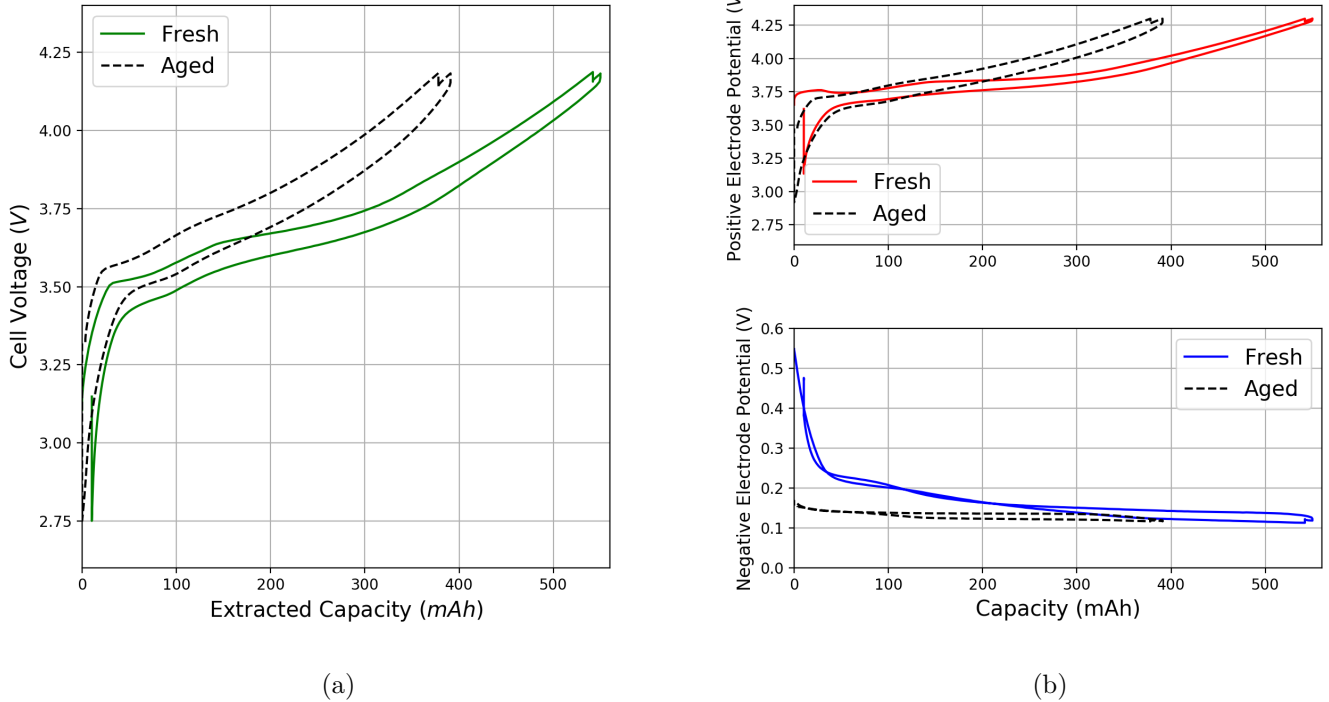


Figure 4.5: Experimental cell voltage (a), positive electrode (b, up), and negative electrode (b, down) potentials during check-up at  $C/5$  before and after aging (cycling conditions)

We define the reversible capacity as the amount of capacity reversibly charged and discharged in a cell during one cycle. The check-up cycles provide the reversible capacities at low C-rate, which are close to the theoretical cell capacity (Figure 4.6). A slight variation of the reversible capacity is observed on the initial and final check-up cycles. During initial check-up, the reversible capacity decreases. Indeed, the growing SEI at the electrode/electrolyte interface is particularly important on the first charge steps [188], but the coulombic efficiency (the ratio between charge and discharge capacity) tends to improve over cycles. Figure 4.6 shows a 1 % reversible capacity loss during initial check-up. On final check-ups, the trend is on reverse. There is a slightly reversible capacity improvement over check-ups, coming from both charge and discharge steps. The final check-up of the same pouch is shown on same Figure 4.6 and presents a 2 % capacity recovery.

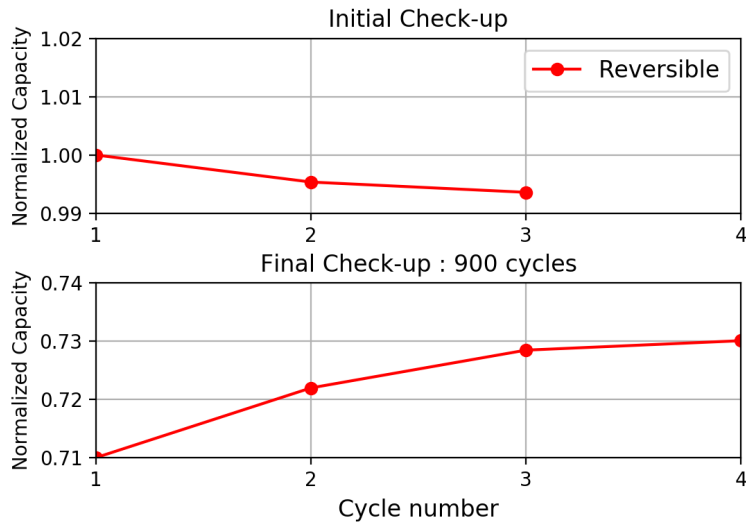


Figure 4.6: Experimental capacity through initial (up) and final (down) check-up cycles for a pouch in cycling conditions

### 4.2.3 Aging during calendar conditions

#### Calendar operating conditions

Six cells are placed in calendar aging conditions. They rest at three different states of charge: 100, 60, and 30 %. Cells are characterized by check-up cycles every two months. In order to accelerate aging, cells are stored at 60 °C. It is shown in literature that temperature accelerates aging mechanism [144, 189, 190].

#### Check-up cycles

The check-up cycles are similar to the cycling ones. A check-up cycle corresponds to a full charge at  $C/5$ , a 30-minute break, followed by a  $C/5$  discharge and another 30-minute break. This cycle is repeated at least three times. At the end of the check-up, the cell is charged at its initial state of charge.

#### Results

Reversible capacities are extracted at each check-up and normalized to the initial cell capacity (Figure 4.7).

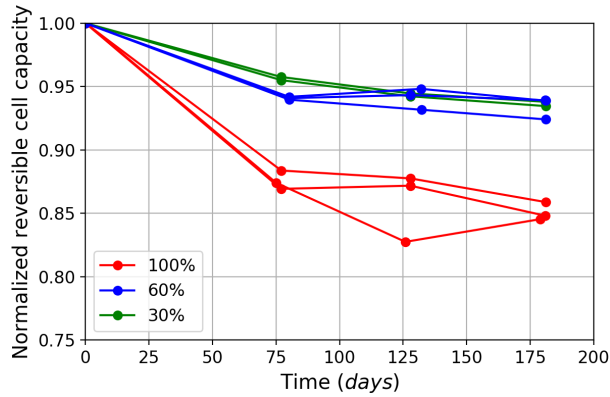


Figure 4.7: Experimental normalized reversible capacity of the cells in calendar aging

The capacity loss between the first and the second check-up is larger than the following ones. After the second check-up, the capacity loss becomes linear with respect to time. These two aging periods make calendar aging similar to the cycling one. Nevertheless, the second check-up happens after 75 days, a duration which corresponds roughly to 400 cycles in cycling conditions. Time constants for these two periods are different between calendar and cycling aging. Due to the lack of measures before 75 days, no conclusion can be driven on time dependency for loss of the first period.

After 175 days, the loss goes up to 15 % of the initial cell capacity in the worst condition (SOC = 100 %). This duration corresponds to 900 cycles, but through cycling conditions almost 30 % of the cell capacity are lost (Figure 4.3a). Calendar aging, even at 60 °C, is less degrading than cycling conditions for the same duration.

The more the cell is charged, larger are the loss (Figure 4.7). This is confirmed also in literature [146, 147]. High state of charge and therefore low graphite electrode potential accelerate SEI formations.

A self-discharge effect can be noticed through electrode potentials. For each electrode, at each check-up, a potential variation is calculated as the difference between the potential at the end of the last check-up and the initial of the current one over the time spend. The potential variation through aging indicates if the electrode lithiates or delithiates (Figures 4.8a and 4.8b). A positive potential variation corresponds to a potential rising and so, a delithiation. A negative variation indicates a potential decreasing and so, a lithiation.

The potential variation at the positive is negative for all SOC cases (Figure 4.8b), and it corresponds to NMC lithiation, at a rate between 0.3 and 1.2 mV · days<sup>-1</sup>. At the negative, cases are different (Figure 4.8a). At 30 % SOC, the potential variation oscillates near zero through the aging, no clear conclusion can be drawn. At 60 % SOC, the potential variation increases above zero, which indicates an electrode delithiation. In addition to the lithiation at the positive, the cell is effectively discharging. At 100 % SOC, the potential variation decreases above zero. It can be a graphite lithiation due to the relaxation after the check-up charge, or, more probably, a growing

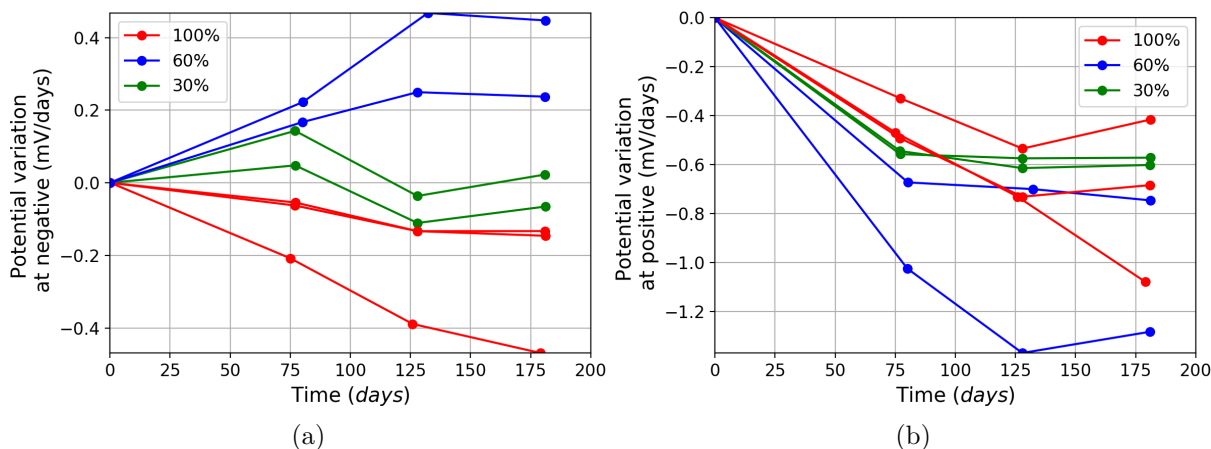


Figure 4.8: Experimental potential variations at the negative side (a) and positive side (b) through calendar aging

SEI which decreases the equilibrium potential and gives an extra cyclable lithium loss compared to the other SOC cases (Figure 4.7).

During the check-up, the capacity losses are recovered slightly throughout cycles. Figure 4.9 shows reversible capacity through cycles on a selected cell for the first and last check-ups.

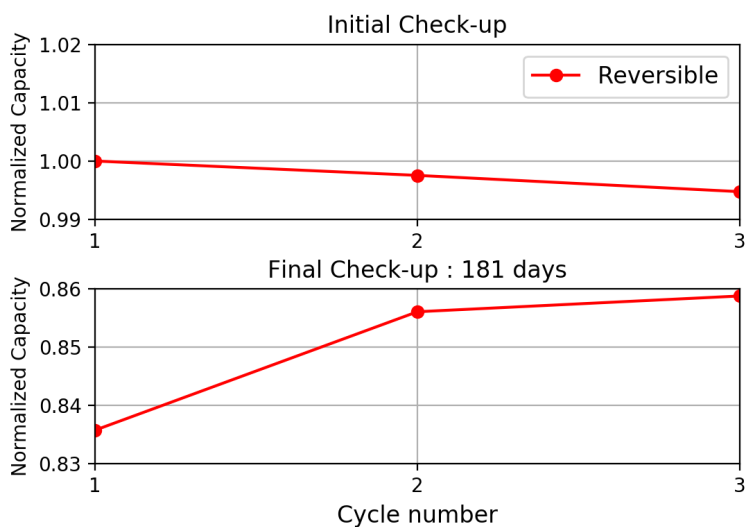


Figure 4.9: Capacity through initial (up) and final (down) check-up cycles for a cell aged in calendar conditions

YAZAMI *et al.* proposes a SEI mechanistic origin to the capacity recovery [191]. During calendar aging, metastable complexes are formed at the electrolyte/electrode interface. These complexes can break down into cyclable lithium that return to the electrochemical system. Their progressive return increases the reversible capacity effectively seen during the check-up cycles. Nevertheless, this hypothesis can not explain the similar recovery after cycling conditions (Figure 4.6).

Figure 4.10 shows a check-up cycle on an element at the beginning of its life and after calendar aging (100 % SOC). The negative electrode potential, fresh and aged, polarizes more than in cycling conditions (Figure 4.5). Nevertheless, plateaus of aged potential are still visible. The reference electrode could be less affected by calendar aging.

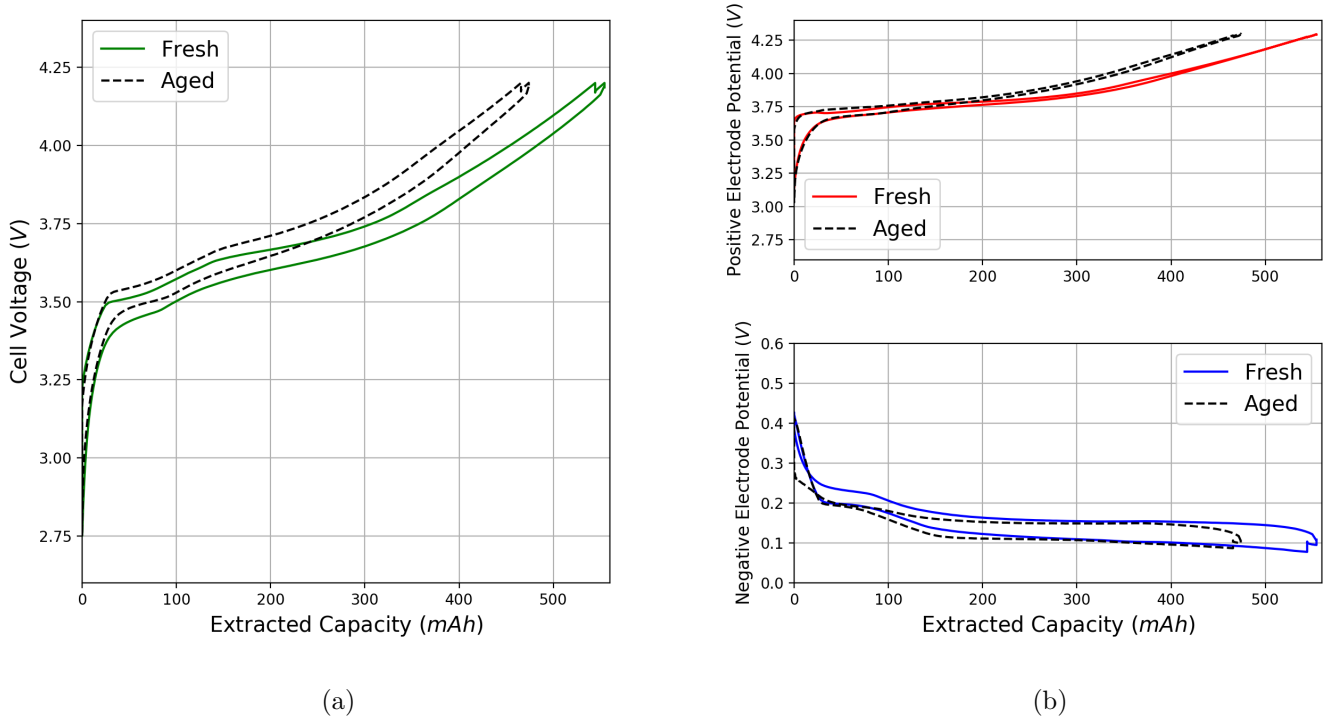


Figure 4.10: Experimental cell voltage (a), negative electrode and positive electrode potential (b) before and after aging during calendar conditions (100 % SOC)

#### 4.2.4 Aging Summary

Among the different aging modes, calendar and cycling, similar trends are observed. These trends can be divided into three steps. This trend concerns the capacity extracted during discharge through cycling or the cell capacity along calendar aging. These steps are summarized in Figure 4.11.

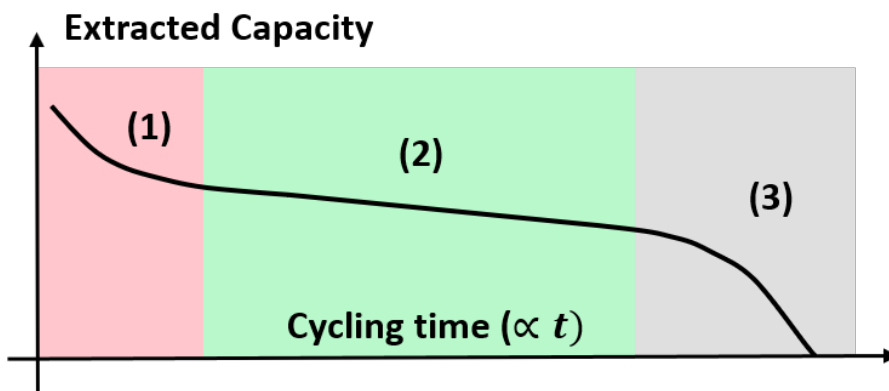


Figure 4.11: Diagram of the different aging phases through cycling

The first step is a loss that does not exceed 10 % of the initial cell capacity. This loss is a quadratic function of time in case of cycling conditions. We cannot conclude in calendar conditions due to the lack of points. Loss in the second step is linear to time, it can reach up to 30 % of the initial cell capacity. The last step, not noticed on all cell but only for cycling mode, is a sudden loss of the extracted capacity.

In both aging modes, the same trends are also observed during the check-up phases. The initial check-up shows a loss of reversible capacity. Later check-ups show a capacity recovery which does not exceed 3 % of the initial cell capacity.

## 4.3 Full cell model development and validation

In this part, the development and validation of a full cell model is explained. The half-cell configuration from the previous chapters ([Chapter 2](#) and [Chapter 3](#)) is upgraded to a full cell configuration, and validated with experimental electrode potentials from initial check-up cycles. Some hypotheses are made on the positive electrode, in order to simplify the numerical resolution. Then, the parameters that contribute to aging are identified and their possible variations related to aging are quantified independently.

### 4.3.1 Model development

The half-cell model must be completed to simulate a full cell configuration. In a full cell, the negative electrode is made of graphite instead of lithium. At the positive side, NMC is used. In addition, the electrode surface ratio should be taken into account because current density differences should be observed between the both electrode. The [Figure 4.12](#) summarizes hypotheses of the full cell model approach.

The 1D approximation of the cell thickness is still valid because electrode surfaces are limited. The porous electrode framework is used for the graphite electrode, in order to explore local

conditions inside its structure [33]. At the other side, the NMC electrode has an homogeneous behavior during lithiation (Chapter 2 and Chapter 3). All the transport phenomena inside the liquid phase can be neglected and doing so, the electrode behavior is modeled as a unique particle. This approach, called “Single Particle”, is often chosen for aging study, because it lowers the numerical complexity, and so the computational cost), and remains valid under medium C-rates ( $< 2C$ ) [27, 192, 193, 180, 77, 187, 194, 195].

The NMC electrode is then represented as an interface where intercalation kinetics occurs, modeled with a Butler-Volmer Equation (Equation 2.5). The ionic potential ( $\phi_2$ ) and the salt concentration ( $c_2$ ) at the NMC surface are taken as at the separator/electrode junction. The electric potential ( $\phi_1$ ) of the particle is considered as an unknown of the model. Inside the representative particle, the lithium transport stays relevant. In order to decrease numerical complexity, the lithium stoichiometry profile along radius ( $x$ ) is approximated as a second order polynomial equation :

$$x_{\text{Li}}(t) = a(t) + b(t) \cdot \left(\frac{x}{r}\right)^2$$

where  $a(t)$  and  $b(t)$  are time-dependent constants, and  $r$ , the particle radius. When lithium transport is modeled via the Fick’s law, SUBRAMANIAN *et al.* demonstrated that the particle surface stoichiometry  $x_{\text{Li}}$  and the averaged particle lithium stoichiometry  $\bar{x}_{\text{Li}}$  are the unknowns of the following two-equations system [116]:

$$\begin{cases} q_{nmc}\rho_{nmc} \frac{d\bar{x}_{\text{Li}}}{dt} + \frac{ni_n}{r} = 0 \\ \frac{D_1}{r} q_{nmc}\rho_{nmc}(x_{\text{Li}} - \bar{x}_{\text{Li}}) = -\frac{i_n}{n+2} \end{cases} \quad (4.1)$$

where  $n$  is the geometrical factor of particle, which equals 3 in NMC, since a spherical representation is used. The polynomial approximation reduces the transport problem from a partial differential equation to two differential algebraic equations. This assumption remains valid for moderate C-rates ( $< 2C$ ) and pseudo-stationary conditions. For large C-rate and fast transient time (when the switch between charge and discharge is faster than time diffusion constant), the parabolic profile approximation is too restrictive.

The electrode surface ratio between graphite and NMC is 1.23. As the charge flux through the cell thickness is constant, the local current density is then higher for a smaller geometrical surface (as the NMC one). Along the modeled cell thickness, current densities are expressed per square meter of graphite electrode surface. So, the geometrical electrode surface ratio is considered for intercalation current at the positive side in order to have a correct lithium stoichiometry value. The boundary flux at this particle surface is then expressed as:

$$\frac{\partial c_1}{\partial t} = \frac{S_p}{S_n} \frac{i_n}{F} \quad (4.2)$$

The surface ratio is given as the ratio of the geometrical positive electrode surface,  $S_p$ , and the

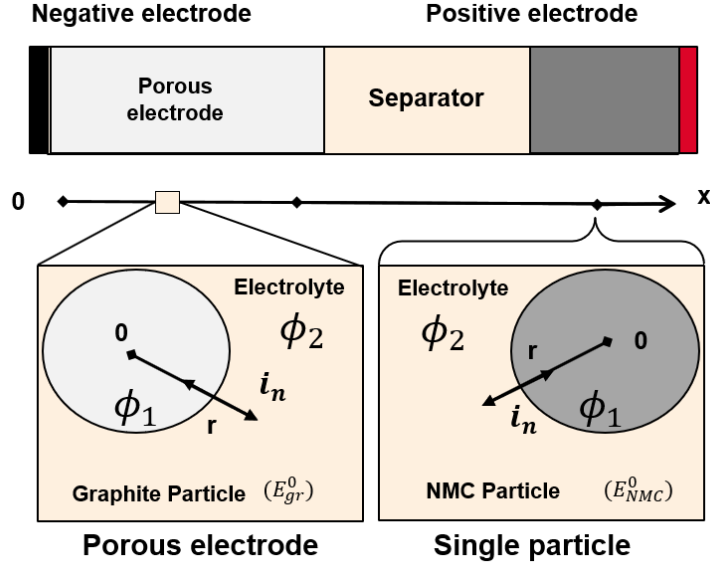


Figure 4.12: Pouch cell model diagram

negative one,  $S_n$ .

The SEI is a predominant factor on aging and has an influence on the intercalation kinetics. The local overpotential of graphite electrode is re-evaluated to:

$$\eta = \phi_1 - \phi_2 - r_{\text{sei}} i_n - E_{gr}^0 \quad (4.3)$$

taking into account  $r_{\text{sei}}$ , the SEI resistance, considered to be null at the beginning of life.

Experimental electrode potentials are used to validate the model. The positive and negative electrode potentials, respectively  $U^+$  and  $U^-$ , are calculated in the model as the potential difference between current collector potentials and the value of the ionic potential ( $\phi_2$ ) at the negative/separator interface.

Thanks to the sensitivity analysis in [Chapter 2](#), only seven parameters need to be adjusted: the intercalation kinetics ( $k_p$  and  $k_n$ ), the active material fractions ( $w_{gr}$  and  $w_{nmc}$ ) and the lithium transport coefficients in solid phases ( $D_{1,nmc}$  and  $D_{1,gr}$ ) and electrolyte ( $D_2$ ).

### 4.3.2 Initial conditions and adjusting parameters

The first step of model calibration is to fit the model capacity to the experimental one. Initial state of lithiation of both electrodes and their capacities are needed.

#### Formation cycle

During formation, cyclable lithiums are consumed inside the electrodes. The initial states of lithiation of both electrodes used as input for the simulation sum up the consequences of all these losses.

When the cell is freshly manufactured, the NMC electrode is completely lithiated and graphite completely delithiated (Step 1 on Figure 4.13). The cell is firstly charged at a low C-rate (C/10), the NMC electrode delithiates and the graphite lithiates. No SEI components exist on the graphite surface at start. Below 0.6 V vs  $\text{Li}^+/\text{Li}$ , electrolyte compounds are reduced and form the passivation layer (SEI), which consumes cyclable lithium (Step 2 on Figure 4.13). When the positive electrode is fully delithiated, the negative electrode, bigger than the positive one, is not fully lithiated. Then, during the first discharge, the negative electrode is delithiated and the positive electrode is re-lithiated. As cyclable lithiums have been consumed in the SEI formation, the NMC electrode is not fully lithiated at the end of the discharge, even if its capacity has been slightly reduced at first charge, due to initial phase transformations. It should be noted that some parts of the graphite electrode are not fully delithiated, lithium may be trapped in the bulk of material [196, 134].

The initial state of the cell used in the simulation is then an almost lithiated positive electrode and an almost delithiated negative electrode. Therefore the cell capacity corresponds to the positive capacity, that is to say the effective quantity of cyclable lithium.

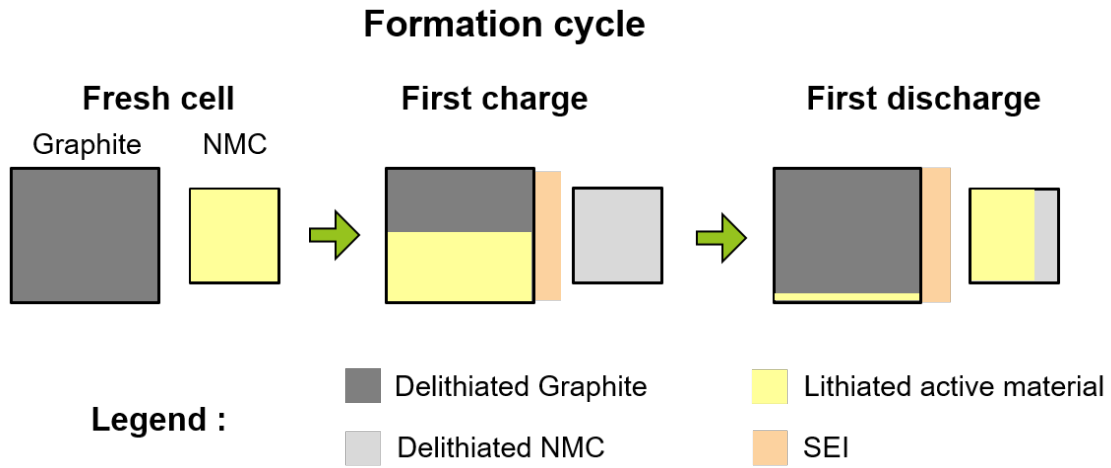


Figure 4.13: Formation cycle and initial conditions in a graphite/NMC cell

### Cell capacity and initial conditions

From the above conclusion, the cell capacity,  $Q_{cell}$ , is deduced as:

$$Q_{cell} = q_{nmc} \Delta x_{\text{Li}} W_{nmc} w_{nmc} S_p \cdot \Delta SOL \quad (4.4)$$

where  $q_{nmc}$  represents the theoretical capacity of NMC ( $\text{mAh} \cdot \text{g}^{-1}$ ),  $\Delta x_{\text{Li}}$  the stoichiometry interval imposed by cycling conditions (0.6),  $W_{nmc}$  the mass-loading ( $7.3 \text{ mg} \cdot \text{cm}^{-2}$ ),  $w_{nmc}$ , the mass fraction of active material in solid phase (0.92), and  $S_p$  the geometrical surface of the electrode.  $\Delta SOL$  is the state of lithiation range in the positive electrode, which corresponds to the ratio of lithium content accessible (above a 0.4 lithium stoichiometry) and the theoretical electrode capacity used on a 0.6 stoichiometry interval.

Active material losses of the positive are assumed to be equal to those found on half-cell configurations (Chapter 2). The theoretical capacity, the stoichiometry interval and the mass loading are supposed accurately known. All the positive surface is supposed to work in the current electrode. Only  $\Delta SOL$  should be adjusted.

A cell can deliver 550 mAh after formation. From Equation 4.4,  $\Delta SOL$  must then equal 0.92. The 8 % lithium content reduction corresponds to a 50 mAh capacity loss. On the other side, the graphite electrode has a theoretical capacity of 935 mAh. As seen in Chapter 2, its irreversibilities on first cycle correspond to 5 % of its capacity. So, 40 mAh are consumed by SEI formation, which is thus the main source of cyclable lithium loss during the first cycle.

The initial  $SOL$  of the negative electrode is known from its initial potential compared to the graphite equilibrium potential. After formation, the graphite potential is 0.5 V. Given the equilibrium potential curve of graphite (Figure 2.8a), a 0.1 %  $SOL$  is sufficient to reach this potential. The initial states of lithiation of both electrodes are summarized in Table 4.1.

### 4.3.3 Simulation results on fresh and aged cells

The parameter values that fit the  $W_2$  mass-loaded electrode models are taken as initial guess because these mass-loadings are close to the cell ones. It is necessary to adjust the electrode parameters  $w$ ,  $k$ ,  $D_1$ , and  $D_2$ . A procedure similar to the Chapter 2 is developed to find the set of parameters that fits the potentials during check-up cycles on a selected fresh cell. Experimental and obtained simulated electrode potentials of a fresh cell are qualitatively similar (Figure 4.14). For comparison, aged results of this cell (900 cycles) are also fitted with the model. Due to the lack of information about electrode stoichiometry and cyclable lithium quantity at the end of life, electrode parameters ( $w$ ,  $k$ ,  $D_1$ , and  $D_2$ ) and initial  $SOL$  are adjusted. Table 4.1 presents adjusted model parameters found and the electrode surfaces. An error below 1 % is obtained on the discharge and charge capacities for fresh and aged conditions. For both conditions, errors reach 30 % on the average potential value of negative, 4 % on the positive one and 6 % on the cell voltage one.

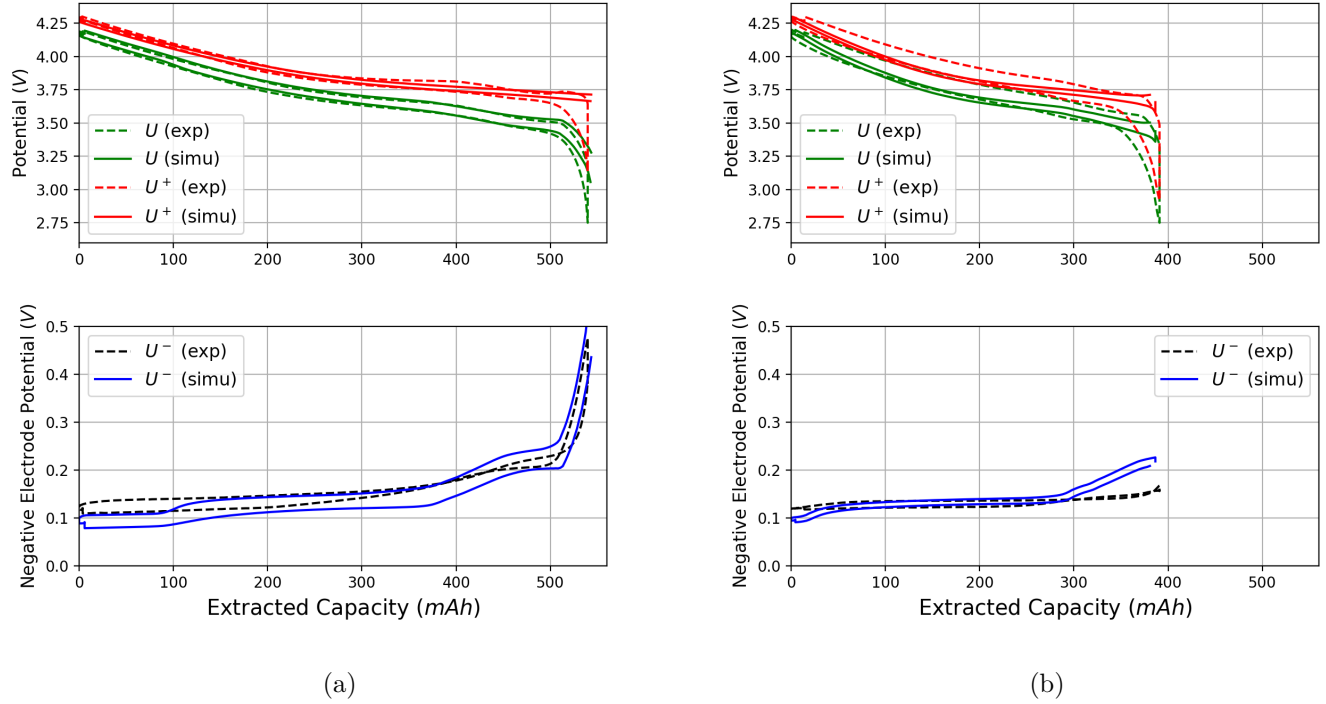


Figure 4.14: Experimental and simulated cell voltage during a check-up cycle on a fresh cell (a) and after 900 cycles (b)

Table 4.1: Parameters of the full cell model

Parameters	Symbol	Positive Electrode		Negative Electrode	
		Fresh	Aged	Fresh	Aged
Active material fraction (wt%)	$w_i$	0.89	0.56	0.93	0.93
Electrode state of lithiation for an empty cell (full)	$SOL$	0.92 (0.01)	0.98 (0.01)	0.01 (0.62)	0.1 (0.52)
Charge transfer coefficient ( $\text{mol} \cdot \text{m}^2 \cdot \text{s}^{-1}$ )	$k$	$5 \cdot 10^{-12}$		$5 \cdot 10^{-11}$	
Lithium diffusion coefficient in active material ( $\text{m}^2 \cdot \text{s}^{-1}$ )	$D_1$	$5 \cdot 10^{-10}$		$5 \cdot 10^{-13}$	
Lithium diffusion coefficient ( $\text{m}^2 \cdot \text{s}^{-1}$ )	$D_2$	$5 \cdot 10^{-11}$			
Electrode surface ( $\text{cm}^2$ )	$S$	292		361	

When fresh, 38 % of the graphite capacity are not used due to its oversize. The experimental

negative potential is smoother than the simulated one, that is to say, the graphite plateaus are not visible. As the cell assembly is different from the coin-cell one, the resulting conditions (inner pressure) are not identical. The lithiation heterogeneity during operations could be enhanced in this case, and explain the potential difference (subsection 3.3.3). For fresh conditions, adjusted parameters are close to the parameters of the porous electrodes (Chapter 2). Nevertheless the NMC charge transfer coefficient is way lower in a full cell configuration ( $5 \cdot 10^{-11} \text{ mol} \cdot \text{m}^2 \cdot \text{s}^{-1}$ ) than in the coin-cell configuration ( $5 \cdot 10^{-6} \text{ mol} \cdot \text{m}^2 \cdot \text{s}^{-1}$ ). Calendaring, resulting inner pressure, electrode structure variations or manufacturing may explain this difference.

On the aged results, some lithiums are still intercalated at the end of discharge (10 % SOL), that is to say, the quantity of cyclable lithium is not a limiting factor to the discharge capacity anymore. The fitting results indicate effectively that the active material quantity is drastically reduced at the positive electrode. In Table 4.1, the amount of working material is lowered by 37 % from fresh to aged conditions. Taking into account both electrode capacities, and their states of lithiation at the end of discharge in aged conditions, the cyclable lithium quantity has been reduced by nearly 15 % (550 to 470 mAh). The other parameters are not drastically affected by aging, but the study of electrode potentials under different C-rates should be necessary to conclude on the cell performance evolution.

To conclude, the full cell model is validated on a fresh cell, thanks to the experimental electrode potentials. Electrode parameters do not deviate strongly from coin-cell experiments. Calibrating the model to aged results shows that cyclable lithium loss is not the limiting factor to discharge performance but rather the positive material loss.

## 4.4 Aging parameter study

Aging mechanisms are not exactly known, but nevertheless, the final cell consequences are the modification of its physical parameters.

In a first approach, the cell model is used to find the parameter variations that cause some specific aging cases. The physical consistency of these parameter variations are discussed. Focus is made on graphite and NMC parameters that are involved into aging: the parameters relative to the quantity of active materials ( $w_{gr}$ ,  $w_{nmc}$ ), the SEI resistance ( $r_{sei}$ ), the graphite electrode structure and particle morphology ( $\epsilon$ ,  $\tau$ ,  $r$ ,  $n$ ), and the SEI thickness corresponding to cyclable lithium loss ( $\delta_{sei}$ ). SEI resistance and thickness are not correlated in this first approach.

### Study Protocol

The model runs a C/2 discharge, initially fully charged. Parameters are from the calibrated fresh cell, presented in Table 4.1. Each parameter is adjusted independently to find the right value that corresponds to a specific aging case. Each fitting parameter corresponds to the nearest local

minimum discovered from the reference value of the calibrated model. Four aging cases are tested: an impedance rise which corresponds to a 30 mV average cell voltage loss during discharge, and a 10, 30 and 50 % loss of the initial discharge capacity.

Table 4.2: Simulated capacity losses and impedance rise fitted by adjusting different model parameters

	Parameter	Symbol	Fresh	-10 %, capacity loss	-30 % capacity loss	-50 % capacity loss	-30 mV
Cell capacity variation	Negative active material fraction (wt%)	$w_{gr}$	0.92	0.54	0.46	0.28	0.78
	Corresponding negative interfacial specific surface ( $m^2 \cdot m^{-3}$ )	$a_{gr}$	$14 \cdot 10^4$	$8.1 \cdot 10^4$	$7 \cdot 10^4$	$4.2 \cdot 10^4$	$12 \cdot 10^4$
	Positive active material fraction (wt%)	$w_{nmc}$	0.91	0.72	0.65	0.41	0.40
	Corresponding positive interfacial specific surface ( $m^2 \cdot m^{-3}$ )	$a_{nmc}$	$6.1 \cdot 10^5$	$3.5 \cdot 10^5$	$3.0 \cdot 10^5$	$2 \cdot 10^5$	$2 \cdot 10^5$
	Cyclable loss in corresponding SEI thickness (nm)	$\delta_{sei}$	0	354	1062	1770	-
Graphite particles	SEI resistance ( $\Omega \cdot cm^2$ )	$r_{sei}$	0	3500	4500	6000	400
	Particle radius ( $\mu m$ )	$r$	8	150	No value found	No value found	35
	Particle shape	$n$	2	1	0.1	No value found	No value found
Graphite electrode structure	Porosity	$\epsilon$	35 %	1 %	0.8 %	0.6 %	0.6 %
	Bruggeman number	$br$	1.5	4.2	4.3	4.5	4.5
	Tortuosity corresponding to the Bruggeman number ( $\epsilon = 0.35$ )	$\tau$	1.69	29	32	40	40

Parameters	Symbol	Value
Density ( $\text{kg} \cdot \text{m}^{-3}$ )	$\rho_{\text{sei}}$	1690
Molar mass ( $\text{g} \cdot \text{mol}^{-1}$ )	$M_{\text{sei}}$	162
Lithium mol consumed per SEI mol formed	$Z_{\text{sei}}$	2

Table 4.3: SEI properties (from [4])

### Parameter relative to cell capacity

Some parameters have an impact either on the cyclable lithium quantity or electrode capacity : the active material in electrodes or the cyclable lithium consumed by SEI formation.

The active material quantities present in both electrodes may influence both the cell discharge capacity and its impedance. Table 4.2 shows the active material quantity variation that corresponds to the four aging case scenarios. The graphite active material reduction must be large in all cases because the loss must overcome graphite oversizing (nearly 38 % does not work). These losses seem not physically acceptable. The NMC capacity is directly correlated to the cell capacity, and so there is a lower loss of NMC than graphite to reach the same aging state.

For both electrodes, reducing the amount of active material lowers also the electrochemical surface. It decreases the intercalation kinetics and contribute also to the discharge capacity shrink via an impedance rise. The developed surface stays in the same order of magnitude through the different aging scenarios.

The quantity of cyclable lithium present in the cell can be derived from the electrode *SOL* and capacities. Parasitic reactions as SEI formation consume these cyclable lithiums to form a passive layer. To go further in the analysis, some assumptions are made to link SEI quantities to a cyclable lithium loss:

- SEI is a non-porous layer, which is formed homogeneously on all electrochemically active surfaces.
- The particle shape has no influence on the layer structure.
- The SEI thickness is uniform through the cell.

Then, the SEI is described by its thickness,  $\delta_{\text{sei}}$ , which corresponds to a  $\Delta Q$  capacity loss:

$$\delta_{\text{sei}} = \frac{M_{\text{sei}}}{\rho_{\text{sei}} Z_{\text{sei}} \cdot a L_{gr} S_{gr} \cdot F} \cdot \Delta Q \quad (4.5)$$

with  $\rho_{\text{sei}}$  the density of SEI ( $\text{kg} \cdot \text{m}^{-3}$ ),  $Z_{\text{sei}}$  the mol of Li consumed per mol of SEI products formed,  $M_{\text{sei}}$  the molar mass of SEI ( $\text{g} \cdot \text{mol}^{-1}$ ), all estimated in [180, 4] and written down in Table 4.3.

Given [Equation 4.5](#), SEI should be 354, 1062, and 1770 nm thick respectively for 10, 30, and 50 % discharge capacity losses. These orders of magnitude seem physically acceptable but a bit larger than experimentally found [[143](#)]. A SEI layer thicker than 1  $\mu\text{m}$  is rarely expected. To explain these large values, SEI may be physically unstable above a given thickness and decomposes in electrolyte, or another capacity loss phenomenon is complementary to SEI growing mechanism.

### Parameters relative to the graphite particles

The shapes, sizes, and surface of graphite particles may evolve through aging, due to fractures, cracks, or agglomerations. Variations on these parameters do not consume cyclable lithium, but modify the cell discharge capacity and impedance at  $C/2$ . As seen in [Table 4.2](#), variations of shape and size that can cause more than 10 % capacity loss are too large to be physically consistent. Their real impacts are then rather limited to the aging performance of the cell. Nevertheless, changes of particle properties could be more visible at larger C-rates, where any cell impedance rise is significant.

On graphite surface, the SEI resistance impacts the intercalation kinetics and increases the cell impedance. The  $r_{\text{sei}}$  values necessary to obtain the 10, 30, and 50 % discharge capacity losses are too high to be physically acceptable. According to the literature, a resistance at a maximum  $1000 \Omega \cdot \text{cm}^2$  is expected from electrochemical impedance spectroscopy (EIS) analysis [[197](#), [198](#)]. However, the cell voltage loss can be explained only with the SEI resistance (-30 mV with  $400 \Omega \cdot \text{cm}^2$ ).

To compare with, SEI is assumed to have a ionic conductivity of  $5 \cdot 10^{-6} \text{ S} \cdot \text{m}^{-1}$  [[4](#)]. In this case, a 3500 and  $400 \Omega \cdot \text{cm}^2$  resistances are due respectively to a 1700 and 200 nm thick layer.

### Parameters relative to the electrode structure

The graphite structure evolves during aging, causing power loss, but no cyclable lithium loss. The porosity and the Bruggeman number of the graphite electrode decrease to explain the losses of capacity in discharge ([Table 4.2](#)). The electrode tortuosity could be obtained via the Bruggeman number (c.f. [Equation 2.18](#)). A Bruggeman number rise corresponds to a larger tortuosity.

The value of these electrode structure parameters to fit the losses are extreme. To explain a loss of 10 % of the capacity, a porosity of 1 % is necessary. That is to say, all the pores are almost clogged. In regard to the four aging cases, the tortuosity must be greater than 29 to explain a noticeable loss of capacity.

### Summary

All parameter evolutions play a role in aging mechanisms. It is possible to size the different aging consequences, impedance rise and capacity loss, by adapting parameters of the cell model. Cyclable lithium loss via SEI thickness growth and active material losses have physically-sized

orders of magnitude that correspond to the observed aging consequences. On the opposite, the particle modification and SEI resistance rise do not physically predict these losses by themselves. Nevertheless these parameters surely evolve and impact cell performance at larger C-rates. The electrode structure modifications do not affect easily the cell impedance or the discharge capacity but extreme values could drastically limit lithium transport and may explain the sudden discharge capacity drop via a pore-clogging mechanism.

To go further, parameters compete each other on aging mechanisms. Aging impacts results from a combination of all these parameter variations, which are beneficial or not. Moreover, the stoichiometry window of the both electrode could be shift through operations, resulting in a less efficient use of the amount of cyclable lithiums present [125].

## 4.5 Conclusion

Aging mechanisms are due to electrode modifications, essentially SEI formation at the graphite side, and active material loss at the NMC side. An experimental aging campaign have highlighted some phenomena: the 2-step mechanisms for discharge capacity loss along cycles, the capacity recovery at low C-rate and sometimes a sudden major discharge capacity loss. The discharge capacity loss is a 2-step mechanism: a first one, quadratic function of time, and a second one, linear function of time.

A full cell model is calibrated to the experimental data of a fresh and cycled cell. By adjusting the parameters of the performance model, the possible origins of the different losses are quantified. The SEI and positive material loss play a fundamental role in cell aging in capacity fade and power loss.

The goal of the next chapter will be to model the different aging mechanisms that were noticed in the experimental campaign.

# Chapter 5

## Aging models of the graphite electrode

### Contents

---

<b>5.1</b>	<b>Primary aging source : the Solid Electrolyte Interface . . . . .</b>	<b>110</b>
5.1.1	A mechanistic approach for SEI modeling . . . . .	110
5.1.2	The SEI analytical models: limited and unlimited growth mechanism . .	112
5.1.3	Fits of experimental capacity fade during cycling . . . . .	115
5.1.4	Implementation into the porous electrode model . . . . .	118
5.1.5	A possible dissolution mechanism . . . . .	122
5.1.6	Conclusion . . . . .	125
<b>5.2</b>	<b>Secondary aging source : the lithium-plating reaction . . . . .</b>	<b>125</b>
5.2.1	Lithium plating reaction model . . . . .	125
5.2.2	The pore clogging mechanism . . . . .	129
5.2.3	Competition between lithium-plating and SEI . . . . .	132
<b>5.3</b>	<b>Conclusion . . . . .</b>	<b>133</b>

---

In this chapter, aging models of the graphite electrode are developed and implemented into the full cell model (Chapter 4). These models are physics-based and validated with the experimental data previously shown. They describe and quantify discharge capacity losses through cycling, capacity recovery through low C-rate cycles, and the sudden appearance of large capacity losses. These losses are explained through two major mechanisms which happen within the graphite electrode: the evolution of the SEI and the occurrence of lithium plating.

## 5.1 Primary aging source : the Solid Electrolyte Interface

The SEI evolution is the main source of cyclable lithium loss in lithium-ion batteries [2]. A SEI growing mechanism is postulated, based on previous published studies. On a first approach, analytical models of this mechanism are built and calibrated on the experimental capacity loss through cycles. Local conditions within electrode such as overpotentials or solvent concentration can also influence SEI evolution. A local SEI model is then implemented in the full cell model, based on the analytical model parameters. The SEI heterogeneities can thus be observed with the same modeling framework as the one used for the graphite lithiation study (Chapter 3).

### 5.1.1 A mechanistic approach for SEI modeling

Different representations are found in literature to deal with SEI influence. The first approach was developed by PELED *et al.* in 1979 [199]. The SEI evolution is described as the growth of a passivation layer on a flat metallic lithium surface in a non-aqueous solution. Two growing modes can be derived according to whether the passivation layer is an electrical conductor or an ionic conductive media. In the first case, the electrolyte is reduced on the SEI surface, while in the second case, the electrolyte penetrates the porous layer to react at the lithium/SEI interface. Whatever the case, the SEI growth can be limited by the reaction kinetics or by the species or charge transport through the layer.

#### Actual SEI representation

In graphite electrode, the SEI is an electrical insulator and a poor ionic conductor [136], composed of various reduced electrolyte components, which come from salt, solvent, or additives [200]. AGUBRA *et al.* describe the different reactions occurring at graphite/electrolyte interface that could lead to SEI components [201]. By-products of these reactions generally precipitate in solid compounds. One or more electrons can be exchanged during these reactions, cyclable lithium may be consumed. Experimental observations demonstrate the location of these reactions [141, 202, 145], but not clearly the mechanisms [203].

In case where the reaction consumes cyclable lithium and is located at the graphite/SEI interface, the SEI growth is generally decomposed into the following steps:

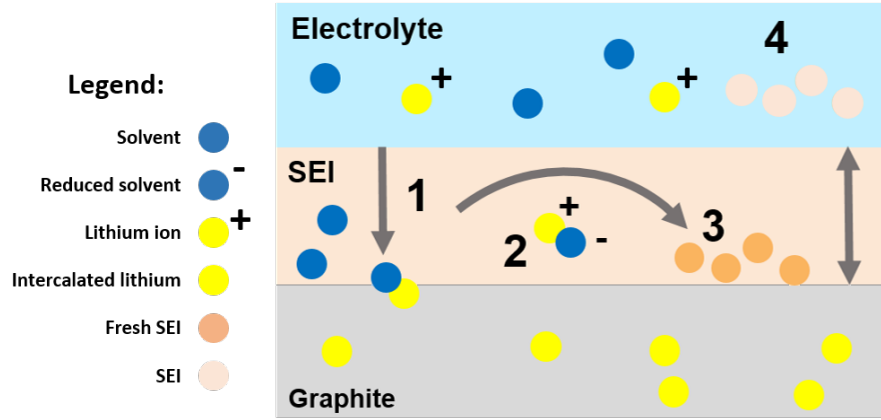


Figure 5.1: SEI growth principles

- An element  $X$  of the electrolyte (solvent, additives,...) diffuses through the porous structure of SEI (Step 1 in Figure 5.1).
- The reduction of  $X$  with  $z_{\text{sei}}$  electron(s) from intercalated lithiums in graphite gives a lithium ion and a reduced electrolyte element  $X^{n-}$  (Step 2 and Equation 5.1).
- The element  $X^{n-}$  precipitates with  $z_{\text{sei}}$  lithium ion(s) into a solid compound which sticks on the graphite surface (Step 3).
- The SEI presumably reaches a thickness limit for which mechanical decomposition and dissolution occur (Step 4).

The reduction and precipitation reactions are synthetized as:



### Former SEI models

Different mathematical models exist in literature to predict SEI growth and its consequences on the graphite electrode operability.

A preliminary case study was proposed by DARLING *et al.* in 1998 [204]. Focus is made on the side reactions at a  $\text{LiMn}_2\text{O}_4$  electrode that are similar to the SEI parasitic reactions. Reactions are modeled by the Tafel's law. CHRISTENSEN *et al.* studied the impact of SEI resistance on the graphite behavior [205]. Then, in a second publication, the SEI evolution is modeled according to a 1D species transport model, and growth through electronic transport limitation [206]. Moreover, the consequences of these parasitic reactions are studied at the cell level through the evolution of the stoichiometry operability window of the two electrodes [125].

A kinetics limited growing model of SEI is proposed by RAMADASS *et al.*. The model shows that the cyclable lithium quantity decreases and the SEI resistance increases through cycles [207].

This study mainly focuses on the charge of a cell (graphite lithiation) in a porous electrode model framework. The model predicts a quite linear loss of capacity through cycles. RAMASAMI *et al.* also develop a capacity fade model based on interface kinetics, during storage conditions. Intercalated lithiums reduce electrolyte species at the graphite surface and doing so, the model predicts the graphite electrode delithiation and potential rise [208]. The simulated results fit quite well the experimental data up to 300 hours of storage and losses are predicted up to five years.

The SEI growing mode due to transport limitation is explored by PLOEHN *et al.* [209]. The loss of cyclable lithium during calendar conditions at constant potential is predicted by an analytical equation derived from the Fick's law. The SEI growth is then a square root function of time. Remarkable correlations are found with data from BROUSSELY *et al.* [175].

SAFARI *et al.* coupled the transport through the SEI and the reaction kinetics at the graphite/SEI interface [180]. These mechanisms are implemented into a single particle model [27]. Transport and kinetics limitations are used to explain two growing modes: a time linear loss when kinetics is the limit factor, quadratic otherwise.

Recently, a framework of analytical equations has been developed by PINSON *et al.* [93]. Equations are based on the growing mechanism previously presented (Figure 5.1).

### 5.1.2 The SEI analytical models: limited and unlimited growth mechanism

Physics-based models developed by PINSON *et al.* predict capacity fade in lithium-ion batteries considering the SEI as the primary cyclable lithium loss [93]. These models provide the orders of magnitude of the SEI parameters for a low computational cost.

#### Unlimited growth mechanism

Some assumptions are made on the SEI growing mechanism, and they concern the layer geometry, kinetics, and transport properties. The SEI forms homogeneously over the entire graphite surface within the electrode. It is thin enough compared to the particle radius so its growth is reduced to its thickness variation,  $\delta_{\text{sei}}$ :

$$\frac{\partial \delta_{\text{sei}}}{\partial t} = z_{\text{sei}} \frac{M_{\text{sei}}}{\rho_{\text{sei}}} \cdot J \quad (5.2)$$

where  $z_{\text{sei}}$  is the quantity of lithium consumed per SEI formed,  $M_{\text{sei}}$ , the molar mass of SEI ( $\text{g} \cdot \text{mol}^{-1}$ ),  $\rho_{\text{sei}}$ , the density of SEI ( $\text{kg} \cdot \text{m}^{-3}$ ), and  $J$  represents the flux density ( $\text{mol} \cdot \text{m}^{-2} \cdot \text{s}^{-1}$ ) of the component  $X$  through the SEI surface. The volume variations of the active material are neglected. Thus, the developed graphite surface, named  $A$  ( $\text{m}^2$ ), where the SEI is formed, remains constant whatever the lithiation state. Moreover, the growth rate is assumed to be independent of graphite properties (potential and lithium concentration). At the graphite/SEI interface, the

reaction kinetics is directly proportional to the concentration of  $X$ :

$$J = k_{\text{sei}} c_X \quad (5.3)$$

where  $k_{\text{sei}}$  is the reaction rate ( $\text{m} \cdot \text{s}^{-1}$ ) and  $c_X$  is the concentration of  $X$  at the graphite/SEI interface ( $\text{mol} \cdot \text{m}^{-3}$ ). The  $X$  species come from the bulk of electrolyte, diffuse through the SEI thickness, and react at the interface. As no accumulation is supposed inside the SEI layer, a linear approximation of the Fick's law is made for transport of  $X$ :

$$J = \frac{D_X}{\delta_{\text{sei}}} (c_X^0 - c_X) \quad (5.4)$$

<sup>1</sup>where  $c_X^0$  is the concentration of  $X$  in the bulk of electrolyte and  $D_X$  the effective diffusion coefficient of  $X$  through the porous structure of the SEI.

The three equations, [Equation 5.2](#), [Equation 5.3](#), and [Equation 5.4](#), correspond respectively to the SEI growth, the reaction kinetics, and the transport (steps 3, 2, and 1 in [Figure 5.1](#)). It is assumed that the SEI initial thickness is null. Therefore, the SEI thickness variation can be expressed analytically versus time:

$$\delta_{\text{sei}} = \sqrt{2 \frac{M_{\text{sei}} c_X^0 D_X}{\rho_{\text{sei}}} \cdot t + \left( \frac{D_X}{k_{\text{sei}}} \right)^2} - \frac{D_X}{k_{\text{sei}}} \quad (5.5)$$

The loss of the cyclable lithium,  $\Delta Q$  (in mAh), corresponding to the SEI formed is then written as:

$$\Delta Q = -z_{\text{sei}} F \cdot \frac{\rho_{\text{sei}}}{M_{\text{sei}}} \cdot A \cdot \delta_{\text{sei}} \quad (5.6)$$

When time tends to zero, a Taylor expansion on [Equation 5.5](#) gives:

$$\Delta Q \sim -z_{\text{sei}} F \cdot A k_{\text{sei}} c_X^0 t \quad (5.7)$$

Initial cyclable lithium loss is a linear function of time, which only depends on active material surface,  $X$  concentration in electrolyte and kinetics. The initial linear loss dependency to the electrode surface is confirmed experimentally [\[38\]](#). On the opposite, when time becomes large, the substitution of the SEI layer in [Equation 5.6](#) with the Taylor expansion of [Equation 5.5](#) gives:

$$\Delta Q \sim -z_{\text{sei}} F \cdot \frac{\rho_{\text{sei}}}{M_{\text{sei}}} A \left( \sqrt{2 \frac{M_{\text{sei}} c_X^0 D_X}{\rho_{\text{sei}}} \cdot t} - \frac{D_X}{k_{\text{sei}}} \right) \quad (5.8)$$

which is a square root function of time.

In the case where transport is the limiting factor ( $k_{\text{sei}} \gg \frac{D_X}{\delta_{\text{sei}}}$ ), only the first term of Equation

---

<sup>1</sup>The notation  $c$  in [\[93\]](#) refers to the solvent concentration in the bulk, named  $c_X^0$  in this document. Thus, the difference  $\Delta c$  corresponds to  $c_X^0 - c_X$ .

Equation 5.5 is conserved, showing a square root time dependency.

$$\Delta Q \sim -z_{\text{sei}} F \cdot \frac{\rho_{\text{sei}}}{M_{\text{sei}}} A \sqrt{2 \frac{M_{\text{sei}} c_X^0 D_X}{\rho_{\text{sei}}} \cdot t}$$

In the other case, when kinetics is a limiting factor ( $k_{\text{sei}} \ll \frac{D_X}{\delta_{\text{sei}}}$ ), Equation 5.7 is obtained again. The loss becomes a linear function of time. These finding agree with numerical works from SAFARI *et al.* [4].

### Limited growth mechanism

Experimentally, SEI is suspected to be mechanically unstable or to be dissolved by acid impurities [177]. So, above a given thickness, SEI continues to be formed at the interface, but outer layers delaminates into the electrolyte. The cyclable lithium loss becomes then independent of the SEI thickness. Replacing Equation 5.6 in Equation 5.2 shows the link between the cyclable lithium loss and the flux density of  $X$ ,  $J$ :

$$\frac{\partial \Delta Q}{\partial t} = -z_{\text{sei}} F A \cdot J \quad (5.9)$$

As the interface properties are no longer evolving, the growing rate  $J$  is constant, and that underlines the time linear dependency of cyclable lithium loss.

The SEI dissolution can be modeled by an additional loss term in the growing Equation 5.2. This term should be an increasing function of the SEI thickness with a maximum value reached at  $\delta_{\text{sei}}^{\text{lim}}$ , the thickness limit. A simple case is expressed in Equation 5.10 where  $t_0$  corresponds to a characteristic time constant of the growing mechanism [93]:

$$\frac{\partial \delta_{\text{sei}}}{\partial t} = \frac{M_{\text{sei}}}{\rho_{\text{sei}}} \cdot J - \frac{\delta_{\text{sei}}}{t_0} \quad (5.10)$$

In Equation 5.10, the SEI growth stops when the thickness reaches a value such that the second member cancels the first member of this equation. In the case where kinetics is infinitely fast, an analytical solution is possible. PINSON *et al.* suggest the following one:

$$\Delta Q = -z_{\text{sei}} F \cdot \frac{\rho_{\text{sei}}}{M_{\text{sei}}} \cdot A \sqrt{\frac{M_{\text{sei}} c_X^0 D_X}{\rho_{\text{sei}}} \cdot t_0 \left( \frac{t}{t_0} + \ln \left( 1 + \sqrt{1 - \exp\left(\frac{-2t}{t_0}\right)} \right) \right)} \quad (5.11)$$

This analytical solution shows a cyclable lithium loss which is a square root function at short times ( $t \ll t_0$ ) and linear at long times ( $t \gg t_0$ ).

### 5.1.3 Fits of experimental capacity fade during cycling

The analytical growth laws (Equation 5.6 and Equation 5.11) are compared with the experimental discharge capacity loss through cycling, presented in Chapter 4. The discharge capacity corresponds to the capacity extracted during a cell discharge at C/2. In a first approach, the discharge capacity loss is assumed to be caused only by the cyclable lithium loss from the SEI growth.

#### SEI assumptions

The ethylene carbonate (EC) reduction is taken as the representative SEI formation reaction, which is commonly found in literature:



Reaction Equation 5.12 is a two-electron reduction process ( $z_{\text{sei}} = 2$ ), which gives lithium ethylene dicarbonate,  $(\text{CH}_2\text{OCO}_2\text{Li}_2)_2$  and ethylene gas, not considered here. The supposed steps of the reduction are discussed in literature [4, 137, 210, 211]. Molar mass and density of SEI are found in [212] and were presented in Table 4.3 in Chapter 4. The solvent concentration ( $c_X^0$ ) is taken at  $4.5 \text{ mol} \cdot \text{L}^{-1}$  [4].

The developed surface,  $A$ , is calculated given the particle representation (cylinder), the mass-loading, the quantity of active material, and the electrode surface of the experimental graphite electrode (Table 4.1 in Chapter 4)

#### Fit procedure

As seen in Chapter 4, two successive aging phases occur through cycling. Up to 200 cycles, the discharge capacity loss is proportional to the square root of time. Beyond this value, the loss becomes linear. The thickness limited growth law (Equation 5.11) predicts this two-phase behavior. This law is thus fitted on all the cycles, adjusting two parameters,  $D_X$  and  $t_0$ .

By contrast, the unlimited SEI growth mechanism (Equation 5.5) predicts a linear loss followed by a quadratic loss. In addition, the adjusted model has shown that the cyclable lithium is the limiting factor of the discharge capacity at the beginning, but not at the end of life (see subsection 4.3.3). In this work, we propose to adjust this law on the first 200 cycles, which represent the quadratic loss phase, with two parameters ( $k_{\text{sei}}$  and  $D_X$ ).

A procedure is developed using Matlab to fit with the growth laws the capacity losses from all the experimental cells. An example of the fit of the two models on a selected cell is presented Figure 5.2a. Average values of adjusted parameters are shown in Table 5.1. Whatever the law considered, the average diffusion coefficient ( $D_X$ ) stays in the same order of magnitude:  $10^{-20} \text{ m}^2 \cdot \text{s}^{-1}$ . In both cases, the SEI growth is diffusion-controlled.

In Figure 5.2b, the thickness limited growth law converges to a thickness value at about of

Parameter	Symbol	Growth law, fit limited 200 cycles (Equation 5.6)	Thickness limited growth law (Equation 5.11)
Solvent diffusion coefficient ( $\text{m}^2 \cdot \text{s}^{-1}$ )	$D_X$	$2.7 \cdot 10^{-20}$	$1.9 \cdot 10^{-20}$
Reaction constant ( $\text{mol} \cdot \text{m}^2 \cdot \text{s}^{-1}$ )	$k_X$	$7.1 \cdot 10^{-12}$	-
Time limit in days (cycle number)	$t_0$	-	35 days (214 cycles)
Average SEI thickness at 900 cycles (nm)	$\delta_{\text{sei}}$	600	130
Cyclable lithium loss at 900 cycles	$\Delta Q$	18 %	25 %
Maximum error	$\zeta$	2 %	1 %

Table 5.1: Fitting results on SEI growing models

130 nm after 200 cycles (about 30 days) for the selected cell. The thickness limit appears low compared to literature (few hundred nanometers). The unlimited growth law gives a 600 nm SEI thick at 900 cycles, which is physically feasible. In both case, under 200 cycles, the error remains very small, 2 % and 1 %, respectively for the unlimited growth law and the thickness limited one. At large time, if the cyclable lithium is the determining factor of the cell capacity, we can conclude than the limited growth model is the accurate one.

### Model limit: the positive electrode influences

The SEI growth is the driving force of the cyclable lithium loss in the system, but it is not always correlated to the discharge capacity loss. The discharge capacity of the cell is given by the amount of cyclable lithium which can intercalate into the positive electrode. The cell capacity is thus determined the limiting factor, either by the positive electrode capacity or the cyclable lithium quantity.

In the previous Chapter (subsection 4.3.3), the adjusted cell model on the last discharge at 900 cycles features a 37 % loss of the positive active material compared to fresh conditions and a resulting 10 % lithium stoichiometry excess at the negative. The positive capacity is lower than the quantity of cyclable lithium, becoming the determining factor of the cell capacity.

At 900 cycles, the resulting lithium content corresponds to 15 % cyclable lithium loss. In one hand, the SEI limited growth law (Equation 5.6) predicts a 18 % cyclable lithium loss (Figure 5.2a),

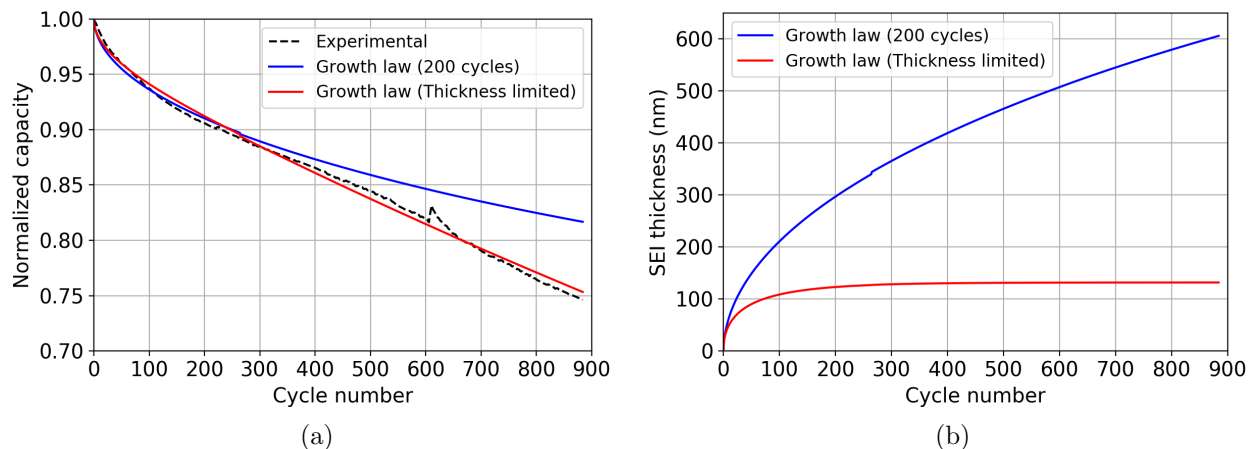


Figure 5.2: Fits of SEI growth models : simulated and experimental normalized capacity (a) and simulated SEI thickness evolutions (b) on a selected cell

which is in the same order of magnitude. On the other hand, the thickness limited growth law, by construction, predicts a 25 % cyclable lithium loss, which overestimates experimental conclusions. These observations imply that the mechanism of dissolution at a limited thickness is not the favored one to analyze these experimental results in a full cell.

During the 200 first cycles, the square root dependency of the cell capacity loss suggests that the cyclable lithium loss via the SEI growth is the predominant factor. As active materials at the positive are in excess during this first cycles compared to cyclable lithium, their loss does not induced a discharge capacity fade. When the capacity of the positive electrode is under the cyclable lithium quantity, it limits the cell capacity. Figure 5.3 decomposes this two-phase mechanism and a similar conclusion and diagram can be found in [213]. The two linear behaviors noticed in this aging phase: impedance increase and capacity loss, could therefore be link to the loss of the positive.

The positive electrode influence is beyond the scope of this thesis, but its exact influence on capacity fade has been studied in multiple references [179, 214]. The active material surface is perhaps blocked with some side effect deposits, which reduce the accessible capacity. Anyway, the dissolution of positive material into the electrolyte is often used to explain experimental results, especially when metal oxide materials are involved [213, 214, 215, 187].

### Perspectives with calendar aging fits

The growth laws may also be fitted on experimental cell capacity losses measured along calendar aging (subsection 4.2.3), for which no positive loss are observed. The fitting results will show the influence of the electrode SOL on the reaction constant  $k_{\text{sei}}$  and diffusion coefficient  $D_X$ . However, the low number of experimental data points does not allow a correct fitting procedure. The influence of state of charge and temperature on SEI growth is studied by SINHA *et al.* [147]: a

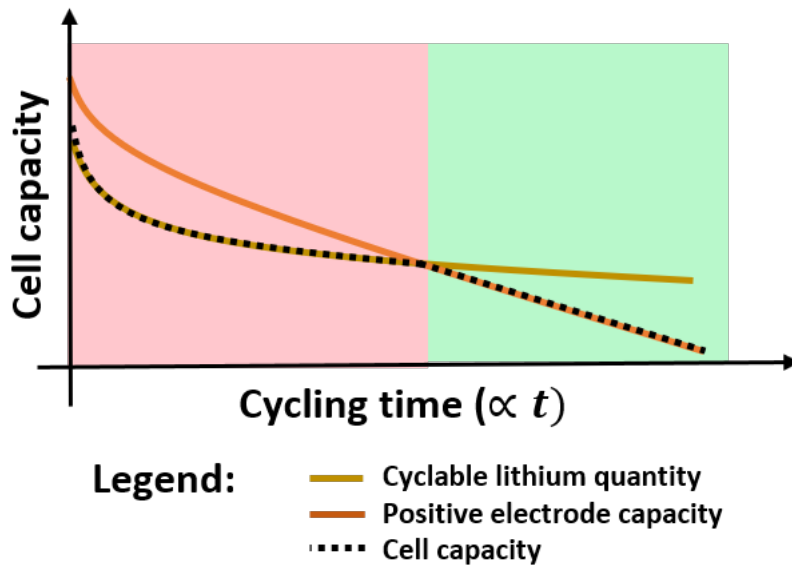


Figure 5.3: Cell capacity decomposed as cyclable lithium loss and positive material loss

high SOC and a high temperature accelerate cyclable lithium loss.

SEI parameters have been found by experimental fits and show a transport-limited growth under 200 cycles (limited or unlimited growth). Long time aging need further investigation to conclude. Physical parameters can now be used into a SEI model, implemented in the porous electrode framework.

#### 5.1.4 Implementation into the porous electrode model

The 0D SEI growth laws are only function of time, regardless of operations. In the electrode, the local electrode potential also influences the SEI production. PINSON *et al.* adapted the SEI growth mechanism on a porous electrode model [93], using the SEI parameters found by LIU *et al.* [216]. In this thesis, the full cell model calibrated in Chapter 4 is used to locally implement these mechanisms, with kinetics and transport properties derived from the unlimited SEI growth law. The electrode conditions affect the growing mechanism.

##### 5.1.4.1 Model development

The following equations characterize the SEI growth and are added to the porous electrode model. At the graphite/SEI interface, the total current is subdivided into intercalation current ( $i_n$ ) and parasitic current ( $i_p$ ), the latter corresponding to the charge transfer of the SEI reaction:

$$i_t = i_n + i_p \quad (5.13)$$

As the reaction is firstly supposed irreversible, the parasitic current is modeled by a Tafel's law, which depends on the amount of solvent at interface.

$$i_p = -Fk_{\text{sei}} \left( \frac{c_X}{c_X^0} \right)^{\alpha_{\text{sei}}} \exp \left( -\frac{(1 - \alpha_{\text{sei}})F}{RT} \eta_p \right) \quad (5.14)$$

A dependence on the amount of intercalated lithium present at the surface can be also relevant [93]. In a first approach, we consider this contribution negligible compared to the solvent concentration at interface [4].

Overpotentials of the intercalation ( $\eta$ ) and parasitic ( $\eta_p$ ) reactions are modified to take into account the ohmic loss related to the low ionic conductivity of SEI:

$$\eta = \phi_1 - \phi_2 - \frac{\delta_{\text{sei}}}{\kappa_{\text{sei}}} i_t - E_{gr}^0 \quad (5.15)$$

$$\eta_p = \phi_1 - \phi_2 - \frac{\delta_{\text{sei}}}{\kappa_{\text{sei}}} i_t - E_{\text{sei}}^0 \quad (5.16)$$

where  $\kappa_{\text{sei}}$  is the ionic conductivity of SEI and  $E_{\text{sei}}^0$  is the equilibrium potential associated to SEI formation. This equilibrium potential is not well-defined, but it has a strong influence on the current value. In literature, SEI formations are noticed from 1 V to 0.2 V vs Lithium. A first guess is taken at 0.45 V, which is an average value of common modeling studies.

In case of lithium plating reaction (Equation 5.1), the growing rate of the SEI thickness is given by the parasitic current:

$$\frac{d\delta}{dt} = -\frac{i_p}{z_{\text{sei}}F} \frac{M_{\text{sei}}}{\rho_{\text{sei}}} \quad (5.17)$$

The parasitic current also gives the value of the electrolyte concentration at the interface:

$$i_p = -F \frac{D_X}{\delta_{\text{sei}}} (c_X^0 - c_X) \quad (5.18)$$

The SEI parameters  $D_X$  and  $k_{\text{sei}}$  are taken from the fitting results of the SEI growth law (Table 5.1) and an initial 5 nm SEI thickness is presumed.

#### 5.1.4.2 Global results

Simulations of the cycling conditions are run with the cell model including the SEI growth model. As a reminder, the cells have performed cycles composed of a full charge (C/2 and then a floating at 4.2 V until C/50), 30-minute rest and a full discharge at C/2.

The simulated discharge capacity is compared with experimental results. The loss is underestimated (Figure 5.4a). This phenomenon is also observed by PINSON *et al.* in their study [93]. Another aging phenomenon, positive active material loss, is necessary to fit the total capacity loss,

but the quadratic tendency is conserved.

The SEI growth is promoted during low potential conditions, that is to say, almost all the time, except at the end of discharge (Figure 5.4b). The potential of the graphite electrode is essentially low and favor SEI production. In Figure 5.4b is displayed the evolution of the average thickness of SEI as well as the negative electrode potential during the first cycle. As expected, the growing rate equals zero at a full discharge state.

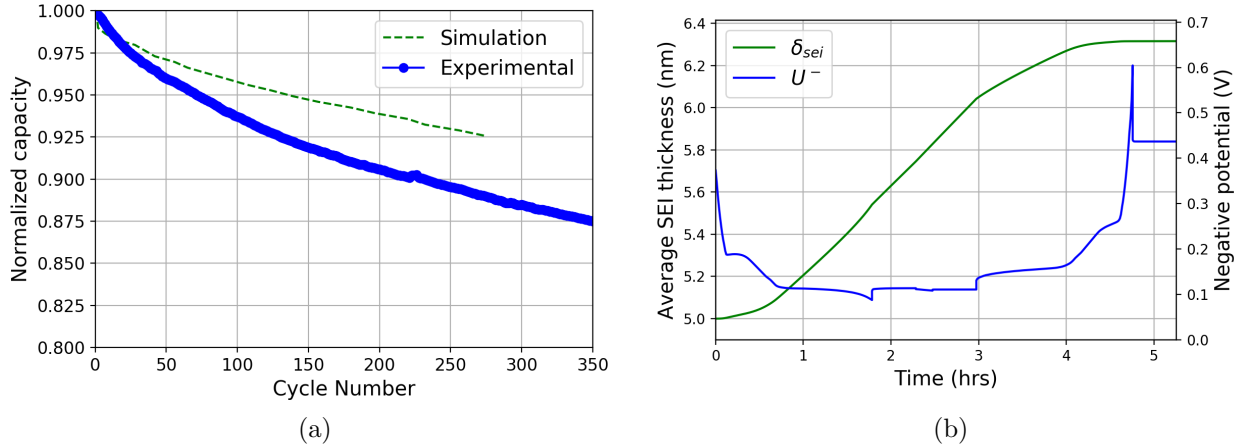
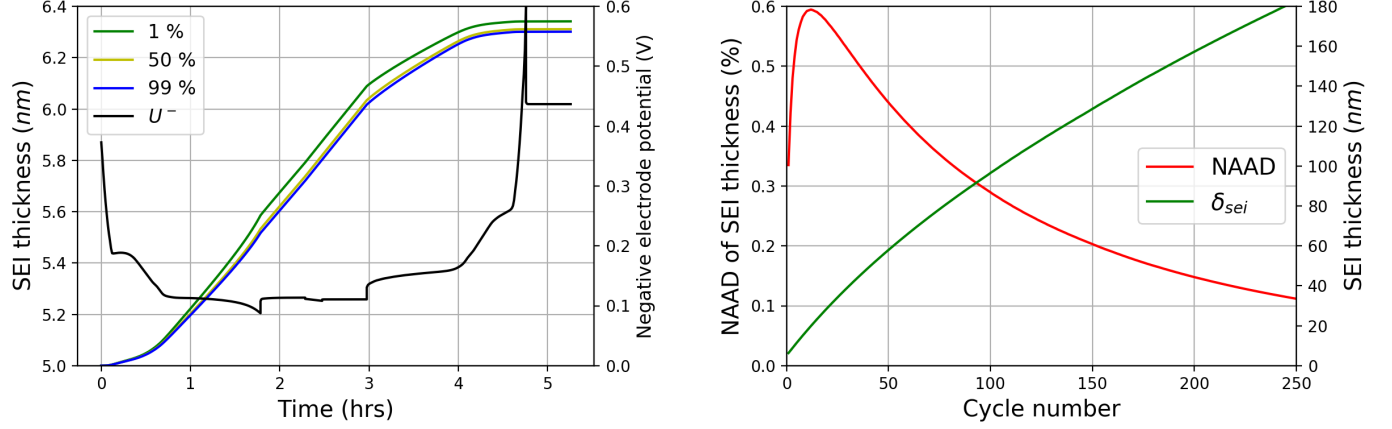


Figure 5.4: Experimental and simulated normalized discharge capacity (a) and simulated average SEI thickness and negative potential during the first cycle at  $C/2$  (b)

### 5.1.4.3 Local results

The local SEI thickness varies between the current collector and the separator. During the first cycle, Figure 5.5a shows the local SEI thickness at 1, 50 and 99 % electrode's depth from the separator. The SEI growth is a bit enhanced close to the separator due to locally higher overpotentials predicted, but overall SEI thickness remains homogeneous. A NAAD value of the SEI thickness ( $\delta_{sei}$ ) is calculated as explained in Chapter 3. The NAAD of  $\delta_{sei}$  stays low through cycles (maximal 0.6 % at 10 cycles in Figure 5.5b). The maximal heterogeneity of 0.6 % at 10 cycles represents less than a 0.1 nm variation along cell thickness, which is less than an atomic layer. Thus, aging is completely uniform through the electrode. This results is explained by the model homogeneous characteristics, the set of parameter choosen, and cycling conditions. To go further, TAHMASBI *et al.* investigates evolution of the span of a SEI thickness distribution on a single particle model [217]. Their simulations indicate that the distribution become narrower as the cell ages. Indeed, due to the single particle approach, the surface overpotential is equal for all the thickness in the SEI distribution.



(a) Simulated SEI thickness at 1 %, 50 %, and 99 % inside electrode from separator during first cycle (b) Simulated NAAD and average thickness of SEI through cycling

Figure 5.5:

#### 5.1.4.4 SEI distribution on a particle size distribution model

As shown in Chapter 3, the one-particle size model has a rather homogeneous behavior, and that causes the SEI distribution to be smoothed. To bring some heterogeneity sources that may influence SEI growing rate distribution, the model has been adapted to the continuous particle size distribution model. Particles lithiate differently over their size (NAAD  $\sim 42\%$  in Chapter ), leading to different local surface lithium stoichiometry ( $x_{Li}$ ). Therefore the parasitic current Equation 5.14 becomes:

$$i_p = -Fk_{sei} \left( \frac{c_X}{c_X^0} \right)^{\alpha_{sei}} (x_{Li})^{\alpha_{sei}} \cdot \exp \left( -\frac{(1 - \alpha_{sei})F}{RT} \eta_p \right) \quad (5.19)$$

SEI properties and cycling conditions are taken as identical to the previous section.

The average thickness obtained at the end of the first cycle is higher than what is obtained with the one-particle size model (Figure 5.6a). Indeed, graphite potential in the continuous particle distribution model is lower than one the one-particle size model (Figure 3.22b), enhancing the SEI growth. Otherwise, the growing rate behavior is identical as in the one-particle size model (Figure 5.5a).

The SEI is quite homogeneously distributed within the electrode. Figure 5.6b shows the SEI thickness obtained at the end of the first lithiation as a function of the position and size of the particle. Even if the differences are low, thicker SEI are found on small particles near the separator, and thinner, on the bigger particles near the current collector. These small particles are indeed more lithiated, have a lower surface potential, and undergo larger intercalation currents than big ones (subsection 3.3.3). The resulting Joule's effect contributes to produce more heat than big particles [218]. As the temperature kinetically improves the SEI growth [146, 148], these small

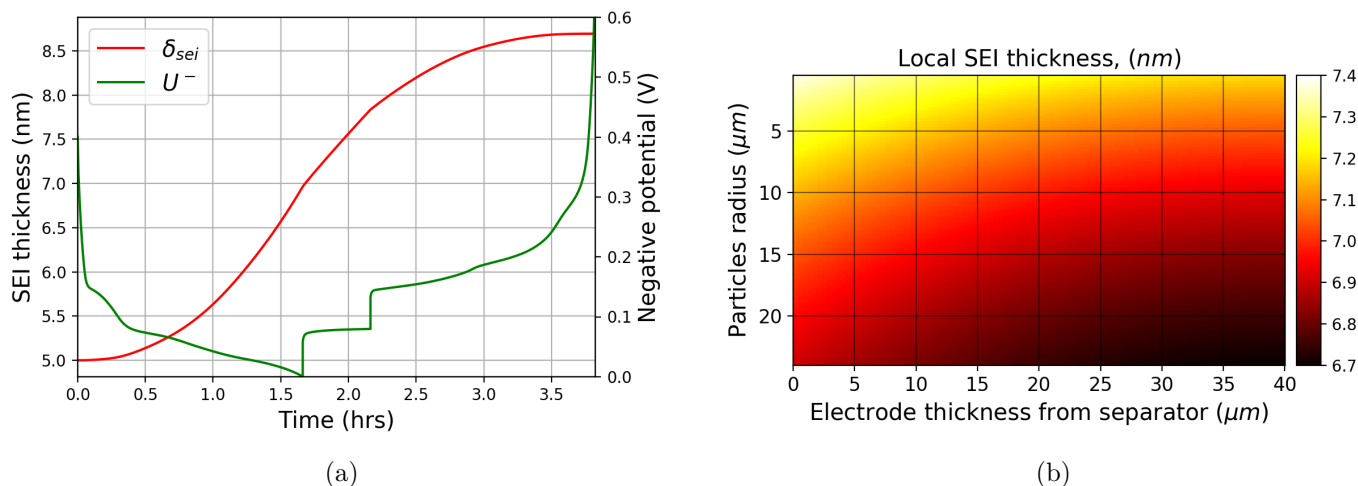


Figure 5.6: Average SEI thickness and graphite potential during first cycle (a) and local SEI thickness at the end of the first lithiation (b) on a continuous size distribution model

particles become the major contributors to the aging. Even for a given SEI thickness, the volume ratio of SEI and active material disadvantages the small particles, which have more probability to lead to the thermal runaway [150, 218]. Reducing the amount of small particles increase then the cell thermal stability at high temperatures.

The SEI heterogeneity is not well captured with Newman’s models and the proposed parameters and SEI models. Experimentally, SEI thickness along electrode can be heterogeneous when the electrode is fresh [141], fairly uniform in thickness after cycling [144] or largely heterogeneous after aging [104], depending on the cell operations. Recently, KLINK *et al.* quantify SEI products at different locations along the electrode thickness, revealing the inhomogeneity of SEI formation [219]. They conclude on the possible mechanism of this heterogeneity: the limited transport through electrode of the electrolyte species that are reduced into SEI. A model which takes into account this transport limitations could enhance and quantify better the SEI distribution.

To go further, the parameters influencing the SEI thickness heterogeneity should be identified. Any parameter which favors the formation of overpotential gradient through cell thickness may promote aging heterogeneities. As previously observed, the parameter involved should be relative to the transport properties of the electrode or its geometrical structure. In addition, the symmetry coefficient,  $\alpha_{sei}$ , could have a significant influence on SEI disparity. A large value of  $\alpha_{sei}$  should increase the overpotential sensibility of the reaction and creates a threshold effect on SEI reaction kinetics.

### 5.1.5 A possible dissolution mechanism

The SEI has a multi-layered structure, often simplified as a dense base inorganic layer, insulating, and an external porous and conductive organic layer. METHEKAR *et al.* explore the formation

of this double layered structure through a monte carlo kinetics model [220]. Simulations are qualitatively in agreement with experimental observations. The surface covered with SEI remains constant on first cycles and increases through aging. RÖDER *et al.* go ahead by coupling monte carlo kinetics with a porous model [221]. The study of different particles sizes shows how the kinetics is affected: more SEI compounds are expected on small particles but the SEI layer grows faster on big ones.

Double layer aspects, inner porosity, and transport in solid and liquid phases of the SEI are modeled by SINGLE *et al.* [222, 223]. They show that the two layers evolve in different ways, highlighting that the growing mechanism could be slightly more complex than a parabolic or linear law.

The SEI complex behavior can also explain some capacity recoveries. YAZAMI *et al.* interpret capacity recovery as the result of the decomposition of unstable SEI components, composed of cyclable lithiums [191]. During rest, SEI metastable complexes are formed at the graphite/SEI interface, lowering the lithium content in graphite. During check-up cycles, these complexes dissociates, releasing cyclable lithium.

A capacity recovery is also noticed on experimental calendar aged cells. During check-up cycles at low C-rates, the reversible capacity goes up gradually (about 2-3 % of the cell capacity recovered). We suspect that SEI decomposes or breaks down at the high graphite potentials obtained at the end of discharge.

The SEI decomposition into the electrolyte has two consequences. Free cyclable lithiums from decomposed products increase the cell capacity, and the SEI thickness decreases. The SEI resistance being reduced, the graphite potential is lowered for further delithiations. If the positive electrode is the limiting factor to the cell capacity, then, more lithium is extracted from the graphite because the cut of voltage is obtained later during discharge.

This hypothetical dissolution reaction is modeled by the Tafel's law:

$$i_{\text{ox}} = i_{0,\text{ox}} \exp\left(\frac{\alpha F}{RT} \eta_{\text{ox}}\right) \quad (5.20)$$

The SEI growing mechanism is still described by Equation 5.17. The lithium salt concentration is considered to have a negligible influence on the dissolution reaction. The electrolyte transport inside SEI (Equation 5.18) is neglected. It is assumed also that only a small amount of the dissolved SEI is actually recovered into cyclable lithium. The total current,  $i_t$ , at the particle surface is then written as:

$$i_t = f \cdot i_{\text{ox}} + i_n + i_p \quad (5.21)$$

The overpotential of the dissolution reaction is written in this case:

$$\eta_{\text{ox}} = \phi_1 - \phi_2 - \frac{\delta_{\text{sei}}}{\kappa_{\text{sei}}} i_t - E_{\text{ox}}^0 \quad (5.22)$$

A 300 nm SEI thickness is supposed. Then the 3 check-up cycles at C/5 are simulated. By adjusting the dissolution kinetics ( $i_{ox}$ ), the equilibrium potential ( $E_{ox}^0$ ), the ionic conductivity of the SEI layer ( $\kappa_{sei}$ ), and the SEI reversibility ( $f$ ), it is possible to model a capacity recovery tendency on the cell model through check-up cycles. Figure 5.7a shows cell reversible capacity obtained for an adequate set of parameters, written down in Table 5.2. The reversible capacity values approach the tendency of the experimental ones (a 15 % capacity recovery simulated instead of a 2 % experimental one). In perspectives, a better parameter optimization could be done, adjusting the SEI reversibility and the equilibrium potential.

Parameter	Symbol	Value
Ionic conductivity ( $S \cdot m^{-1}$ )	$\kappa$	$5 \cdot 10^{-6}$
Exchange current density ( $A \cdot m^{-2}$ )	$i_{ox}$	$10^{-2}$
Equilibrium potential (V)	$E_{ox}^0$	0.5
SEI reversibility (%)	$f$	10
Initial thickness (nm)	$\delta_{sei}^{ini}$	300

Table 5.2: Parameters for the reversible SEI model

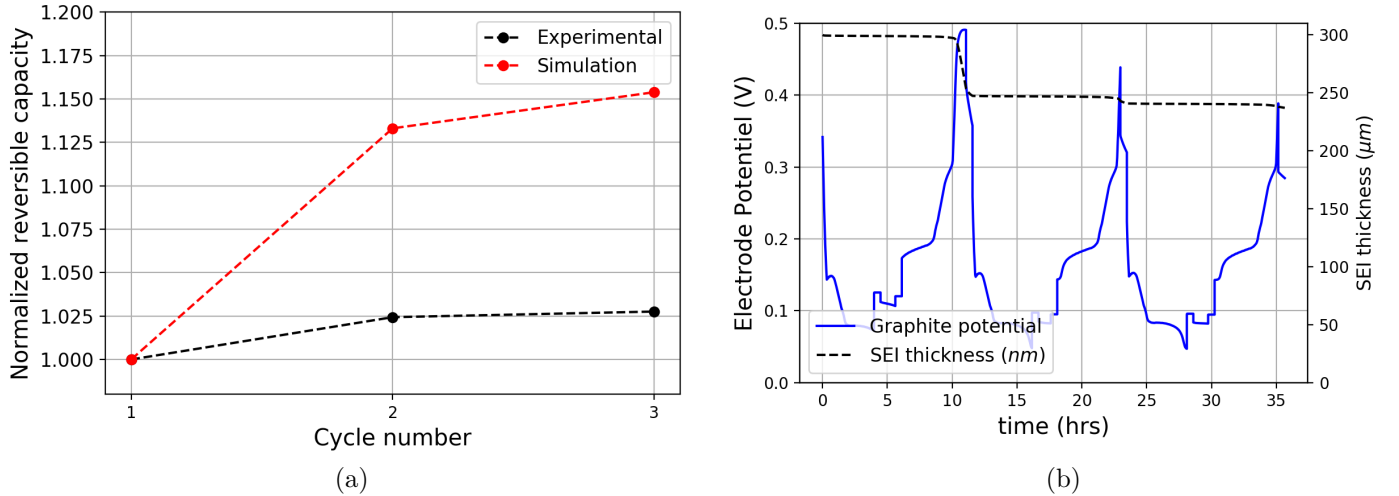


Figure 5.7: Experimental and simulated reversible capacity (a) and average SEI thickness evolution and negative electrode potential (b) during the last check-up

During check-up cycles, graphite tends towards high potentials at the end of discharge, which activates the dissolution reaction. The graphite potential along cycles is displayed in Figure 5.7b as well as the value of the average SEI thickness. The SEI thickness decreases at the end of the cell discharge, its resistance is lowered. Cell polarization is decreased and slowed down the dissolution reaction on following cycles. Over all cycles, the SEI decreases from 300 to less than 250 nm thick. The cell discharge capacity increases due to both a lower impedance and a large amount of cyclable lithiums.

Estimation of the capacity available in real time is a critical issue for battery management system. For now, REDONDO *et al.* propose an empirical approach to model both the reversible and irreversible capacity loss [224]. Unfortunately, this method relies on non-physical parameters. Here, the dissolution mechanism modeled can explain the the capacity recovery and could be investigated, validated and used into a more complete physics-based model for cell diagnostic.

### 5.1.6 Conclusion

SEI is the major source of capacity and power loss in lithium-ion batteries. Its modeling is sufficient to predict the cell capacity loss or, at least, the loss of cyclable lithiums. Capacity recovery could be explained by a SEI dissolution mechanism. However, the SEI behavior at low rates of discharge is probably more complex than a growing layer with diffusion/kinetic limitations. We have shown that a Newman type model based only on kinetic and diffusion, is not sufficient to predict the heterogeneous SEI growth often observed experimentally. The particle size distribution model, allows to increase these heterogeneities but other physical phenomena seems crucial to understand this behavior.

## 5.2 Secondary aging source : the lithium-plating reaction

Another major aging source is encountered in lithium-ion batteries. The lithium plating at the graphite electrode limits the cell performance during charge at high C-rate or low temperatures. This phenomenon could explain the sudden occurrence of a large capacity loss that cannot be predicted by SEI growth only.

### 5.2.1 Lithium plating reaction model

First models of lithium plating were initiated by ARORA *et al.* [225]. A lithium plating mechanism is implemented on a porous electrode model to predict the deposits which occur on graphite during cell overcharge. The parameters having the greatest influence on the lithium plating are: electrodes mass ratio, thickness and particle size. The protective effect of a negative electrode excess is thus demonstrated. High cell voltage reached during overcharge clearly favor the reaction. Thick electrodes and big particles induce lithium transport problems which enhance the growing rate of lithium deposits. Notably, ARORA *et al.* show that graphites with less staged equilibrium potentials (such as Coke), allow less lithium deposit. Indeed, according to subsection 3.2.3, these electrodes operate more homogeneously, given their equilibrium potential being a strictly decreasing function of lithium content. Therefore maximum local overpotentials are reduced and less lithium is electrodeposited.

This model framework for lithium plating has been reproduced for many studies: low temperature influence [226], lithium deposition at electrode edges [155], estimation of plated lithium in a reconstructed structure [227, 32], or integration into the Battery Management System (BMS) [228]. However, comparisons between model and experiment are pretty rare in literature [154]. Recently, YANG *et al.* presented a lithium plating model, validated experimentally, which predicts the transition between a linear and nonlinear aging, corresponding to the observed sudden capacity loss [161].

In this thesis, the lithium plating reaction is implemented into the cell model of the previous section. Thermodynamically, the lithium plating reaction happens when the potential difference at particle surface is lower than equilibrium potential of lithium reduction ( $E_{Li}^0$ ) [154]. At a position  $x$  inside electrode, when the SEI resistance is negligible, this condition is written :

$$\phi_1(x) - \phi_2(x) < E_{Li}^0 \quad (5.23)$$

A potential decomposition of the electrode potential ( $U^-$ ), which is the potential difference between the collector and the reference potential, could be:

$$U^- = \phi_1(0) - \phi_1(x) + \phi_1(x) - \phi_2(x) + \phi_2(x) - \phi_2(L_{gr}) \quad (5.24)$$

Similar to the [subsection 3.2.1](#), the potential difference at active material interface is:

$$\phi_1(x) - \phi_2(x) = U^- - R_{ohm}(x) \cdot aL_{gr}i_n(x) \quad (5.25)$$

where  $R_{ohm}$  corresponds to the the ohmic transport resistances in respectively the solid phase and the liquid phase ([Equation 3.6](#)). [Equation 5.23](#) can be written using [Equation 5.25](#):

$$U^- < E_{Li}^0 + R_{ohm}(x) \cdot aL_{gr}i_n(x) \quad (5.26)$$

As  $R_{ohm}$  is positive and  $i_n$  is always negative during lithiation, a lithium plating occurrence implies in any case a negative electrode potential. Nevertheless, a negative electrode potential, given a reference electrode in the separator, does not always imply lithium plating. In area near the separator,  $R_{ohm}$  is only due to the electronic conductivity of the solid phase and the corresponding potential drop can be negligible in a first approach. In these areas, a negative electrode potential ( $U^-$ ) below 0 V can actually induce lithium plating.

Locally, the total interfacial current,  $i_t$ , is equal to the sum of the parasitic current  $i_{Li}$  and intercalation current,  $i_n$ . The parasitic reaction is assumed irreversible in a first approach and therefore is modeled by a Tafel's law:

$$i_{Li} = -i_{Li}^0 \left( \frac{c_2}{c_2^0} \right)^{1-\alpha_{Li}} \exp \left( -\frac{(1-\alpha_{Li})F}{RT} \eta_{Li} \right) \quad (5.27)$$

Parameter	Symbol	Value
Molar mass of lithium ( $\text{g} \cdot \text{mol}^{-1}$ )	$M_{\text{Li}}$	6.94
Density of lithium ( $\text{kg} \cdot \text{m}^{-3}$ )	$\rho_{\text{Li}}$	534
Exchange current ( $\text{A} \cdot \text{m}^{-2}$ )	$i_{\text{Li}}^0$	$10^{-7}$
Symmetry coefficient	$\alpha_{\text{Li}}$	0.01
Equilibrium potential (V)	$E_{\text{Li}}^0$	0

Table 5.3: Lithium plating reaction parameters

where,  $i_{\text{Li}}^0$  and  $\alpha_{\text{Li}}$  are respectively the exchange current ( $\text{A} \cdot \text{m}^{-2}$ ) and the symmetry coefficient of the lithium plating reaction. The overpotential,  $\eta_{\text{Li}}$  is then written:

$$\eta_{\text{Li}} = \phi_1 - \phi_2 - \frac{\delta_{\text{sei}}}{\kappa_{\text{sei}}} i_t - E_{\text{Li}}^0 \quad (5.28)$$

The growth of the lithium deposit layer is described as presented in [Equation 5.17](#):

$$\frac{d\delta_{\text{Li}}}{dt} = -\frac{i_{\text{Li}}}{F} \frac{M_{\text{Li}}}{\rho_{\text{Li}}} \quad (5.29)$$

where  $M_{\text{Li}}$  and  $\rho_{\text{Li}}$  are respectively the molar mass and the density of lithium. Model parameters are found in literature and presented in [Table 5.3](#). The symmetry coefficient and the exchange current are adjusted to allow a fast reaction when the potential difference at the graphite interface outreaches the equilibrium potential of the lithium plating reaction. It should be noted that the value of  $\alpha_{\text{Li}}$  chosen here is not correlated to any physical value.

The model predicts that the negative electrode potential ( $U^-$ , see [subsection 4.3.1](#)) falls regularly below 0 V during charge ([Figure 5.8a](#)). At 2C, 90 % of the charge happens when the graphite electrode potential is under 0 V vs Li. Experimentally, the local potential difference at the graphite interface could be rather different due to the heterogeneous current distribution.

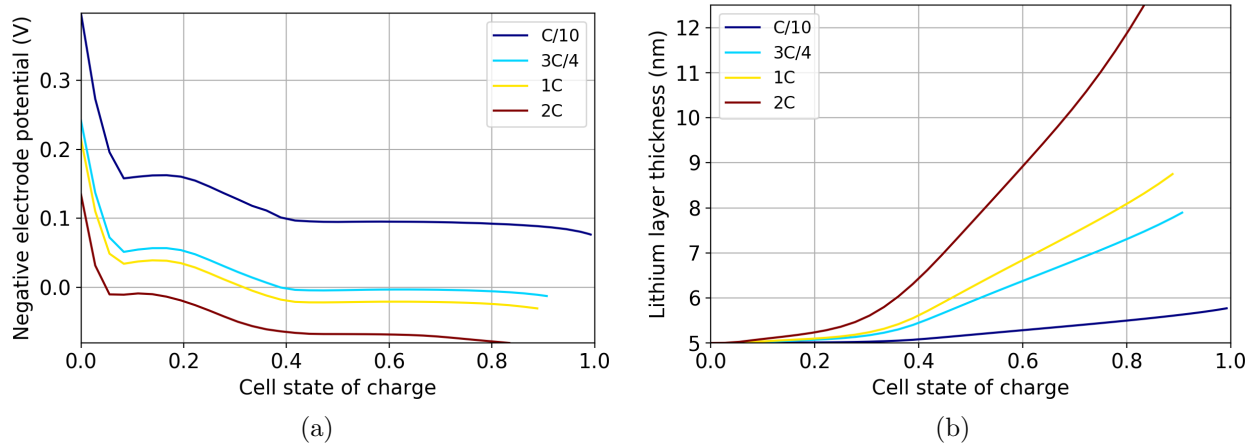


Figure 5.8: Negative electrode potential (a) and lithium layer (b) during simulated cell charge at C/10, 3C/4, 1C, and 2C.

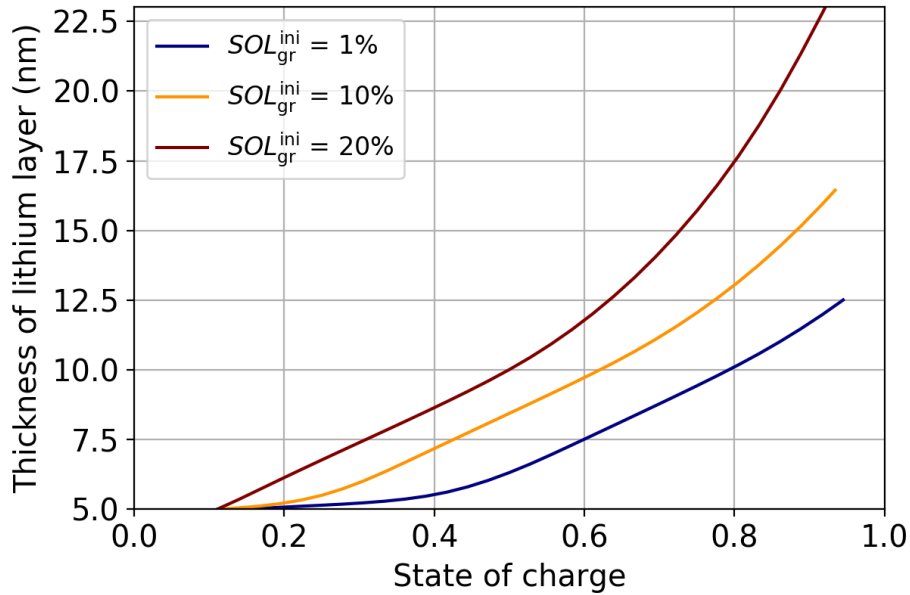


Figure 5.9: Average thickness of the lithium layer during a simulated 2C charge for different initial states of lithiation of the graphite electrode ( $SOL_{gr}^{ini}$ )

We are aware that the lithium plating kinetics is only guessed, however parasitic reaction tendencies can be drawn.

The average thickness of deposited lithium can be quantified (Figure 5.8b). When the C-rate increases, the deposit growth rate increases. Up to 30 % SOC, the C-rate does not impact the amount of lithium deposited. Indeed, the graphite electrode remains rather delithiated at the beginning of charge, its potential being far from 0 V. Up to 2C, this SOC zone allows fast charges. After 30 % SOC, precautions have to be taken according to the C-rate. On this principle, optimized protocols for fast charge have been proposed in literature [229].

Aging causes a shift on the lithium stoichiometry window of both electrodes [125]. As seen in the previous section, the cyclable lithium becomes a non-limiting factor of the cell capacity. A remaining amount of lithium can be found in the graphite electrode at the end of discharge. The graphite potential is thus lowered during the next charge and promotes a sooner appearance of lithium deposits. The simulation of 2C charges at different initial states of lithiation confirms this assumption (Figure 5.9) Given the lithium plating kinetics, the developed surface of active material, the density and molar mass of lithium, a homogeneous 22 nm lithium layer thickness formed corresponds nearly to a 12 mAh cyclable lithium loss in this system. .

In general, any phenomenon decreasing the local graphite potential below 0 V vs  $Li^+/Li$  favors the lithium plating. The model shows that large C-rates or local high state of lithiation of graphite at beginning of charge enhance the lithium plating reaction.

## 5.2.2 The pore clogging mechanism

Important lithium deposits could modify the structure of the electrode, which impacts its effective transport properties [161]. Electrode pores can be closed due to lithium deposits.

### Pore-clogging via porosity variation

Any passivation layer formed on particle surface causes a loss of the liquid phase and therefore the reduction of the electrode porosity,  $\epsilon$ . Geometrically, the porosity variation is linearly linked to the electrochemically active material surface of the electrode,  $a$ , to the thickness variation of any additional layer on graphite surface,  $\delta_t$ :

$$\frac{\partial \epsilon}{\partial t} = -a \cdot \frac{\partial \delta_t}{\partial t} \quad (5.30)$$

The parameter  $a$  dictates the impact of the layer thickness on porosity. When the particle swelling is not negligible along operations (as in silicon), variation of the parameter  $a$  is noticed, and that modifies the layer thickness impact on porosity. In case of lithiated cylindrical graphite particles, the lithiated state particle volume increases up to 10 % compared to the delithiated state. It corresponds to a 5 % radius rise on the active material surface (3 % in case of spherical particles).

The linear relation between porosity and the layer thickness is drawn in Figure 5.10 for graphite particle, lithiated or delithiated. Porosity variation is shown for spherical particles of same radius for comparison.

### Model validity

To close all the pores, the volume of the passivation layer must be equal to the volume of the liquid phase given by the initial porosity. From the electrode characteristics, as seen in Figure 5.10, particle swelling does not have a significant impact on pore-clogging. Lithiated or delithiated, at least a 2.2  $\mu\text{m}$  layer thickness is needed to close the pore (1.5  $\mu\text{m}$  for spherical particle).

From Chapter 5, a discharge capacity loss due to porosity variation is noticed under 0.06 %. From Figure 5.10, this value corresponds to a thickness layer of 1.8  $\mu\text{m}$  (1.25 for spherical particles). These values are uncommon for a SEI layer. Experimentally, a SEI thicker than 1  $\mu\text{m}$  is rarely expected, due to mechanical stress. Moreover, a homogeneous SEI thickness of this value indicates a huge cyclable lithium loss (Table 4.2 in Chapter 5). In case of a pure lithium layer, it is even less physical. Indeed, at a given thickness, a lithium layer has 10 times more lithium content than a SEI one.

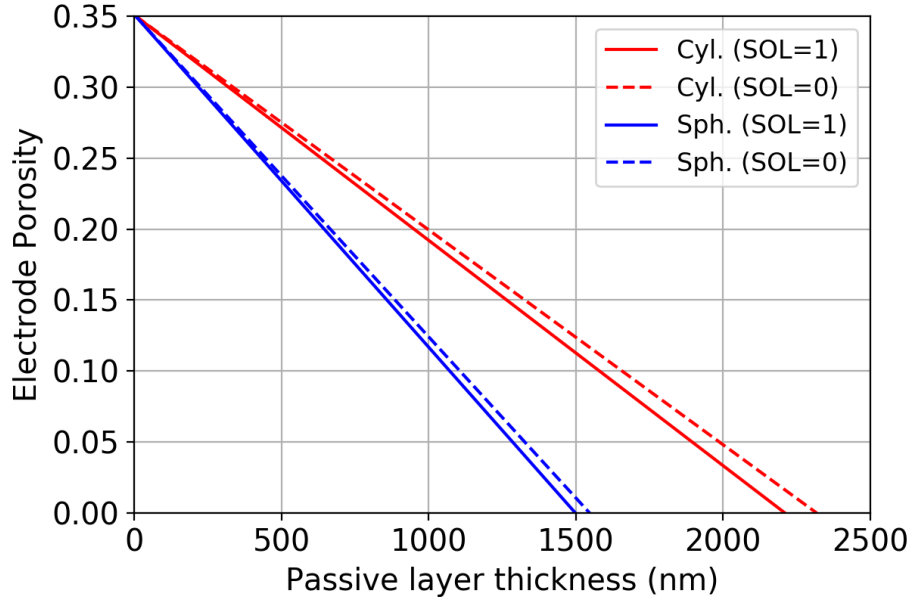


Figure 5.10: Porosity versus SEI thickness evolution

### Pore-clogging via a tortuosity evolution

In this thesis, another physical phenomenon is proposed to explain the pore-clogging mechanism. As a start, effective transport properties inside electrode are re-written in such a way that by contrast to the Bruggeman relation, tortuosity and porosity are not considered correlated.

$$P^{\text{eff}} = P \frac{\epsilon}{\tau} \quad (5.31)$$

The impact of the porosity variation due to passivation layer growth is assumed to be negligible throughout aging. The following hypothesis explains an alternative transport properties degradation : pore entrances are sealed due to growing layers closing pathways between particles (Figure 5.11a). When an inter-particle pathway is closed, the average transport path becomes longer, and tortuosity drastically rises. A thickness limit exists, namely  $\delta_t^{\text{lim}}$ , beyond which all the inter-particle paths are closed.

An empirical law is chosen to approach this behavior (Equation 5.32). It links the passive layer thickness and the porosity to the tortuosity. The first member of Equation 5.32 gives the base value of the tortuosity from the Bruggeman relation (Equation 2.18). The second member models the sudden rise of tortuosity over a thickness limit,  $\delta_t^{\text{lim}}$ . The exponential function and the exponent are picked up to ensure a drastically rise over the thickness limit and are not correlated to any physical mechanism.

$$\tau = \frac{1}{\sqrt{\epsilon}} - 1 + \exp \left[ \left( \frac{\delta_t}{\delta_t^{\text{lim}}} \right)^5 \right] \quad (5.32)$$

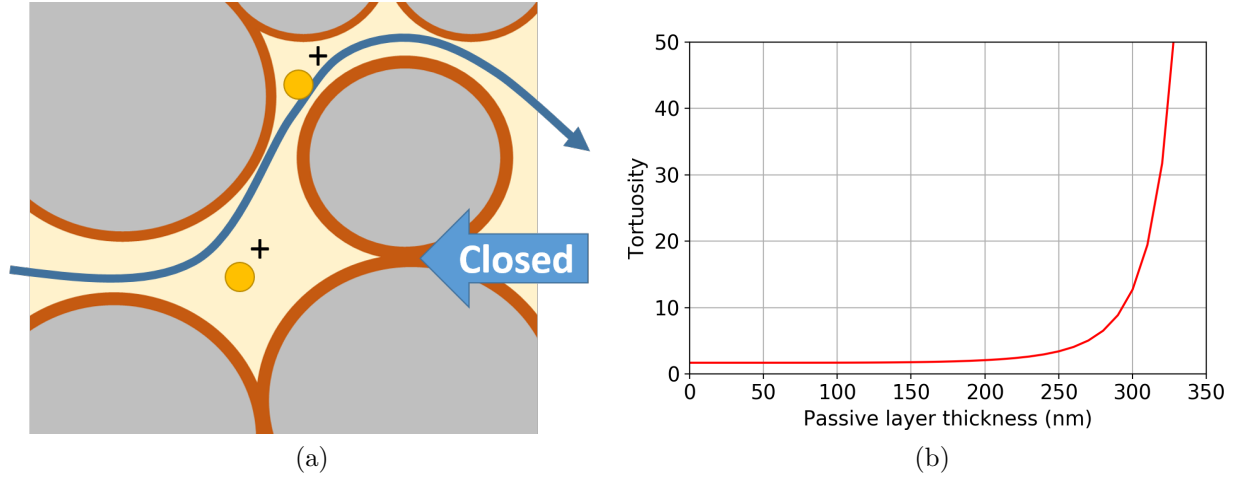


Figure 5.11: Pore-clogging model (a) and tortuosity model (Equation 5.32) versus SEI thickness evolution (b)

A better understanding of the microstructure could provide a more physical relation between porosity and the passive layer thickness. For instance, a 3D study on geometrically reconstructed electrode already gives information about the local tortuosity and porosity through the cell thickness [101, 168, 54]. The geometrical study of the passive layer thickness impact on the tortuosity of these electrode structures would provide a more physically correlated law.

The Equation 5.32 is added to the full cell model with a limited thickness of 300 nm ( $\delta_t^{lim}$ ). The relation between  $\delta_t$  and  $\tau$  is drawn on Figure 5.11b. and appears in effective transport properties (conduction and diffusion) of the electrode, according to Equation 5.31. Lithium plating and SEI models are added with respective initial thicknesses of 0 and 150 nm. The total thickness of the two passivation layers is expressed as the sum of the lithium plating and SEI layer:

$$\delta_t = \delta_{sei} + \delta_{Li} \quad (5.33)$$

After a 20-cycle simulation performed at C/2, the discharge capacity starts to decrease (Figure 5.12). On the 26<sup>th</sup> cycle, the cut off voltage is reached during the first minute of the discharge. In Figure 5.12 is displayed the discharge capacity and the tortuosity at different points along the electrode thickness. At the end, the tortuosity exceeds 80 near electrode surface. It falls to less than 20 at 5% electrode's depth and has not evolved in the middle of the electrode (a 1.7 value). The pore clogging is an electrode surface phenomenon in this configuration, as demonstrated also by YANG *et al.* [161]. Indeed the overpotential and lithium salt concentrations are higher near the separator, which favor the passivation layer growth. In these areas, the largest tortuosity evolution takes place via Equation 5.32. Doing so, the transport properties are lowered in these zones, increasing overpotential, accelerating growth, and finally pore clogging.

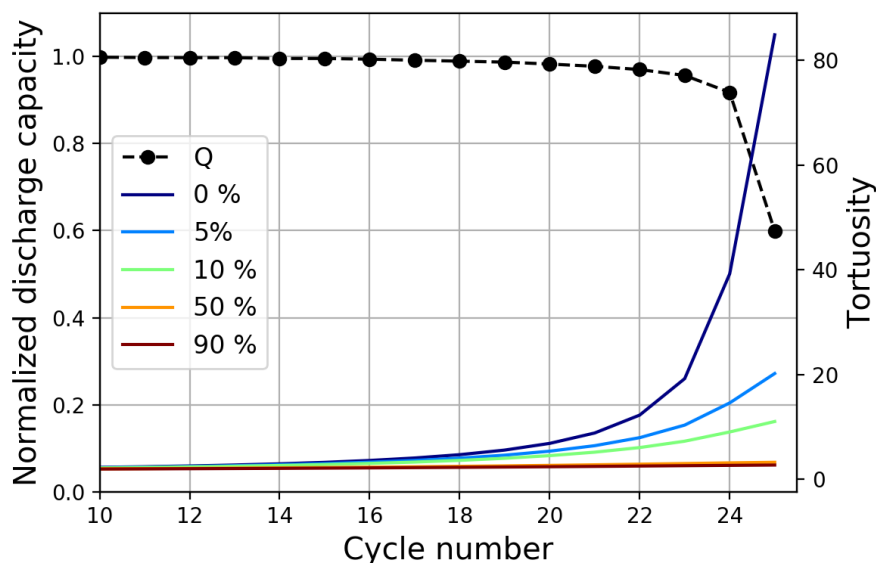


Figure 5.12: Simulated discharge capacity and local tortuosity evolution (0, 5, 10, 50, and 90 % depth from the separator) throughout cycling ( $C/2$ ) with a tortuosity model

### 5.2.3 Competition between lithium-plating and SEI

SEI growth and lithium plating can jointly close the pores and reduce local transport properties. By contrast, the cooperation of the two mechanisms may be beneficial in some cases. GRIMSMANN *et al.* show that aged cells are less sensitive to lithium plating [230]. In the specific case of cycled cell, the maximum tolerated charge current at 0 °C without lithium plating is increased by 25 % compared to fresh cells.

Aging through cycling is assumed to increase the SEI thickness. Different charge simulations are performed on the full cell model with the two parasitic reactions: SEI and lithium plating. SEI parameters come from the previous section, and different initial thicknesses are supposed, corresponding to hypothetical various aged states. The C-rate is fixed at 2C. In Figure 5.13, the lithium deposition rate of each charge simulation is displayed as a function of the SEI thickness. This rate is calculated as the ratio of the total amount of lithium deposited and the charge duration, normalized to the rate value at for a charge at zero SEI thickness.

Between 0 and 400 nm SEI thickness, the deposition rate is reduced by 4 %. Indeed, a larger value of SEI protects the surface from excessive overpotential which favor SEI growth and also lithium plating. This tendency is also confirmed by the numerical results of ARORA *et al.*. The protection via SEI layer is simulated but is weak compared to experimental findings [230]. Other aging phenomena can also promote or cancel the protection. As instance, the graphite lithiation state at the end of discharge promote lithium plating (Figure 5.9). The electrochemically active surface could be also modified, due to particle pulverization. An increase of this parameter would lower the lithium plating reaction rate by reducing the local current density at the interface and

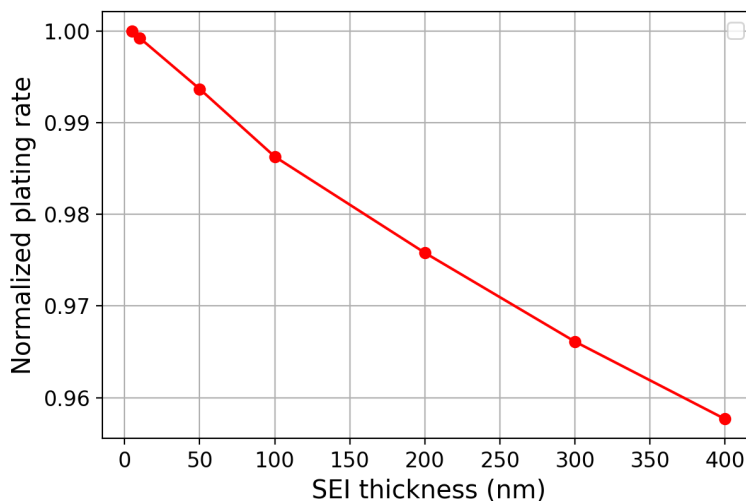


Figure 5.13: Normalized plating rate as a function of SEI thickness at a 2C cell charge

therefore the overpotential.

Lithium plating deposits are reversible, as indirectly observed on the cell thickness variation during relaxation [163, 152, 231]. Some mechanism assumptions differentiate plated lithiums, considering them either reversible or irreversible. Lithium deposits are supposed to form under the SEI. When the deposits exceed the SEI thickness or are disconnected from the conductive phase, they passivate and break down into the electrolyte (named as *dead Li*) [158].

### 5.3 Conclusion

The growth of the SEI layer is the primary source of aging in lithium-ion batteries. Its evolution, which involves the consumption of lithium and interfacial resistance modification, is predictable. In this work, the discharge capacity loss and the recovery of cyclable lithium through low C-rate cycles have been successfully modeled.

The sudden discharge capacity loss appearing at the end of life can be predicted via a lithium-plating model coupled with a pore clogging model. Its influence on some parts of the electrode structure explains the experimental observations. However, the different degradation mechanisms and the competition between them are complex to quantify due to the difficulty to study separate mechanisms. A unique, predictive, exhaustive, and complete aging model of a graphite electrode is complex to adjust due to the microstructure specificity and the interdependence of aging mechanisms.

# Chapter 6

## Perspectives and Conclusion

During this thesis, the performance and aging of porous graphite electrodes has been studied during calendar and cycling aging. Electrochemical models have been derived through this experiments to understand local heterogeneities during operations. Furthermore, principal aging mechanisms, which have been observed experimentally, are studied through corresponding implements into a validated full cell model. The modeling approach allows to experiment, validate and quantify different aging mechanism assumptions, as instance here SEI growth, sudden capacity loss and capacity recovery.

In a first part of this thesis, a porous electrode model in a half-cell configuration is then developed and validated on experimental results to explore internal graphite conditions during operations. Experimental results come from the study of graphite lithiation (Timcal SLP30) in lithiation and delithiation. Graphite shows a limited rate capability, reached at a current density of  $4 \text{ mA} \cdot \text{cm}^{-2}$  whatever the mass-loading. This limitation comes from the graphite material properties and electrode structure. Despite a lot of physical parameters, a sensitivity analysis coupled with a parameter review targets the most critical model parameters. We define a sensitivity coefficient describing the lithiation rate capability and the impact on the electrode potential. This information can be used for quick experimental fits (Tables 2.4 and 2.5).

Parameters related to intercalation kinetics, species transport through the porous material, and active material quantities express the main physical limitations of the cell and need to be adjusted in order to calibrate the model on the experimental data.

The calibrated model predicts with a good accuracy (90 %) the graphite electrode potential and capacity under various constant currents (C/10 to 3C) and mass-loadings (5.7 to  $12 \text{ mg} \cdot \text{cm}^{-2}$ ). The model gives access to *operando* conditions within the electrode such as local potentials, lithium concentration in electrolyte and inside active material. Thus, the lithium distribution through the electrode thickness (throughout lithiation or delithiation) can be observed. The staged equilibrium potential of graphite is the main driving force of lithiation heterogeneities. Closer lithiation states

with constant equilibrium potential emphasize lithiation heterogeneity, whereas strictly monotonic potential promotes a relative homogeneity. Its heterogeneity prevents the optimal operations of the graphite electrode and, at the end, the cell performance. The parameters associated with the three limiting phenomena (kinetics and transport in the liquid and the solid phases) drive the cell performance and compete with each other to modulate the lithiation distribution: better kinetics increases the magnitude of heterogeneity periods, and lower transport properties increase the whole cell heterogeneity. This study of the parameter impact on the electrode performance gives guidelines to develop a homogeneous operating graphite. Thus, the equilibrium potential shape of the active material on its own may explain actual lithiation distribution difference, such as between NMC, graphite, and LFP.

Many other factors enhance the heterogeneity of the lithium distribution, hiding the homogeneity/heterogeneity mechanism due to the equilibrium potential shape. For example, the distribution of particle shapes and sizes produce lithiation heterogeneities that exceed the one due to the equilibrium potential. The electrode model including an experimental particle size distribution demonstrates that big particles are not fully lithiated at the end of charge (70 % maximum), whereas small ones operate on their full stoichiometry ranges, but suffer for large intercalation current variations. So, it can be supposed that particles age at different rates: small ones near separator should fail earlier than big ones located near current collector. Experimental aging data are needed to confirm this statement.

To compare simulated lithiation heterogeneities with experiments, the local graphite lithium stoichiometry distribution has been measured *operando* using micro-Xray diffraction from a synchrotron source. The lithium distribution through the electrode thickness is indeed heterogeneous, even at low C-rates, but only for specific lithium-graphite phase transitions. This behavior should be confirmed by other results, performed during this thesis. Furthermore, future experiments could be done with narrower particle size distributions (as MCMB graphite for instance). Decreasing the size span will increase the homogeneity/heterogeneity mechanism due to the staged equilibrium potential for which experimental validation does not exist yet.

In a second part, the analysis of an experimental campaign on graphite-NMC cells with reference electrodes has highlighted a two-step aging mechanism. Throughout cycles, the discharge capacity loss is, at the beginning, a quadratic function of time, and after 200 cycles, a linear function of time. Capacity recovery is observed at low C-rates and sometimes sudden capacity loss at the end of life. To go further, the post-mortem analyses of this campaign should bring more information about the final lithium content of the both electrodes and their structure.

Based on the half-cell porous model, a full cell model (Graphite-NMC) is developed and calibrated on check-up cycles at the beginning and the end of life. Based on a literature review and on the model results, it is shown that the SEI and positive material loss are probably the principal contributors to the cell capacity fades and power losses. Furthermore, a sensitivity analysis on

the physical parameters impact on capacity loss shows that shape and size variations of particles have a limited effect on aging. Nevertheless, porosity and tortuosity can reach nonphysical global values (respectively 0.6 % and 40) beyond which the discharge capacity drastically falls down.

The primary aging source in a lithium-ion battery is the growth of the SEI layer, which decreases the lithium content in the cell. Its evolution predicts the discharge capacity loss when the lithium content is the limiting factor to the cell capacity (below 200 cycles). For the studied experimental campaign, it is observed that the limiting factor becomes the active material quantity at the positive in the long run. Unlike the literature, no obvious SEI heterogeneities inside the cell are derived from modeling, mainly due to the electrode geometry and physic simplifications and missing consideration regarding solvent species diffusion through the cell thickness. The recovery of cyclable lithium through low C-rate cycles can be modeled through a SEI thickness dissolution mechanism at high potential.

The occurrence of a sudden capacity loss at the end of life is explained by a lithium-plating mechanism. The latter locally degrades the electrode structure: the tortuosity is supposed to drastically increase when the lithium layer reaches a thickness limit. The resulting pore clogging comes from the degradation of electrode transport properties. A geometrical study of the exact electrode structure could provide a physics-based dependency between the passive layer thickness and geometrical properties.

To go further on the lithium plating mechanism, its possible reversibility and interaction with SEI coverage should be studied. It is presumed that SEI thickness favors the reversibility of lithium plating. Different cells were cycled and experienced lithium plating every 100 cycles. Future analysis could quantify the impact of aging on the lithium-plating reversibility.

The particular modes of degradation, their local issue and interdependency inside electrode are complex to model and predict. A unique, predictive, exhaustive, and complete physics-based aging model of a graphite electrode tends to be difficult to obtain due to the particular microstructure, the electrode interdependence and complex chemistry of aging mechanisms. Nevertheless, modeling and simulation are powerful predictive and comprehensive tools, which give a first step into the understanding of the complex physics of the lithium-ion system. Local conditions, which are rarely accessible experimentally, are simulated and the consequences of various hypothesis and supposed degradation phenomena are predicted and quantified.

# Bibliography

- [1] C. Schlasza, P. Ostertag, D. Chrenko, R. Kriesten, and D. Bouquain. Review on the aging mechanisms in li-ion batteries for electric vehicles based on the fmea method. In *2014 IEEE Transportation Electrification Conference and Expo (ITEC)*, pages 1–6, June 2014.
- [2] J. Vetter, P. Novak, M.R. Wagner, C. Veit, K.-C. Moller, J.O. Besenhard, M. Winter, M. Wohlfahrt-Mehrens, C. Vogler, and A. Hammouche. Ageing mechanisms in lithium-ion batteries. *Journal of Power Sources*, 147(1 : 2):269–281, 2005.
- [3] Jens Groot. *State-of-health estimation of Li-ion batteries: Ageing models*. Chalmers University of Technology, 2014.
- [4] M. Safari, M. Morcrette, A. Teysot, and C. Delacourt. Multimodal physics-based aging model for life prediction of li-ion batteries. *Journal of The Electrochemical Society*, 156(3):A145–A153, 2009.
- [5] Jos Barlow, Filipe França, Toby A. Gardner, Christina C. Hicks, Gareth D. Lennox, Erika Berenguer, Leandro Castello, Evan P. Economo, Joice Ferreira, Benoit Guénard, Cecília Gontijo Leal, Victoria Isaac, Alexander C. Lees, Catherine L. Parr, Shaun K. Wilson, Paul J. Young, and Nicholas A. J. Graham. The future of hyperdiverse tropical ecosystems. *Nature*, 559(7715):517–526, July 2018.
- [6] Anthony D. Barnosky, Elizabeth A. Hadly, Jordi Bascompte, Eric L. Berlow, James H. Brown, Mikael Fortelius, Wayne M. Getz, John Harte, Alan Hastings, Pablo A. Marquet, Neo D. Martinez, Arne Mooers, Peter Roopnarine, Geerat Vermeij, John W. Williams, Rosemary Gillespie, Justin Kitzes, Charles Marshall, Nicholas Matzke, David P. Mindell, Eloy Revilla, and Adam B. Smith. Approaching a state shift in earth s biosphere. *Nature*, 486:52, June 2012.
- [7] Philippe Bihouix. *L’age des low tech, vers une civilisation techniquement soutenable*. Seuil, 2014.
- [8] Pablo Servigne and Raphael Stevens. *Comment tout peut s’effondrer, petit manuel de colla-sologie à l’usage des générations présentes*. Seuil, 2015.

- [9] Behnam Zakeri and Sanna Syri. Electrical energy storage systems: A comparative life cycle cost analysis. *Renewable and Sustainable Energy Reviews*, 42:569 – 596, 2015.
- [10] George E. Blomgren. The development and future of lithium ion batteries. *Journal of The Electrochemical Society*, 164(1):A5019–A5025, 2017.
- [11] Panasonic. Reference : the ncr18650 lithium-ion cell.
- [12] Kai Liu, Yayuan Liu, Dingchang Lin, Allen Pei, and Yi Cui. Materials for lithium-ion battery safety. *Science Advances*, 4(6), 2018.
- [13] Christian M. Julien, Alain Mauger, Karim Zaghib, and Henri Groult. Comparative issues of cathode materials for li-ion batteries. *Inorganics*, 2(1):132–154, 2014.
- [14] Ali Eftekhari. Low voltage anode materials for lithium-ion batteries. *Energy Storage Materials*, 7:157 – 180, 2017.
- [15] Kian Kerman, Alan Luntz, Venkatasubramanian Viswanathan, Yet-Ming Chiang, and Zhebo Chen. Practical challenges hindering the development of solid state li ion batteries. *Journal of The Electrochemical Society*, 164(7):A1731–A1744, 2017.
- [16] Tobias Placke, Richard Kloepsch, Simon Dühnen, and Martin Winter. Lithium ion, lithium metal, and alternative rechargeable battery technologies: the odyssey for high energy density. *Journal of Solid State Electrochemistry*, 21(7):1939–1964, Jul 2017.
- [17] Tsutomu Ohzuku, Yasunobu Iwakoshi, and Keiji Sawai. Formation of lithium-graphite intercalation compounds in nonaqueous electrolytes and their application as a negative electrode for a lithium ion (shuttlecock) cell. *Journal of The Electrochemical Society*, 140(9):2490–2498, 1993.
- [18] Victor Agubra and Jeffrey Fergus. Lithium ion battery anode aging mechanisms. *Materials*, 6(4):1310–1325, 2013.
- [19] F. Grimsman, T. Gerbert, F. Brauchle, A. Gruhle, J. Parisi, and M. Knipper. Determining the maximum charging currents of lithium-ion cells for small charge quantities. *Journal of Power Sources*, 365(Supplement C):12 – 16, 2017.
- [20] K.a Jalkanen, J.b Karppinen, L.b Skogström, T.b Laurila, M.a Nisula, and K.a Vuorilehto. Cycle aging of commercial nmc/graphite pouch cells at different temperatures. *Applied Energy*, 154:160–172, 2015. cited By 0.
- [21] Yan Ji, Yancheng Zhang, and Chao-Yang Wang. Li-ion cell operation at low temperatures. *Journal of The Electrochemical Society*, 160(4):A636–A649, 2013.

- [22] Todd M. Bandhauer, Srinivas Garimella, and Thomas F. Fuller. A critical review of thermal issues in lithium-ion batteries. *Journal of The Electrochemical Society*, 158(3):R1–R25, 2011.
- [23] G. Hautier. Prediction of new battery materials based on ab initio computations. In *Electrochemical Storage Materials: Supply, Processing, Recycling and Modelling*, volume 1765, 2016. cited By 0.
- [24] Elena Zvereva, Damien Caliste, and Pascal Pochet. Interface identification of the solid electrolyte interphase on graphite. *Carbon*, 111:789 – 795, 2017.
- [25] Siqi Shi, Peng Lu, Zhongyi Liu, Yue Qi, Jr. Louis G. Hector, Hong Li, and Stephen J. Harris. Direct calculation of li-ion transport in the solid electrolyte interphase. *Journal of the American Chemical Society*, 134(37):15476–15487, 2012. PMID: 22909233.
- [26] Seyed Mohammad Rezvanizani, Zongchang Liu, Babor L, and Jay Lee. Review and recent advances in battery health monitoring and prognostics technologies for electric vehicle ev safety and mobility. *Journal of Power Sources*, 256:110–124, 2014.
- [27] Ali Jokar, Barzin Rajabloo, Martin Désilets, and Marcel Lacroix. Review of simplified pseudo-two-dimensional models of lithium-ion batteries. *Journal of Power Sources*, 327:44 – 55, 2016.
- [28] Shriram Santhanagopalan, Qingzhi Guo, Premanand Ramadass, and Ralph E. White. Review of models for predicting the cycling performance of lithium ion batteries. *Journal of Power Sources*, 156(2):620–628, 2006.
- [29] Yufei Chen and James W. Evans. Thermal analysis of lithium-ion batteries. *Journal of The Electrochemical Society*, 143(9):2708–2712, 1996.
- [30] Robert Darling and John Newman. Modeling a porous intercalation electrode with two characteristic particle sizes. *Journal of The Electrochemical Society*, 144(12):4201–4208, 1997.
- [31] Meng Xu, Zhuqian Zhang, Xia Wang, Li Jia, and Lixin Yang. A pseudo three-dimensional electrochemical-thermal model of a prismatic lifepo4 battery during discharge process. *Energy*, 80:303–317, 2015.
- [32] Timo Danner, Madhav Singh, Simon Hein, Jorg Kaiser, Horst Hahn, and Arnulf Latz. Thick electrodes for li-ion batteries: A model based analysis. *Journal of Power Sources*, 334:191–201, 2016.
- [33] J. Newman and W. Tiedemann. Porous-electrode theory with battery applications. *AICHE J.*, 21:25–41, 1975.

- [34] D Aurbach, K Gamolsky, B Markovsky, Y Gofer, M Schmidt, and U Heider. On the use of vinylene carbonate (vc) as an additive to electrolyte solutions for li-ion batteries. *Electrochimica Acta*, 47(9):1423 – 1439, 2002.
- [35] Rod McMillan, Helen Slegel, Z.X Shu, and Weidong Wang. Fluoroethylene carbonate electrolyte and its use in lithium ion batteries with graphite anodes. *Journal of Power Sources*, 81-82:20 – 26, 1999.
- [36] S.R. Sivakkumar, J.Y. Nerkar, and A.G. Pandolfo. Rate capability of graphite materials as negative electrodes in lithium-ion capacitors. *Electrochimica Acta*, 55(9):3330 – 3335, 2010.
- [37] Seong Jin An, Jianlin Li, Claus Daniel, Debasish Mohanty, Shrikant Nagpure, and David L. Wood. The state of understanding of the lithium-ion-battery graphite solid electrolyte interphase (sei) and its relationship to formation cycling. *Carbon*, 105:52 – 76, 2016.
- [38] Martin Winter, Petr Novak, and Alain Monnier. Graphites for lithium-ion cells: The correlation of the first-cycle charge loss with the bet surface area. *Journal of The Electrochemical Society*, 145(2):428–436, 1998.
- [39] Kevin G. Gallagher, Stephen E. Trask, Christoph Bauer, Thomas Woehrle, Simon F. Lux, Matthias Tschech, Peter Lamp, Bryant J. Polzin, Seungbum Ha, Brandon Long, Qingliu Wu, Wenquan Lu, Dennis W. Dees, and Andrew N. Jansen. Optimizing areal capacities through understanding the limitations of lithium-ion electrodes. *Journal of The Electrochemical Society*, 163(2):A138–A149, 2016.
- [40] Takashi Yamauchi, Koichi Mizushima, Yuji Satoh, and Shuji Yamada. Development of a simulator for both properly and safety of a lithium secondary battery. *Journal of Power Sources*, 136:99–107, 2004.
- [41] Hironori Kobayashi, Yoshinori Arachi, Shuichi Emura, Hiroyuki Kageyama, Kuniaki Tatsumi, and Takashi Kamiyama. Investigation on lithium de-intercalation mechanism for  $\text{Li}_{1-y}\text{Ni}_{1/3}\text{Mn}_{1/3}\text{Co}_{1/3}\text{O}_2$ . *Journal of Power Sources*, 146(1):640 – 644, 2005. Selected papers presented at the 12th International Meeting on Lithium Batteries.
- [42] Naoki Nitta, Feixiang Wu, Jung Tae Lee, and Gleb Yushin. Li-ion battery materials: present and future. *Materials Today*, 18(5):252–264, 2015.
- [43] John Newman and Karen E. Thomas-Alyea. *Electrochemical Systems : third Edition*. Electrochemical Society, 2004.
- [44] C.M. Doyle. *Design and Simulation of Lithium Rechargeable Batteries*. PhD thesis, Lawrence Berkeley National Laboratory, 1995.

- [45] Yinsheng Guo, Raymond B. Smith, Zhonghua Yu, Dmitri K. Efetov, Junpu Wang, Philip Kim, Martin Z. Bazant, and Louis E. Brus. Li intercalation into graphite: Direct optical imaging and cahn-hilliard reaction dynamics. *The Journal of Physical Chemistry Letters*, 7(11):2151–2156, 2016. PMID: 27203128.
- [46] Kristin Persson, Yoyo Hinuma, Ying Shirley Meng, Anton Van der Ven, and Gerbrand Ceder. Thermodynamic and kinetic properties of the li-graphite system from first-principles calculations. *Phys. Rev. B*, 82:125416, September 2010.
- [47] Long Cai and Ralph E. White. Mathematical modeling of a lithium ion battery with thermal effects in comsol inc. multiphysics (mp) software. *Journal of Power Sources*, 196:5985–5989, 2011.
- [48] Raymond B. Smith, Edwin Khoo, and Martin Z. Bazant. Intercalation kinetics in multiphase-layered materials. *The Journal of Physical Chemistry C*, 121(23):12505–12523, 2017.
- [49] Madeleine Ecker, Stefan Kabitz, Izaro Laresgoiti, and Dirk Uwe Sauer. Parameterization of a physico-chemical model of a lithium-ion battery: Ii. model validation. *Journal of The Electrochemical Society*, 162(9):A1849–A1857, 2015.
- [50] Madeleine Ecker, Nerea Nieto, Stefan Katz, Johannes Schmalstieg, Holger Blanke, Alexander Warnecke, and Dirk Uwe Sauer. Calendar and cycle life study of li(nimnco)<sub>2</sub>-based 18650 lithium-ion batteries. *Journal of Power Sources*, 248:839 – 851, 2014.
- [51] M. Doyle, T. F. Fuller, and J. Newman. Modeling of galvanostatic charge and discharge of the lithium/polymer/insertion cell. *J. Electrochem. Soc.*, 140:1526–1533, 1993.
- [52] Meng Guo and Ralph E. White. A distributed thermal model for a li-ion electrode plate pair. *Journal of Power Sources*, 221(0):334–344, 2013.
- [53] E. E. Petersen. Diffusion in a pore of varying cross section. *AIChE Journal*, 4(3):343–345, 1958.
- [54] Martin Ebner, Ding-Wen Chung, R. Edwin Garcia, and Vanessa Wood. Tortuosity anisotropy in lithium-ion battery electrodes. *Advanced Energy Materials*, 4(5):1301278–n/a, 2014. 1301278.
- [55] F.L. Tye. Tortuosity. *Journal of Power Sources*, 9(2):89–100, 1983.
- [56] M. Doyle, J. Newman, A.S. Gozdz, C. N. Schmutz, and J.-M. Tarascon. Comparison of modeling predictions with experimental data from plastic lithium ion cells. *J. Electrochem. Soc.*, 143(6):1890–1903, 1996.

- [57] Ding-Wen Chung, Martin Ebner, David R Ely, and Vanessa Wood. Validity of the bruggeman relation for porous electrodes. *Modelling and Simulation in Materials Science and Engineering*, 21(7):074009, 2013.
- [58] Pankaj Arora and Zhengming Zhang. Battery separators. *Chemical Reviews*, 104(10):4419–4462, 2004. PMID: 15669158.
- [59] M. Safari and C. Delacourt. Modeling of a commercial graphite/lifepo4 Cell. *J. Electrochem. Soc.*, 158(5):A562–A571, 2011.
- [60] Pierre-Etienne Calbегuen. *Analyse de la microstructure des materiaux actifs d electrode positive de batteries lithium-ion*. PhD thesis, IMEP2, 2016.
- [61] M Giona and H E Roman. Fractional diffusion equation on fractals: one-dimensional case and asymptotic behaviour. *Journal of Physics A: Mathematical and General*, 25(8):2093, 1992.
- [62] Shlomo Havlin and Daniel Ben-Avraham. Diffusion in disordered media. *Advances in Physics*, 51(1):187–292, 2002.
- [63] John Newman, Karen E. Thomas and Robert M. Darling. *Mathematical Modeling of Lithium Batteries*, chapter Mathematical Modeling of Lithium Batteries, pages –. Springer, 2002.
- [64] Shao-Ling Wu, Anna E. Javier, Didier Devaux, Nitash P. Balsara, and Venkat Srinivasan. Discharge characteristics of lithium battery electrodes with a semiconducting polymer studied by continuum modeling and experiment. *Journal of The Electrochemical Society*, 161(12):A1836–A1843, 2014.
- [65] Allen J. Bard and Larry R. Faulkner. *Electrochemical Methods : Fundamentals and Application Second Edition*. John Wiley and Sons, 2001.
- [66] Sergey Y. Vassiliev, Eduard E. Levin, and Victoria A. Nikitina. Kinetic analysis of lithium intercalating systems : cyclic voltammetry. *Electrochimica Acta*, 1(1):1, January 2015. 1.
- [67] Simon Malifarge, Bruno Delobel, and Charles Delacourt. Determination of tortuosity using impedance spectra analysis of symmetric cell. *Journal of The Electrochemical Society*, 164(11):E3329–E3334, 2017.
- [68] Bharatkumar Suthar, Johannes Landesfeind, Askin Eldiven, and Hubert A. Gasteiger. Method to determine the in-plane tortuosity of porous electrodes. *Journal of The Electrochemical Society*, 165(10):A2008–A2018, 2018.

- [69] E. Markevich, M.D. Levi, and D. Aurbach. Comparison between potentiostatic and galvanostatic intermittent titration techniques for determination of chemical diffusion coefficients in ion-insertion electrodes. *Journal of Electroanalytical Chemistry*, 580(2):231–237, 2005.
- [70] Dennis W. Dees, Shigehiro Kawauchi, Daniel P. Abraham, and Jai Prakash. Analysis of the galvanostatic intermittent titration technique (gitt) as applied to a lithium-ion porous electrode. *Journal of Power Sources*, 189(1):263–268, 2009.
- [71] Moses Ender. An extended homogenized porous electrode model for lithium-ion cell electrodes. *Journal of Power Sources*, 282:572 – 580, 2015.
- [72] Lars Ole Valoen and Jan N. Reimers. Transport properties of lipf6 based li-ion battery electrolytes. *Journal of The Electrochemical Society*, 152(5):A882–A891, 2005.
- [73] Hooman Hafezi and John Newman. Verification and analysis of transference number measurements by the galvanostatic polarization method. *Journal of The Electrochemical Society*, 147(8):3036–3042, 2000.
- [74] Mohammad Farkhondeh, Mark Pritzker, Michael Fowler, and Charles Delacourt. Transport property measurement of binary electrolytes using a four-electrode electrochemical cell. *Electrochemistry Communications*, 67:11–15, 2016.
- [75] D. Djian, F. Alloin, S. Martinet, and H. Lignier. Macroporous poly(vinylidene fluoride) membrane as a separator for lithium-ion batteries with high charge rate capacity. *Journal of Power Sources*, 187(2):575–580, 2009.
- [76] Guillaume Tonin, Gavin Vaughan, Renaud Bouchet, Fannie Alloin, Marco Di Michiel, Laura Boutafa, Jean-Francois Colin, and Celine Barchasz. Multiscale characterization of a lithium/sulfur battery by coupling operando x-ray tomography and spatially-resolved diffraction. *Scientific Reports*, 7(1):2755, June 2017.
- [77] C. Edouard, M. Petit, C. Forgez, J. Bernard, and R. Revel. Parameter sensitivity analysis of a simplified electrochemical and thermal model for li-ion batteries aging. *Journal of Power Sources*, 325:482–494, 2016.
- [78] Madeleine Ecker, Thi Kim Dung Tran, Philipp Dechent, Stefan Katz, Alexander Warnecke, and Dirk Uwe Sauer. Parameterization of a physico-chemical model of a lithium-ion battery: I. determination of parameters. *Journal of The Electrochemical Society*, 162(9):A1836–A1848, 2015.
- [79] Sarah Stewart and John Newman. Measuring the salt activity coefficient in lithium-battery electrolytes. *Journal of The Electrochemical Society*, 155(6):A458–A463, 2008.

- [80] Sarah G. Stewart and John Newman. The use of UV/vis absorption to measure diffusion coefficients in lipf6 electrolytic solutions. *Journal of The Electrochemical Society*, 155(1):F13–F16, 2008.
- [81] Thomas F. Fuller, Marc Doyle, and John Newman. Simulation and optimization of the dual lithium ion insertion cell. *Journal of The Electrochemical Society*, 141(1):1–10, 1994.
- [82] Xing Jin, Ashish Vora, Vaidehi Hoshing, Tridib Saha, Gregory Shaver, R. Edwin García, Oleg Wasynczuk, and Subbarao Varigonda. Physically-based reduced-order capacity loss model for graphite anodes in li-ion battery cells. *Journal of Power Sources*, 342:750 – 761, 2017.
- [83] Mehrdad Mastali Majdabadi, Siamak Farhad, Mohammad Farkhondeh, Roydon A. Fraser, and Michael Fowler. Simplified electrochemical multi-particle model for lifepo4 cathodes in lithium-ion batteries. *Journal of Power Sources*, 275:633 – 643, 2015.
- [84] Bharatkumar Suthar, Paul W. C. Northrop, Derek Rife, and Venkat R. Subramanian. Effect of porosity, thickness and tortuosity on capacity fade of anode. *Journal of The Electrochemical Society*, 162(9):A1708–A1717, 2015.
- [85] Jorge Vazquez-Arenas, Leonardo E. Gimenez, Michael Fowler, Taeyoung Han, and Shih ken Chen. A rapid estimation and sensitivity analysis of parameters describing the behavior of commercial li-ion batteries including thermal analysis. *Energy Conversion and Management*, 87:472–482, 2014.
- [86] Z. Mao, M. Farkhondeh, M. Pritzker, M. Fowler, and Z. Chen. Multi-particle model for a commercial blended lithium-ion electrode. *Journal of The Electrochemical Society*, 163(3):A458–A469, 2016.
- [87] Shunyi Yang, Xianyou Wang, Xiukang Yang, Yansong Bai, Ziling Liu, Hongbo Shu, and Qiliang Wei. Determination of the chemical diffusion coefficient of lithium ions in spherical li[ni0.5mn0.3Co0.2]o2. *Electrochimica Acta*, 66:88–93, 2012.
- [88] K. Amine and I. Liu, J. Belharouak. High-temperature storage and cycling of C-LiFePO4/graphite Li-ion cells. *Electrochem. Com.*, 7:669–673, 2005.
- [89] D. Bernardi, E. Pawlikowski, and J. Newman. A general energy balance for battery systems. *Journal of The Electrochemical Society*, 132(1):5–12, 1985.
- [90] W. B. Gu and C. Y. Wang. Thermal electrochemical modeling of battery systems. *Journal of The Electrochemical Society*, 147(8):2910–2922, 2000.

- [91] Karen E. Thomas and John Newman. Thermal modeling of porous insertion electrodes. *Journal of The Electrochemical Society*, 150(2):A176–A192, 2003.
- [92] Y Ye, Y. Shi, N. Cai, J. Lee, and X. He. Electro-thermal modeling and experimental validation for lithium ion battery. *J. Power Sources*, 199:227–238, 2012.
- [93] M. B. Pinson and M. Z. Bazant. Theory of sei formation in rechargeable batteries: Capacity fade, accelerated aging and lifetime prediction. *J. Electrochem. Soc.*, 160(2):A243–A250, 2011.
- [94] Venkat R Subramanian, Ping Yu, Branko N Popov, and Ralph E White. Modeling lithium diffusion in nickel composite graphite. *Journal of Power Sources*, 96(2):396–405, 2001.
- [95] Irene J. Ong and John Newman. Double-layer capacitance in a dual lithium ion insertion cell. *Journal of The Electrochemical Society*, 146(12):4360–4365, 1999.
- [96] Jeremy P. Meyers, Marc Doyle, Robert M. Darling, and John Newman. The impedance response of a porous electrode composed of intercalation particles. *Journal of The Electrochemical Society*, 147(8):2930–2940, 2000.
- [97] Thomas F. Fuller, Marc Doyle, and John Newman. Relaxation phenomena in lithium-ion-insertion cells. *Journal of The Electrochemical Society*, 141(4):982–990, 1994.
- [98] Frank M. Kindermann, Patrick J. Osswald, Stefan Klink, Günter Ehlert, Jörg Schuster, Andreas Noel, Simon V. Erhard, Wolfgang Schuhmann, and Andreas Jossen. Measurements of lithium-ion concentration equilibration processes inside graphite electrodes. *Journal of Power Sources*, 342:638 – 643, 2017.
- [99] Frank M. Kindermann, Patrick J. Osswald, Günter Ehlert, Jörg Schuster, Alexander Rhein-feld, and Andreas Jossen. Reducing inhomogeneous current density distribution in graphite electrodes by design variation. *Journal of The Electrochemical Society*, 164(11):E3105–E3113, 2017.
- [100] Stephen J. Harris and Peng Lu. Effects of inhomogeneities :nanoscale to mesoscale on the durability of li-ion batteries. *The Journal of Physical Chemistry C*, 117(13):6481–6492, 2013.
- [101] Dirk Kehrwald, Paul R. Shearing, Nigel P. Brandon, Puneet K. Sinha, and Stephen J. Harris. Local tortuosity inhomogeneities in a lithium battery composite electrode. *Journal of The Electrochemical Society*, 158(12):A1393–A1399, 2011.
- [102] Daniel Burow, Kseniya Sergeeva, Simon Calles, Klaus Schorb, Alexander Börger, Christina Roth, and Paul Heitjans. Inhomogeneous degradation of graphite anodes in automotive lithium ion batteries under low-temperature pulse cycling conditions. *Journal of Power Sources*, 307:806 – 814, 2016.

- [103] Veronika Zinth, Christian von Laders, Jarn Wilhelm, Simon V. Erhard, Michael Hofmann, Stefan Seidlmayer, Joana Rebelo-Kornmeier, Weimin Gan, Andreas Jossen, and Ralph Gilles. Inhomogeneity and relaxation phenomena in the graphite anode of a lithium-ion battery probed by in situ neutron diffraction. *Journal of Power Sources*, 361:54 – 60, 2017.
- [104] M.J. Mühlbauer, O. Dolotko, M. Hofmann, H. Ehrenberg, and A. Senyshyn. Effect of fatigue/ageing on the lithium distribution in cylinder-type li-ion batteries. *Journal of Power Sources*, 348:145 – 149, 2017.
- [105] H. Gu. Mathematical analysis of a zn/niooh cell. *Journal of The Electrochemical Society*, 130(7):1459–1464, 1983.
- [106] J. R. Dahn. Phase diagram of lic6. *Phys. Rev. B*, 44:9170–9177, November 1991.
- [107] Peyman Taheri, Abraham Mansouri, Maryam Yazdanpour, and Majid Bahrami. Theoretical analysis of potential and current distributions in planar electrodes of lithium-ion batteries. *Electrochimica Acta*, 133(0):197–208, 2014.
- [108] Chunsheng Wang, Imran Kakwan, A. John Appleby, and Frank E Little. In situ investigation of electrochemical lithium intercalation into graphite powder. *Journal of Electroanalytical Chemistry*, 489(1 : 2):55–67, 2000.
- [109] Dawn M. Bernardi and Joo-Young Go. Analysis of pulse and relaxation behavior in lithium-ion batteries. *Journal of Power Sources*, 196(1):412–427, 2011.
- [110] Xiaosong Liu, Dongdong Wang, Gao Liu, Venkat Srinivasan, Zhi Liu, Zahid Hussain, and Wanli Yang. Distinct charge dynamics in battery electrodes revealed by in situ and operando soft x-ray spectroscopy. *Nature Communications*, 4:2568, October 2013.
- [111] C. Delmas, M. Maccario, L. Croguennec, F. Le Cras, and F. Weill. Lithium deintercalation in lifepo4 nanoparticles via a domino-cascade model. *Nature Materials*, 7:665, July 2008.
- [112] Jun Liu, Martin Kunz, Kai Chen, Nobumichi Tamura, and Thomas J. Richardson. Visualization of charge distribution in a lithium battery electrode. *The Journal of Physical Chemistry Letters*, 1(14):2120–2123, 2010.
- [113] T. R. Ferguson and M. Z. Bazant. Phase Transformation Dynamics in Porous Battery Electrodes. *ArXiv e-prints*, January 2014.
- [114] Kun Lee and Dongsuk Kum. The impact of inhomogeneous particle size distribution on li-ion cell performance under galvanostatic and transient loads. In *2016 IEEE Transportation Electrification Conference and Expo, Asia-Pacific (ITEC Asia-Pacific)*, pages 454–459, June 2016.

- [115] Fridolin Röder, Sören Sonntag, Daniel Schröder, and Ulrike Krewer. Simulating the impact of particle size distribution on the performance of graphite electrodes in lithium-ion batteries. *Energy Technology*, 4(12):1588–1597, 12 2016.
- [116] Venkat R. Subramanian, Vinten D. Diwakar, and Deepak Tapriyal. Efficient macro-micro scale coupled modeling of batteries. *Journal of The Electrochemical Society*, 152(10):A2002–A2008, 2005.
- [117] E. Redondo-Iglesias. *etude du vieillissement des batteries lithium-ion dans les applications "vehicule electrique" : Combinaison des effets de vieillissement calendaire et de cyclage*. PhD thesis, 2017.
- [118] Rujian Fu, Meng Xiao, and Song-Yul Choe. Modeling, validation and analysis of mechanical stress generation and dimension changes of a pouch type high power li-ion battery. *Journal of Power Sources*, 224:211 – 224, 2013.
- [119] Guangsheng Zhang, Christian E. Shaffer, Chao-Yang Wang, and Christopher D. Rahn. In-situ measurement of current distribution in a li-ion cell. *Journal of The Electrochemical Society*, 160(4):A610–A615, 2013.
- [120] See-How Ng, Fabio La Mantia, and Petr Novák. A multiple working electrode for electrochemical cells: A tool for current density distribution studies. *Angewandte Chemie International Edition*, 48(3):528–532, 2009.
- [121] Stephen J. Harris, Adam Timmons, Daniel R. Baker, and Charles Monroe. Direct in situ measurements of li transport in li-ion battery negative electrodes. *Chemical Physics Letters*, 485:265–274, 2010.
- [122] Pascal Maire, Anna Evans, Hermann Kaiser, Werner Scheifele, and Petr Novák. Colorimetric determination of lithium content in electrodes of lithium-ion batteries. *Journal of The Electrochemical Society*, 155(11):A862–A865, 2008.
- [123] Neelima Paul, Jonas Keil, Frank M. Kindermann, Sebastian Schebesta, Oleksandr Dolotko, Martin J. Mühlbauer, Ludwig Kraft, Simon V. Erhard, Andreas Jossen, and Ralph Gilles. Aging in 18650-type li-ion cells examined with neutron diffraction, electrochemical analysis and physico-chemical modeling. *Journal of Energy Storage*, 17:383 – 394, 2018.
- [124] Kevin G. Gallagher, Dennis W. Dees, Andrew N. Jansen, Daniel P. Abraham, and Sun-Ho Kang. A volume averaged approach to the numerical modeling of phase-transition intercalation electrodes presented for lixc6. *Journal of The Electrochemical Society*, 159(12):A2029–A2037, 2012.

- [125] John Christensen and John Newman. Cyclable lithium and capacity loss in li-ion cells. *Journal of The Electrochemical Society*, 152(4):A818–A829, 2005.
- [126] Christoph R. Birkl, Matthew R. Roberts, Euan McTurk, Peter G. Bruce, and David A. Howey. Degradation diagnostics for lithium ion cells. *Journal of Power Sources*, 341:373 – 386, 2017.
- [127] Stefan Schindler and Michael A. Danzer. A novel mechanistic modeling framework for analysis of electrode balancing and degradation modes in commercial lithium-ion cells. *Journal of Power Sources*, 343:226 – 236, 2017.
- [128] Pankaj Arora, Ralph E. White, and Marc Doyle. Capacity fade mechanisms and side reactions in lithium-ion batteries. *Journal of The Electrochemical Society*, 145(10):3647–3667, 1998.
- [129] Christopher Hendricks, Nick Williard, Sony Mathew, and Michael Pecht. A failure modes, mechanisms, and effects analysis (FMmea) of lithium-ion batteries. *Journal of Power Sources*, 297:113–120, 2015.
- [130] Arihant Bhandari and Jishnu Bhattacharya. Manganese dissolution from spinel cathode: Few unanswered questions. *Journal of The Electrochemical Society*, 164(2):A106–A127, 2017.
- [131] C. Delacourt, A. Kwong, X. Liu, R. Qiao, W. L. Yang, P. Lu, S. J. Harris, and V. Srinivasan. Effect of manganese contamination on the solid-electrolyte-interphase properties in li-ion batteries. *Journal of the Electrochemical Society*, 160(8):A1099–A1107, May 2013.
- [132] M. Marcinek, J. Syzdek, M. Marczewski, M. Piszcz, L. Niedzicki, M. Kalita, A. Plewa-Marczewska, A. Bitner, and P. Wiczorek. Electrolytes for li-ion transport - review. *Solid State Ionics*, 276:107–126, 2015.
- [133] Oleg Borodin, Xiaoming Ren, Jenel Vatamanu, Arthur von Wald Cresce, Jaroslaw Knap, and Kang Xu. Modeling insight into battery electrolyte electrochemical stability and interfacial structure. *Accounts of Chemical Research*, 50(12):2886–2894, 2017. PMID: 29164857.
- [134] Y. Matsumura, S. Wang, and J. Mondori. Mechanism leading to irreversible capacity loss in li ion rechargeable batteries. *Journal of The Electrochemical Society*, 142(9):2914–2918, 1995.
- [135] Y.a Qian, P.a Niehoff, M.a Barner, M.a Gatzke, X.a Mannighoff, P.a Behrends, S.a Nowak, M.a b Winter, and F.M.a Schappacher. Influence of electrolyte additives on the cathode electrolyte interphase (cei) formation on nmc in half cells with li metal counter electrode. *Journal of Power Sources*, 329:31–40, 2016. cited By 0.

- [136] Magali Gauthier, Thomas J. Carney, Alexis Grimaud, Livia Giordano, Nir Pour, Hao-Hsun Chang, David P. Fenning, Simon F. Lux, Odysseas Paschos, Christoph Bauer, Filippo Maglia, Saskia Lupart, Peter Lamp, and Yang Shao-Horn. Electrode-electrolyte interface in li-ion batteries: Current understanding and new insights. *J. Phys. Chem. Lett.*, 6(22):4653–4672, November 2015.
- [137] Roman Imhof and Petr Novak. In situ investigation of the electrochemical reduction of carbonate electrolyte solutions at graphite electrodes. *Journal of The Electrochemical Society*, 145(4):1081–1087, 1998.
- [138] E. Peled, D. Golodnitsky, and G. Ardel. Advanced model for solid electrolyte interphase electrodes in liquid and polymer electrolytes. *Journal of The Electrochemical Society*, 144(8):L208–L210, 1997.
- [139] S. Malmgren, K. Ciosek, M. Hahlin, T. Gustafsson, M. Gorgoi, H. Rensmo, and K. Edstrom. Comparing anode and cathode electrode/electrolyte interface composition and morphology using soft and hard x-ray photoelectron spectroscopy. *Electrochimica Acta*, 97:23 – 32, 2013.
- [140] Arthur v. Cresce, Selena M. Russell, David R. Baker, Karen J. Gaskell, and Kang Xu. In situ and quantitative characterization of solid electrolyte interphases. *Nano Letters*, 14(3):1405–1412, 2014. PMID: 24475938.
- [141] E. Peled, D. Bar Tow, A. Merson, A. Gladkich, L. Burstein, and D. Golodnitsky. Composition, depth profiles and lateral distribution of materials in the sei built on hopg-tof sims and xps studies. *Journal of Power Sources*, 97 : 98:52–57, 2001. Proceedings of the 10th International Meeting on Lithium Batteries.
- [142] Pallavi Verma, Pascal Maire, and Petr Novak. A review of the features and analyses of the solid electrolyte interphase in li-ion batteries. *Electrochimica Acta*, 55(22):6332–6341, 2010.
- [143] Toshihiro Yoshida, Michio Takahashi, Satoshi Morikawa, Chikashi Ihara, Hiroyuki Katsukawa, Tomoyuki Shiratsuchi, and Jun-ichi Yamaki. Degradation mechanism and life prediction of lithium-ion batteries. *Journal of The Electrochemical Society*, 153(3):A576–A582, 2006.
- [144] M. Uitz, M. Sternad, S. Breuer, C. Taubert, T. Traunig, V. Hennige, I. Hanzu, and M. Wilkening. Aging of tesla’s 18650 lithium-ion cells: Correlating solid-electrolyte-interphase evolution with fading in capacity and power. *Journal of The Electrochemical Society*, 164(14):A3503–A3510, 2017.
- [145] M. Lu, H. Cheng, and Y. Yang. A comparison of solid electrolyte interphase (sei) on the artificial graphite anode of the aged and cycled commercial lithium ion cells. *Electrochimica Acta*, 53(9):3539–3546, 2008.

- [146] Peter Keil, Simon F. Schuster, Jan Wilhelm, Julian Travi, Andreas Hauser, Ralph C. Karl, and Andreas Jossen. Calendar aging of lithium-ion batteries: I. impact of the graphite anode on capacity fade. *Journal of The Electrochemical Society*, 163(9):A1872–A1880, 2016.
- [147] Nupur Nikkan Sinha, T. H. Marks, H. M. Dahn, A. J. Smith, J. C. Burns, D. J. Coyle, J. J. Dahn, and J. R. Dahn. The rate of active lithium loss from a soft carbon negative electrode as a function of temperature, time and electrode potential. *Journal of The Electrochemical Society*, 159(10):A1672–A1681, 2012.
- [148] T. Waldmann, M. Wilka, M. Kasper, M. Fleischhammer, and M. Wohlfahrt-Mehrens. Temperature dependent ageing mechanisms in lithium-ion batteries - a post-mortem study. *Journal of Power Sources*, 262:129–135, 2014. cited By 0.
- [149] Hosang Park, Taeho Yoon, Junyoung Mun, Ji Heon Ryu, Jae Jeong Kim, and Seung M. Oh. A comparative study on thermal stability of two solid electrolyte interphase (sei) films on graphite negative electrode. *Journal of The Electrochemical Society*, 160(9):A1539–A1543, 2013.
- [150] Ortal Haik, Svetlana Ganin, Gregory Gershinsky, Ella Zinigrad, Boris Markovsky, Doron Aurbach, and I. Halalay. On the thermal behavior of lithium intercalated graphites. *Journal of The Electrochemical Society*, 158(8):A913–A923, 2011.
- [151] R. Spotnitz and J. Franklin. Abuse behavior of high-power, lithium-ion cells. *Journal of Power Sources*, 113(1):81–100, 2003.
- [152] Thomas Waldmann, Bjarn-Ingo Hogg, and Margret Wohlfahrt-Mehrens. Li plating as unwanted side reaction in commercial li-ion cells. *Journal of Power Sources*, 384:107 – 124, 2018.
- [153] Zhe Li, Jun Huang, Bor Yann Liaw, Viktor Metzler, and Jianbo Zhang. A review of lithium deposition in lithium-ion and lithium metal secondary batteries. *Journal of Power Sources*, 254:168–182, 2014.
- [154] N. Legrand, B. Knosp, P. Desprez, and F. Lapique. Physical characterization of the charging process of a li-ion battery and prediction of li plating by electrochemical modelling. *Journal of Power Sources*, 245:208–216, 2014.
- [155] Maureen Tang, Paul Albertus, and John Newman. Two-dimensional modeling of lithium deposition during cell charging. *Journal of The Electrochemical Society*, 156(5):A390–A399, 2009.

- [156] Cheon-Soo Kim, Kyung Min Jeong, Keon Kim, and Cheol-Woo Yi. Effects of capacity ratios between anode and cathode on electrochemical properties for lithium polymer batteries. *Electrochimica Acta*, 155:431 – 436, 2015.
- [157] John Cannarella and Craig B. Arnold. The effects of defects on localized plating in lithium-ion batteries. *Journal of The Electrochemical Society*, 162(7):A1365–A1373, 2015.
- [158] Mathias Petzl and Michael A. Danzer. Nondestructive detection, characterization, and quantification of lithium plating in commercial lithium-ion batteries. *Journal of Power Sources*, 254:80–87, 2014.
- [159] Bernhard Bitzer and Andreas Gruhle. A new method for detecting lithium plating by measuring the cell thickness. *Journal of Power Sources*, 262:297 – 302, 2014.
- [160] Claudia Birkenmaier, Bernhard Bitzer, Matthias Harzheim, Andreas Hintennach, and Thomas Schleid. Lithium plating on graphite negative electrodes: Innovative qualitative and quantitative investigation methods. *Journal of The Electrochemical Society*, 162(14):A2646–A2650, 2015.
- [161] Xiao-Guang Yang, Yongjun Leng, Guangsheng Zhang, Shanhai Ge, and Chao-Yang Wang. Modeling of lithium plating induced aging of lithium-ion batteries: Transition from linear to nonlinear aging. *Journal of Power Sources*, 360:28 – 40, 2017.
- [162] E. Sarasketa-Zabala, F. Aguesse, I. Villarreal, L. M. Rodriguez-Martinez, C. M. Lopez, and P. Kubiak. Understanding lithium inventory loss and sudden performance fade in cylindrical cells during cycling with deep-discharge steps. *J. Phys. Chem. C*, 119(2):896–906, January 2015.
- [163] Thomas Waldmann and Margret Wohlfahrt-Mehrens. Effects of rest time after li plating on safety behavior arc tests with commercial high-energy 18650 li-ion cells. *Electrochimica Acta*, 230:454 – 460, 2017.
- [164] Meike Fleischhammer, Thomas Waldmann, Gunther Bisle, Björn-Ingo Hogg, and Margret Wohlfahrt-Mehrens. Interaction of cyclic ageing at high-rate and low temperatures and safety in lithium-ion batteries. *Journal of Power Sources*, 274:432 – 439, 2015.
- [165] H. Buqa, A. Würsig, D. Goers, L.J. Hardwick, M. Holzapfel, P. Novák, F. Krumeich, and M.E. Spahr. Behaviour of highly crystalline graphites in lithium-ion cells with propylene carbonate containing electrolytes. *Journal of Power Sources*, 2005. Selected papers presented at the 12th International Meeting on Lithium Batteries 12th International Meeting on Lithium Batteries.

- [166] O. Dolotko, A. Senyshyn, M.J. Mahlbauer, K. Nikolowski, and H. Ehrenberg. Understanding structural changes in nmc li-ion cells by in situ neutron diffraction. *Journal of Power Sources*, 255:197 – 203, 2014.
- [167] J. Cannarella and C. B. Arnold. Stress evolution and capacity fade in constrained lithium-ion pouch cells. *J. Power Sources*, 245:745–751, 2014.
- [168] Moses Ender, Jochen Joos, Thomas Carraro, and Ellen Ivers-Tiffée. Three-dimensional reconstruction of a composite cathode for lithium-ion cells. *Electrochemistry Communications*, 13(2):166 – 168, 2011.
- [169] Moses Ender, Jochen Joos, André Weber, and Ellen Ivers-Tiffée. Anode microstructures from high-energy and high-power lithium-ion cylindrical cells obtained by x-ray nano-tomography. *Journal of Power Sources*, 269:912 – 919, 2014.
- [170] Sandeep Bhattacharya, A. Reza Riahi, and Ahmet T. Alpas. A transmission electron microscopy study of crack formation and propagation in electrochemically cycled graphite electrode in lithium-ion cells. *Journal of Power Sources*, 196(20):8719 – 8727, 2011.
- [171] S. Frisco, A. Kumar, J.F. Whitacre, and S. Litster. Understanding li-ion battery anode degradation and pore morphological changes through nano-resolution x-ray computed tomography. *Journal of the Electrochemical Society*, 163(13):A2636–A2640, 2016. cited By 0.
- [172] Bongki Son, Myung-Hyun Ryou, Jaecheol Choi, Sang-Hern Kim, Jang Myoun Ko, and Yong Min Lee. Effect of cathode/anode area ratio on electrochemical performance of lithium-ion batteries. *Journal of Power Sources*, 243(Supplement C):641 – 647, 2013.
- [173] P. Ramadass, Bala Haran, Ralph White, and Branko N. Popov. Performance study of commercial licoo2 and spinel-based li-ion cells. *Journal of Power Sources*, 111(2):210 – 220, 2002.
- [174] P Ramadass, Bala Haran, Ralph White, and Branko N Popov. Capacity fade of sony 18650 cells cycled at elevated temperatures: Part ii. capacity fade analysis. *Journal of Power Sources*, 112(2):614–620, 2002.
- [175] M. Broussely, Ph. Biensan, F. Bonhomme, Ph. Blanchard, S. Herreyre, K. Nechev, and R.J. Staniewicz. Main aging mechanisms in li ion batteries. *Journal of Power Sources*, 146:90–96, 2005. Selected papers presented at the 12th International Meeting on Lithium Batteries 12th International Meeting on Lithium Batteries.

- [176] A. Blyr, C. Sigala, G. Amatucci, D. Guyomard, Y. Chabre, and J.-M. Tarascon. Self-discharge of  $\text{LiMn}_2\text{O}_4/\text{C}$  li-ion cells in their discharged state: Understanding by means of three-electrode measurements. *Journal of The Electrochemical Society*, 145(1):194–209, 1998.
- [177] R. Spotnitz. Simulation of capacity fade in lithium-ion batteries. *Journal of Power Sources*, 113(1):72–80, 2003.
- [178] Honghe Zheng, Qingna Sun, Gao Liu, Xiangyun Song, and Vincent S. Battaglia. Correlation between dissolution behavior and electrochemical cycling performance for  $\text{LiNi}_{1/3}\text{Co}_{1/3}\text{Mn}_{1/3}\text{O}_2$ -based cells. *Journal of Power Sources*, 207:134–140, 2012.
- [179] Xianke Lin, Jonghyun Park, Lin Liu, Yoonkoo Lee, A. M. Sastry, and Wei Lu. A comprehensive capacity fade model and analysis for li-ion batteries. *Journal of The Electrochemical Society*, 160(10):A1701–A1710, 2013.
- [180] M. Safari and C. Delacourt. Simulation-based analysis of aging phenomena in a commercial graphite/lifepo4 cell. *Journal of The Electrochemical Society*, 158(12):A1436–A1447, 2011.
- [181] M. Dubarry and B. Y. Liaw. Identify capacity fading mechanism in a commercial lifepo4 cell. *J. Power Sources*, 194:541–549, 2009.
- [182] F. La Mantia, C.D. Wessells, H.D. Deshazer, and Yi Cui. Reliable reference electrodes for lithium-ion batteries. *Electrochemistry Communications*, 31:141 – 144, 2013.
- [183] J. Costard, M. Ender, M. Weiss, and E. Ivers-Tiffée. Three-electrode setups for lithium-ion batteries: II. experimental study of different reference electrode designs and their implications for half-cell impedance spectra. *Journal of The Electrochemical Society*, 164(2):A80–A87, 2017.
- [184] Moses Ender, Andre Weber, and Ivers-Tiffée Ellen. Analysis of three-electrode setups for ac-impedance measurements on lithium-ion cells by fem simulations. *Journal of The Electrochemical Society*, 159(2):A128–A136, 2011.
- [185] C. Heubner, U. Langklotz, M. Schneider, and A. Michaelis. Analysis of the counter-electrode potential in a 3-electrode lithium ion battery cell. *Journal of Electroanalytical Chemistry*, 759, Part 2:91–94, 2015.
- [186] Thorsten Baumhofer, Manuel Bruhl, Susanne Rothgang, and Dirk Uwe Sauer. Production caused variation in capacity aging trend and correlation to initial cell performance. *Journal of Power Sources*, 247:332 – 338, 2014.
- [187] Qi Zhang and Ralph E. White. Capacity fade analysis of a lithium ion cell. *Journal of Power Sources*, 179(2):793–798, 2008.

- [188] A. J. Smith, J. C. Burns, Xuemei Zhao, Deijun Xiong, and J. R. Dahn. A high precision coulometry study of the sei growth in li/graphite cells. *Journal of The Electrochemical Society*, 158(5):A447–A452, 2011.
- [189] Sébastien Grolleau, Arnaud Delaille, Hamid Gualous, Philippe Gyan, Renaud Revel, Julien Bernard, Eduardo Redondo-Iglesias, and Jérémy Peter. Calendar aging of commercial graphite/lifepo4 cell: Predicting capacity fade under time dependent storage conditions. *Journal of Power Sources*, 255:450–458, 2014.
- [190] M Broussely, S Herreyre, P Biensan, P Kaszlejna, K Nechev, and R.J Staniewicz. Aging mechanism in li ion cells and calendar life predictions. *Journal of Power Sources*, 97 : 98:13–21, 2001. Proceedings of the 10th International Meeting on Lithium Batteries.
- [191] Rachid Yazami and Yvan F Reynier. Mechanism of self-discharge in graphite : lithium anode. *Electrochimica Acta*, 47(8):1217–1223, 2002.
- [192] C. Delacourt and M. Safari. Life simulation of a graphite/lifepo4 Cell under cycling and storage. *Journal of The Electrochemical Society*, 159(8):A1283–A1291, 2012.
- [193] M. Safari and C. Delacourt. Aging of a commercial graphite/lifepo4 cell. *J. Electrochem. Soc.*, 158(10):A1123–A1135, 2011.
- [194] J. Li, N. Lotfi, R. G. Landers, and J. Park. A single particle model for lithium-ion batteries with electrolyte and stress-enhanced diffusion physics. *Journal of The Electrochemical Society*, 164(4):A874–A883, 2017.
- [195] Jie Li, Nima Lotfi, Robert G Landers, and Jonghyun Park. A single particle-based battery degradation model including chemical and mechanical degradation physics. *ECS Transactions*, 77(11):1003–1014, 2017.
- [196] Yue Qi and Stephen J. Harris. In situ observation of strains during lithiation of a graphite electrode. *Journal of The Electrochemical Society*, 157(6):A741–A747, 2010.
- [197] Arie Zaban, Ella Zinigrad, and Doron Aurbach. Impedance spectroscopy of li electrodes. 4. a general simple model of the li-solution interphase in polar aprotic systems. *J. Phys. Chem.*, 100(8):3089–3101, January 1996.
- [198] E. Peled and S. Menkin. Review sei: Past, present and future. *Journal of The Electrochemical Society*, 164(7):A1703–A1719, 2017.
- [199] E. Peled. The electrochemical behavior of alkali and alkaline earth metals in nonaqueous battery systems - the solid electrolyte interphase model. *J. Electrochem. Soc.*, 126(12):2047–2051, 1979.

- [200] Doron Aurbach. *The Role Of Surface Films on Electrodes in Li-Ion Batteries*, chapter The Role Of Surface Films on Electrodes in Li-Ion Batteries, pages –. Springer, 2002.
- [201] Victor A. Agubra and Jeffrey W. Fergus. The formation and stability of the solid electrolyte interface on the graphite anode. *Journal of Power Sources*, 268:153–162, 2014.
- [202] E. Peled, D. Golodnitsky, A. Ulus, and V. Yufit. Effect of carbon substrate on sei composition and morphology. *Electrochimica Acta*, 50(2 : 3):391–395, 2004. Polymer Batteries and Fuel Cells: Selection of Papers from First International Conference.
- [203] John Collins, Gerald Gourdin, Michelle Foster, and Deyang Qu. Carbon surface functionalities and sei formation during li intercalation. *Carbon*, 92:193–244, 2015.
- [204] Robert Darling and John Newman. Modeling side reactions in composite liymn2o4 electrodes. *Journal of The Electrochemical Society*, 145(3):990–998, 1998.
- [205] J. Christensen and J. Newman. Effect of anode film resistance on the charge/discharge capacity of a lithium-ion battery. *Journal of The Electrochemical Society*, 150(11):A1416–A1420, 2003.
- [206] John Christensen and John Newman. A mathematical model for the lithium-ion negative electrode solid electrolyte interphase. *Journal of The Electrochemical Society*, 151(11):A1977–A1988, 2004.
- [207] P. Ramadass, Bala Haran, Parthasarathy M. Gomadam, Ralph White, and Branko N. Popov. Development of first principles capacity fade model for li-ion cells. *Journal of The Electrochemical Society*, 151(2):A196–A203, 2004.
- [208] Ramaraja P. Ramasamy, Jong-Won Lee, and Branko N. Popov. Simulation of capacity loss in carbon electrode for lithium-ion cells during storage. *Journal of Power Sources*, 166(1):266–272, 2007.
- [209] Harry J. Ploehn, Premanand Ramadass, and Ralph E. White. Solvent diffusion model for aging of lithium-ion battery cells. *Journal of The Electrochemical Society*, 151(3):A456–A462, 2004.
- [210] D Aurbach, B Markovsky, I Weissman, E Levi, and Y Ein-Eli. On the correlation between surface chemistry and performance of graphite negative electrodes for li ion batteries. *Electrochimica Acta*, 45(1 : 2):67–86, 1999.
- [211] Yixuan Wang, Shinichiro Nakamura, Makoto Ue, and Perla B. Balbuena. Theoretical studies to understand surface chemistry on carbon anodes for lithium-ion batteries reduction mechanisms of ethylene carbonate. *Journal of the American Chemical Society*, 123(47):11708–11718, 2001. PMID: 11716728.

- [212] Oleg Borodin, Grant D. Smith, and Peng Fan. Molecular dynamics simulations of lithium alkyl carbonates. *The Journal of Physical Chemistry B*, 110(45):22773–22779, 2006. PMID: 17092027.
- [213] A. J. Smith, Hannah M. Dahn, J. C. Burns, and J. R. Dahn. Long-term low-rate cycling of licoo2/graphite li-ion cells at 55°C. *Journal of The Electrochemical Society*, 159(6):A705–A710, 2012.
- [214] Frank M. Kindermann, Jonas Keil, Alexander Frank, and Andreas Jossen. A sei modeling approach distinguishing between capacity and power fade. *Journal of The Electrochemical Society*, 164(12):E287–E294, 2017.
- [215] Dongjiang Li, Dmitri L. Danilov, Barbara Zwickersch, Maximilian Fichtner, Yong Yang, RÃ(E)ediger-A. Eichel, and Peter H.L. Notten. Modeling the degradation mechanisms of c6/lifepo4 batteries. *Journal of Power Sources*, 375:106 – 117, 2018.
- [216] P. Liu, J. Wang, J. Hicks-Garner, E. Sherman, S. Soukiazian, M. Verbrugge, H. Tataria, J. Musser, and P. Finamore. Aging mechanisms of LiFePO4 batteries deduced by electrochemical and structural analyses. *J. Electrochem. Soc.*, 157(4):A499–A507, 2010.
- [217] A. A. Tahmasbi, T. Kadyk, and M. H. Eikerling. Statistical physics-based model of solid electrolyte interphase growth in lithium ion batteries. *Journal of The Electrochemical Society*, 164(6):A1307–A1313, 2017.
- [218] Yoon-Soo Park and Sung-Man Lee. Effects of particle size on the thermal stability of lithiated graphite anode. *Electrochimica Acta*, 54(12):3339 – 3343, 2009.
- [219] Stefan Klink, Philipp Weide, Martin Muhler, Wolfgang Schuhmann, and Fabio La Mantia. New insights into sei formation in lithium ion batteries: Inhomogeneous distribution of irreversible charge losses across graphite electrodes. *ECS Transactions*, 62(1):265–271, 2014.
- [220] R.N. Methekar, P. W.C. Northrop, K. Chen, Braatz R.D., and Subramanian V. R. Kinetic Monte Carlo simulation of surface heterogeneity in graphite anodes for lithium-ion batteries: Passive layer formation. *J. Electrochem. Soc.*, 158:A363–A370, 2011.
- [221] Fridolin Röder, Richard D. Braatz, and Ulrike Krewer. Multi-scale simulation of heterogeneous surface film growth mechanisms in lithium-ion batteries. *Journal of The Electrochemical Society*, 164(11):E3335–E3344, 2017.
- [222] Fabian Single, Birger Horstmann, and Arnulf Latz. Dynamics and morphology of solid electrolyte interphase (sei). *Phys. Chem. Chem. Phys.*, 18:17810–17814, 2016.

- [223] Fabian Single, Birger Horstmann, and Arnulf Latz. Revealing sei morphology: In-depth analysis of a modeling approach. *Journal of The Electrochemical Society*, 164(11):E3132–E3145, 2017.
- [224] E. Redondo-Iglesias, P. Venet, and S. Pelissier. Global model for self-discharge and capacity fade in lithium-ion batteries based on the generalized eyring relationship. *IEEE Transactions on Vehicular Technology*, PP(99):1–1, 2017.
- [225] Pankaj Arora, Marc Doyle, and Ralph E. White. Mathematical modeling of the lithium deposition overcharge reaction in lithium-ion batteries using carbon-based negative electrodes. *Journal of The Electrochemical Society*, 146(10):3543–3553, 1999.
- [226] Hao Ge, Tetsuya Aoki, Nobuhisa Ikeda, Sohei Suga, Takuma Isobe, Zhe Li, Yuichiro Tabuchi, and Jianbo Zhang. Investigating lithium plating in lithium-ion batteries at low temperatures using electrochemical model with nmr assisted parameterization. *Journal of The Electrochemical Society*, 164(6):A1050–A1060, 2017.
- [227] Simon Hein and Arnulf Latz. Influence of local lithium metal deposition in 3d microstructures on local and global behavior of lithium-ion batteries. *Electrochimica Acta*, 201:354 – 365, 2016.
- [228] Roger D. Perkins, Alfred V. Randall, Xiangchun Zhang, and Gregory L. Plett. Controls oriented reduced order modeling of lithium deposition on overcharge. *Journal of Power Sources*, 209:318–325, 2012.
- [229] Thomas Waldmann, Michael Kasper, and Margret Wohlfahrt-Mehrens. Optimization of charging strategy by prevention of lithium deposition on anodes in high-energy lithium-ion batteries : Electrochemical experiments. *Electrochimica Acta*, 178:525 – 532, 2015.
- [230] F. Grismann, F. Brauchle, T. Gerbert, A. Gruhle, J. Parisi, and M. Knipper. Impact of different aging mechanisms on the thickness change and the quick-charge capability of lithium-ion cells. *Journal of Energy Storage*, 14, Part 1:158 – 162, 2017.
- [231] Mathias Petzl, Michael Kasper, and Michael A. Danzer. Lithium plating in a commercial lithium-ion battery: A low-temperature aging study. *Journal of Power Sources*, 275:799–807, 2015.





## **Modélisation multi-physique de l'électrode de graphite au sein d'une batterie lithium-ion : Étude des hétérogénéités en lithiation et des mécanismes de vieillissement.**

L'électrode négative des batteries lithium-ion est communément en graphite. Bien qu'ayant une capacité spécifique intéressante, le vieillissement, la cinétique d'intercalation et le transport du lithium à la fois dans le matériau actif et les porosités de cette électrode limitent son fonctionnement optimal et homogène. Dans ce travail de thèse, les mécanismes à l'origine de ces limites sont explicités grâce à un modèle multi-physique de type électrode poreuse.

Une étude de sensibilité du modèle a montré l'importance des paramètres liés à la cinétique d'intercalation et au transport du lithium en phase solide et liquide. L'exploitation du modèle, validé expérimentalement, montre que, lors du fonctionnement de l'électrode, les apparitions d'hétérogénéité de lithiation sont corrélées à la forme particulière du potentiel d'équilibre du graphite vis-à-vis de son taux de lithiation. La modélisation de la distribution de taille des particules, amplifie grandement ces hétérogénéités et dégrade fortement la performance globale de l'électrode. En première approche, une mesure *operando* de la distribution des états de lithiation confirme l'aspect hétérogène du fonctionnement de l'électrode.

Les données des performances en cyclages et en calendrier de cellules graphite-NMC ont permis de construire différents modèles de vieillissement de l'électrode. La croissance de la couche de passivation (SEI) peut expliquer ainsi à elle seule la perte de lithium cyclable. Sa croissance hétérogène est obtenue par le modèle, mais sa quantification est à améliorer. En vieillissement, les gains de capacités et les pertes brutales sont expliqués respectivement par des mécanismes de dissolution de SEI et de formation de lithium-plating, impactant la structure de l'électrode.

**Mots-clefs :** Batteries lithium-ion; Graphite; Modélisation multi-physique; Mécanismes de vieillissement

## **Physics-based models of graphite electrode in a lithium-ion battery: Study of lithiation heterogeneities and aging mechanisms.**

Negative electrodes of lithium-ion batteries are mainly based on graphite, because of their good electrochemical properties. Unfortunately, intercalation kinetics, aging phenomena and lithium transport through active material and electrode porosity decay the optimal and homogeneous operations of this electrode. Origins of these limits are investigated in this work thanks to a porous electrode model.

A sensitivity study indicates that preponderant model parameters are related to the kinetics and lithium transport in solid and liquid phases. The model is experimentally validated at a cell scale and predicts the appearances of lithium heterogeneities during the graphite lithiation. They are correlated to the staged shape of the graphite equilibrium potential. Modeling additional inhomogeneity sources, especially particle distribution, amplifies these heterogeneities and decrease drastically cell performance. In a first approach, an *operando* measure of the local lithiation state confirms this heterogeneity aspect during operations.

In a second part, data of cycled and calendar aged graphite-NMC cell validates different aging models. The growth of the passive layer on the graphite surface (SEI) explains the cyclable lithium loss on its own. SEI heterogeneities exist but are negligible in the classical porous model in opposition to experimental finding. Capacity recoveries and sudden loss are explained respectively via a SEI dissolution mechanism and lithium-plating correlated to the degradation of the electrode transport properties.

**Keywords:** Lithium-ion battery; Graphite electrode; physics-based models; aging mechanism

